USING TIME-RESOLVED FLUORESCENCE TO INVESTIGATE EXCITON HARVESTING IN ORGANIC PHOTOVOLTAIC BLENDS

Alexander J. Ward

A Thesis Submitted for the Degree of PhD
at the
University of St Andrews

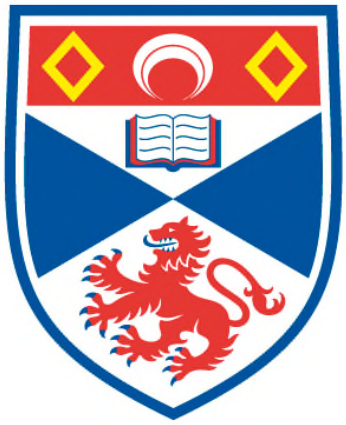

2015

USING TIME-RESOLVED FLUORESCENCE TO INVESTIGATE EXCITON HARVESTING IN ORGANIC PHOTOVOLTAIC BLENDS

Alexander J. Ward

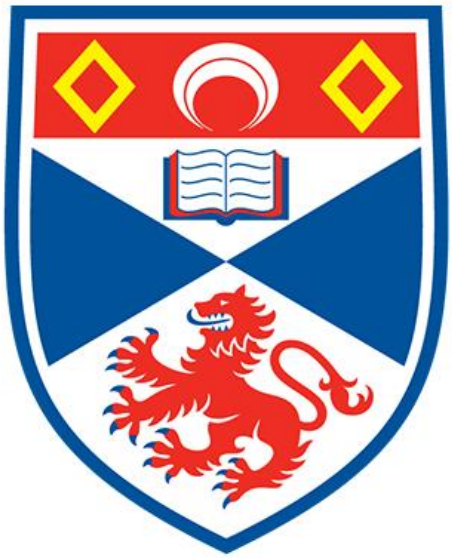

University of St Andrews

This thesis is submitted to the School of Physics & Astronomy for the degree of Doctor of Philosophy at the University of St Andrews

19/09/14

ABSTRACT

This thesis is an investigation of the photophysical processes that occur in organic photovoltaic blends in the time between light being absorbed and free charges being generated. The purpose of all solar cells is to generate a photocurrent. The free charges, as they flow out of the device, make up the photocurrent, so understanding the processes by which they are created is vitally important to organic photovoltaic research.

The main experimental method used was time-resolved fluorescence spectroscopy. This technique was used to probe the exciton population with respect to time for a variety of blends of organic semiconductors, including the high performance photovoltaic materials PCDTBT, PTB7, C_{71}-PCBM and P3HT. The main goal of the work was to characterise the exciton diffusion lengths of these materials by developing a technique called *volume quenching*. Volume quenching involves blending a small quantity of quenching material into a thin film of semiconducting material. These introduced quenching sites render excitons unemissive on contact. Thus, from the drop in fluorescence compared with the 'unquenched' material, it was possible to work out what proportion of the initial excitons have encountered a quenching site in the blends. The results can then be fitted to quantify how diffusive the excitons are – i.e. how far they move.

By looking at the rate constant of the quenching process and how it varies with respect to time, quencher concentration and quencher type, it was possible to generate a wealth of additional information, not just about exciton diffusion, but about all the inter-related processes that contribute to exciton harvesting. These processes included the measurement of long-range energy transfer from the donor to the acceptor, electron transfer at the interface with the acceptor and the understanding of nanomorphology of donor-acceptor heterojunctions.

CANDIDATE'S DECLARATIONS

I, Alexander J. Ward hereby certify that this thesis, which is approximately 49,000 words in length, has been written by me, and that it is the record of work carried out by me, or principally by myself in collaboration with others as acknowledged, and that it has not been submitted in any previous application for a higher degree.

I was admitted as a research student in September, 2010 and as a candidate for the degree of Doctor of Philosophy in September, 2010; the higher study for which this is a record was carried out in the University of St Andrews between 2010 and 2014.

Date …… signature of candidate ……

SUPERVISOR'S DECLARATION

I hereby certify that the candidate has fulfilled the conditions of the Resolution and Regulations appropriate for the degree of Doctor of Philosophy in the University of St Andrews and that the candidate is qualified to submit this thesis in application for that degree.

Date …….…… signature of supervisor ……

PERMISSION FOR PUBLICATION

In submitting this thesis to the University of St Andrews I understand that I am giving permission for it to be made available for use in accordance with the regulations of the University Library for the time being in force, subject to any copyright vested in the work not being affected thereby. I also understand that the title and the abstract will be published, and that a copy of the work may be made and supplied to any bona fide library or research worker, that my thesis will be electronically accessible for personal or research use unless exempt by award of an embargo as requested below, and that the library has the right to migrate my thesis into new electronic forms as required to ensure continued access to the thesis. I have obtained any third-party copyright permissions that may be required in order to allow such access and migration, or have requested the appropriate embargo below. The following is an agreed request by candidate and supervisor regarding the publication of this thesis:

PRINTED AND ELECTRONIC EMBARGO

Embargo on all print and electronic publication for a period of 1 years, on the following ground: because publication would preclude future publication.

Date …….. Signature of candidate ……

Signature of supervisor ……

PUBLICATION LIST

Accepted

Ward, A. J.; Ruseckas, A.; Samuel, I. D. W., A Shift from Diffusion Assisted to Energy Transfer Controlled Fluorescence Quenching in Polymer–Fullerene Photovoltaic Blends. *The Journal of Physical Chemistry C* 2012, *116* (45), 23931-23937.

Hedley, G. J.; Ward, A. J.; Alekseev, A.; Howells, C. T.; Martins, E. R.; Serrano, L. A.; Cooke, G.; Ruseckas, A.; Samuel, I. D. W., Determining the optimum morphology in high-performance polymer-fullerene organic photovoltaic cells. *Nat Commun* 2013, *4*.

Submitted

The Impact of Driving Force on Electron Transfer Rates in Photovoltaic Donor-Acceptor Blends, *Alexander J. Ward, Arvydas Ruseckas, Bernd Ebenhoch, Mohanad Mousa Kareem, Luis A. Serrano, Manal Al-Eid, Brian Fitzpatrick, Vincent M. Rotello, Graeme Cooke, Ifor D. W. Samuel*

Submitted to Advanced Materials

In Preparation

Uncovering The Nanoscale Morphology in PTB7 Blends With Time-Resolved Photoluminescence, *Gordon J. Hedley, Alexander J. Ward, Alexander Aleeksev, Iain Robertson, Bernd Ebenhoch, Arvydas Ruseckas, Ifor D.W. Samuel*
Target Journal: JPCC

Blend Demixing in a Highly Crystallizable Low-Bandgap Photovoltaic Polymer:Fullerene Blend, *Gordon J. Hedley, Alexander Aleeksev, Alexander J. Ward, Xiaoli Zhao, Zhaobin Chen, Xiaoniu Yang, Ifor D.W. Samuel*
Target Journal: PCCP

Phase Separation in Additive Processed Polymer-Fullerene film blends, *Yun Long, Alexander J Ward, Arvydas Ruseckas, Ifor D W Samuel*

Controlling exciton diffusion and fullerene distribution in ternary photovoltaic blends by side chain modification, *M. Tariq Sajjad, Alexander J. Ward, C. Kastner, A. Ruseckas, H. Hoppe and Ifor D. W. Samuel*

ACKNOWLEDGMENTS

There are many people who contributed significantly to work carried out in this thesis and ought to be sincerely thanked.

Firstly I would like to thank my supervisor, Professor Ifor Samuel, who has spent a herculean effort over the course of my PhD guide me in the right direction. I very much appreciate the opportunity he gave me when he invited me to join his research group and am very grateful for how supportive he has been, not just throughout my PhD but also as I took a few steps into the commercial world.

A particular gratitude goes to Arvydas and Gordon for patiently answering my physics questions with almost daily regularity. It is no exaggeration to say I learnt all the photophysics I know (and actually pretty much all the physics I know) from these two individuals. I will miss Gordon's soap-box polemics and the extended debates they kindle. Arvydas, all the way through my PhD has acted as a wise and gentle guide through the strange land of organic semiconductor physics, and none of the work in this thesis would have been possible without him.

I would like to express thanks to Jane Bristow (who was particularly excited to get a mention here), for proof reading the first draft of this document which she did at a time when she already had a lot going on.

Finally many thanks go to my parents, Simon and Chris for their love and support (and also a huge amount of proof reading).

CONTENTS PAGE

1

INTRODUCTION

This thesis investigates the photophysics of organic solar cells, an emerging class of solar cell material. It explores what happens in the first fleeting fractions of a second after these materials are exposed to light, as it is these moments that determines whether the energy of an absorbed photon is wasted as heat or harvested into an electrical current. What critical processes must occur and what are the necessary conditions to efficiently perform this conversion of incident light into free charges and then photocurrent? If these mechanisms could be understood and optimised, would solar cell efficiencies improve?

In future decades it is likely that an ever increasing proportion of our industrial and scientific efforts will be applied towards maintaining the high standard of living we have already attained rather than, as it always has been historically, to improve the comfort and ease with which we live our lives. We will almost certainly have reduced food production[1,2] and crop yields[3] due to climate change as well as a depletion of accessible phosphate reserves[4]; a major feedstock for many fertilisers. Extreme weather phenomena such as hurricanes, heatwaves and flash flooding will in all likelihood become more common[5-8]. Throughout all these challenges, we, as a society, urgently need to transition away from fossil fuels to more sustainable energy sources.

The need to continue powering our world, with looming need to cease releasing carbon dioxide into the atmosphere, is typically referred to as the energy crisis[9]. The only possible way to resolve this impending crisis is to shift energy generation towards low-carbon energy generation technologies. The problem can be approached in three ways; firstly, it may be possible for traditional fossil fuel burning power stations to be converted so that the carbon dioxide emitted is captured and stored rather than being released into the atmosphere. This is termed carbon capture and storage (CCS)[10]. The second method is to shift to low-carbon energy sources, that are not truly renewable, but will not run out in the short or medium term[11]. These are predominantly nuclear; either conventional fission, fast breeder fission reactors or fusion reactors. The final possibility is to transition to truly renewable energy generation techniques. These include wind, solar, hydropower, tidal and geothermal energy[12].

The first option, CCS, while requiring the smallest infrastructure investment, uses a significant portion of the chemical energy in the fossil fuels in order to capture the carbon[13]. In addition long-term storage is problematic with little information as to how to keep the CO_2 sequested over the geological timescales required[14]. Finally, fossil fuels are a finite resource so this option merely postpones the inevitable by a few decades[15].

The second option, nuclear energy, offers a more robust solution but has definite downsides. The reserves of uranium required by conventional nuclear power stations will only last a further 100 years, though this is increased to 3000 years if fast-breeder nuclear reactors become widespread[11]. If the use of nuclear power becomes commonplace, the chance of the proliferation of an associated

technology; nuclear armaments, increases too, adding to the risk of global nuclear war. In addition there is the serious issue of disposing of the hazardous nuclear waste produced, a problem for which there is not, so far, a satisfactory solution[16]. Finally the public perception that nuclear power is unsafe is major detractor to additional nuclear power plant construction[17].

The final options, the true renewables, would be the most sustainable in the long term but require the most infrastructure investment, both in terms of energy generation and distribution. They also tend to provide an inconsistent source of electricity and are often quite site specific – for example, a hydroelectric power station can only be constructed in areas where a river can be dammed. With the exception of hydroelectric power, they tend to be much more costly per kilowatt hour than currently available non-renewable technologies, though the trend is towards a decline in costs, while fossil fuel technologies are becoming more expensive[18]. Although the sustainable solution to the energy crisis is likely to be a combination of all the options listed, one very promising avenue of research is in solar photovoltaic cells.

Solar photovoltaic devices directly convert solar radiation into electrical power. Solar energy is an obvious choice because it is so plentiful; there is the potential to generate approximately 100W/m^2 from *any* flat surface in the UK[19]. This value dwarfs the total energy potential of any other green energy .The first practical photovoltaic was developed in the Bell Telephone Laboratories in 1954[20]. Since this early 6% power conversion efficiency (PCE), solar cells have improved to the point that a mass produced silicon solar cell has a PCE of 12-16%[21]. While these efficiencies are high enough to be useful, especially for off-grid power

generation in areas with high incident solar radiation[22], they are still a much more expensive way of generating electricity than other conventional and renewable energy sources. A major reason for the high price is the high energy cost caused by the lengthy purification of electronic grade silicon and the necessity of growing large crystals of the material at high vacuum[23]. An emerging type of photovoltaic device, the organic photovoltaic (OPV), offers a promising way to retain the advantages of solar cells while significantly pushing the energy cost and the financial cost down to levels comparable to or lower than current methods of power generation.

Organic photovoltaic devices almost could not be more different to the traditional black crystalline silicon solar cell. The semiconducting materials that they are made from, organic semiconductors, are flexible, brightly coloured and solution processable; meaning that they can printed using a roll-to-roll process with little more difficulty than we currently produce newspapers. These unique properties have already seen their use in new light sources[24], transistors[25] and they have had widespread commercial success in smartphone display technology[26]. Though solar cells made using organic semiconductors have the potential be a low-cost and versatile way to generate green energy, there are several technical drawbacks that need to be overcome as well as some significant gaps in our understanding of how these devices function. One of the major unique features that distinguishes an organic semiconductor from a conventional, inorganic, semiconductor is that when light is absorbed and an excited state formed, it consists of an electron-hole pair that is very strongly bound. Because the dielectric constant of an organic material is so much lower than an inorganic material, when

the electron is promoted to the first excited state it remains coulombically bound to the hole. This exciton has a lifetime of up to a nanosecond (10^{-9} s) before it relaxes down to the ground state and the energy of the photon is lost as heat or through fluorescence. It is within this narrow window of opportunity that an efficient OPV must wrench apart the electron and hole to generate free charges, which when they flow out of the device, deliver a current.

Converting the energetic but useless excitons into useful free charges is known as exciton harvesting. Understanding the processes that lead to exciton harvesting is the major focus of this work. The energetic driving force to split the excitons is provided by the introduction of a second organic material with slightly different electronic properties. This second material has a higher electron affinity, meaning that an additional electron would be much lower in energy if it resided on this new material than on the original material. This new material is known as the electron acceptor because it has a propensity to accept electrons and the original material is known as the electron donor because it has the propensity to donate electrons. When these two materials are mixed, an exciton, which consists of a bound electron and hole, has an energetic incentive to split at the interface between them, as the electron would be more stable to jump onto the electron acceptor, but the hole would be more stable to remain on the electron donor. This process is called charge transfer.

Unfortunately, because this process only happens at the interface between the electron donor and the electron acceptor, excitons must migrate to these interfaces in order for efficient exciton harvesting to occur. Excitons move via a random hopping process between nearby sections of the organic semiconductor.

This process is called exciton diffusion and is another critical process in exciton harvesting because the rate at which the excitons are diffusing will determine the number of excitons near enough to the interface to undergo charge transfer.

A third critical parameter which controls exciton harvesting in these donor-acceptor blends is known as the blend morphology. This is the degree of mixing; how large the domains of donor and acceptor are, in the solid film. If the domains are very large, then the surface area between the two components is small and consequently exciton harvesting, which only happens at this interface, will be less efficient. In this scenario it may be necessary for the exciton to diffuse a very long way before encountering the interface and it may not occur at all in the exciton's short lifetime. If the two components mix very well, then it is possible that every single donor molecule will be close enough to an acceptor molecule for charge separation to occur, and exciton harvesting will be very efficient.

In this thesis, the kinetics of exciton harvesting are investigated using time-resolved fluorescence spectroscopy. By varying a number of parameters and by applying appropriate models to explain the results, the roles of exciton diffusion, blend morphology and the parameters controlling charge transfer are elucidated. This work builds up a complete and cohesive picture of exciton harvesting in organic semiconductor based solar cells.

In chapter 2, the unique properties of organic semiconductors are described with relation to how the electronic structure of these materials makes them ideal for photovoltaic devices. The structure and internal processes that lead to the generation of photocurrent in an organic photovoltaic device are also described.

In chapter 3, the experimental methods used to investigate the photophysics of organic semiconductors are described. The predominant focus being the measurement of the time-resolved fluorescence of these materials.

The theoretical methods used to model exciton diffusion; a critical process in organic photovoltaic devices, are described in chapter 4. Mainly this consists of using solution to Fick's laws of diffusion to predict the behaviour of the excitons, and ways to account for the other, non-diffusive, processes occurring concurrently in these materials.

In chapter 5, the kinetics of exciton harvesting in the high performance photovoltaic blend PCDTBT:C_{71}-PCBM are investigated. This blend is compared with the model system MEH-PPV:C_{61}-PCBM. The highly time-dependent rate constant for fluorescence quenching which is dependent on the mass ratio of C_{71}-PCBM in the blend indicates that the excitons are hastened to the interface by a long-range process. This long-range process is assigned to Förster resonance energy transfer (FRET). The conclusion is that this materials combination could deliver very efficient exciton harvesting, despite a low exciton diffusion coefficient, by enhancing the concentration of excitons near the interface using FRET. This mechanism has been subsequently suggested to have a major role in other high performance blends[27,28].

In chapter 6, a single high photovoltaic performance donor material, PTB7, is prepared in blends with a wide variety of different acceptor materials. The quenching kinetics of excitons in these blends showed a strong trend with respect to the electronic properties of the acceptor used. As electron acceptors were used with progressively higher electron affinities (leading to increasing driving forces

for charge transfer) then the rates of electron transfer increased. This trend reached a maximum at an electron affinity offset of 0.6 eV and acceptor materials with a higher offset led to lower rates of charge transfer. This approximately Gaussian dependence on driving force is characteristic of electron transfer as described using a commonly used theory of electron transfer – Marcus theory.

In Chapter 7, rather than investigating a donor material, the exciton diffusion coefficient of a ubiquitous electron acceptor, C_{71}-PCBM, is measured. The moderate exciton diffusion length of 4.4 nm measured indicates that this acceptor material is able to contribute to exciton harvesting in the blend, but exciton harvesting ought to be efficient only when the domain sizes in the morphology are on approximately this length-scale. This reasoning was extended further, by using solutions for the diffusion equation with spherical boundary conditions to model the rate of quenching of excitons in spherical domains, with the assumption that quenching occurred only on the surface of the sphere (which represented the donor-acceptor interface). This was fitted to the time-resolved fluorescence of device blends, in conjunction with the previously measured exciton diffusion coefficient to predict the size of the domains in the blend. The predictions given by this method, 60 nm diameter, were significantly smaller than those observed in the topology of the film as measured with AFM which was about 200 nm. The prediction of a smaller domain size was, however, validated when a horizontal cross-section of the film showed a clear substructure with 60 nm domains.

Chapter 8 focusses on exciton harvesting of the extremely well studied material, P3HT. The rate of harvesting with the conventional electron accepters C_{61}-PCBM and C_{71}-PCBM is compared with the rate of electron harvesting when a

new non-fullerene electron acceptor, M10 was used. M10 increased the rate of exciton harvesting by a factor of ~5. After ruling out other factors, such as differences in morphology, it was concluded that the charge transfer step must be significantly faster in M10 compared to the fullerene acceptors. This is a significant departure from the conventional view in the literature that usually assumes that electron transfer is much more rapid than the rate at which excitons are delivered to the interface through exciton diffusion[29,30]. That the system is primarily limited by the rate at which charge transfer can occur, will mean that quenching will be dependent on the size of the area of the interface at which this process is occurring. Two different models are discussed and applied to use the rate of exciton harvesting to predict the amount of donor-acceptor interface per unit volume, which can then be translated into a measure of the morphology.

1.2. REFERENCES

1 Parry, M., Rosenzweig, C., Iglesias, A., Fischer, G. & Livermore, M. Climate change and world food security: a new assessment. *Global Environmental Change* **9, Supplement 1**, S51-S67, doi:http://dx.doi.org/10.1016/S0959-3780(99)00018-7 (1999).

2 Schmidhuber, J. & Tubiello, F. N. Global food security under climate change. *Proceedings of the National Academy of Sciences* **104**, 19703-19708, doi:10.1073/pnas.0701976104 (2007).

3 Schlenker, W. & Roberts, M. J. Nonlinear temperature effects indicate severe damages to U.S. crop yields under climate change. *Proceedings of the National Academy of Sciences* **106**, 15594-15598, doi:10.1073/pnas.0906865106 (2009).

4 Abelson, P. H. A Potential Phosphate Crisis. *Science* **283**, 2015, doi:10.1126/science.283.5410.2015 (1999).

5 Meehl, G. A. *et al.* Trends in Extreme Weather and Climate Events: Issues Related to Modeling Extremes in Projections of Future Climate Change*. *Bulletin of the American Meteorological Society* **81**, 427-436, doi:10.1175/1520-0477(2000)081<0427:tiewac>2.3.co;2 (2000).

6 Meehl, G. A. *et al.* An Introduction to Trends in Extreme Weather and Climate Events: Observations, Socioeconomic Impacts, Terrestrial Ecological Impacts, and Model Projections*. *Bulletin of the American Meteorological Society* **81**, 413-416, doi:10.1175/1520-0477(2000)081<0413:aittie>2.3.co;2 (2000).

7 Rosenzweig, C., Iglesias, A., Yang, X. B., Epstein, P. & Chivian, E. Climate Change and Extreme Weather Events; Implications for Food Production, Plant Diseases, and Pests. *Global Change & Human Health* **2**, 90-104, doi:10.1023/a:1015086831467 (2001).

8 Banholzer, S., Kossin, J. & Donner, S. in *Reducing Disaster: Early Warning Systems For Climate Change* (eds Ashbindu Singh & Zinta Zommers) Ch. 2, 21-49 (Springer Netherlands, 2014).

9 Richardson, G. L. in *OCEANS 2011.* 1-10.

10 Pires, J. C. M., Martins, F. G., Alvim-Ferraz, M. C. M. & Simões, M. Recent developments on carbon capture and storage: An overview. *Chemical Engineering Research and Design* **89**, 1446-1460, doi:http://dx.doi.org/10.1016/j.cherd.2011.01.028 (2011).

11 Saito, S. Role of nuclear energy to a future society of shortage of energy resources and global warming. *Journal of Nuclear Materials* **398**, 1-9, doi:http://dx.doi.org/10.1016/j.jnucmat.2009.10.002 (2010).

12 Baños, R. *et al.* Optimization methods applied to renewable and sustainable energy: A review. *Renewable and Sustainable Energy Reviews* **15**, 1753-1766, doi:http://dx.doi.org/10.1016/j.rser.2010.12.008 (2011).

13 Rubin, E. S., Chen, C. & Rao, A. B. Cost and performance of fossil fuel power plants with CO2 capture and storage. *Energy Policy* **35**, 4444-4454, doi:http://dx.doi.org/10.1016/j.enpol.2007.03.009 (2007).

14 Haszeldine, R. S. Carbon Capture and Storage: How Green Can Black Be? *Science* **325**, 1647-1652, doi:10.1126/science.1172246 (2009).
15 Shafiee, S. & Topal, E. When will fossil fuel reserves be diminished? *Energy Policy* **37**, 181-189, doi:http://dx.doi.org/10.1016/j.enpol.2008.08.016 (2009).
16 Hannum, W. H. Modern and future nuclear fuel cycles and the relationship with nuclear waste management. *Wiley Interdisciplinary Reviews: Energy and Environment* **3**, 323-329, doi:10.1002/wene.99 (2014).
17 Kessides, I. N. The future of the nuclear industry reconsidered: Risks, uncertainties, and continued promise. *Energy Policy* **48**, 185-208, doi:http://dx.doi.org/10.1016/j.enpol.2012.05.008 (2012).
18 Esteban, M. D., Diez, J. J., López, J. S. & Negro, V. Why offshore wind energy? *Renewable Energy* **36**, 444-450, doi:http://dx.doi.org/10.1016/j.renene.2010.07.009 (2011).
19 MacKay, D. J. *Sustainable Energy – Withough the hot air!* , (UIT Cambridge, 2009).
20 Chapin, D. M., Fuller, C. S. & Pearson, G. L. A New Silicon p-n Junction Photocell for Converting Solar Radiation into Electrical Power. *Journal of Applied Physics* **25**, 676-677, doi:doi:http://dx.doi.org/10.1063/1.1721711 (1954).
21 Shah, A., Torres, P., Tscharner, R., Wyrsch, N. & Keppner, H. Photovoltaic Technology: The Case for Thin-Film Solar Cells. *Science* **285**, 692-698, doi:10.1126/science.285.5428.692 (1999).
22 Szabó, S., Bódis, K., Huld, T. & Moner-Girona, M. Energy solutions in rural Africa: mapping electrification costs of distributed solar and diesel generation versus grid extension. *Environmental Research Letters* **6**, 034002 (2011).
23 Espinosa, N., Hosel, M., Angmo, D. & Krebs, F. C. Solar cells with one-day energy payback for the factories of the future. *Energy & Environmental Science* **5**, 5117-5132, doi:10.1039/c1ee02728j (2012).
24 Tyan, Y.-S. Organic light-emitting-diode lighting overview. *PHOTOE* **1**, 011009-011009-011015, doi:10.1117/1.3529412 (2011).
25 Allard, S., Forster, M., Souharce, B., Thiem, H. & Scherf, U. Organic Semiconductors for Solution-Processable Field-Effect Transistors (OFETs). *Angewandte Chemie International Edition* **47**, 4070-4098, doi:10.1002/anie.200701920 (2008).
26 Lee, H., Park, I., Kwak, J., Yoon, D. Y. & Lee, C. Improvement of electron injection in inverted bottom-emission blue phosphorescent organic light emitting diodes using zinc oxide nanoparticles. *Applied Physics Letters* **96**, -, doi:doi:http://dx.doi.org/10.1063/1.3400224 (2010).
27 Kandada, A. R. S. *et al.* Ultrafast Energy Transfer in Ultrathin Organic Donor/Acceptor Blend. *Sci. Rep.* **3**, doi:10.1038/srep02073 http://www.nature.com/srep/2013/130625/srep02073/abs/srep02073.html#supplementary-information (2013).
28 Coffey, D. C., Ferguson, A. J., Kopidakis, N. & Rumbles, G. Photovoltaic Charge Generation in Organic Semiconductors Based on Long-Range Energy Transfer. *ACS Nano* **4**, 5437-5445, doi:10.1021/nn101106b (2010).

29 Mikhnenko, O. V. *et al.* Exciton diffusion length in narrow bandgap polymers. *Energy & Environmental Science* **5**, 6960-6965 (2012).
30 Ruseckas, A., Shaw, P. E. & Samuel, I. D. W. Probing the nanoscale phase separation in binary photovoltaic blends of poly(3-hexylthiophene) and methanofullerene by energy transfer. *Dalton Transactions*, 10040-10043 (2009).

2

INTRODUCTION TO ORGANIC SEMICONDUCTORS AND ORGANIC PHOTOVOLTAIC DEVICES

2.1. INTRODUCTION

In this chapter I introduce the theory of conjugated molecules and why the sp^2 hybridisation of the atoms in these molecules leads to their semiconducting optoelectronic properties. The focus is then narrowed to their application in organic photovoltaic devices.

In section 2.2 a brief history of semiconductors and organic semiconductors is described. In section 2.3 molecular orbital theory is touched upon and the Hückel approach of describing the frontier molecular orbital of conjugated materials as linear combinations of atomic p-orbitals is explained, with relevance to the emergence of semiconducting properties of these materials. In section 2.4, the potential advantages of organic solar cells compared to their inorganic counterparts are explained, and the critical process leading to photocurrent generation is described, as is the device structure of organic photovoltaic devices.

2.2. INTRODUCTION TO ORGANIC SEMICONDUCTORS

Since the discovery of the transistor at Bell Telephone Laboratory in 1948[1], the use of semiconductor devices has exponentially increased in society. In the developed world it is hard to be more than a few metres from a device incorporating a semiconducting component, be it the Light Emitting Diode (LED) lighting in homes and offices or the CPU in a smartphone, or the microcontroller in a washing machine. Integrated circuits incorporating millions of semiconducting transistors surround us.

A semiconductor is material typically defined as having a conductivity that is intermediate between a metal and an insulator[2]. If this was their only property then they would be pretty uninteresting materials. The uniquely useful feature of these materials is that structures made out of specially treated semiconductors allow current to pass only under very well defined conditions. This feature allows their use as electronic switches and valves. A semiconducting transistor, for example, can be made to conduct electricity or insulate depending on whether a second voltage is applied to it[2]. A photovoltaic device essentially allows the electrons to only pass through it in one direction and holes in the other. As incident light creates electrons and holes (bound or otherwise) and these are forced to move in opposite directions, the result is a photocurrent[2].

The first semiconductors used for transistors, LEDs and photovoltaics and indeed the vast majority of semiconductors used today are inorganic semiconductors, typically single crystal materials composed of the metalloids of

group 13-16, though compounds of many other elements exhibit semiconducting properties[2-4].

2.3. ELECTRONIC STRUCTURE OF CONJUGATED MATERIALS

2.3.1 Molecular Orbital Theory

Carbon has the atomic number 6, having 6 protons in its nucleus and 6 electrons occupying its atomic orbitals. Atomic orbitals are populated from lowest to highest energy; 1s, 2s then 2p. The atomic orbitals that determine the electronic properties of an element are the highest energy orbitals, known as the valence atomic orbitals. As two electrons reside in carbon's 1s orbital, there are 4 electrons to populate carbon's highest energy orbitals 2s, $2p_x$, $2p_y$ and $2p_z$. A diagram of the shapes of these orbitals is shown below.

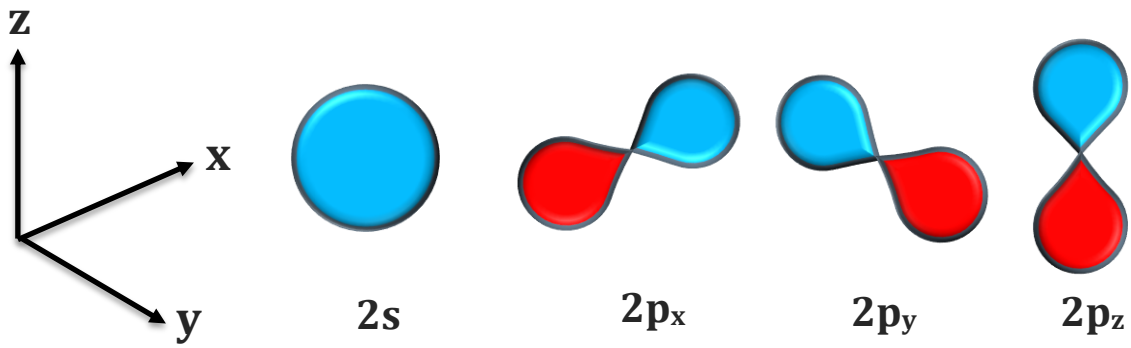

Figure 2.1. A cartoon represention of the valence atomic orbitals in carbon. 2s has rotation symmetry in all directions while the $2p_x$, $2p_y$ and $2p_z$ orbitals have complete rotational symmetry around only the axis which gives them their name.

The 2s orbital has the lowest energy while $2p_x$, $2p_y$ and $2p_z$ are degenerate at a higher energy.

When forming bonds with other carbon atoms, these atomic orbitals can undergo mixing, known as hybridisation to produce 4 new orbitals. Because these new orbitals have different symmetries, the symmetries of the bonds formed will depend on the hybridisation of the atomic orbitals. Carbon commonly undergoes three possible hybridisations. The 2s orbital can mix with a single 2p orbital leaving the other p-orbitals unhybridised. The hybridisation is known as sp^1 hybridisation and the simplest example of a molecule with this hybridisation would be acetylene (ethyne). The next possible hybridisation is when the 2s orbital mixes with two 2p orbitals leaving just a single 2p orbital unhybridised. This is known as sp^2 hybridisation and the simplest example of a molecule with carbon in this hybridisation is ethene. The final hybridisation is when the 2s orbital hybridises with all three 2s orbitals. This hybridisation is known as sp^3 hybridisation and a molecular example would be ethane. These different hybridisations are shown below. For simplicity only the bonding orbitals between the carbons are shown (anti-bonding orbitals are omitted, as are bonding orbitals between the carbon and the hydrogen atoms).

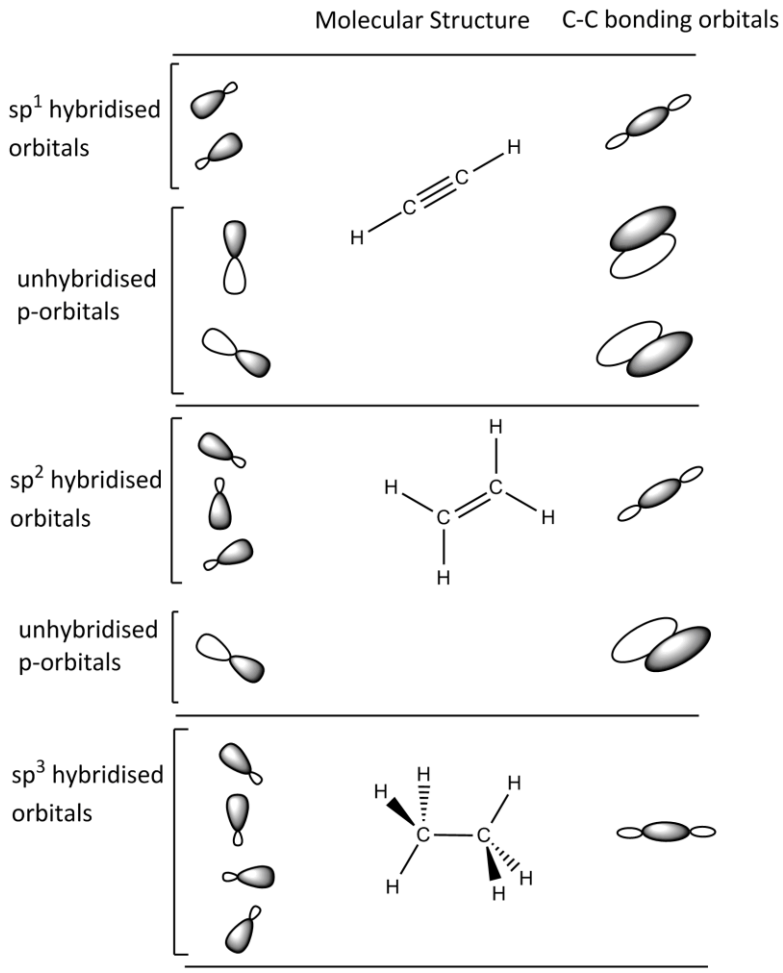

Figure 2.2. An illustration of the different hybridisations of carbon. Only the carbon-carbon bonding orbitals are shown, with antibonding orbitals and carbon-hydrogen bonding and antibonding orbitals neglected. The orbitals are not to scale and the depiction of sp^1 hybridised orbitals as being identical to sp^3 hybridised orbitals is not accurate, in reality the larger lobe would be more bulbous in the sp^1 hyridised orbital and the sizes of the two lobes in the sp^3 hybridised orbitals would be closer to being equally sized than depicted.

Thus the electronic structure of carbon-carbon bonds can be very different depending on the hybridisation of the atomic orbital from which it is formed. This is the cause of the very different optoelectronic and physical properties of its allotropes. Diamond, one of the sp^3 hybridised allotropes of carbon, is transparent and insulating. A buckminsterfullerene (C_{60}), on the other hand, is an sp^2 hybridised allotrope that is black/purple and semiconducting.

The materials studied in this thesis are small molecules and polymers, with long contiguous sections of atoms, predominantly carbon, with sp^2 hybridisation. One of the reasons for carbon's electronic versatility is that as well as the σ-bond forming between the hybridised orbitals of two fragments of a molecule, the unhybridised p-orbitals also strongly interact to form what is known as a π-bond. The reason why carbon appears to be ambivalent as its orbital hybridisation, is that the π-interaction often brings about approximately the same stabilisation as would be caused by forming a new σ-bond. This can be illustrated by considering that in graphite, an sp^2 hybridised allotrope of carbon in which each carbon atom is partaking in three carbon-carbon σ-bonds and one carbon-carbon π-bond, is actually a lower energy configuration of carbon than sp^3 diamond in which each carbon atom is partaking in four σ-bonds, though their energies are extremely close[5]. This is by no means common among elements. Silicon for example, an element in the same group, one period down on the periodic table, can be coaxed into forming double bonds only if the possibility of forming an additional σ-bond is prevented through extreme steric hindrance by the other substituents[6]. Nitrogen on the other hand, just one position to the right of carbon in the periodic table is far more stable as a triple bonded (sp^1) dimer than any other hybridisation. Compounds made from nitrogen-nitrogen bonds with hybridisations of sp^2 or sp^3 are often highly explosive[7], as the decomposition product is molecular (sp^1) N_2, a much more stable electronic configuration for the element.

This ability of carbon to form bonds to itself, remaining almost energetically indifferent as to the hybridisation, is one of the reasons it is such a ubiquitous building block for chemical synthesis, not just artificially through organic

chemistry, but also as the bricks and mortar with which nature builds living organisms. In the context of semiconducting physics, this ability to construct molecules derived from different hybridisations of carbon is important, not for its difference in structural properties, but because by changing the hybridisation, the electronic properties of the molecule are hugely altered, including the HOMO-LUMO gap (the energy difference between the highest occupied molecular orbital and the lowest unoccupied molecular orbital).

2.3.2 HOMO-LUMO Gap in Conjugated Materials

A system that has an extended chain of sp^2 hybridised carbons is usually depicted as a carbon chain with alternating single and double bonds. Such a system is referred to as being conjugated. Because the unhybridised p-orbital is higher in energy than the other three orbitals, the frontier molecular orbitals; those close to and including the HOMO and LUMO of the conjugated molecule can be described well using only linear combinations of the atomic p-orbitals. Additionally, because all the unhybridised p-orbitals in a conjugated system have the correct symmetry to interact with every other unhybridised p-orbital, the net result it that the molecular orbitals produced stretch the entire length of the conjugation. Because the molecular orbitals are comprised of contributions from p-orbitals all along the conjugated section of the chain, the overall energies of the orbitals depend on the length of the chain. For example, the ionization potential of a conjugated system decreases as the length increases[8] while this can be compared to the almost insignificant dependence on ionization potential with respect to chain length in the equivalent straight chain alkanes[9,10].

A quantitative theoretical framework based on this approach, of representing the frontier molecular orbitals as simply linear combinations of atomic p-orbitals was developed by Erich Hückel[11], and offered a compelling explanation as to why the conjugated systems which react, do so, and at what orientation, as well as why particular cyclic conjugated systems are so stable (aromaticity). Hückel theory also offers an explanation as to why the HOMO-LUMO gap in conjugated materials is as it is measured. Hückel theory, though a simplified approach to understanding the molecular orbital theory, is highly predictive, and is still widely used. Considering the π-orbitals as linear combinations of the atomic p orbitals, the following frontier molecular orbitals can be produced, demonstrating why conjugated materials have reduced HOMO-LUMO gaps[12].

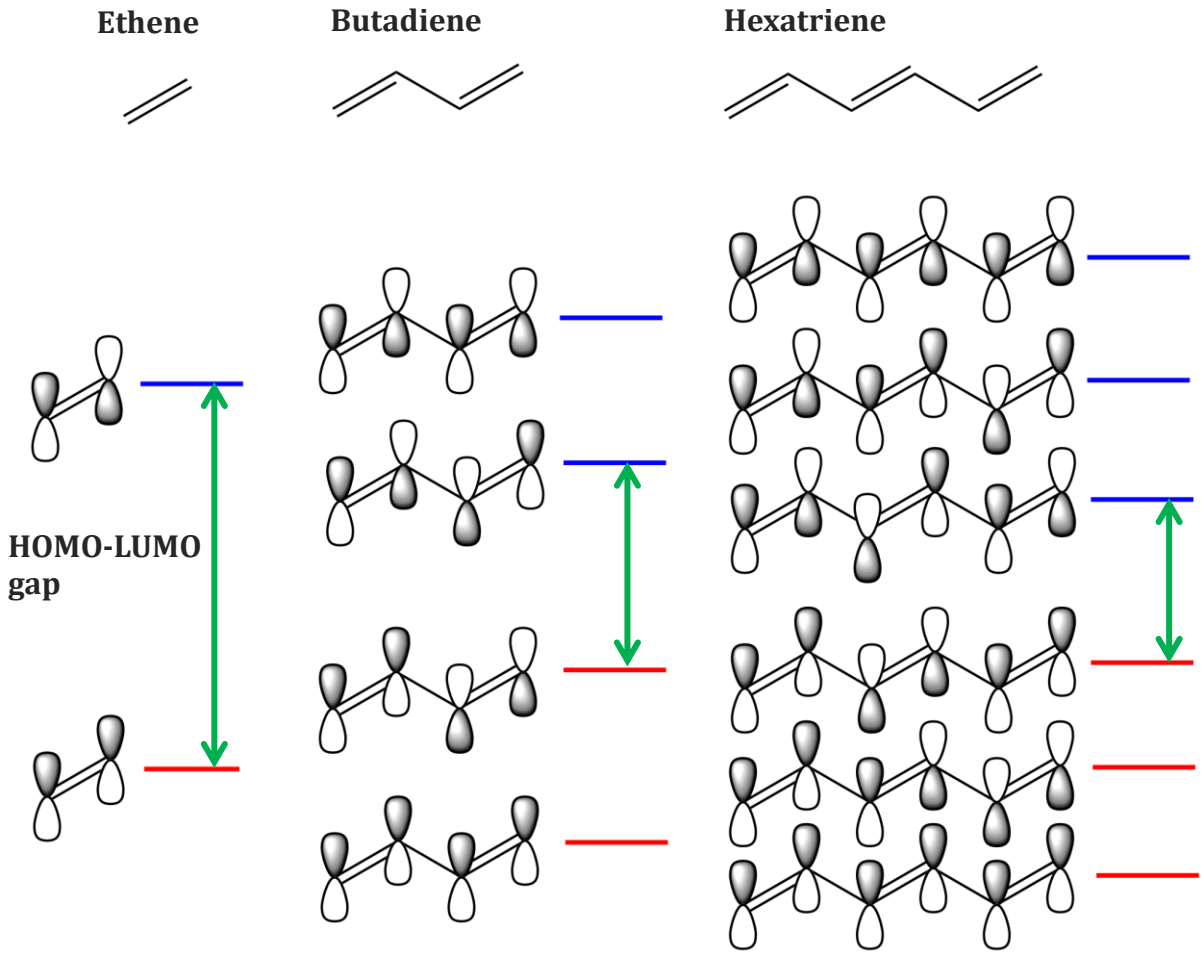

Figure 2.3. The frontier molecular orbitals of the three simplest conjugated materials represented as linear combinations of their atomic p-orbitals. Filled molecular orbitals are shown as red and vacant orbitals are shown as blue. As the conjugation length increases the HOMO-LUMO gap decreases.

As the length of the conjugated system is increased the distance between the HOMO and the LUMO is decreased. Qualitatively the system is very well described by a particle in a one-dimension box. Each higher molecular orbital is distinguished by the introduction of a new node into the wavefunction. The wavefunction is held at zero at the edges of the box (the ends of the molecule). As the box is made longer the energy spacing of the orbitals becomes smaller, because the energy penalty for introducing a new node is smaller.

In conjugated polymers, at first glance at the molecular structure, the length of the conjugated system could be considered nearly infinite. See the structure of polyacetylene below.

Figure 2.4. The molecular structure of polyacetylene. The dashed lines represent how the molecule continues for many hundred of repeat units.

Because the sp^2 hybridised system is shown in the molecular structure to extend over many hundreds of repeat units it may be thought that the HOMO-LUMO gap would reflect this, reducing to nearly zero. In reality, this does not occur for two reasons. Firstly, there is a fundamental limit imposed on the band-gap first described by Ooshika [13] and Longuet-Higgins and Salem[14]. This effect arises from Hückel theory as the resonance integral between neighbouring p-atomic orbitals, known as β, which determines the stabilisation when those two orbitals interact, has an exponential dependence on distance. This is the intuitive realisation; one might expect that two very close atomic orbitals would experience a greater interaction than those at a greater distance. This fall-off with distance is even a requirement of Hückel theory, as atomic orbitals further than nearest neighbour separation are assumed not to interact whatsoever. The less obvious implication of this distance dependence of the resonance integral is that an infinite chain of sp^2 hybridised carbon will always distort such that the double bonds are shorter than the single bonds. This effect is a special case of the Peierls distortion[15] which is a distortion that applies to all 1-dimension crystals.

The second reason why the band-gap does not keep reducing as the chain length increases is that the atomic p-orbitals will only hybridise to form π-orbitals

if they have the correct symmetry, meaning that the dihedral angle between adjacent C-H carbons must be approximately equal to 180° or 0° (trans or cis isomers). Because of disorder in the molecules, as well as chemical defects, there are frequent locations where the conjugation is broken and the node in the π-orbital is enforced.

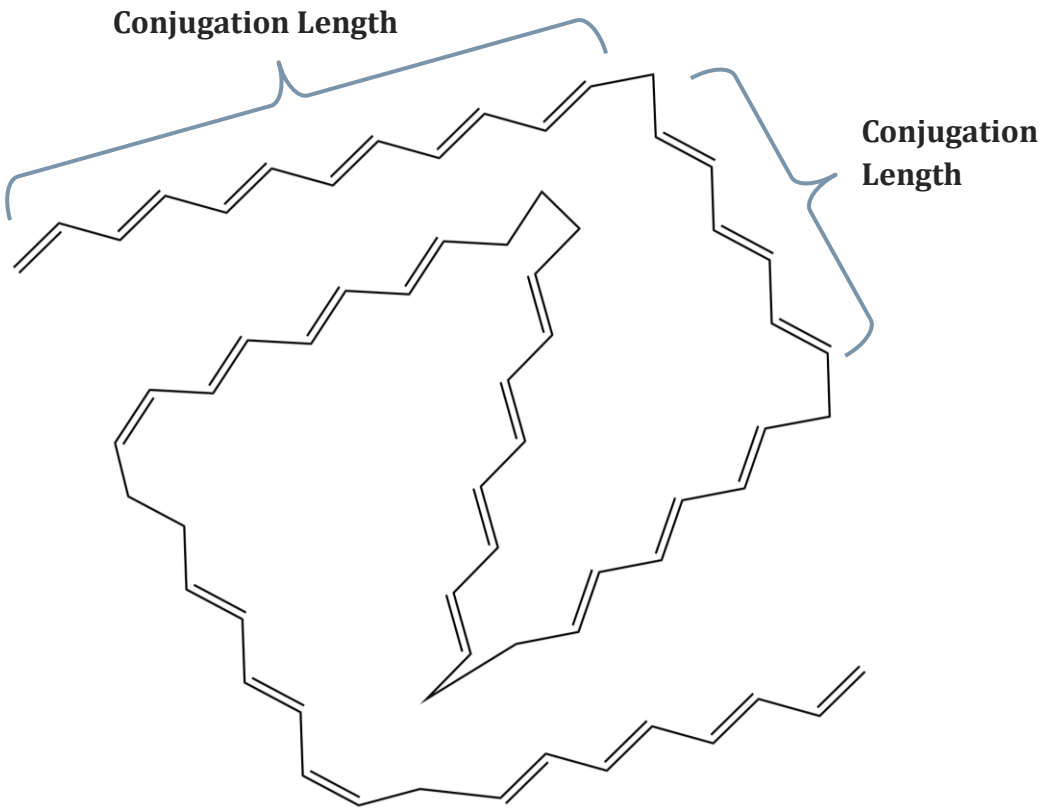

Figure 2.5. Though the molecular structure of polyacetylene indicates that the sp^3 hybridisation extends the entire length of the molecule, in reality kinks in the chain mean that the π-orbitals resemble a series of shorter molecules with a distribution of lengths.

The above figure illustrates why, as you increase the chain beyond a particular length, known as the conjugation length, the HOMO-LUMO gap stops decreasing; kinks in the chain break the conjugation. In a solid film there will be areas of the chain which have longer and shorter spaces between kinks. Because this length determines the size of the HOMO-LUMO gap, it means that the

chromophores will have a distribution of energies. This distribution broadens the absorption of the polymer and is known as inhomogeneous broadening.

2.4. ORGANIC PHOTOVOLTAIC DEVICES

2.4.1 Potential Advantages over Conventional Solar Cells

Conjugated polymers and small molecules are the subject of concerted research efforts as they have potential to overcome many of the problems associated with traditional, inorganic photovoltaic devices. These organic photovoltaic devices (OPVs) have seen huge improvements in power conversion efficiency (PCE) in recent years, growing from 2.5% in 2001[16] to close to 11% in 2013[17], though this is still less than typical PCEs of commercial single crystal silicon solar cells which operate at 12-16% efficiency[18]. OPVs are being pursued because of several important differences between organic semiconductors and inorganic semiconductors. The sought-after properties of organic semiconductors include low-weight and flexibility, tuneable optical absorption, lower energy pay-back time, cheaper manufacturing and integration into areas inaccessible to conventional solar materials such as fabrics and living tissue[19]. The most important of these unique features will be discussed in the next sections.

2.4.1.1 *Tuneable Optical Absorption*

As described in section 2.3, the absorption of the semiconductor, which is essentially dictated by the HOMO-LUMO gap, will depend on how confined the excited states are and what substituents are included in, or attached to, the conjugated backbone. This means that unlike inorganic crystals which are essentially restricted to a single band-gap; an intrinsic property of the material,

OPV materials can have their electronic structure tweaked, through chemical modification to alter the electronic properties towards an ideal HOMO-LUMO gap. For a single junction organic solar cell the ideal HOMO-LUMO gap has been determined using empirical and theoretical considerations to be in the region of 1.3 eV [20], a material that absorbs in the near infrared.

Though most OPVs will be optimised to absorb as much useful energy from the incident solar radiation this is not always the case. Organic solar cells have been optimised to absorb IR and UV light, in order to harvest energy from light incident on a window while remaining transparent in the visible region[21].

2.4.1.2 *Lower Energy Pay-Back time*

A key factor when weighing up different green energy options, is the time taken to recoup the energy expended when building the technology itself. The following table, from data presented by Espinosa *et al.*[22] shows the time in years for a given renewable energy source to produce enough energy to produce an identical copy of itself.

Type of technology		Energy Payback Time (years)
Wind	On land	0.26
	Offshore	0.39
Photovoltaic Technologies	Silicon mono- and polycrystalline	1.65–4.12
	Amorphous silicon	1.13
	GaAs PV	2.36–5
	GaInP/GaAs	2.14–4.6
	CdTe	0.73–1.61
	CIS	2.02–2.26
	OPV	0.2–4
Hydropower		0.5
Geothermal		0.54
Biomass	Gasification	<5
	Combustion	5–10

Figure 2.6. Table of energy payback times from a selection of renewable energies. From Espinosa *et al.*[22].

From the above table it is worth noting that in the best possible conditions, inorganic solar cells of all types have much longer energy payback times than all other renewable energies with the exception of biomass (gasification or combustion). One reason is because these traditional photovoltaic technologies require highly pure starting materials; electronic grade silicon, for example, has less than a few parts per million impurities[3]. To get down to this this level of purity requires numerous chemical reactions and purification steps which makes it very energy intensive. After electronic grade ingots of silicon are produced, single crystals must be grown under vacuum at very high temperature to make wafers suitable for solar cell applications. This process again has high energy demands due to the energy requirements to create and maintain an ultrahigh vacuum. Only OPVs have the potential to bring down the energy payback time to less than half a year and they have considerable scope to improve as they are still very immature technologies. This is because their manufacture relies on none of these highly energetic processes (the manufacturing advantages of OPVs will be discussed in

the next section). Espinosa *et al*. predict, with proper scale-up techniques, the energy payback time could be reduced to a single day[22].

Energy payback time is not the only concern when deciding the most effective way to produce energy while reducing CO_2 emissions. One other very significant parameter is the lifetime of the technology. For example an offshore wind turbine may be expected to have a lifetime for 20 years, but will need a gearbox replacing every 7 years[23]. Hence there will be additional energy expenditure in maintenance and the renewable energy only makes a net contribution from the end of its energy payback time to the end of its operating lifetime. While silicon solar cells can operate outdoors continuously and only have an efficiency drop-off of 10% in twenty years[24], organic solar cells in a lab-based environment are highly oxygen and moisture-sensitive, experiencing a similar drop in efficiency in hours or days. If properly encapsulated, the longest surviving OPVs have been reported to drop to 80% of efficiency (initial efficiency taken after a burn-in period) in just 7 years[25] while a commercial manufacturer of OPVs, Heliatek report a 21 year lifetime for their modules[26].

Organic solar cells are a worthwhile area of exploration in the search for practical green energy because they have the potential to have very short energy payback times and fairly long lifetimes. They are an early stage technology and currently do not deliver either of these characteristics reliably, even in the laboratory setting. The important factor, however, is that they have been demonstrated to have the *potential* to do so.

2.4.1.3 *Low-Cost Manufacturing*

As hinted at in the previous section, one of the great strengths of OPVs is their ease of manufacture. Organic semiconductors are distinct molecules, rather than being extended crystals, which means that they can be dissolved into a solution and redeposited without hugely changing their electronic properties. This property of organic semiconductors makes them *solution-processable*. Instead of growing a solar cell as a single crystal under high vacuum, as one would manufacture a silicon solar cell, an organic semiconductor can be processed like an ink, to be spray-coated or printed onto almost any substrate. Once deposited, organic semiconductors maintain the physical properties of the closely related materials, plastics, which means they can be bent and deformed without damaging them.

The compatibility with solution processing and the flexibility of the material combined means that OPVs could in the future be manufactured using a continuous mass production method, of which the generic term is roll-to-roll printing[27]. This is the same way newspapers are produced and is an extremely rapid and low-cost process. An additional advantage is that the solar cells produced are on a large roll that can be transported and then installed simply by unrolling and adhering to a pre-existing substrate by the end-user.

2.4.2 Key Steps in the Operation of Organic Solar Cells

The rest of this chapter describes the key processes that contribute to the functioning of an organic solar cell. These physical processes are summarised with a diagram of a functioning organic solar cell at the end of this chapter in figure 2.9.

2.4.2.1 *Light Absorption*

When a photon with an energy that exceeds the HOMO-LUMO gap of an organic semiconductor strikes the material, it has a probability of being absorbed, depending on the molar absorption coefficient of the material. Organic semiconductors have extremely high molar absorption coefficients as a result of a strong wavefunction overlap between the ground and excited states[28], as well as conforming to the spin and symmetry selection rules for absorption. This means that organic photovoltaics can be much thinner (~100 nm) that the equivalent silicon photovoltaic cell (~100 μm[29]).

Similarly to the process in an inorganic semiconductor, the absorbed energy promotes an electron from the highest occupied state to the lowest unoccupied state. Typically in an inorganic semiconductor, such as silicon, this promoted electron and the positively charged vacancy (known as the hole) are free to move independently. However, in an organic semiconductor these two species remain strongly bound. This difference in behaviour is due to the difference in the dielectric constant. A typical dielectric constant of an inorganic semiconductor is 15 compared to just 4 for an organic semiconductor[30]. As the coulomb interaction scales with the reciprocal of the dielectric constant, at a given distance, the electron and hole will feel an attractive force almost 4 times stronger in the organic material. This means that while in an inorganic solar cell, the charges can easily overcome the mutual attraction at room temperature, in an organic semiconductor a strong external driving force is required to split these bound electron-hole pairs.

2.4.2.2 *Exciton Diffusion*

The bound electron-hole pair, known as an exciton, after being created by the absorption of a photon at a particular chromophore, will migrate through the film via a process called exciton diffusion. Singlet exciton diffusion occurs because the emission of the exciton overlaps in energy with the ground state absorption of the chromophores surrounding it. This means that instead of reemitting a photon, the emission dipole of the exciton can resonate with the absorption dipole of a nearby chromophore and the exciton energy can be transferred through space. This process is known as Förster Resonance Energy Transfer (FRET) and is described in greater detail in chapter 4. This energy transfer can happen multiple times to many consecutive chromophores, the net result being that over time an individual exciton would be observed to move following a random walk. Such diffusive motion is also described in greater detail in chapter 4. An exciton will only have a finite lifetime, on the order of hundreds of picoseconds. At the end of its lifetime, the exciton decays back to the ground state, a process that can be radiative, emitting a photon or non-radiative, dissipating the energy as heat. Any exciton that relaxes down to the ground state represents an absorbed photon's worth of energy that has been wasted. In order to harvest an exciton's energy, it is necessary for that exciton to reach the interface with the other blend component and undergo charge separation (described in the next section). Thus, exciton diffusion is a critical process in organic solar cells because the chance of an exciton encountering a heterojunction will depend on the rate at which it diffuses through the material.

2.4.2.3 *Charge Separation*

In order to split the exciton into its constituent electron and hole it is necessary to overcome the coulombic barrier by introducing an energetic incentive for the electron and hole to travel in opposite directions. This is achieved in an organic solar cell by introducing a second organic semiconductor to create a heterojunction. A heterojunction in this context is the interface between two materials with different electronic properties. One of the materials, known as the electron donor is more energetically stable donating an electron (to form a cation) and one material is more stable accepting an electron (forming an anion).

In the following figure the process of charge separation is explained. For simplicity I have shown the exciton as comprising of an electron at an energy state labelled as the LUMO and a hole in an energy state labelled as the HOMO, as it is commonly represented in the literature[26,28,31]. In reality when an electron is introduced into what was formally the LUMO, the molecular orbital undergoes mixing with other molecular orbitals to lower the energy. In addition, the surrounding electron density is polarised and this stabilises the dipole. Finally the coulombic binding energy reduces the energy further[32]. These influences also raise the energy of the orbital, formerly the HOMO, now the first SOMO (singularly occupied molecular orbital). For clarity and conciseness, this stabilisation is neglected in the diagram below.

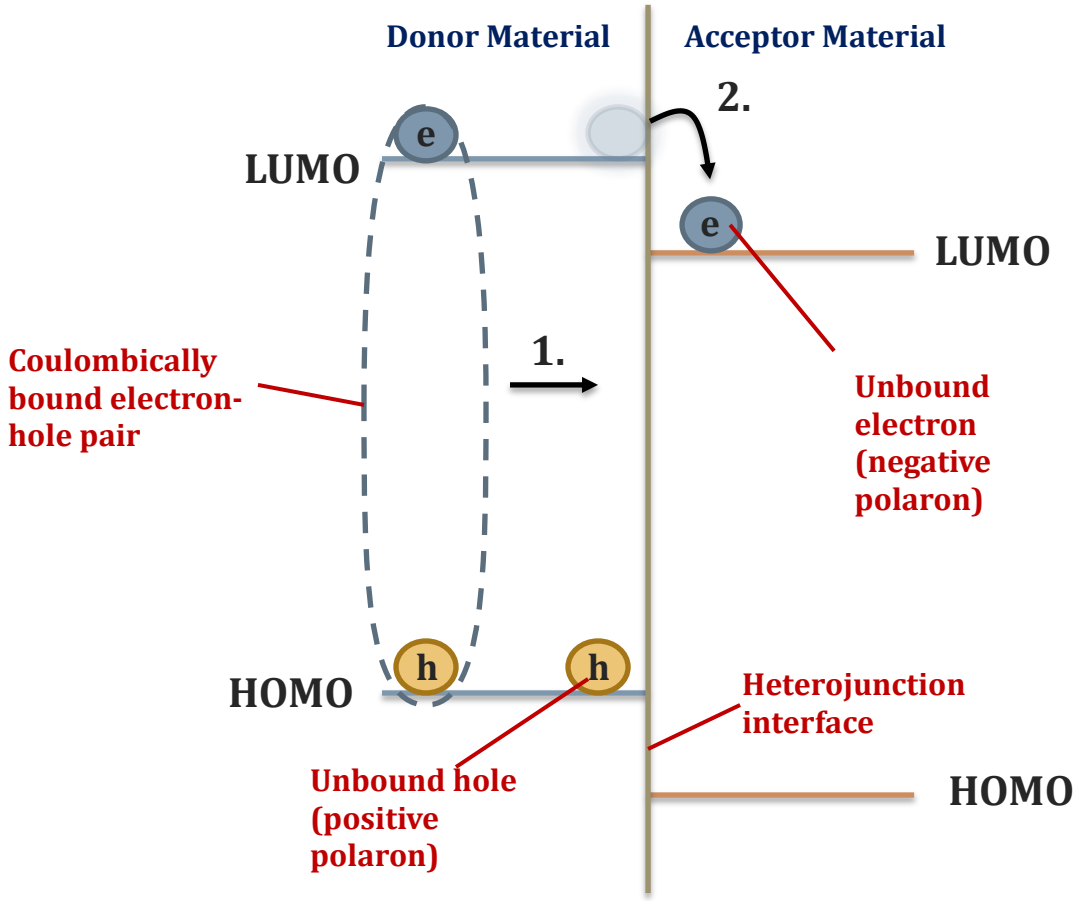

Figure 2.7. The process of charge separation. After the photon is aborbed an electron and a hole are bound to each other through a coulombic interaction. (1.) the exciton migrates through the donor material through a process called exciton diffusion. (2.) Upon encountering a heterojunction interface, an interface with the acceptor material, an energetic incentive to physically separate the electron and the hole is provided. As the electron can lower its energy by transfering onto the donor material, but the hole would raise its energy by transfering, the exciton is split when the electron moves onto the acceptor material.

In order to generate any useful photocurrent, charge transfer must occur at the interface. The offset between the LUMO of the donor and the LUMO of the acceptor will determine whether the charge transfer step is energetically favoured. Typically in the literature it is cited that this difference needs to be more than approximately 0.2-0.3 eV because this, it is hypothesised, is the energy needed to overcome the exciton binding energy[33-35]. In Chapter 6, the function of this energy offset is investigated in greater detail.

Once the electron has transferred onto the electron acceptor, it has a probability of never escaping the coulombic attraction of its corresponding hole and hence being trapped at the interface and eventually recombining. This process is known as geminate recombination[36,37].

2.4.2.4 *Charge Extraction*

Once the charges have completely migrated away from each other, they need to proceed in opposite directions to separate electrodes and hence generate a photocurrent. This charge extraction involves a series of electron transfer steps from chromophore to chromophore[38]. If a charge encounters an opposite charge it has a probability of recombining back to the ground-state. This recombination process is distinct from geminate recombination, discussed in the previous section, because it is a bimolecular process and so depends on the square of the population of charges[39,40], while geminate recombination just depends monomolecularly on the recombination of charges[41]. A very high surface area heterojunction will mean that a charge will be more likely to encounter the interface with the other component of the blend and hence be more likely to encounter its opposite charge[42,43].

Unlike an exciton, the charges have a net coulombic charge and hence are motivated towards travelling in a useful direction by the built-in field. If the charges migrate all the way to the correct electrode they contribute towards the photocurrent and in doing so contribute to the conversion of light energy into electrical energy.

2.4.3 Device Structure

As discussed in section 2.4.2.2 any exciton that does not encounter the heterojunction will undergo recombination, either radiatively or non-radiatively and hence the energy that it carries will be wasted. The only means by which an exciton can migrate is through exciton diffusion and such exciton diffusion lengths are typically short (<10 nm)[44-57], meaning that this source of inefficiency can seriously impact on the effectiveness of devices. As the exciton diffusion length is an intrinsic property of the material, and cannot easily be modified, an alternative technique to improve the chance of an encounter between an exciton and the heterojunction is to increase the surface area of heterojunction. To achieve this, instead of having a planar interface between the electron donor and the electron acceptor as would be the case in a typical silicon p-n junction, the electron donor and electron acceptor are dissolved in the same solvent and deposited to form an intermixed nanostructure. This nanostructure, known as a bulk heterojunction, gives an extremely high surface area per volume, ensuring a high degree of exciton harvesting. There is a trade-off to having a high heterojunction surface area. The more surface area available, the more likely the charges, once separate will spend time next to the heterojunction over the course of their journey to the electrodes. As their opposite charges will reside predominantly in the other material, it is near the interface that they have the greatest likelihood of meeting an oppositely charged species and recombining down to the ground state. The differences between the simpler *planar heterojunction* and the *bulk heterojunction* are shown in the diagram below.

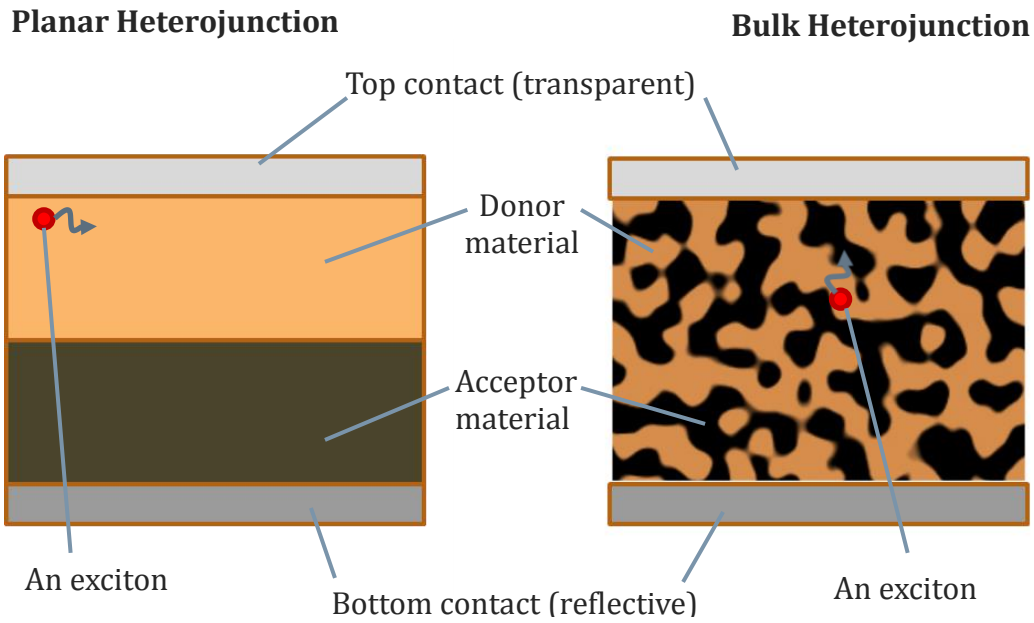

Figure 2.8. The above structures illustrate the difference between a planar hetrojunction, in which the donor and acceptor are in distinct layers, and the bulk heterojunction, in which the donor and acceptor are mixed.

As can be seen in the diagram, due to the very short exciton diffusion length, an exciton created in the planar heterojunction further than a certain short distance away from the interface between the two materials, is doomed to recombine before reaching the interface. In the bulk heterojunction, because of the ubiquity of the interface within the film, the exciton is almost certain to find the interface and hence undergo charge separation. On the other hand, if the exciton does undergo charge separation in the planar heterojunction device, the path for the separated charges to reach the correct electrode is simple; the electron can go straight down and the hole straight up, following the built-in field. In the bulk heterojunction, charge extraction is more challenging because the election and hole must each navigate the labyrinth created by the complex morphology, without the electron and hole recombining at the interface. The overall structure of the OPV and the critical processes leading to photocurrent generation are summarised in the diagram below.

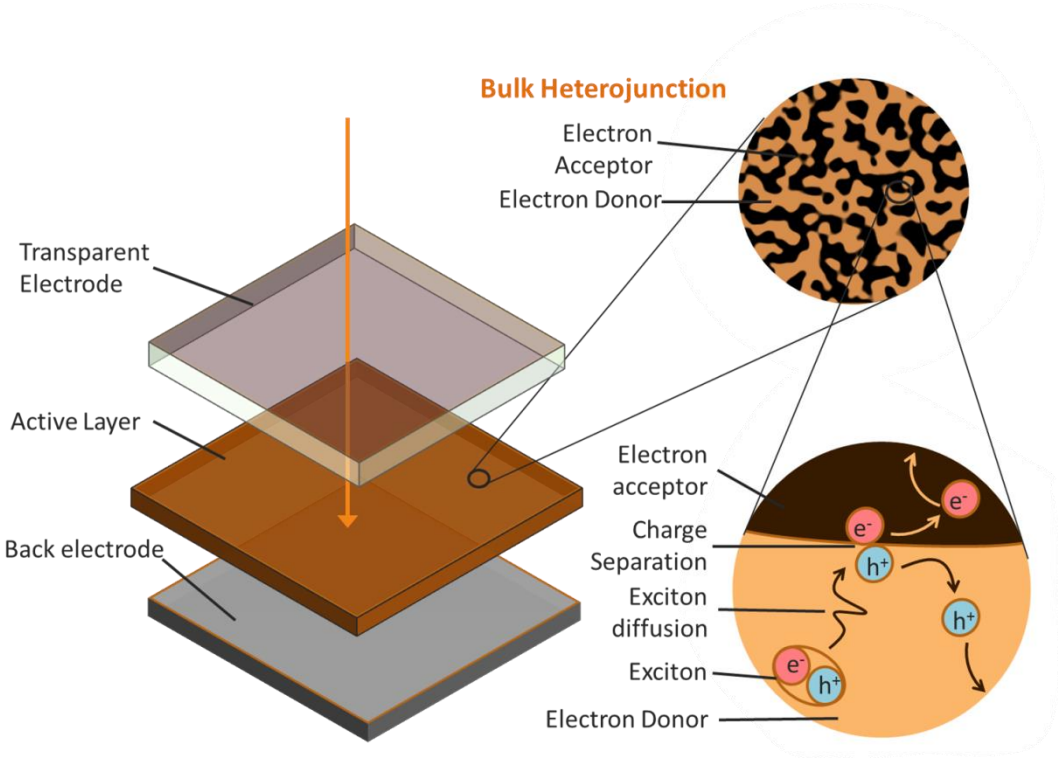

Figure 2.9. The device structure and the key processes leading to photocurrent generation in a bulk heterojunction.

The strongly bound exciton is *the* defining feature of an organic solar cell. This thesis investigates the processes by which the excitons are harvested, with a predominant focus on the rate at which the excitons diffuse. Chapter 4 describes the theory and past literature on the subject of exciton diffusion. Chapter 5 investigates blends in which long range energy transfer enhances exciton harvesting in some high performance photovoltaic blends. Chapter 6 describes how fast electron transfer occurs once the exciton is delivered to the acceptor by exciton diffusion. Chapter 7 investigates exciton diffusion in the acceptor C_{71}-PCBM and then, by measuring the rate of exciton harvesting, derives information about the degree of mixing in the bulk heterojunction, Chapter 8 uses similar reasoning to investigate electron transfer in P3HT blends and then uses this information to calculate domain sizes and morphology in bulk heterojunctions.

2.5. REFERENCES

1 Bardeen, J. & Brattain, W. H. The Transistor, A Semi-Conductor Triode. *Physical Review* **74**, 230-231 (1948).

2 Gurnee, E. F. Fundamental principles of semiconductors. *Journal of Chemical Education* **46**, 80, doi:10.1021/ed046p80 (1969).

3 Dunlap, W. C. Recent developments in semiconductors. *Journal of Chemical Education* **38**, 238, doi:10.1021/ed038p238 (1961).

4 in *Semiconductor Materials Microdevices* Ch. 6, 135-170 (Springer US, 2003).

5 Xiao, P. & Henkelman, G. Communication: From graphite to diamond: Reaction pathways of the phase transition. *The Journal of Chemical Physics* **137**, -, doi:doi:http://dx.doi.org/10.1063/1.4752249 (2012).

6 West, R. Chemistry of the Silicon-Silicon Double Bond. *Angewandte Chemie International Edition in English* **26**, 1201-1211, doi:10.1002/anie.198712013 (1987).

7 Klapötke, T. M. & Piercey, D. G. 1,1′-Azobis(tetrazole): A Highly Energetic Nitrogen-Rich Compound with a N10 Chain. *Inorganic Chemistry* **50**, 2732-2734, doi:10.1021/ic200071q (2011).

8 Bredas, J. L., Silbey, R., Boudreaux, D. S. & Chance, R. R. Chain-length dependence of electronic and electrochemical properties of conjugated systems: polyacetylene, polyphenylene, polythiophene, and polypyrrole. *Journal of the American Chemical Society* **105**, 6555-6559, doi:10.1021/ja00360a004 (1983).

9 *CRC Handbook of Chemistry and Physics, 95th Edition*. (CRC Press, 2014).

10 Cao, C. & Yuan, H. On Molecular Polarizability. 4. Evaluation of the Ionization Potential for Alkanes and Alkenes with Polarizability. *Journal of Chemical Information and Computer Sciences* **42**, 667-672, doi:10.1021/ci010344o (2002).

11 Hückel, E. Quantentheoretische Beiträge zum Benzolproblem. *Z. Physik* **70**, 204-286, doi:10.1007/bf01339530 (1931).

12 Hadziioannou, M. G. G. *Polymer Electronics*. 29 (Oxford University Press, 2013).

13 Ooshika, Y. A Semi-empirical Theory of the Conjugated Systems I. General Formulation. *Journal of the Physical Society of Japan* **12**, 1238-1245, doi:10.1143/jpsj.12.1238 (1957).

14 Longuet-Higgins, H. C. & Salem, L. The Alternation of Bond Lengths in Long Conjugated Chain Molecules. *Proceedings of the Royal Society of London. Series A. Mathematical and Physical Sciences* **251**, 172-185, doi:10.1098/rspa.1959.0100 (1959).

15 Heeger, A. J., Kivelson, S., Schrieffer, J. R. & Su, W. P. Solitons in conducting polymers. *Reviews of Modern Physics* **60**, 781-850 (1988).

16 Shaheen, S. E. *et al.* 2.5% efficient organic plastic solar cells. *Applied Physics Letters* **78**, 841-843, doi:doi:http://dx.doi.org/10.1063/1.1345834 (2001).

17 Green, M. A., Emery, K., Hishikawa, Y., Warta, W. & Dunlop, E. D. Solar cell efficiency tables (version 41). *Progress in Photovoltaics: Research and Applications* **21**, 1-11, doi:10.1002/pip.2352 (2013).
18 Shah, A., Torres, P., Tscharner, R., Wyrsch, N. & Keppner, H. Photovoltaic Technology: The Case for Thin-Film Solar Cells. *Science* **285**, 692-698, doi:10.1126/science.285.5428.692 (1999).
19 Scharber, M. C. & Sariciftci, N. S. Efficiency of bulk-heterojunction organic solar cells. *Progress in Polymer Science* **38**, 1929-1940, doi:http://dx.doi.org/10.1016/j.progpolymsci.2013.05.001 (2013).
20 Scharber, M. C. *et al.* Design Rules for Donors in Bulk-Heterojunction Solar Cells—Towards 10 % Energy-Conversion Efficiency. *Advanced Materials* **18**, 789-794, doi:10.1002/adma.200501717 (2006).
21 Lunt, R. R. & Bulovic, V. Transparent, near-infrared organic photovoltaic solar cells for window and energy-scavenging applications. *Applied Physics Letters* **98**, -, doi:doi:http://dx.doi.org/10.1063/1.3567516 (2011).
22 Espinosa, N., Hosel, M., Angmo, D. & Krebs, F. C. Solar cells with one-day energy payback for the factories of the future. *Energy & Environmental Science* **5**, 5117-5132, doi:10.1039/c1ee02728j (2012).
23 Guezuraga, B., Zauner, R. & Pölz, W. Life cycle assessment of two different 2 MW class wind turbines. *Renewable Energy* **37**, 37-44, doi:http://dx.doi.org/10.1016/j.renene.2011.05.008 (2012).
24 Dunlop, E. D. in *Photovoltaic Energy Conversion, 2003. Proceedings of 3rd World Conference on.* 2927-2930 Vol.2923.
25 Peters, C. H. *et al.* High Efficiency Polymer Solar Cells with Long Operating Lifetimes. *Advanced Energy Materials* **1**, 491-494, doi:10.1002/aenm.201100138 (2011).
26 Darling, S. B. & You, F. The case for organic photovoltaics. *RSC Advances* **3**, 17633-17648, doi:10.1039/c3ra42989j (2013).
27 Krebs, F. C. Polymer solar cell modules prepared using roll-to-roll methods: Knife-over-edge coating, slot-die coating and screen printing. *Solar Energy Materials and Solar Cells* **93**, 465-475, doi:http://dx.doi.org/10.1016/j.solmat.2008.12.012 (2009).
28 Kippelen, B. & Bredas, J.-L. Organic photovoltaics. *Energy & Environmental Science* **2**, 251-261, doi:10.1039/b812502n (2009).
29 Tiedje, T., Yablonovitch, E., Cody, G. D. & Brooks, B. G. Limiting efficiency of silicon solar cells. *Electron Devices, IEEE Transactions on* **31**, 711-716, doi:10.1109/t-ed.1984.21594 (1984).
30 Gregg, B. A. & Hanna, M. C. Comparing organic to inorganic photovoltaic cells: Theory, experiment, and simulation. *Journal of Applied Physics* **93**, 3605-3614, doi:doi:http://dx.doi.org/10.1063/1.1544413 (2003).
31 Al-Ibrahim, M., Roth, H. K., Zhokhavets, U., Gobsch, G. & Sensfuss, S. Flexible large area polymer solar cells based on poly(3-hexylthiophene)/fullerene. *Solar Energy Materials and Solar Cells* **85**, 13-20, doi:http://dx.doi.org/10.1016/j.solmat.2004.03.001 (2005).
32 Bredas, J.-L. Mind the gap! *Materials Horizons* **1**, 17-19, doi:10.1039/c3mh00098b (2014).

33 Brédas, J.-L., Cornil, J. & Heeger, A. J. The exciton binding energy in luminescent conjugated polymers. *Advanced Materials* **8**, 447-452, doi:10.1002/adma.19960080517 (1996).
34 Alvarado, S. F., Seidler, P. F., Lidzey, D. G. & Bradley, D. D. C. Direct Determination of the Exciton Binding Energy of Conjugated Polymers Using a Scanning Tunneling Microscope. *Physical Review Letters* **81**, 1082-1085 (1998).
35 Kern, J., Schwab, S., Deibel, C. & Dyakonov, V. Binding energy of singlet excitons and charge transfer complexes in MDMO-PPV:PCBM solar cells. *physica status solidi (RRL) – Rapid Research Letters* **5**, 364-366, doi:10.1002/pssr.201105430 (2011).
36 Credgington, D., Jamieson, F. C., Walker, B., Nguyen, T.-Q. & Durrant, J. R. Quantification of Geminate and Non-Geminate Recombination Losses within a Solution-Processed Small-Molecule Bulk Heterojunction Solar Cell. *Advanced Materials* **24**, 2135-2141, doi:10.1002/adma.201104738 (2012).
37 Groves, C., Blakesley, J. C. & Greenham, N. C. Effect of Charge Trapping on Geminate Recombination and Polymer Solar Cell Performance. *Nano Letters* **10**, 1063-1069, doi:10.1021/nl100080r (2010).
38 Sirringhaus, H. *et al.* Two-dimensional charge transport in self-organized, high-mobility conjugated polymers. *Nature* **401**, 685-688 (1999).
39 Koster, L. J. A., Mihailetchi, V. D. & Blom, P. W. M. Bimolecular recombination in polymer/fullerene bulk heterojunction solar cells. *Applied Physics Letters* **88**, -, doi:doi:http://dx.doi.org/10.1063/1.2170424 (2006).
40 Blom, P. W. M., de Jong, M. J. M. & Breedijk, S. Temperature dependent electron-hole recombination in polymer light-emitting diodes. *Applied Physics Letters* **71**, 930-932, doi:doi:http://dx.doi.org/10.1063/1.119692 (1997).
41 Cowan, S. R., Roy, A. & Heeger, A. J. Recombination in polymer-fullerene bulk heterojunction solar cells. *Physical Review B* **82**, 245207 (2010).
42 van Duren, J. K. J. *et al.* Relating the Morphology of Poly(p-phenylene vinylene)/Methanofullerene Blends to Solar-Cell Performance. *Advanced Functional Materials* **14**, 425-434, doi:10.1002/adfm.200305049 (2004).
43 Guo, J., Ohkita, H., Benten, H. & Ito, S. Charge Generation and Recombination Dynamics in Poly(3-hexylthiophene)/Fullerene Blend Films with Different Regioregularities and Morphologies. *Journal of the American Chemical Society* **132**, 6154-6164, doi:10.1021/ja100302p (2010).
44 Scully, S. R. & McGehee, M. D. Effects of optical interference and energy transfer on exciton diffusion length measurements in organic semiconductors. *Journal of Applied Physics* **100**, 034907 (2006).
45 Mikhnenko, O. V. *et al.* Exciton diffusion length in narrow bandgap polymers. *Energy & Environmental Science* **5**, 6960-6965 (2012).
46 Mikhnenko, O. V. *et al.* Effect of thermal annealing on exciton diffusion in a diketopyrrolopyrrole derivative. *Physical Chemistry Chemical Physics* **14**, 14196-14201, doi:10.1039/c2cp41359k (2012).
47 Raisys, S. *et al.* Exciton diffusion enhancement in triphenylamines via incorporation of phenylethenyl sidearms. *Journal of Materials Chemistry C* **2**, 4792-4798, doi:10.1039/c4tc00262h (2014).

48 Markov, D. E., Amsterdam, E., Blom, P. W. M., Sieval, A. B. & Hummelen, J. C. Accurate Measurement of the Exciton Diffusion Length in a Conjugated Polymer Using a Heterostructure with a Side-Chain Cross-Linked Fullerene Layer. *The Journal of Physical Chemistry A* **109**, 5266-5274, doi:10.1021/jp0509663 (2005).
49 Halls, J. J. M., Pichler, K., Friend, R. H., Moratti, S. C. & Holmes, A. B. Exciton diffusion and dissociation in a poly(p-phenylenevinylene)/C[sub 60] heterojunction photovoltaic cell. *Applied Physics Letters* **68**, 3120-3122 (1996).
50 Gulbinas, V. *et al.* Exciton diffusion and relaxation in methyl-substituted polyparaphenylene polymer films. *The Journal of Chemical Physics* **127**, 144907 (2007).
51 Mikhnenko, O. V. *et al.* Temperature Dependence of Exciton Diffusion in Conjugated Polymers. *The Journal of Physical Chemistry B* **112**, 11601-11604, doi:10.1021/jp8042363 (2008).
52 Shaw, P. E., Ruseckas, A. & Samuel, I. D. W. Exciton Diffusion Measurements in Poly(3-hexylthiophene). *Advanced Materials* **20**, 3516-3520, doi:10.1002/adma.200800982 (2008).
53 Cook, S., Furube, A., Katoh, R. & Han, L. Estimate of singlet diffusion lengths in PCBM films by time-resolved emission studies. *Chemical Physics Letters* **478**, 33-36, doi:10.1016/j.cplett.2009.06.091 (2009).
54 Ward, A. J., Ruseckas, A. & Samuel, I. D. W. A Shift from Diffusion Assisted to Energy Transfer Controlled Fluorescence Quenching in Polymer–Fullerene Photovoltaic Blends. *The Journal of Physical Chemistry C* **116**, 23931-23937, doi:10.1021/jp307538y (2012).
55 Hedley, G. J. *et al.* Determining the optimum morphology in high-performance polymer-fullerene organic photovoltaic cells. *Nat Commun* **4**, doi:10.1038/ncomms3867 (2013).
56 Masri, Z. *et al.* Molecular Weight Dependence of Exciton Diffusion in Poly(3-hexylthiophene). *Advanced Energy Materials* **3**, 1445-1453, doi:10.1002/aenm.201300210 (2013).
57 Tamai, Y., Matsuura, Y., Ohkita, H., Benten, H. & Ito, S. One-Dimensional Singlet Exciton Diffusion in Poly(3-hexylthiophene) Crystalline Domains. *The Journal of Physical Chemistry Letters* **5**, 399-403, doi:10.1021/jz402299a (2014).

3

EXPERIMENTAL METHODS AND EQUIPMENT

3.1. INTRODUCTION

In this chapter the experimental methods and instruments used to measure the data presented in this thesis are described.

Section 3.2 describes the process of spin-coating samples. Section 3.3 describes the steady-state measurements carried out, including the absorption spectroscopy and the calculation of the photoluminescence quantum yield. Section 3.4 describes the instrumentation used to measure time-resolved fluorescence as well a description of how data produced using this method is best displayed.

3.2. SAMPLE PREPARATION

All thin films produced for this thesis were made using a technique called spin-coating. This is a technique to make nanometre smooth films of material deposited from solution. Spin-coating has a wide variety of uses, and was historically used to apply the phosphor to colour (cathode-ray tube) television screens and is still used to apply coatings for microelectronics and applying smooth layers of photoresist on top of semiconducting wafers[1]. The technique is frequently used in science to create very thin, smooth polymer films[2-4] and is

widely adopted as a way to deposit solution processable organic semiconductors in the laboratory context[5-8].

The organic semiconductors (or combination of semiconductors) under investigation were first dissolved in a suitable solvent, which in this thesis is chlorobenzene unless otherwise specified. After being left to dissolve overnight, the solutions were dripped on a clean fused silica disk and then spun at 2000 rpm for 60 seconds. Shortly after the start of this process the majority of the solution has been thrown off the film due to the centrifugal effect, but the remaining solution dries into a thin, smooth solid film.

These films were stored under nitrogen and transferred to the sample container, also under nitrogen.

3.3. STEADY-STATE MEAUREMENTS

3.3.1 Absorption Spectroscopy

In order to measure the optical absorbance of the thin films a Varian Cary 300 Bio UV-Vis spectrometer was used. Absorbance is simply a measure of the reduction in intensity of light passing through a sample relative to its incident intensity;

EQUATION 3.1. $$\frac{I}{I_0} = T = 10^{-A}$$

Where I is the intensity of light that passes through a sample, I_0 is the intensity of light incident on the sample, T is the transmission and A is the optical absorbance.

An important measure of the strength of a molecule's absorbance is the molar extinction coefficient, ε. This is defined by the Beer-Lambert law[9];

EQUATION 3.2. $$A = \varepsilon l c$$

Where l is the path-length through which the light travels and c is the molar concentration of the material.

The spectrometer measures the absorbance of the film by passing light from a lamp light through a monochromator before being sent down sample and reference arms, with the sample absorbance being deduced by recording how much light is lost when compared with the reference as it is measured by a photon multiplier tube.

3.3.2 PLQY Integrating Sphere

In order to calculate how fluorescent a material is, a parameter called the photoluminescent quantum yield (PLQY) must be measured. The PLQY represents the number of photons fluoresced divided by the number of photons absorbed; essentially how likely an excited state is to decay radiatively compared to non-radiatively.

PLQY is measured using the integrating sphere method. Because the organic thin film has a thickness that is on the order of the wavelength of light, thin-film interference effects can emerge, meaning that the amount of light escaping the film is highly angle-dependent. Consequently, it is not sufficient to measure the light emitted from any one angle to calculate the PLQY, it is also necessary to measure the total light emitted over all angles. To do this, an integrating sphere is used as described by Suzuki *et al*[10]. This is an improvement on the previously employed

integrating sphere method developed by Greenham *et al*[11]. An integrating sphere is a hollow sphere with a highly reflective internal surface.

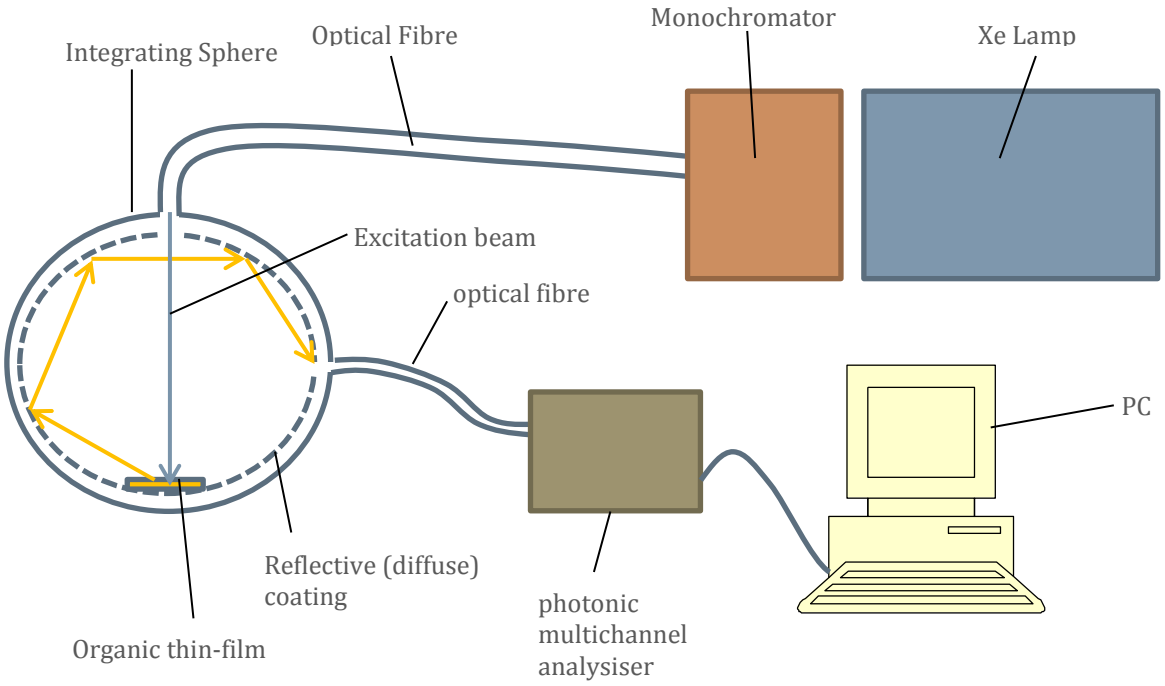

Figure 3.1. A schematic of the Hamamatsu PLQY instrumentation.

Because the inside of the sphere is very reflective, fluoresced light from all directions bounces around the inside of the sphere until it reaches the exit optical fibre which waveguides the light into the photonic multichannel analyser. The analyser consists of a back-thinned CCD which measures the whole spectral range of fluorescence with high sensitivity. By comparing the attenuation of the excitation light when the sample is present or not present, the number of photons absorbed can be measured. Likewise, by selecting a wavelength above which all photons are considered to have been fluoresced, the photodetecter can measure the number of photons fluoresced. This can be used to calculate the PLQY from the following relation[10].

EQUATION 3.3.

$$\text{PLQY} = \frac{Ph_{em}}{Ph_{abs}} = \frac{\int \frac{\lambda}{hc}[I^s_{em}(\lambda) - I^r_{em}(\lambda)]d\lambda}{\int \frac{\lambda}{hc}[I^s_{ex}(\lambda) - I^r_{ex}(\lambda)]d\lambda}$$

In the equation above, Ph_{em} and Ph_{abs} are photons emitted from the sample and photons absorbed by the sample, respectively. I^s_{em} and I^r_{em} are the emission intensity from the sample and from the reference (the intensity of fluoresced light when the empty quartz sample holder is excited) and I^s_{ex} and I^r_{ex} is the intensity of the excitation beam with, and without, the sample present.

3.3.3 Fluorescence Spectroscopy

The majority of the steady-state fluorescence spectra reported here were measured using the Hamamatsu integrating sphere as described in the previous section. The (I^s_{em} - I^r_{em}), instead of being integrated and divided by the absorbance as is shown in the above equation, was instead plotted with respect to wavelength to give the fluorescence spectrum of the polymer or small molecule.

3.4. TIME-RESOLVED MEASUREMENTS

3.4.1 Laser System

In order to probe processes that occur on a picosecond time-scale, such as exciton diffusion and charge separation, the excitation pulse must be on a shorter timescale. This is achieved by using pulsed laser excitation. In this thesis, the Spectra-Physics Mai Tai oscillator, a modelocked Ti:Sapphire laser, was used as the excitation source for all time-resolved measurements.

The Mai Tai consists of two lasing components, a continuous wave laser that acts as a pump for the Ti:Sapphire gain medium, which then produces ultra-short

pulses. The continuous wave laser consists of a laser diode that pumps neodymium ions (Nd^{3+}) in an yttrium vanadate (YVO_4) gain medium. This produces continuous wave 1064 nm laser output. This is frequency doubled to 532 nm using a lithium triborate nonlinear crystal[12] and used as the pump source for the Ti:Sapphire gain medium.

The Ti:Sapphire, when pumped at 532 nm in the resonator, can produce pulsed laser emission in the Mai Tai oscillator at any wavelength between 750 nm and 850 nm. The ability of Ti:Sapphire to produce such extraordinarily short pulses, on the order of 100 femtoseconds, is because of an effect called Kerr lensing. Kerr lensing arises in particular materials where the refractive index changes as a function of light intensity. If this material is the gain medium in a laser resonator then the higher index around the peak of the laser pulse acts like a lens, continually shortening the pulse as it travels through the gain medium. This effect is called self modelocking and was developed for Ti:Sapphire lasers at the University of St Andrews[13].

The femtosecond pulses produced with a repetition rate of 80 MHz from the Mai Tai were tuneable in the range 750 to 850 nm, were sent through a beta barium borate (BBO) frequency doubler, giving pulses in the wavelength range of 375–425 nm. This light was then used to excite the sample (with the exception of the red excitation of PTB7 in chapter 6, which used the fundamental 750 nm excitation).

3.4.2 Time-resolved Fluorescence

3.4.2.1 *The Streak Camera*

A streak camera is an instrument that measures the intensity and wavelength of the fluoresced light from a sample on the timescale of 2-2000 ps after the film is excited. The most common way to detect light and turn it into a digital signal is by using a Charge-Coupled Device (CCD). A CCD is an array of light sensitive domains that experience a change in voltage when they are struck by light. In a similar way as to how the light sensitive cells in a retina are used by the brain to build up an image, the changes in voltage across the CCD are used to build up an image in a digital camera. One of the major problems with using a CCD to measure the change in light as part of a time-resolved fluorescence set up is that at best the time response of a CCD is a few nanoseconds, a thousand times slower than the shortest times that need to be measured[14].

A streak camera is an ingenious way to get around the slow time response of the electronics. The basic premise of a streak camera is that when monitoring a fluorescence signal, it is much easier to detect *where* the light is incident on the CCD rather than *when* the light strikes the CCD. Thus if you can convert a difference in time to a change in position, the time-resolution can be improved drastically. The inner working of the Hamamatsu Synchroscan streak camera is shown below (figure and technical information from *Guide to Streak Cameras* by Hamamatsu[15]).

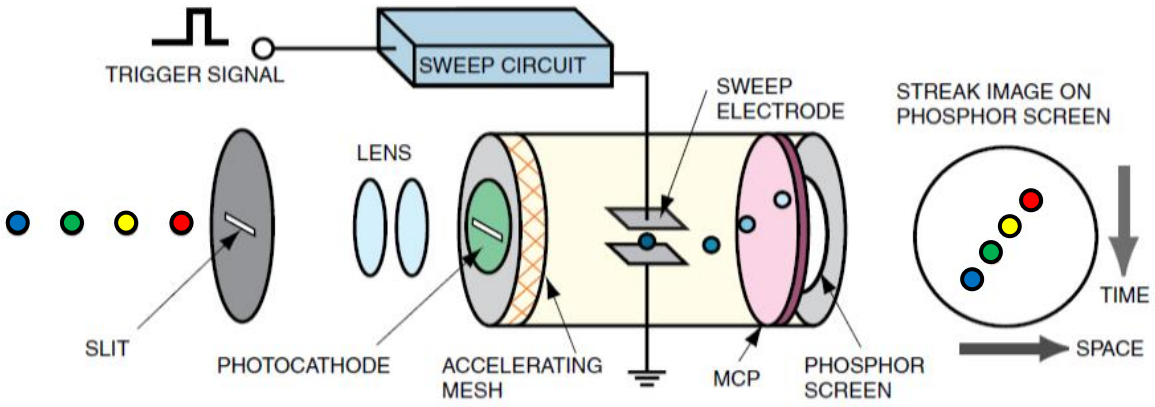

Figure 3.2. Diagram of the inner workings of a streak camera, adapted from *Guide to Streak Cameras* by Hamamatsu[15].

Light enters the streak camera through the horizontal slit at the far left of the diagram. It then goes through a series of lenses before impacting on a photocathode. When a photon is incident on a photocathode, an electron is ejected into the vacuum in the central tube. These electrons are accelerated (in the direction to the right on the diagram) by the electric field given by an accelerating mesh. This process has converted a stream of photons entering the streak camera into a stream of electrons travelling in the same direction with the same time delay. If the stream of photons was initially very high intensity but dropped in intensity rapidly with respect to time, this would be represented in the density of electrons in the stream, with a high density of electrons towards the front of the stream dropping down to a low density of electrons towards the back of the stream. The next step in the operation is when the stream of electrons passes through the sweep electrode. The sweep electrode causes a rapidly changing electric field in response to a trigger, which synchronises the sweep to happen just after the laser pulse. As the voltage is rapidly changing, the electrons at the front of the stream will experience a different voltage than the electrons at the rear of the stream. As

the voltage will deflect a moving electron, and the magnitude of the deflection will depend on the magnitude of the electric field, electrons arriving earlier or later will experience different electric fields and follow different trajectories than earlier ones. The electrons then impact onto a Microchannel Plate Detector (MCP) which is conceptually very similar to an array of photomultiplier tubes. An electron entering a MCP in one area will be multiplied many thousands of times, so that thousands of electrons exit the same area on the opposite side of the MCP. This enhances the signal carried by the electron stream. The electrons then impact onto a phosphor screen which converts the highly multiplied electrons back into photons which are then detected on a CCD.

As the electric field undergoes a linear sweep, an incoming beam of photons will produce a 'streak' on the CCD. Because the vertical position at which the electrons impact on the CCD determines the time the photon was incident on the photocathode, the temporal information has been accurately converted into easily measured, spatial, information.

There is an additional level of sophistication to the streak camera. Though it is not obvious from the above diagram, the most blue photon entered the initial slit to the far left (from its perspective) while the most red photon entered the initial slit from the far right. In the final streak image, the entire process has not altered this, the blue spot on the CCD is still on the far left of the image while the red spot is still on the right, though they have been both translated along the y-axis according to the time they were incident on the photocathode. That the x-position of incident photons is preserved offers a new opportunity to derive additional information about the wavelength of the time-resolved fluorescence of the film. The emission

can be focussed into a spectrograph which will split the emission based on wavelength and output it as a horizontal streak with shorter wavelength photons on one edge and longer wavelength photons on the other edge. If this is then fed into the horizontal slit of the streak camera, this means that the image detected on the CCD will be a 2 dimensional graph, with time on the vertical axis and wavelength on the horizontal axis, with the intensity at each pixel representing the intensity of light entering the streak camera at the corresponding intensity and wavelength.

Below is a diagram of the optical set-up prior to the streak camera with which the majority of the results reported in this thesis were derived.

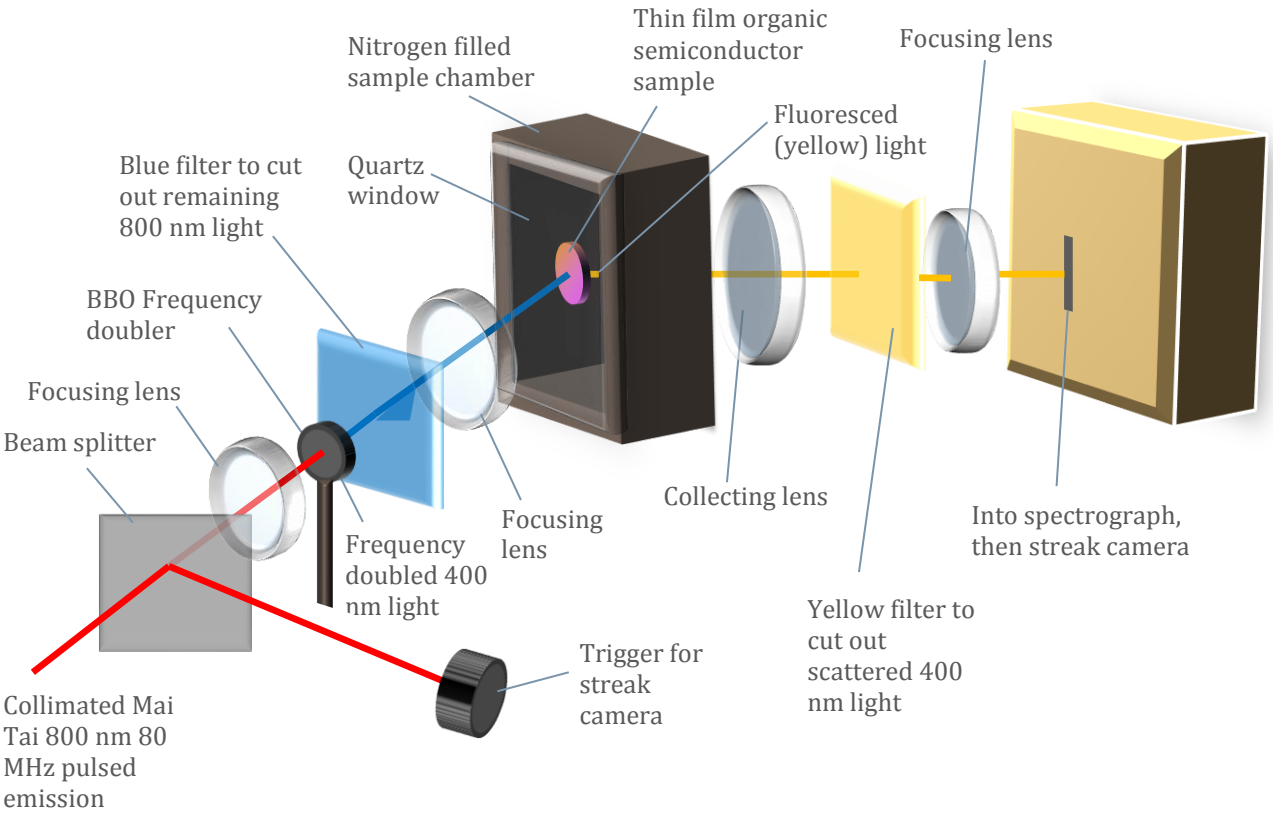

Figure 3.3. The optical set-up for time-resolved fluorescence measurements

The 800 nm, 80 MHz pulsed light from the Mai Tai was first sent through a beam splitter so that a portion of the beam intensity could be sent into the trigger by which the streak camera synchronises the voltage sweep with the excitation pulse. The remainder of the Mai Tai beam enters the BBO frequency doubler, and the 400 nm light produced travels through a blue filter to cut out residual 800 nm light. This beam is then focussed onto a spot in the sample. The organic semiconductor sample is kept in a nitrogen atmosphere (or under vacuum where indicated) and when excited with 400 nm light, will fluoresce at a wavelength red-shifted from the absorption (due to the Stokes Shift). This fluorescence will be emitted into a wide range of angles, so it is necessary to have a large collecting lens to collimate the fluorescence. It is also necessary to have the excitation beam path far from parallel to the fluorescence beam path so that the amount of excitation laser light being collected is minimised. Additionally a yellow optical filter is used after the collection lens in order to cut out any collected 400 nm excitation light. Finally a focussing lens is used to focus the light into the spectrograph.

3.4.2.2 *Calculation of the Response Function*

All time-resolved instrumentation will have an error associated with the difference between when a photon enters the instrument and the precise moment that it is recorded as entering the streak camera. The function that determines the time error of incoming light is approximately Gaussian, and is known as the instrument response function (IRF). The recorded PL decay will be a convolution of this function with the true decay.

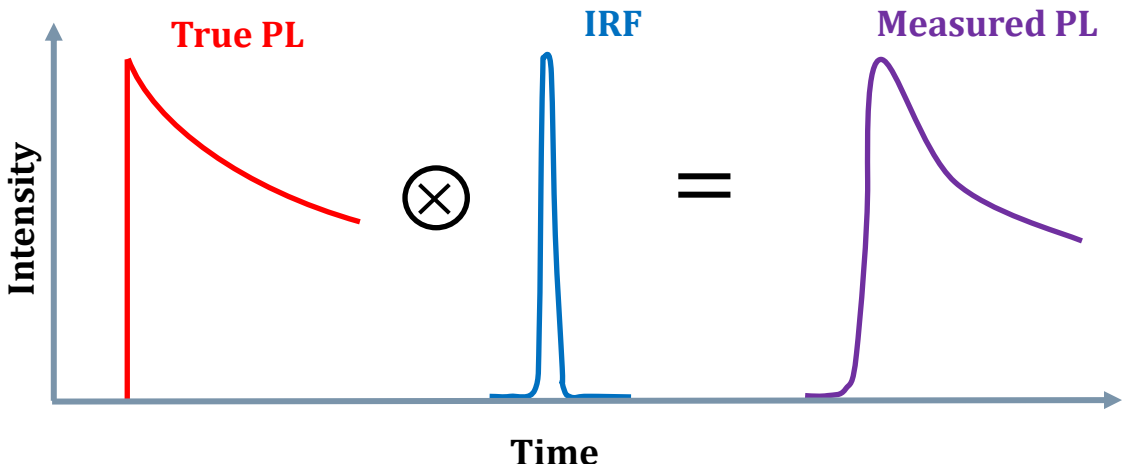

Figure 3.4. A cartoon illustrating the influence of the instrument response function (IRF) on the shape of the measured PL decay. Any information pertaining to a sharp drop in intensity of the population that occurs within the timescale of the IRF is lost due to the 'blurring' of the decay due to the Gaussian convolution.

If the underlying functional form of the decay is known, the best fit can be generated by convoluting the function with the IRF and then fitting directly to the measured PL. For this, the response function of the instrument must first be measured. The excitation pulse is much faster (~100fs) than the response function of the instrument (~2 ps), so if the excitation beam is directly incident on the streak camera, this will be well approximated by a delta function. Because a convolution of a function with a δ-function just returns the original function, the PL decay measured of the incident light pulse will be an accurate representation of the IRF. Below is the instrument function of the streak camera measured in this way (using a heavily attenuated excitation beam).

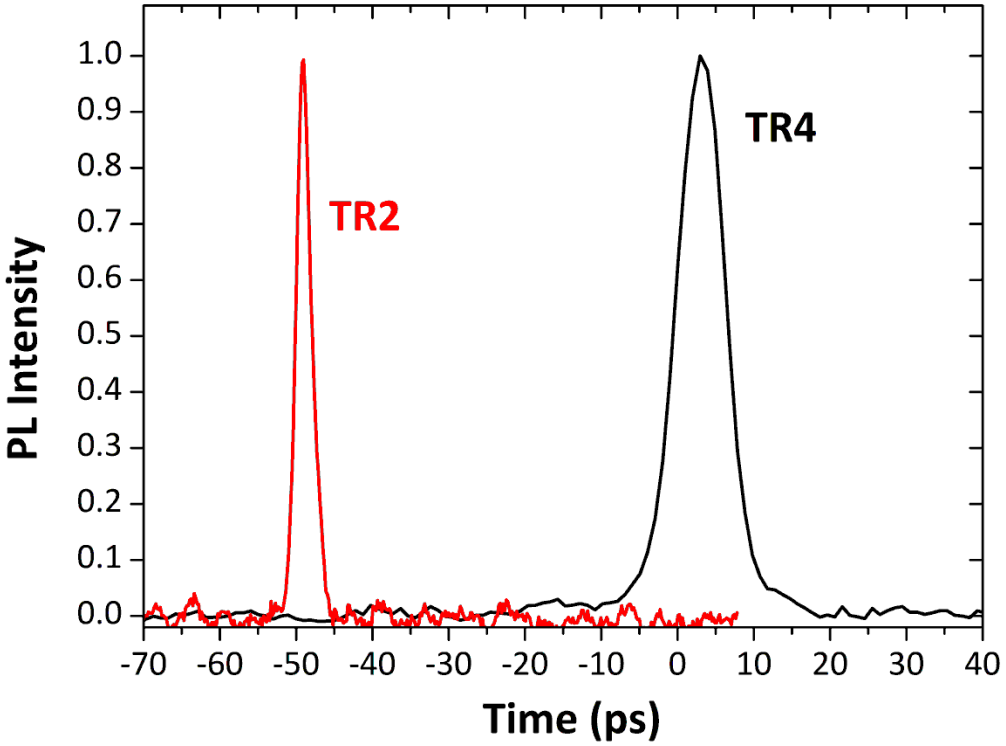

Figure 3.5. The streak camera response function for the most commonly used time-ranges in this thesis; time ranges 2 and 4.

3.4.2.3 *Modelling the PL decays*

In this thesis, the predominant focus is on the rate that the fluorescence intensity declines in a blend compared with the equivalent blend in the pristine material. Firstly the lifetime of the pristine material is calculated, by fitting with typically a one or two exponential decay function.

EQUATION 3.4. $$\mathrm{PL}_{prist}(t) = F_{exp}(t) * IRF(t)$$

Where $\mathrm{PL}_{\mathrm{prist}}$ is the PL decay as measured by the streak camera, $\mathrm{F}_{\mathrm{exp}}$ is a one or two exponential function and $*$ denotes a convolution. The quenching rate can then calculated from the following equation

EQUATION 3.5. $$\mathrm{PL}_{quench}(t) = Q(t, N_q)F_{exp}(t) * IRF(t)$$

where PL_{quench} is the PL decay of the quenched films and Q is a function that describes the population of excitons being subjected to a quenching process. Q will be dependent on what quenching model is used (see chapter 4) but will typically depend on the concentration of quencher, N_q.

An example of fitting using this technique is shown below, where it used to investigate blends of the commonly used solar cell donor material, P3HT with the electron acceptor C_{61}-PCBM . Equation 3.4 was fitted to the pristine film while equation 3.5 was fitted to the blend films, which had quantities of C_{61}-PCBM ranging from 0.2 wt% to 5 wt% mass ratio. In this particular case Q is defined by the Smoluchowski model (discussed in chapter 4). Fits are the black solid lines.

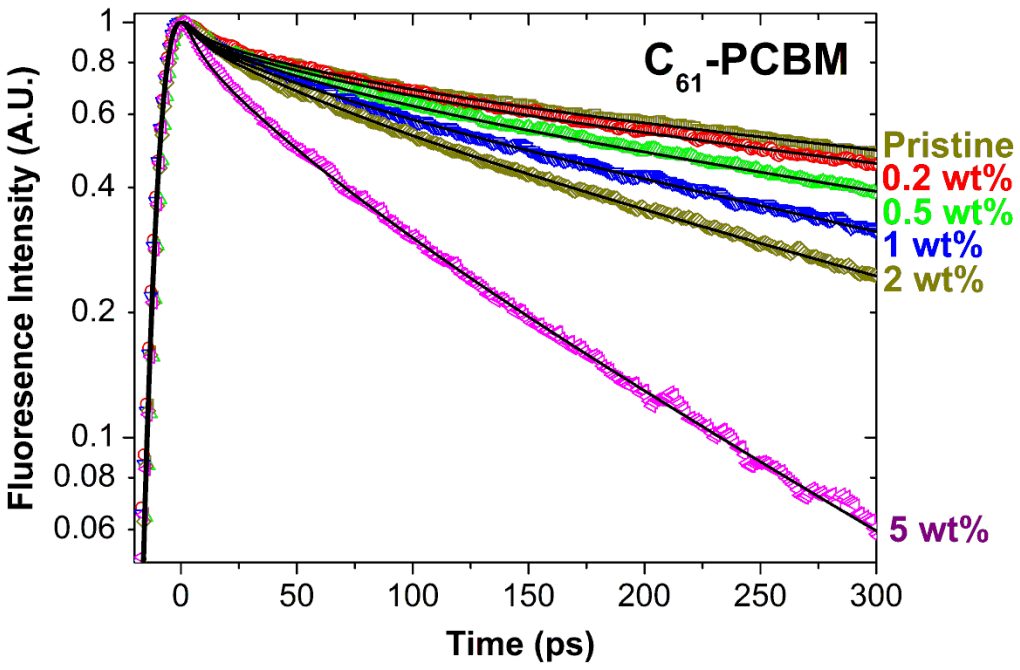

Figure 3.6. A plot of the fluoresence intensity of several blends with respect to time. Equations 3.4 and 3.5 are fitted to the data to allow parameters in quenching function Q to be fitted.

3.4.3 Displaying the data as a ln(PL Ratio)

3.4.3.1 *Introduction*

Throughout this thesis, the preferred method to calculate the quenching rate constant is not by fitting directly to the PL decays, as described in the previous section, but by fitting to what is referred to as the ln(PL ratio). The ln(PL ratio) is the natural logarithm of the quenched PL decay divided by the pristine PL decay and is commonly used to represent quenching information[16,17]. The gradient of the ln(PL decay) corresponds to the rate constant for the quenching process (derivation below)[16].This method is used because it allows the visual representation of the rate of quenching without making any assumptions about the functional form of the quenching process, as is required by the previously described method.

3.4.3.2 *Derivation and example*

The excitons in the pristine film will have a rate of change of population defined as

EQUATION 3.6. $$\frac{dN_{prist}}{dt} = -k(t)N_{prist}$$

where N_{prist} is the population of excitons in the pristine film and k(t) is the rate at which these excitons decay. The rate of change of the population of the excitons in the blend film will be

EQUATION 3.7. $$\frac{dN}{dt} = -k_q(t)N - k(t)N$$

where k_q is the rate of quenching.

If we define the ratio of N/N_{prist} as being equal to g(t), then

EQUATION 3.8.
$$N = g(t)N_{prist}$$

EQUATION 3.9.
$$\frac{dN}{dt} = g(t)\frac{dN_{prist}}{dt} + N_{prist}\frac{dg(t)}{dt}$$

substituting equation 3.6 and 3.7;

EQUATION 3.10.
$$-k_q(t)N - k(t)N = -g(t)k(t)N_{prist} + N_{prist}\frac{dg(t)}{dt}$$

therefore

EQUATION 3.11.
$$-k_q(t)g(t) = \frac{dg(t)}{dt}$$

which has the solution

EQUATION 3.12.
$$-k_q(t) = \frac{dln(g(t))}{dt}$$

Thus the gradient of the ln(PL ratio) is equal to the rate of quenching regardless of the functional form of k(t) or $k_q(t)$.

Below shows the same data as in figure 3.6, but plotted as a ln(PL ratio).

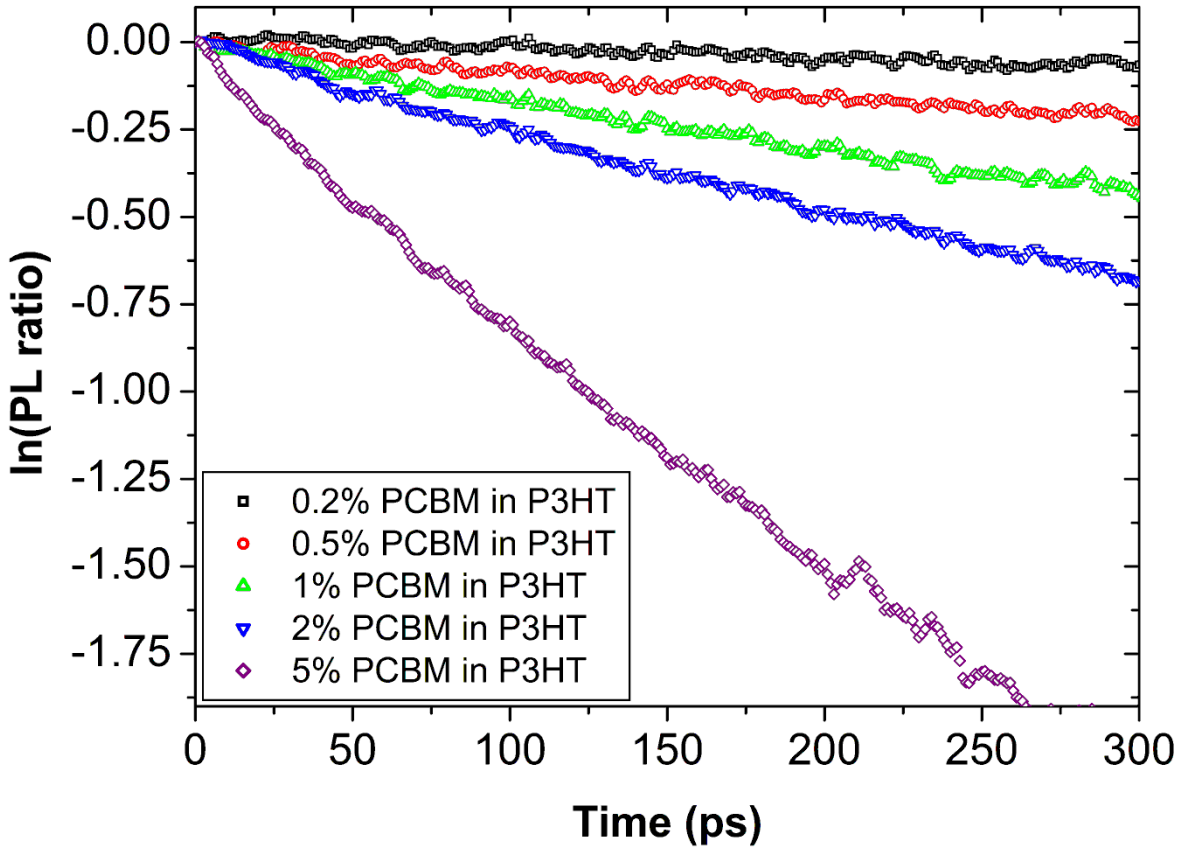

Figure 3.7. The ln(PL ratio) of blends of P3HT with C_{61}-PCBM.

3.4.3.3 *Advantages and Disadvantages*

The data as it is presented in figures 3.6 and 3.7, will now be compared. In figure 3.6 the PL decays are shown directly. This means the y-axis, the fluorescence intensity is a far more intuitive quantity than the y-axis in figure 3.7. Thus, someone unfamiliar with fluorescence quenching would find figure 3.6 much easier to understand. On the other hand, because the rate constant for quenching is merely the derivative of the ln(PL ratio), far more information is immediately apparent from figure 3.7. The linear traces in figure 3.7 indicate that the rate constant k_q is nearly completely time independent. The equivalent information in figure 3.6 is obscured because the pristine decay itself has a fast component at short time, so it is challenging to attribute the drop in population in the quenched

decays to this fast component or a time-dependence in the rate of quenching. An example of the very time-dependent ln(PL ratio) is given in chapter 5, figure 5.2. Thus it is usually more revealing to appreciate the time-dependence in the rate constant when the data is plotted as a ln(PL ratio), so it is this form which is used for the majority of the data shown in this thesis.

3.5. REFERENCES

1 Lawrence, C. J. The mechanics of spin coating of polymer films. *Physics of Fluids (1958-1988)* **31**, 2786-2795, doi:doi:http://dx.doi.org/10.1063/1.866986 (1988).

2 Extrand, C. W. Spin coating of very thin polymer films. *Polymer Engineering & Science* **34**, 390-394, doi:10.1002/pen.760340503 (1994).

3 Frank, C. W. *et al.* Structure in Thin and Ultrathin Spin-Cast Polymer Films. *Science* **273**, 912-915, doi:10.1126/science.273.5277.912 (1996).

4 Hall, D. B., Underhill, P. & Torkelson, J. M. Spin coating of thin and ultrathin polymer films. *Polymer Engineering & Science* **38**, 2039-2045, doi:10.1002/pen.10373 (1998).

5 Shaheen, S. E. *et al.* 2.5% efficient organic plastic solar cells. *Applied Physics Letters* **78**, 841-843, doi:doi:http://dx.doi.org/10.1063/1.1345834 (2001).

6 Martens, T. *et al.* Disclosure of the nanostructure of MDMO-PPV:PCBM bulk hetero-junction organic solar cells by a combination of SPM and TEM. *Synthetic Metals* **138**, 243-247, doi:http://dx.doi.org/10.1016/S0379-6779(02)01311-5 (2003).

7 Kim, J.-S., Ho, P. K. H., Murphy, C. E. & Friend, R. H. Phase Separation in Polyfluorene-Based Conjugated Polymer Blends: Lateral and Vertical Analysis of Blend Spin-Cast Thin Films. *Macromolecules* **37**, 2861-2871, doi:10.1021/ma035750i (2004).

8 Mikhnenko, O. V. *et al.* Exciton Quenching Close to Polymer−Vacuum Interface of Spin-Coated Films of Poly(p-phenylenevinylene) Derivative. *The Journal of Physical Chemistry B* **113**, 9104-9109, doi:10.1021/jp9012637 (2009).

9 Swinehart, D. F. The Beer-Lambert Law. *Journal of Chemical Education* **39**, 333, doi:10.1021/ed039p333 (1962).

10 Suzuki, K. *et al.* Reevaluation of absolute luminescence quantum yields of standard solutions using a spectrometer with an integrating sphere and a back-thinned CCD detector. *Physical Chemistry Chemical Physics* **11**, 9850-9860, doi:10.1039/b912178a (2009).

11 Greenham, N. C. *et al.* Measurement of absolute photoluminescence quantum efficiencies in conjugated polymers. *Chemical Physics Letters* **241**, 89-96, doi:http://dx.doi.org/10.1016/0009-2614(95)00584-Q (1995).

12 Velsko, S. P., Webb, M., Davis, L. & Huang, C. Phase-matched harmonic generation in lithium triborate (LBO). *Quantum Electronics, IEEE Journal of* **27**, 2182-2192, doi:10.1109/3.135177 (1991).

13 Spence, D. E., Kean, P. N. & Sibbett, W. 60-fsec pulse generation from a self-mode-locked Ti:sapphire laser. *Opt. Lett.* **16**, 42-44, doi:10.1364/ol.16.000042 (1991).

14 Mitchell, A. C., Wall, J. E., Murray, J. G. & Morgan, C. G. Measurement of nanosecond time-resolved fluorescence with a directly gated interline CCD camera. *Journal of Microscopy* **206**, 233-238, doi:10.1046/j.1365-2818.2002.01030.x (2002).

15 Hamamatsu. in *http://www.hamamatsu.com/resources/pdf/sys/e_streakh.pdf* (ed Hamamatsu) (2008).
16 Powell, R. C. & Kepler, R. G. Evidence for Long-Range Exciton-Impurity Interaction in Tetracene-Doped Anthracene Crystals. *Physical Review Letters* **22**, 636-639 (1969).
17 Ward, A. J., Ruseckas, A. & Samuel, I. D. W. A Shift from Diffusion Assisted to Energy Transfer Controlled Fluorescence Quenching in Polymer–Fullerene Photovoltaic Blends. *The Journal of Physical Chemistry C* **116**, 23931-23937, doi:10.1021/jp307538y (2012).

4

MODELLING EXCITON DIFFUSION IN POLYMERS AND SMALL MOLECULES

4.1. INTRODUCTION

Exciton diffusion is a fundamental photophysical process in organic semiconductors and a critical process in the functioning of organic photovoltaic devices. Because the diffusion lengths of an exciton in a solution processed material are typically very short, on the order of ten nanometres, there are huge challenges involved in the measurement of their diffusive behaviour.

In section 4.2 the fundamental mechanism for diffusion in organic semiconductors is discussed. Secondly, in section 4.3, I discuss the motivation for measuring exciton diffusion and the challenges involved, putting this in the context of literature on the subject. In section 4.4, I talk about the theoretical methods used to model exciton diffusion in this work. In the last section, section 4.5, I discuss a selection of techniques I developed over the course of my PhD to derive information about morphology in photovoltaic blends from the fluorescence of the blend by modelling the exciton diffusion.

4.2. THE MECHANISM OF EXCITON DIFFUSION

4.2.1 Introduction to Diffusive Processes

Exciton diffusion is the means by which excitons migrate from the place they are created, typically by the absorption of the photon, to their final location, some distance away. Unlike charged species, such as polarons, excitons are neutral and thus cannot be motivated into moving preferentially in one direction by an electric field. Thus there is on average no particular energetic incentive to move to any particular direction, though there may be local undulations in the energy landscape. If excitons on the microscopic level move in random directions, more excitons will move out of a volume with a high concentration than out of a volume with a low concentration of excitons. Thus, though a single diffusing exciton will appear to move in a wholly unpredictable way, a population will always move from a high concentration to a low concentration as in any diffusive process. This is illustrated in the schematic below;

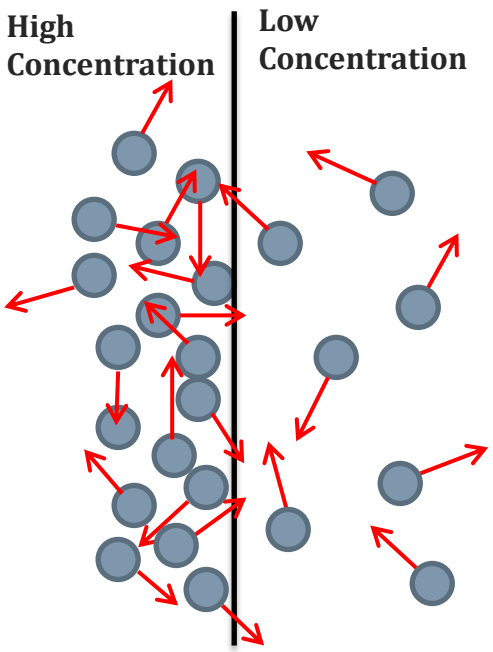

Figure 4.1. A simple visual representation of why ensemble populations of diffusive species, on average, move from higher to lower regions following concentration gradients. Though on average each exciton hops in a random direction (red arrows), when their collective properties are viewed, it is clear that there are more excitons crossing the black line from left to right (4) than from right to left (1). This means that on average the high concentration side is reducing in concentration whereas the concentration is increasing on the low concentration side resulting in an apparent shift of population from left, to right down the concentration gradient.

If the exciton hopping rate is on average a constant then the ensemble movement of excitons can be quantified by Fick's laws of diffusion which apply to molecules, the movement of heat through a bar and any other diffusive species. Ficks' first law describes the rate of mass transport through a certain area

EQUATION 4.1.

$$J = -D\frac{d\varphi}{dx}$$

where J is the mass transport through a unit area along the x-axis. D is the diffusion coefficient and describes the diffusivity of the exciton and φ(x,y,z,t) is the population of excitons at position (x,y,z) and time, t.

Fick's second law, herein described as *the diffusion equation* can be written as

EQUATION 4.2. $$\frac{d\varphi}{dt} = D\nabla^2\varphi + G - R$$

where G is equal to the rate that excitons are being generated (for experiments where all excitons are generated at t=0 via an fs laser pulse, this will be zero when t≠0) and R represents the rate at which excitons are lost from the system (which in most cases will be due to fluorescence decay $R=k_f(\varphi)$).

To make predictions about the diffusion equation, or other properties of the excitons from the photophysical measurements performed on the film, a variety of solutions of equation 4.2 are used with boundary conditions appropriate for the context in which they are used. This is described in section 4.4. One trivial case, which is worth mentioning here, is the solution to equation 4.2 in one dimension with infinite boundary conditions and the initial condition that at t=0, the population is entirely localised at the point x=0. Neglecting the generation and loss terms, from inspection it can be seen that under these conditions, the following is a possible solution for equation 4.2.

EQUATION 4.3. $$\varphi(x,t) = \frac{1}{\sqrt{4\pi Dt}} e^{-\frac{x^2}{4Dt}}$$

The physical implication being that the probability of finding an exciton at a given place, after its creation at x=0, is Gaussian with the peak at x=0 and it spreads out as time goes on. If we wish to calculate the mean-squared displacement from

its starting position we need to integrate the probability of finding the exciton at a given displacement (φ(x,t)), multiplied by the displacement squared;

EQUATION 4.4.

$$\langle S^2 \rangle = \int_{-\infty}^{\infty} \frac{x^2}{\sqrt{4\pi D t}} e^{-\frac{x^2}{4Dt}} dx = 2Dt$$

Thus the mean-squared displacement increases linearly with time. An average exciton has a lifetime of τ, so will undergo a root-mean-squared displacement over the course of its lifetime of

EQUATION 4.5.

$$L_D = \sqrt{2D\tau}$$

This root-mean-squared displacement is typically known as the one dimensional diffusion length and is a convenient and intuitive measure of diffusivity. Often, in the literature, the factor of $\sqrt{2}$ is neglected for convenience and L_D is taken to be $\sqrt{(D\tau)}$.

4.2.2 The Hopping Leading to Diffusion

Let us now consider the case where the overall diffusion of species is due to individual hops between lattice sites. This is known as a discrete diffusion model (as opposed to a continuum model). For simplicity, the model discussed will assume diffusion on a cubic lattice, where each site has 6 nearest neighbours, which have a lattice spacing of length a. After a set time, t_{hop}, all excitons will hop to a nearest neighbour site at random. Thus the change in population at the site (i,j,k) after t_{hop} can be described as

EQUATION 4.6.

$$\Delta n_{i,j,k} = +\frac{1}{6}n_{i+1,j,k} + \frac{1}{6}n_{i-1,j,k} + \frac{1}{6}n_{i,j+1,k} + \frac{1}{6}n_{ij-1,k} + \frac{1}{6}n_{i,j,k+1} + \frac{1}{6}n_{i,j,k-1} - n_{i,j,k}$$

This can be rearranged to the form

EQUATION 4.7.

$$\frac{\Delta n_{i,j,k}}{\Delta t} = \frac{a^2}{6t_{hop}}\left(\frac{n_{i+1,j,k} + n_{i-1,j,k} - 2n_{i,j,k}}{a^2} + \frac{n_{i,j+1,k} + n_{i,j-1,k} - 2n_{i,j,k}}{a^2} + \frac{n_{i,j,k+1} + n_{i,j,k-1} - 2n_{i,j,k}}{a^2}\right)$$

This is the discrete form of Fick's second law of diffusion (equation 4.2) where G and R are equal to zero and D is defined as

EQUATION 4.8.

$$D = \frac{a^2}{6t_{hop}}$$

where t_{hop} is the time for every exciton to undergo a single hop to a neighbouring site and *a* is the spacing between nearest neighbours.

Though equation 4.8 requires the assumption of a cubic lattice of equal spacing, *a,* in order to be valid, and only considers diffusion due to nearest neighbour hops, it is nonetheless qualitatively useful to link the ensemble property of the material, D, with the microscopic property of the exciton t_{hop} and the structural property of the material *a*. Clearly the mechanism, and consequently the rate, by which excitons are transferred from chromophore to chromophore is extremely important to the diffusion of excitons.

It is worth considering whether this discretised description of diffusion is a valid descriptor of continuous diffusive behaviour. Consider that $\Delta y/\Delta x$ is only a good approximation of dy/dx when Δx or d^2y/dx^2 is small. Monte-Carlo models involving discrete hopping are commonplace in the literature of diffusive processes[1-6] and give accurate descriptions, even of continuous diffusive processes. In section 4.4.3.1.1, a discrete and a continuous description of quenching due to a diffusive process are compared and it is found that they give almost identical predictions.

4.2.3 Hopping Mechanism

The predominant mechanism by which singlet excitons move from chromophore to chromophore in an organic semiconductor is by Förster Resonance Energy Transfer (FRET). FRET occurs when the optical dipole of an excited chromophore (an exciton) resonates with the optical dipole of a nearby ground-state chromophore. This means that instead of the fluorescence of a photon, the excited state energy is transferred through space to a second chromophore. This resonant energy transfer is analogous to the energy transfer observed between two coupled pendulums. The rate at which this process happens depends on the spacing between the donor and acceptor chromophores and the degree to which the excited state optical dipole can resonate with the ground optical state dipole. Because resonance will require matched energy between the donor and acceptor, the rate of FRET will depend not just on the oscillator strength

of the donor emission and acceptor absorption but also on the spectral overlap between these two transitions.

This can be quantified as[7]

EQUATION 4.9.

$$k_{FRET} = \frac{1}{\tau}\left(\frac{R_0}{r}\right)^6$$

where τ is the lifetime of the excited state, R_0 is known as the *Förster radius* and is the chromophore separation at which there is a 50% chance of energy transfer in the lifetime of the excited state and r is the distance of separation. R_0 can be calculated from

EQUATION 4.10.

$$R_0^6 = \frac{9PLQY(ln10)\kappa^2 J}{128\pi^5 n^4 N_A}$$

where PLQY is the PLQY of the donor, κ is an orientation factor representing the relative orientation of the two dipoles, n is the refractive index of the medium, N_A is Avogadro's number and J is the spectral overlap factor as defined by

EQUATION 4.11.

$$J = \int f_D(\lambda)\epsilon_A(\lambda)\lambda^4 d\lambda$$

Where f_D is the normalised fluorescence intensity of the donor, ε_A is the molar extinction coefficient of the acceptor and λ is the wavelength.

Thus from equation 4.8., one might expect an R_0^6 dependence on D which translates to a linear dependence on spectral overlap, J.

In reality this is a very simplistic description of resonance energy transfer. The above equations are only valid if the dipoles involved can be considered to have zero spatial extent, i.e. they can be considered point dipoles. In conjugated

materials, typically the chromophore extends in one direction much more than the others and is much better represented by a line dipole[8,9]. There is some evidence to suggest that in stationary dipoles, such as chromophores, the dipole approximations inherent in the derivation of the Förster equation break down when the excitons are closer than ~ 5 nm; much closer than nearest neighbour chromophores in a conjugated film[10].

4.2.4 Downhill (Dispersive) Diffusion

Up until this point within this section it has been assumed that the diffusion coefficient, and consequently the average hopping rate, is entirely time-independent. While this is entirely appropriate for the diffusion of molecules through solution, it is not necessarily valid for excitons moving through an organic semiconductor, especially an amorphous polymer semiconductor, for the following reasons. As described in section 2.3.2 of chapter 2, the size of a chromophore in a conjugated polymer is determined by its conjugation length. As described in that section, the conjugation length can vary from site to site as randomly situated defects, caused by kinks in the polymer backbone as well as other distortions of the molecule, break the conjugation. A distribution of the conjugation lengths will lead to a distribution in the S_1 energies of the different chromophores, and this broadening of the absorption energies is typically known as inhomogeneous broadening. This is to distinguish the effect from homogeneous broadening, which just broadening which each chromophore experiences equally, and is in large part due to vibrations associated with the ambient temperature.

Inhomogeneous broadening can be distinguished from homogeneous broadening because if an absorption spectrum was purely homogeneously broadened, the excitation at any wavelength would result in emission at a consistent wavelength. This is because the thermal energy in the film will quickly redistribute the possible emission states. On the other hand, if the system is inhomogeneously broadened, then by exciting on the far red edge, only low energy sites are being excited. Because FRET from these low energy sites will be energetically disfavoured, the excited states will be trapped on these low energy sites and emission will be red-shifted[11].

When the organic semiconductor is illuminated, the photons striking the semiconductor have to have a higher energy than the $S_0 \rightarrow S_1$ transition to be absorbed and often have significant excess energy. In this thesis, the majority of photophysical measurements were conducted with fs-pulsed 400 nm light, which typically produced excitons way above typical band-gap energies. This blue-tail excitation has the potential to preferentially excite the high energy chromophores affecting the measured exciton diffusion.

In the previous section, 4.2.3, it was demonstrated that the diffusion coefficient will be proportional to the spectral overlap between the emission of the donor chromophore and the absorption of the acceptor chromophore, *J*. Because the S_1 state undergoes relaxation between absorption and emission, the absorption peak will typically be bluer than the emission peak. A high energy chromophore will have a blue absorption, but also a bluer emission and thus a higher value of *J* when transferring to a chromophore of lower energy. Thus if the exciton is created at a high energy site, it will preferentially transfer to lower and lower energy sites

until it reaches thermal equilibrium, at which point it is making as many uphill hops as downhill hops. Until it equilibrates, the effective diffusion coefficient will decrease with respect to time. This dispersive transport has been modelled extensively by Heinz Bässler and co-workers[1-3] as well more recently by Burlakov *et al.*[12] This literature is discussed in section 4.3.

4.2.5 Direct FRET to Photovoltaic Acceptors

Previously in this section we have been discussing diffusion that proceeds via hops that are completely randomly directed. An exciton is neither more nor less likely to go towards or away from the heterojunction interface in the active layer of an organic photovoltaic device. The exception to this is if the exciton can undergo FRET to the other component of the photovoltaic blend. This will occur if there is spectral overlap between the emission of one of the photovoltaic materials; be it the electron donor or the electron acceptor, and the absorption of the other component of the blend. If this overlap is stronger than the overlap with the surrounding material, the exciton will preferentially hop directly to the other material. As this hop is to a chromophore at the heterojunction interface, it is very likely to be followed by extremely rapid electron transfer hence it will almost certainly be the final hop in the excitons journey. In this way exciton harvesting may be enhanced beyond that given by purely diffusive transport. This is described in more detail in Chapter 5 and is discussed in the literature[13,14].

4.3. MOTIVATION AND LITERATURE REVIEW

As discussed in section 2.4.2 of chapter 2, exciton diffusion is a critical process in the functioning of organic photovoltaic devices. In that section it is explained that excitons that do not reach the heterojunction interface during their lifetimes are wasted, and this potential leads to a drop in efficiency. Whether or not the exciton reaches the interface is dependent on the exciton diffusion length, and the short exciton diffusion lengths reported in the literature necessitates the introduction of a device structure called the bulk heterojunction, in which the donor and acceptor materials are finely blended, leading to significantly shorter distances that are required to be traversed by excitons in order to reach the highly distributed interface.

Even in a bulk heterojunction, exciton diffusion is believed to have a critical role. If the length scale of the phase segregation between the donor and acceptor is too large, then excitons still will not reach the interface and undergo charge separation in the device blend. This can be identified as photoluminescence from the blend, as emitted photons are characteristic of unharvested excitons undergoing radiative recombination. This is observed in P3HT where some fluorescence is observed in blends with 50 wt% fullerene (device concentrations) as well as 90 wt% fullerene concentrations[15] indicating a phase segregation on the order of a diffusion length. Such fluorescence has been observed in blends of PTB7:C_{71}-PCBM, the highest performance single junction OPV, when a critical solvent additive is omitted from the cell's manufacture. This fluorescence in conjunction with topological measurements indicated that the solvent additive leads to finer mixing and a more optimised morphology[16].

Because exciton diffusion is such a key step in the functioning of an organic solar cell, there have been numerous attempts in the literature to measure it in different materials[4,6,17-26,]. Typically because a diffusion length is so short, on the order of 10 nm or less, indirect methods must be used to infer the distance travelled by an exciton. This typically involves designing an experiment where an exciton is either harvested in some way or induced to decay non-radiatively, but only after it undergoes a diffusion limited process.

The major differences between the methods to measure exciton diffusion relate to how these quenchers are distributed in the film, the nature of the quencher and how the rate of quenching is measured. The quencher can be distributed in the film as a flat interface, distributed through the film evenly, or any other well defined geometry. It is necessary to have a very well defined geometry because the morphology of the quencher blend, particularly the interfacial area between the quencher and the material under investigation, will have as strong an influence over the kinetics of exciton quenching as the rate at which the excitons are diffusing. Thus the only morphologies where this influence can be ruled out are well defined 'trivial' morphologies, either a single planar quenching interface or an intimate mixture of low concentration quencher molecules spread throughout the film.

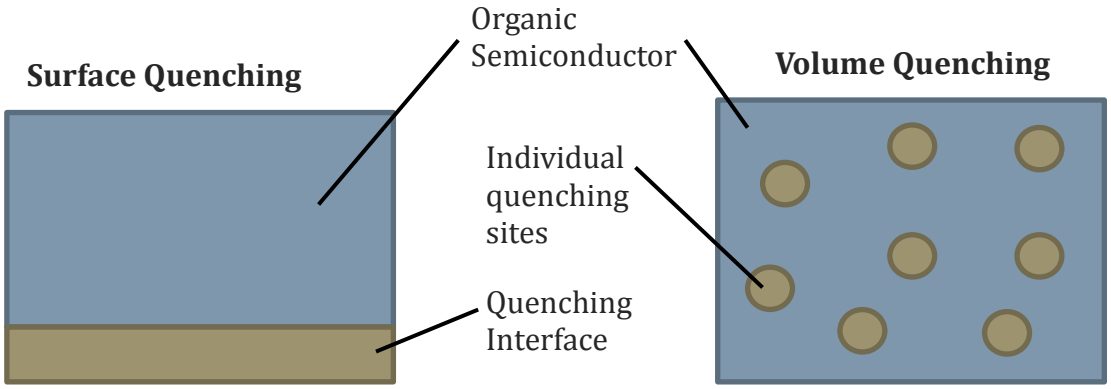

Figure 4.2. Both the surface quenching (left) and the volume quenching films (right) have well defined interfaces. In the surface quenching case, the interface is well defined because it has only a single planar interface. In the volume quenching case, the interface is well defined because each quencher molecule is dispersed in the organic semiconductor and the amount of interface will depend only on the concentration of quenching molecules.

The quencher can be a molecule designed to have an electron affinity (or ionisation potential) tuned so that an exciton will transfer an electron (or hole) after an encounter. Alternatively a quencher may be a FRET acceptor, leading to energy transfer after an encounter. Finally the role of quencher may be taken up by the excitons themselves, as at a high exciton concentration the excitons themselves will annihilate after encountering each other, and as a result, decay non-radiatively.

The terms *Surface Quenching* and *Volume Quenching* will be used to describe exciton diffusion measurements using quenching by a planar interface and by quenching by an intimately blended quencher. These two methods will be discussed in greater detail in the following sections, section 4.3.1 and 4.3.2.

The final option to be discussed is the form of detection. The most intuitive way of probing exciton harvesting is to combine the planar quenching interface with a solar cell and measure photocurrent. Assuming that recombination is low, one harvested exciton will lead to one electron of photocurrent. In reality it is extremely challenging to create an otherwise efficient device with a perfectly

quenching interface that does not diffuse into the active layer, obscuring the true diffusion length. Another method of probing the rate at which the excitons are being quenched is to observe the drop in population of excitons relative to the population of excitons in an unquenched sample. The first way of doing this is by detecting the fluorescence of the sample. As singlet excitons in fluorescent materials have a finite probability of emitting a photon over the course of their lifetime, the rate at which photons are emitted is a quantitative measure of the total population of excitons in the film. The steady state fluorescence intensity of the film with quencher, divided by the fluorescence intensity of an otherwise identical film without quencher will give the ratio of excitons quenched, and hence the ratio of excitons harvested.

Steady-state measurements are more susceptible to errors however. The absolute intensity depends on the alignment of the instrument as well as the thickness of the film. Thus it is critically important that the quenched film and the control are as similar as possible and have exactly the same alignment. In addition, if the quencher absorbs any excitation light this will impact on the experiment; any photons absorbed by the quencher rather than material under investigation will reduce the initial population of excitons and consequently the resulting fluorescence. This will make it appear as if additional quenching has taken place when in actuality the initial population of excitons was lower.

Time-resolved fluorescence measurements overcome all of these problems, as well as providing a vast amount of additional kinetic information about how the

rate of exciton harvesting changes with respect to time. Another well used method to monitor the population of excitons is through transient absorption measurements. Using this technique the change in population of excitons can be observed with respect to time by observing the change in absorption of the film after excitation with a pump pulse of light. Because the excitons themselves absorb light at particular wavelengths, and prevent light from being absorbed at other by 'bleaching' the chromophores they reside on, the population of excitons will be directly proportional to the change in absorption of the probe beam, in the absence of other excited states in the film. Herein lies one of the major challenges in transient absorption; because the absorption of the excited species tend to significantly overlap, it is very hard to isolate the transient population of a single species.

In this thesis transient-fluorescence spectroscopy, as described in chapter 3, section 3.4.2 will be used to probe exciton population in the film. It is limited to emissive materials, but is selective; fluoresced light can have no origin other than singlet excitons. For the purposes of modelling I will thus equate the normalised transient fluorescence intensity to the normalised population of singlet excitons.

4.3.1 Surface Quenching

The use of a planar quenching surface to measure the diffusion coefficient of excitons has continued since the 1960s[27,28] though until recent years it has been confined to use with molecular crystals. This is because molecular crystals, such as tetracene[27] and perylene derivatives[28] have fairly long exciton diffusion lengths on the order of hundreds of nanometres. These long diffusion lengths mean that sources of error that ruin the measurement if the diffusion lengths are less than 10

nm are fairly insignificant in molecular crystals. These sources of error include intermixing at the interface[17,29], failure to account for long-range quenching and thin film interference effects[20]. These sources of error are discussed later in this section as they become relevant.

An early example of surface quenching being used to measure exciton diffusion coefficients in OPV relevant materials was conducted by Theander *et al.*[30] in 2000. In that work, the exciton diffusion coefficient of a substituted polythiophene was measured using a quenching surface consisting of C_{60}. The acceptor C_{60} is a reasonable choice of quencher because it is commonly used as an electron acceptor in solar cells, and has been demonstrated from photoinduced optical absorption and photoinduced electron spin resonance to rapidly accept electrons from donor materials[31]. It has the added benefit that being a similar conjugated organic material, it has a low dielectric index contrast, and hence less strong thin-film interference effects[20]. Theander *et al.* use the steady-state photoluminescence from the planar heterojunction films to measure the exciton diffusion length and find it to be ~5 nm in the polythiophene they investigate. The model they use however, does not account for FRET to the interface, which has subsequently been found to play a major role in exciton harvesting[32,33]. Additionally the work was later criticised for not considering the diffusion of C_{60} molecules into the donor material, which likely enhanced the photoluminescence quenching[17,19].

In a later work, Markov *et al.*[17] directly address the issue of C_{60} diffusion by using a fullerene derivative that contains alkyne side groups that can be cross-linked after spin-coating to form an insoluble quenching layer. They use time-resolved fluorescence as their probe of exciton quenching but integrate the decays, thus neglecting the kinetics of the quenching process. They calculate a rather long diffusion length of 28 nm for a polyphenylvinylene derivative but still fail to take into account FRET, which may have a strong influence on the measured diffusion length when the quencher is a slab of electron accepting molecules[34].

In recent years titanium dioxide (TiO_2) has found wide use as a quenching interface for surface quenching measurements on OPV films. It is believed to be an efficient quencher, accepting electrons rapidly[35] with further evidence of efficient exciton harvesting being that hybrid solar cell using TiO_2 as the electron acceptor have been produced[36]. It has the added advantage that smooth films can easily be produced through evaporation and the film created has no chance of diffusing into the organic material as it is an inorganic crystal. A final advantage as that as a high bandgap inorganic semiconductor, its absorption range is far too blue to overlap with the emission of almost all solar cell materials[19].

One attempt at using TiO_2 in a surface quenching experiment was by Savenjie *et al.*[37] who measured the diffusion length of MEH-PPV, monitoring the material's steady-state PL. Unfortunately the authors fail to account for one of the biggest disadvantages of TiO_2 as a quenching interface; its high refractive index and prominent thin-film interference effects. Later work by Scully and McGhee[20] has shown that this failure introduced an error as large as the diffusion length measured.

Burlakov *et al*.[12] also investigated the surface quenching of MEH-PPV on TiO_2 but use a dispersive exciton hopping model to analyse the time-resolved PL data. The authors assign the strong time-dependence of the quenching in these materials as evidence of dispersive transport, but do not adequately model the thin-film interference from the TiO_2 surface.

In 2008, Shaw *et al.*[19] also used TiO_2 but overcame the problem of thin-film interference by using a TiO_2 thickness selected using optical modelling that minimises the effect for the wavelength of light used in excitation (400 nm). The authors measured the diffusion length of P3HT to be 8.5 nm and compared this value with that calculated from a complementary technique, exciton-exciton annihilation. The two techniques were in very good agreement meaning that the value generated may be considered reliable. One downside of this work was that the authors concede that their value is a lower limit, because it is necessary to assume that quenching occurs instantly when excitons come into contact with the titanium dioxide. Later studies have found that exciton quenching on titanium dioxide surfaces can be enhanced when the surface is functionalised, indicating that electron transfer is, to some extent, limiting harvesting at this interface[38,39].

4.3.2 Volume Quenching

Using volume quenching to probe exciton diffusion has had less widespread use. Like surface quenching, the first published application of the technique was in molecular crystals. Powell and Kepler[40] used time-resolved fluorescence to determine the exciton diffusion rates in anthracene crystals doped with the

quencher, tetracene. Powell and Kepler saw a strongly time-dependent rate of quenching which they assigned to a small diffusion coefficient in conjunction with a long range quenching process; FRET. This was easily testable, because the quencher used, tetracene, was itself highly emissive, meaning that the fluorescence of quencher detected in the work (after the donor was excited) is strong evidence of FRET.

Early work in modelling the motion of excitons and polarons in organic semiconductors was carried out by Heinz Bässler and co-workers[1-3]. The authors simulated a grid of lattice sites which have a Gaussian distribution of energies. Hopping occurs between nearest neighbours with a weighted probability that is a constant for isoenergetic and downhill transitions but declines with $\exp(-\Delta E/kT)$ for a transition to a site ΔE higher in energy. The authors found that broader energy distributions gave more highly time-dependent diffusion, and found the model fitted well to experimental data on the polymer (poly(9-vinylcarbazole)).

Markov *et al*[21] use small concentrations of commonly used electron acceptor, C_{61}-PCBM in the well-studied polymer, MEH-PPV, to calculate the diffusion coefficient of the polymer. To analyse the data they use a model describing discrete hopping in the presence of traps, originally developed by Balagurov and Vaks[41]. Markov *et al.* find a poor agreement between their measured value of diffusion calculated from volume quenching, compared to their value calculated from surface quenching, which they attribute to the occurrence of one-dimensional diffusion.

Perhaps due to the wider availability computing power there has been a resurgence in recent years of kinetic Monte-Carlo modelling of exciton diffusion.

One of the most prolific publishers of volume quenching analysed using this form of modelling are Mikhnenko and co-workers[4-6,26,42] as well as other groups who have published using the same model, which has been made publically available[43]. The simulation used consists of a fine cubic grid of lattice sites upon which excitons hop between nearest neighbours with a rate determined by their diffusion coefficient (see equation 4.8). All hops are considered to be isoenergetic; no dispersive transport is considered. Later in this chapter it is demonstrated that this model very closely reproduced the results given by the Smoluchowski rate equation, and that results generated from this simulation can be considered to be equivalent to those fitted with the analytical quenching solution. While the model does allow the simulation of quenching due to the clustering of fullerene, a big omission is that, similar to the Smoluchowski rate equation (section 4.4.3.1), once an exciton encounters a quenching site it is considered to be immediately quenched. In Chapter 6 and 8 of this thesis strong evidence is presented indicating that the rate of quenching is more strongly determined by the rate of electron transfer once the exciton is at the quencher, rather than the rate the excitons will encounter the quenching sites. Additionally the model produced by Mikhnenko *et al.* does not account for long-range quenching due to FRET which may be significant if there is spectral overlap between the donor and the acceptor.

4.4. METHODS TO MEASURE EXCITON DIFFUSION

4.4.1 Introduction

In this section the theoretical methods used throughout this thesis to model exciton diffusion in the techniques volume quenching and surface quenching are described.

4.4.2 Surface Quenching

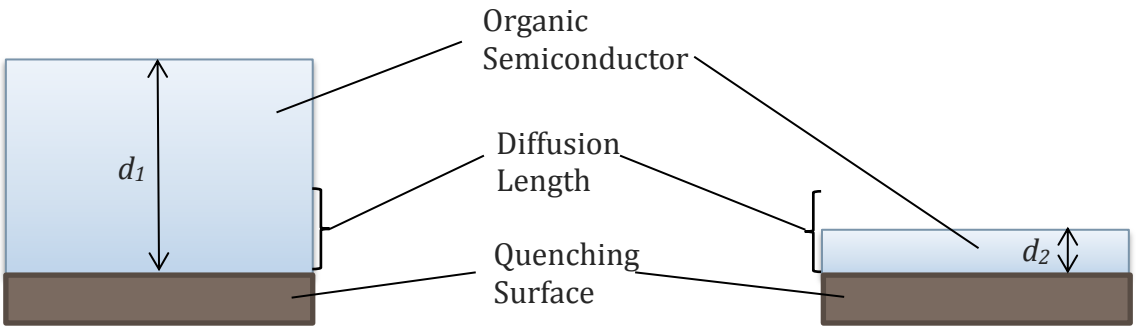

Figure 4.3. The population of excitons in the thick film (left) will decay much more slowly than in the thin film (right), as a much smaller ratio of excitons created within the film will have a chance of diffusing to the quenching surface. In the above cartoon excitons created at the top face of the thick film are more than two times the average diffusion length of an exciton in the film so have a vanishingly small chance of being quenched. On the other hand an exciton created on the top face of the thin film is well below a diffusion length from the surface, so has a good chance of being quenched.

Surface quenching as described in the previous section, requires a geometry where there is a smooth, planar interface of a quenching material in contact with a thin film of the organic semiconductor under investigation. Intuitively it might be expected that the fluorescence lifetime of a very thin film on a quenching interface would be shorter than a thicker film on a quenching interface, which itself will be shorter than the lifetime of a film on a non-quenching interface.

To quantify this observation it is necessary to model the change in exciton lifetime with respect to time, and thus a solution of the diffusion equation be found, with the boundary condition that the concentration of excitons on the quenching

interface is held at zero, whereas the top (vacuum) interface is assumed to be a perfectly reflecting interface. The loss term in this case is the loss due to unquenched fluorescence decay of the excitons, and will have a rate of $1/\tau$. Thus in order to predict the decay in population, and hence the drop in fluorescence emission with respect to time the following differential equation must be solved;

EQUATION 3.24.

$$\frac{d\varphi(x,t)}{dt} = D\frac{\mathrm{d}^2\varphi(x,t)}{dx^2} - \frac{\varphi(x,t)}{\tau}$$

The initial condition, $\varphi(x,0)$ is equal to the amount of light absorbed in each area of the film and will have the form of a decaying exponential function when $0<x<L$, where L is the film thickness, but will be equal to zero otherwise. The boundary conditions will be $\varphi(0,t)=0$ with $\varphi(L,t)$ being a perfectly reflecting interface so $d\varphi/dt=0$ at $x=L$. The above equation was solved numerically and the answer is plotted below.

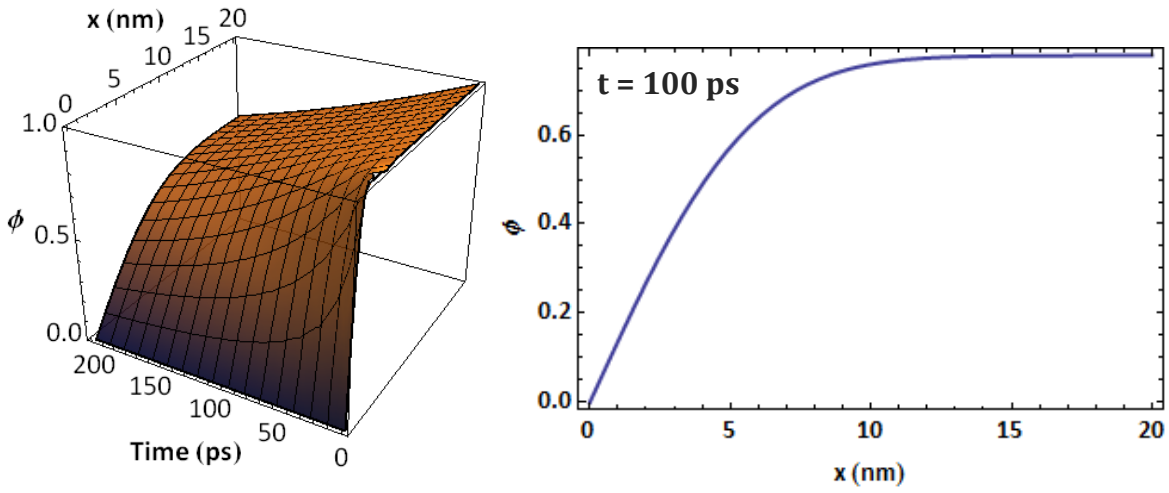

Figure 4.4. On the left is a plot of φ, calculated from the numerical solution of equation 4.12. using the values D = 0.1 nm²ps⁻¹, *L* = 20 nm and τ = ∞. On the right, a cross-section of this

surface is shown, showing how the population of excitons is distributed through the film at t = 100 ps.

In order to model the time-resolved fluorescence of a surface quenched film, φ(x,t) must be integrated over x. Figure 4.4 shows the modelled time-resolved decay for several different film thicknesses and diffusion coefficients.

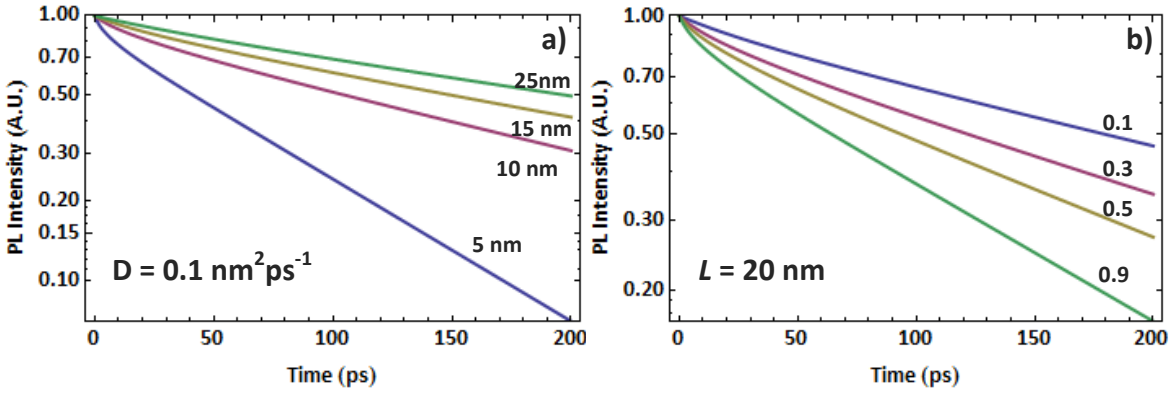

Figure 4.5. a) While keeping D constant, the thickness of the film is changed from 5 nm to 25 nm. The thinner films experience more rapid quenching because on average an exciton will be created closer to the quenching interface and hence have a greater chance of being quenched as it diffuses. b) The thickness of the film is held at 20 nm and the diffusion coefficient is varied from 0.1 to 0.9 nm^2ps^{-1}. The higher the diffusion coefficient the more rapid the drop in population, as the more mobile excitons are more likely to encounter the interface.

4.4.2.1.1 Modelling FRET in Surface Quenching Measurements

The thickness of the film can be measured via ellipsometry or absorption spectroscopy, and can be controlled through solution concentration and spin speed during spin-coating. Thus to calculate the diffusion coefficient, all that is necessary is to fit the numerical solution of equation 4.12 to normalised fluorescence intensity for a series of films with a known spread of thicknesses.

To generate the relationship between absorption and thickness, 8-10 films were fitted to a single model which consisted of a Cauchy layer on top of a fused silica surface. To model the predicted optical absorption of the peak absorption wavelength, as the polymer film thickness on top of the fused silica was varied, the

absorption of the entire stack was modelled using the optical constant calculated from spectrographic ellipsometry. By modelling the absorption of the entire stack the changes in measured absorption due to thin-film interference effects were accounted for, and an accurate measure of thickness could be calculated from the optical absorption.

4.4.2.2 *Accounting for direct energy transfer to the quenching interface*

As described in section 4.2.5, it was described how excitons may undergo through-space FRET to an acceptor, if the absorption of that acceptor overlaps with the emission of the donor material. If this occurs, quenching will not just occur at the interface as described in the previous section, but will have a probability of occurring that declines with distance away from the interface. The probability that FRET will occur between two individual sites will decay with inverse sixth power of distance as described in equation 4.9. The probability that FRET will occur to a slab of acceptor chromophores will decay with x^{-3} where x is the distance from the interface with the slab[34,28]. By replacing this slab with a monolayer of acceptor molecules[14,15], this dependence becomes x^{-4}.

A monolayer is a single layer of closely packed molecules on a surface. It is formed when a molecule can bind either through chemical bonding (chemisorption) or other attractive interactions (physisorption) more strongly to a surface than to itself. This means the reaction will continue only until all exposed surface is saturated and a single layer of molecules has been formed.

Thus surface quenching using a monolayer of acceptor molecules for which the Förster radius for the transition is defined as R_0 can be described by the following equation[20,33], which is derived from the diffusion equation 4.2, with an r^{-4} sink term as the distance independent loss term.

EQUATION 4.13.

$$\frac{d\varphi(x,t)}{dt} = D\frac{\mathrm{d}^2\varphi(x,t)}{dx^2} - k_F(x)\varphi(x,t) - \frac{\varphi(x,t)}{\tau}$$

where

EQUATION 4.14.

$$k_F(x) = \frac{{C_A}^{1/2}\pi {R_0}^6}{2\tau x^4}$$

Where C_A is the number of chromophores per unit area in the monolayer and τ is the lifetime of the exciton in the donor material (in the absence of quenching).

This additional quenching term will make a small but significant difference to the rate at which the population decreases, and this effect is largest in very thin films. Numerical solutions of 4.13 are compared with numerical solutions of 4.12. in the figure below, using representative values of D, R_0 and C_A.

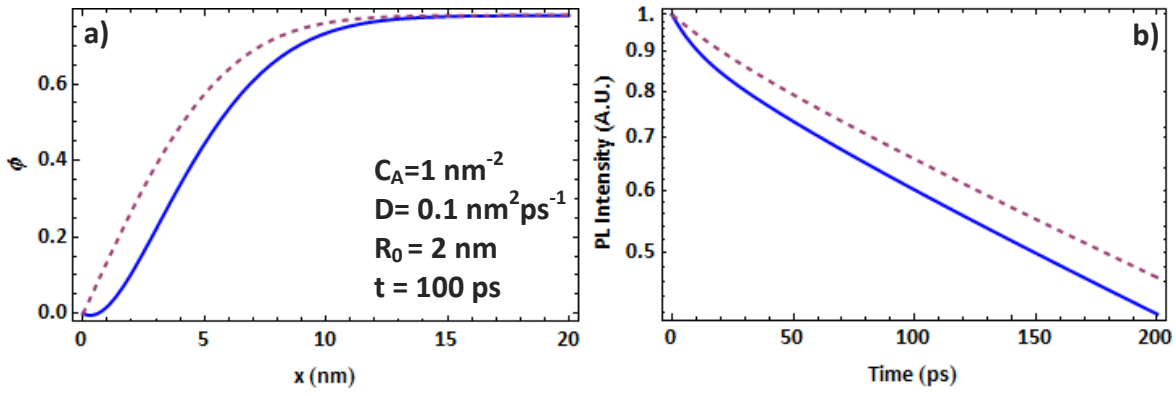

Figure 4.6. a) The spatial distribuion of excitons in the film where FRET is accounted for (solid blue line) compared with the decay in which it is not (dashed pink line). b) Simulated PL decay in film with direct FRET to a monolayer (solid blue line) and no FRET (dashed pink line).

4.4.3 Volume Quenching

4.4.3.1 *Smoluchowski Quenching Rate Constant*

As described in section 4.3.2 volume quenching is an exciton diffusion measurement where a small, known quantity of a quenching material is blended with the material under investigation, and each quenching site is distributed at random throughout the film, ie no clusters of quencher form. If this condition is met, and the concentration of quencher is low, then the concentration of quencher can be calculated from the mass ratio using[15] $N_c=m_r\rho N_A / M_w$, where N_c is the concentration of quenchers (nm^{-3}), m_r is the mass ratio of quencher in the blend, ρ is the density of the non-quencher (gnm^{-3}), N_A is Avogadro's number and M_w is the quencher molecular weight.

Quenching is assumed to happen the instant that a diffusing exciton in the donor comes within a critical radius, r_c of a quenching site, but an exciton outside of this radius will be completely unaffected.

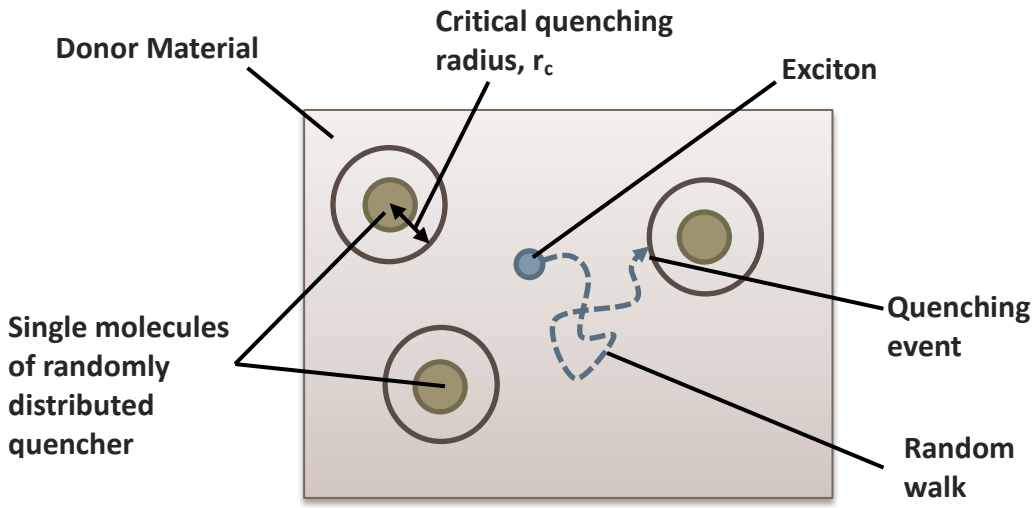

Figure 4.7. A figure illustrating the mechanism by which excitons are quenched in volume quenching.

Solving equation 4.2 in spherical polar coordinates with the above semi-infinite boundary conditions, if the generation and loss terms G and R are neglected, with the initial condition being of uniform population gives the following solution, where φ(r,t) is the concentration of excitons at radius r and time t at any angle[44].

EQUATION 4.15.

$$\varphi(r,t) = \left(1 - \frac{r_c}{r} + \frac{r_c}{r} ERF\left(\frac{(r-r_c)}{2\sqrt{Dt}}\right)\right)$$

it is clear from inspection that the above is a solution to equation 4.2 because

EQUATION 4.16.

$$\frac{\delta\varphi(r,t)}{\delta t} = \frac{D}{r^2}\frac{\delta}{\delta r}\left(r^2\frac{\delta}{\delta r}\varphi(r,t)\right) = \frac{e^{-\frac{(r-r_c)^2}{4Dt}} r_c(r_c - r)}{2r\sqrt{\pi D t^3}}$$

The radial distribution function is plotted below for D=0.1 nm^2ps^{-1}, r_c=1 nm and t=10 ps. It is clear that population very near the critical quenching radius, r=1 nm are highly quenched but further away the population is unperturbed from the initial condition φ(r,0) =1.

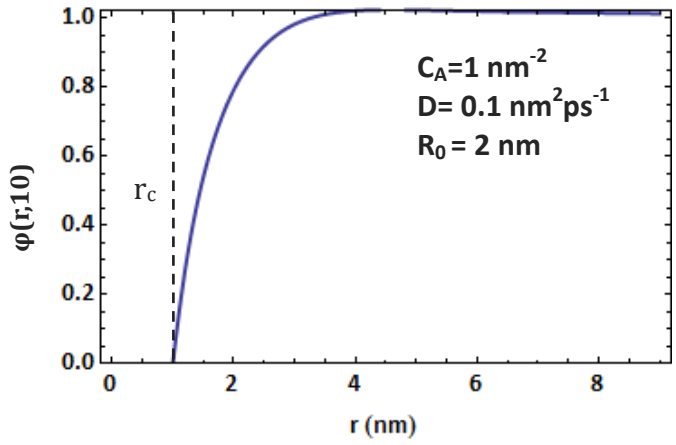

Figure 4.8. A plot of the population of excitons with respect to distance from the centre of the quenching site (equation 4.15). The representantive values used were r_c=1 nm, D= 10^{-3} cm^2s^{-1} and t= 10 ps.

From Fick's first law (equation 4.1), the rate at which excitons will be quenched can be defined as the concentration gradient with respect to r and the point where r=r_c multiplied by the surface area per unit volume of the quenching interface multiplied by the diffusion coefficient[44]

EQUATION 4.17.

$$k_q = AD\left|\frac{\mathrm{d}\varphi(\mathrm{r},\mathrm{t})}{dr}\right|_{r=r_c}$$

The surface area per unit volume will be defined by the surface area of a sphere, radius r_c, multiplied by the concentration of quenching sites, N_c. Substituting in equation 4.15;

EQUATION 4.18.

$$k_q = 4\pi {r_c}^2 N_c D\frac{\mathrm{d}}{dr}\left[\left(1-\frac{r_c}{r}+\frac{r_c}{r}ERF\left(\frac{(r-r_c)}{2\sqrt{Dt}}\right)\right)\right]_{r=r_c}$$

EQUATION 4.19.

$$k_q = 4\pi r_c D N_c\left(1+\frac{r_c}{\sqrt{\pi Dt}}\right)$$

Because this rate constant is for a monomolecular process, the PL decay in the absence of unquenched decay processes, Q (see equation 3.5) can be described as

EQUATION 4.20.

$$Q(t,N_c) = exp\left(-4\pi r_c D N_c\left(t+\frac{2r_c\sqrt{t}}{\sqrt{\pi D}}\right)\right)$$

this is plotted below for different values of D and r_c.

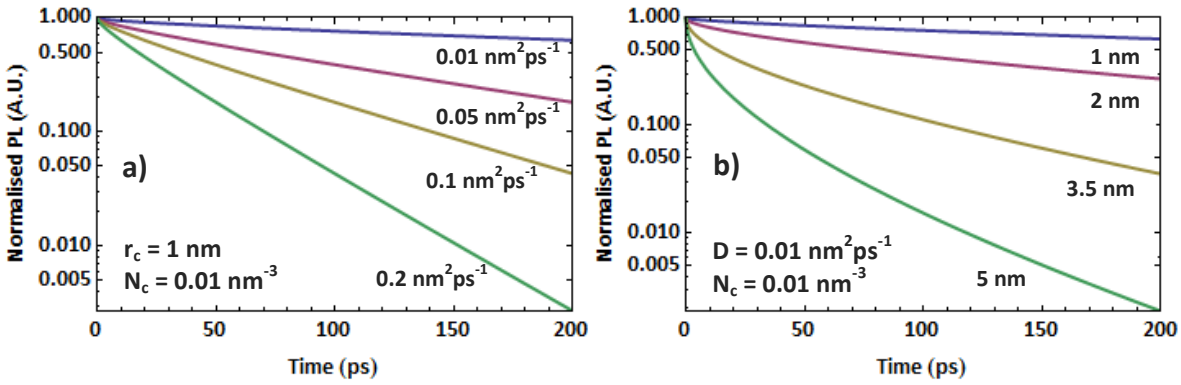

Figure 4.9. a) Equation 4.20 is plotted with varying values of D. b) Equation 4.20 is plotted with varying values of r_c.

It is clear from the plots above that varying values of D predominantly influences the slope of the log plot, whereas changing the critical radius, r_c influences both the slope and the curvature of the log plot.

It is important to consider the critical assumptions required to derive the Smoluchowski rate constant in this way;

- Excitons and quenchers are spherical.
- When the excitons approach the quencher at the critical quenching distance they have a near certain probability of being quenched (ie the rate constant for the quenching process as the acceptor is orders of magnitude faster than the rate at which the exciton approaches the quencher through diffusion).
- The rate constant for the overall quenching is simply the linear combination of the rate constant of all the individual quenching sites. This means that the each quenching site must be far enough away from the other that they each do not perturb the population of excitons around their neighbours. The quenching sites must be widely spaced, meaning that concentration of quencher must be low and evenly distributed.

4.4.3.1.1 Testing the Smoluchowski Rate Equation against Monte Carlo Modelling

This final point, whether it is valid to find the solution of the diffusion equation for a single quenching site and then to calculate the total rate of quenching by multiplying this solution by the concentration of quenching sites, can be addressed in more detail. The major concern is that for high concentrations of quenchers, and high diffusion coefficients each quenching site will perturb the population of excitons in their immediate vicinity (as illustrated in figure 4.7) but will begin to influence the population of excitons around nearby quenching sites. One way to calculate the population of excitons without having to solve the diffusion equation is to create a kinetic Monte Carlo model to fit the data. Mikhnenko *et al*. have widely published volume quenching results using one such Monte-Carlo model which they have made freely available. The program consists of a fine grid (lattice spacing 1 Å) around which excitons can hop randomly and there is a random distribution of spherical quencher sites which upon encountering, the excitons are removed from the model. Full details are available in the authors' publication[6]. The value of Q calculated using the Smoluchowski rate equation (equation 4.20) is plotted against the output of Mikhnenko *et al.'s* model below. The Monte Carlo results are hollow markers while the Smoluchowski solutions is shown with solid black lines.

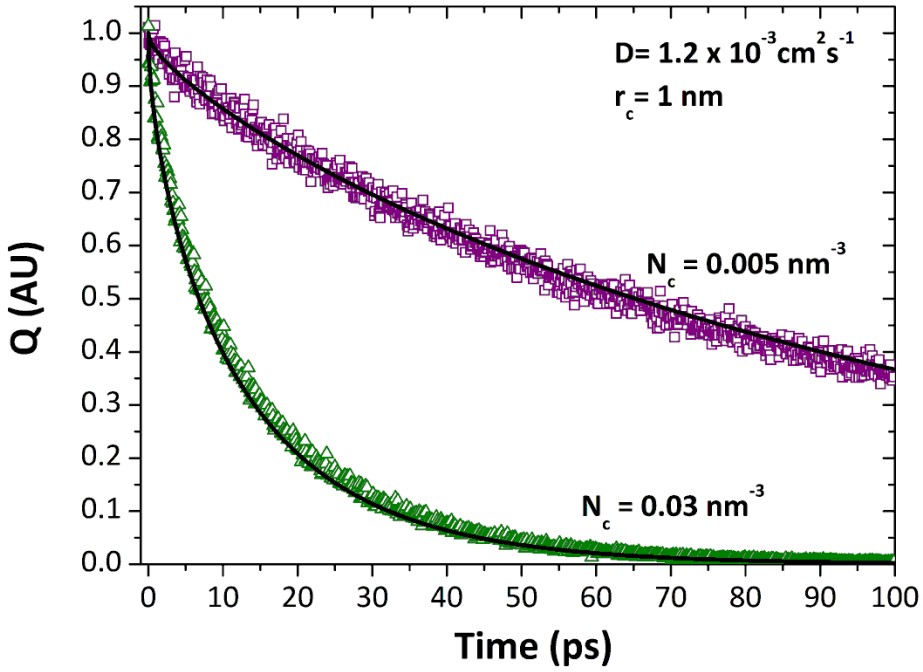

Figure 4.10. A comparison of the population of excitons calcualted by a Monte Carlo model that considers the excitons to be moving randomly on a lattice and being quenched on contact with randomly placed spherical quenching sites (hollow plot markets) and the equivalent parameter calculated from the solution of the diffusion equation with Smoluchowski boundary conditions (equation 4.20).

It is immediately noticeable the analytical solution, equation 4.20, fits the Monte Carlo Model remarkably well. The analytical solution is most likely to break down at high diffusion coefficient and high concentration of quenching sites, so a value more than twice any diffusion coefficient measured in this thesis was used as the trial value of D. The analytical solution fits well for a concentration of 0.005 nm^{-3}, the lowest concentration of quencher used in this thesis, as well as 0.03 which is above the maximum concentration used in conjunction with a derivative of the Smoluchowski equation in this thesis. In conclusion, in the absence of phase segregation, the use of the Smoluchowski rate equation is valid in the context of exciton diffusion, as long as the other assumptions are also satisfied.

4.4.3.2 *Accounting for FRET in Volume Quenching*

Similarly to the discussion in section 4.4.2.1.1, if the absorption of the quencher has spectral overlap with the emission of the material under investigation, then the contact quenching model described in the previous section is no longer an appropriate description of the quenching present in the film.

In this case it is necessary to introduce an r^{-6} quenching term to account for the excitons quenched at a distance. Gösele *et al.* derived an interpolation formula, based on the work of Yokota and Tanimoto[47], that is valid in the regime where both diffusion and quenching from a distance via FRET contribute to the quenching[48-50]. The following is analogous to equation 4.20 after FRET is accounted for.

EQUATION 4.21. $$Q(t, N_c) = exp\left(-4\pi D r_F N_c t - \frac{4}{3}\pi N_c \left[\frac{\pi {R_0}^6 t}{\tau}\right]^{1/2}\right)$$

Where;

EQUATION 4.21. $$r_F = 0.676\left[\frac{R_0^6}{D\tau}\right]^{1/4}$$

The above intermediate formula becomes applicable when FRET is large enough to operate on the same timescale as the diffusive process. This can be quantitatively defined using the unitless parameter Z_0.

EQUATION 4.23. $$Z_0 = \frac{1}{2r_{AD}}\left[\frac{R_0^6}{Dt}\right]^{\frac{1}{2}}$$

Where r_{AD} is the distance of closest approach. When $Z_0>1$, the rate is controlled by both the rate of resonance energy transfer and by the rate of diffusion and the system is in the regime that can be described accurately with equation 4.21.[28]

Equation 4.21 is compared with equation 4.20 in the plot below with representative values of typical diffusion coefficients and Förster radii.

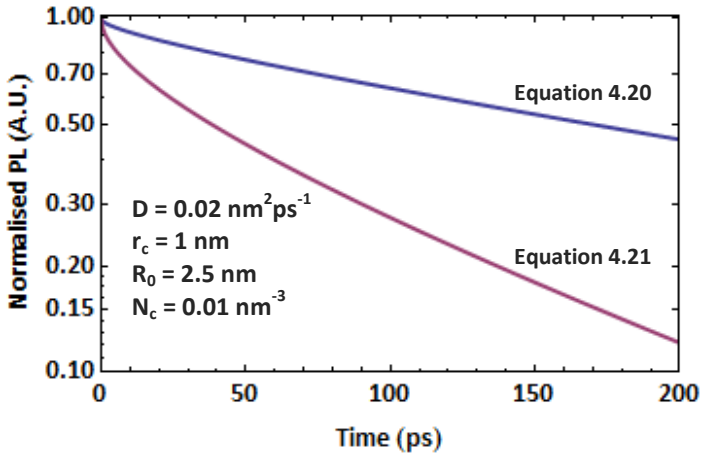

Figure 4.11. Including the influence of direct FRET to the acceptor significantly increases the amount of quenching observed. On a log scale both the gradient and the curvature of the decay are increased.

4.4.4 Smoluchowski-Collins-Kimball Model

In materials where the quenching is short-range but varies significantly from quencher to quencher, it is possible that the rate of quenching at the interface (typically the rate of electron transfer), is limiting the rate. In this case excitons may be reaching the quenching site via diffusion, but have a finite probability of not being quenched upon the encounter, instead moving away from the quencher again. This can be described mathematically by changing the totally absorbing boundary condition in the derivation of the Smoluchowski rate constant in section

4.4.3.1, to a partially reflective boundary condition. Collins and Kimball[45] derived a solution to equation 4.2 in 1949 using the above boundary conditions. Firstly, it is necessary to properly define this partially reflective boundary condition. Because the population of *w(r,t)* when r=r_c will very rapidly reach a steady state with the incoming excitons replacing those quenched, the following equality is true

EQUATION 4.24. $$k_a\varphi(r_c,t) = 4\pi {r_c}^2 \frac{d}{dr}[\varphi(r,t)]_{r=r_c}$$

Where k_a is the rate of quenching for an exciton at the critical radius away from a quenching site. The left-hand side of the equation represent the rate of quenching occurring at the quenching site, while the right-hand side represents the flux with which more excitons are arriving at the quenching site. In steady state these two processes will be equal. From this boundary condition, equation 4.24, Collins and Kimball[45] found the following as a solution for φ(r,t) in equation 4.2;

EQUATION 4.25.

$$\varphi(r,t) = 1 - \frac{r_c}{r}\cdot\frac{k_a}{k_a+k_d}\left\{ERFC\left(\frac{(r-r_c)}{2\sqrt{Dt}}\right) - exp\left[\frac{(k_a+k_d)(r-r_c)}{4\pi {r_c}^2 D}\right]\cdot exp\left[\frac{(k_a+k_d)^2 t}{(4\pi {r_c}^2)^2 D}\right]\cdot ERFC\left(\frac{k_a+k_d}{4\pi {r_c}^2\sqrt{D/t}} + \frac{(r-r_c)}{2\sqrt{Dt}}\right)\right\}$$

Where k_d is the steady-state exciton encounter rate constant is given by $4\pi Dr_c$ and ERFC is the complimentary error function. ERFC(0)=1 while ERFC(∞)=0.

Substituting equation 4.24 into equation 4.17 to find the SCK quenching rate constant gives

EQUATION 4.26.
$$k_q = \frac{N_c k_a}{k_a + k_d}\left\{1 + \frac{k_a}{k_d} exp\left(\frac{Dt}{{r_c}^2}\left(1 + \frac{k_a}{k_d}\right)^2\right) \cdot ERFC\left(\frac{\sqrt{Dt}}{r_c}\left(1 + \frac{k_a}{k_d}\right)\right)\right\}$$

if the rate constant of quenching at the quenching site, k_a, is much larger than the rate at which the excitons are arriving at the quenching site ($k_a >> k_d$) then equation 4.26 reduces to equation 4.19. If k_a is much smaller than k_d, k_q tends towards k_a and the rate of quenching becomes limited by the rate of electron transfer at the interface.

By taking the expontential of the integral with respect to time, the population of excitons in the absence of non-quenching decay processes, Q, can be calculated (see equation 3.5).

EQUATION 4.27.

$$Q(t, N_c) = exp\left(\frac{k_a N_c}{k_a + k_d}\left(\frac{8k_a {r_c}^{3/2}\sqrt{k_d t}}{k_a + k_d} + k_d t + \frac{16Dexp\left(\frac{(k_a + k_d)^2 Dt}{(k_d)^2 {r_c}^2}\right) k_a \pi^2 {r_c}^4 ERFC\left(\frac{(k_a + k_d)\sqrt{Dt}}{k_d r_c}\right)}{(k_a + k_d)^2}\right)\right)$$

4.5. USING EXCITON DIFFUSION AS A TOOL TO PROBE MORPHOLOGY

4.5.1 Introduction

In an organic solar cell two components, an electron donor and an electron acceptor, are blended to form a bulk heterojunction. The length-scale and the types of structures that self-assemble in these heterojunctions have a large impact on the efficient functioning of OPV devices. This is discussed in detail in section 2.4.2 of chapter 2. If the exciton diffusion coefficient is known then, by solving the diffusion equation 4.2 with carefully selected boundary conditions, it is possible to fit the morphology parameters when fitting to the PL lifetime of a photovoltaic blend. Crudely, this is because an exciton will be quenched when it encounters an interface with the other material in the blend, and the shorter the length scale of the phase segregation, the more interface there is and hence the faster this quenching will occur. Examples of the theory behind these morphology determining techniques is discussed in this section.

4.5.2 Planar Interface Thickness Determination

In a planar heterojunction solar cell, the thickness of one (or both) of the photovoltaic layers could be determined from the PL quenching of the active layer. The lifetime of an exciton in a planar heterojunction will be subject to the same quenching rate as an exciton in a surface quenching experiment (section 4.4.2). If the exciton diffusion coefficient has already been determined by other means, equation 3.9 can be solved using surface quenching boundary conditions to

determine the PL lifetime, the difference being in this case the film thickness, rather than D, is the fitting parameter.

This technique is likely to be of limited use as there are numerous reliable methods of measuring thickness of films including ellipsometry, AFM, Dektak and interferometry.

4.5.3 Quenching to the External Surface of a Sphere

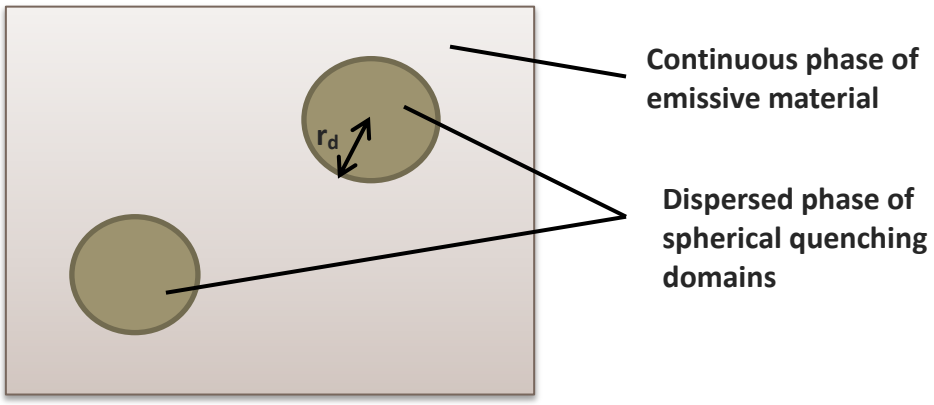

Figure 4.12. An illustration of blend in which spherical domains of quencher are dispersed in a continuous phase of emissive material. If the mass ratio of quencher is known the entire morphology can be specified in a single parameter, the size of the domain r_d.

If the material being probed can be approximated as a continuous phase with a dispersed phase of spherical quenching domains, then the boundary conditions described in the volume quenching section, section 4.4.3.1, are valid[15]. The only modification to equation 4.19 required is that now neither the concentration nor size of the quenching species is known. What is known is that the concentration multiplied by the volume will give the volume ratio of quencher in the blend.

EQUATION 4.28. $$n_d \frac{4}{3}\pi {r_d}^3 = \frac{V_q}{V_{total}} = \frac{m_r \rho_{film}}{\rho_q}$$

where n_d is the domain concentration, r_d is the characteristic domain radius, V_q is the total quencher volume, V_{total} is the volume of the film, m_r is the mass ratio of quencher, ρ_{film} is the average film density and ρ_q is the quencher mass density.

Substituting r_d and n_d for r_c and N_q in equation 4.28 and combining with equation 4.21 gives

EQUATION 4.29. $$Q(t, m_r) = exp\left(-\frac{3 m_r \rho_{film} D}{\rho_q {r_d}^2}\left(t + \frac{2 r_d \sqrt{t}}{\sqrt{\pi D}}\right)\right)$$

As the only unknown is the characteristic domain size r_d, this measure of morphology can be calculated from the time-resolved fluorescence of the blend.

4.5.4 Quenching to the Internal Surface of a Sphere

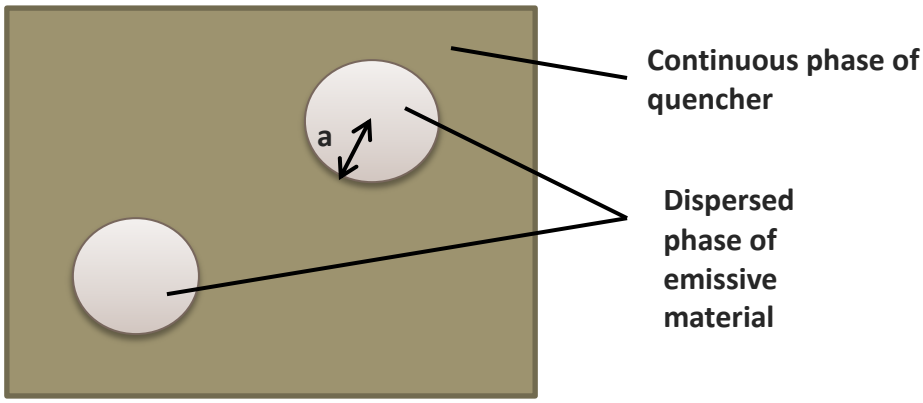

Figure 4.13. A dispersed phase of emissive material in a continuous phase of quenching material

The morphology closely related to that in the previous section is one where the excitons being observed reside inside the dispersed phase of spherical domains

whereas the quencher is the surrounding continuous phase. A solutions to the diffusion equation, equation 4.2 for these geometries is given below[46]

EQUATION 4.30. $$Q(t,a) = \frac{6}{\pi^2}\sum_{n=1}^{\infty}\frac{1}{n^2}exp\left(\frac{-Dn^2\pi^2t}{a^2}\right)$$

where a is the size of the spherical domains. By fitting equation 4.30 to the PL decay in film where it is known the pure domains of emissive material have formed spheres surrounded by a continuous phase of quenching material it is possible to calculate a characteristic domain size for the blend.

4.6. REFERENCES

1 Scheidler, M., Cleve, B., Bässler, H. & Thomas, P. Monte Carlo simulation of bimolecular exciton annihilation in an energetically random hopping system. *Chemical Physics Letters* **225**, 431-436, doi:http://dx.doi.org/10.1016/0009-2614(94)87107-8 (1994).

2 Schnönherr, G., Eiermann, R., Bässler, H. & Silver, M. Dispersive exciton transport in a hopping system with gaussian energy distribution. *Chemical Physics* **52**, 287-298, doi:http://dx.doi.org/10.1016/0301-0104(80)85232-3 (1980).

3 Schönherr, G., Bässler, H. & Silver, M. Dispersive hopping transport via sites having a Gaussian distribution of energies. *Philosophical Magazine Part B* **44**, 47-61, doi:10.1080/01418638108222366 (1981).

4 Mikhnenko, O. V. *et al.* Temperature Dependence of Exciton Diffusion in Conjugated Polymers. *The Journal of Physical Chemistry B* **112**, 11601-11604, doi:10.1021/jp8042363 (2008).

5 Mikhnenko, O. V. *et al.* Exciton Quenching Close to Polymer–Vacuum Interface of Spin-Coated Films of Poly(p-phenylenevinylene) Derivative. *The Journal of Physical Chemistry B* **113**, 9104-9109, doi:10.1021/jp9012637 (2009).

6 Mikhnenko, O. V. *et al.* Exciton diffusion length in narrow bandgap polymers. *Energy & Environmental Science* **5**, 6960-6965 (2012).

7 Förster, T. Zwischenmolekulare Energiewanderung und Fluoreszenz. *Annalen der Physik* **437**, 55-75, doi:10.1002/andp.19484370105 (1948).

8 Westenhoff, S. *et al.* Exciton migration in a polythiophene: Probing the spatial and energy domain by line-dipole Förster-type energy transfer. *The Journal of Chemical Physics* **122**, -, doi:doi:http://dx.doi.org/10.1063/1.1855292 (2005).

9 Barford, W. Exciton transfer integrals between polymer chains. *The Journal of Chemical Physics* **126**, -, doi:doi:http://dx.doi.org/10.1063/1.2714516 (2007).
10 Muñoz-Losa, A., Curutchet, C., Krueger, B. P., Hartsell, L. R. & Mennucci, B. Fretting about FRET: Failure of the Ideal Dipole Approximation. *Biophysical Journal* **96**, 4779-4788, doi:http://dx.doi.org/10.1016/j.bpj.2009.03.052 (2009).
11 Demchenko, A. P. The red-edge effects: 30 years of exploration. *Luminescence* **17**, 19-42, doi:10.1002/bio.671 (2002).
12 Burlakov, V. M. *et al.* Discrete hopping model of exciton transport in disordered media. *Physical Review B* **72**, 075206 (2005).
13 Liu, Y., Summers, M. A., Edder, C., Fréchet, J. M. J. & McGehee, M. D. Using Resonance Energy Transfer to Improve Exciton Harvesting in Organic–Inorganic Hybrid Photovoltaic Cells. *Advanced Materials* **17**, 2960-2964, doi:10.1002/adma.200501307 (2005).
14 Kandada, A. R. S. *et al.* Ultrafast Energy Transfer in Ultrathin Organic Donor/Acceptor Blend. *Sci. Rep.* **3**, doi:10.1038/srep02073 http://www.nature.com/srep/2013/130625/srep02073/abs/srep02073.html#supplementary-information (2013).
15 Ruseckas, A., Shaw, P. E. & Samuel, I. D. W. Probing the nanoscale phase separation in binary photovoltaic blends of poly(3-hexylthiophene) and methanofullerene by energy transfer. *Dalton Transactions*, 10040-10043 (2009).
16 Hedley, G. J. *et al.* Determining the optimum morphology in high-performance polymer-fullerene organic photovoltaic cells. *Nat Commun* **4**, doi:10.1038/ncomms3867 (2013).
17 Markov, D. E., Amsterdam, E., Blom, P. W. M., Sieval, A. B. & Hummelen, J. C. Accurate Measurement of the Exciton Diffusion Length in a Conjugated Polymer Using a Heterostructure with a Side-Chain Cross-Linked Fullerene Layer. *The Journal of Physical Chemistry A* **109**, 5266-5274, doi:10.1021/jp0509663 (2005).
18 Lewis, A. J. *et al.* Singlet exciton diffusion in MEH-PPV films studied by exciton–exciton annihilation. *Organic Electronics* **7**, 452-456, doi:10.1016/j.orgel.2006.05.009 (2006).
19 Shaw, P. E., Ruseckas, A. & Samuel, I. D. W. Exciton Diffusion Measurements in Poly(3-hexylthiophene). *Advanced Materials* **20**, 3516-3520, doi:10.1002/adma.200800982 (2008).
20 Scully, S. R. & McGehee, M. D. Effects of optical interference and energy transfer on exciton diffusion length measurements in organic semiconductors. *Journal of Applied Physics* **100**, 034907 (2006).
21 Markov, D. E. & Blom, P. W. M. Anisotropy of exciton migration in poly(p-phenylene vinylene). *Physical Review B* **74**, 085206 (2006).
22 Kroeze, J. E., Savenije, T. J., Vermeulen, M. J. W. & Warman, J. M. Contactless Determination of the Photoconductivity Action Spectrum, Exciton Diffusion Length, and Charge Separation Efficiency in Polythiophene-Sensitized TiO2

Bilayers. *The Journal of Physical Chemistry B* **107**, 7696-7705, doi:10.1021/jp0217738 (2003).
23 Athanasopoulos, S., Emelianova, E. V., Walker, A. B. & Beljonne, D. Exciton diffusion in energetically disordered organic materials. *Physical Review B* **80**, 195209 (2009).
24 Gaab, K. M. & Bardeen, C. J. Anomalous Exciton Diffusion in the Conjugated Polymer MEH–PPV Measured Using a Three-Pulse Pump–Dump–Probe Anisotropy Experiment. *The Journal of Physical Chemistry A* **108**, 10801-10806, doi:10.1021/jp0464472 (2004).
25 Haugeneder, A. *et al.* Exciton diffusion and dissociation in conjugated polymer/fullerene blends and heterostructures. *Physical Review B* **59**, 15346-15351 (1999).
26 Mikhnenko, O. V. *et al.* Trap-Limited Exciton Diffusion in Organic Semiconductors. *Advanced Materials*, n/a-n/a, doi:10.1002/adma.201304162 (2013).
27 Geacintov, N., Pope, M. & Kallmann, H. Photogeneration of Charge Carriers in Tetracene. *The Journal of Chemical Physics* **45**, 2639-2649 (1966).
28 Popovic, Z. D., Hor, A.-m. & Loutfy, R. O. A study of carrier generation mechanism in benzimidazole perylene/tetraphenyldiamine thin film structures. *Chemical Physics* **127**, 451-457, doi:Doi: 10.1016/0301-0104(88)87143-x (1988).
29 Schlebusch, C., Kessler, B., Cramm, S. & Eberhardt, W. Organic photoconductors and C60. *Synthetic Metals* **77**, 151-154, doi:Doi: 10.1016/0379-6779(96)80077-4 (1996).
30 Theander, M. *et al.* Photoluminescence quenching at a polythiophene/C_{60} heterojunction. *Physical Review B* **61**, 12957 (2000).
31 Sariciftci, N. S., Smilowitz, L., Heeger, A. J. & Wudl, F. Photoinduced Electron Transfer from a Conducting Polymer to Buckminsterfullerene. *Science* **258**, 1474-1476, doi:10.1126/science.258.5087.1474 (1992).
32 Coffey, D. C., Ferguson, A. J., Kopidakis, N. & Rumbles, G. Photovoltaic Charge Generation in Organic Semiconductors Based on Long-Range Energy Transfer. *ACS Nano* **4**, 5437-5445, doi:10.1021/nn101106b (2010).
33 Ward, A. J., Ruseckas, A. & Samuel, I. D. W. A Shift from Diffusion Assisted to Energy Transfer Controlled Fluorescence Quenching in Polymer–Fullerene Photovoltaic Blends. *The Journal of Physical Chemistry C* **116**, 23931-23937, doi:10.1021/jp307538y (2012).
34 Shaw, P. E., Ruseckas, A. & Samuel, I. D. W. Distance dependence of excitation energy transfer between spacer-separated conjugated polymer films. *Physical Review B* **78**, 245201 (2008).
35 Anderson, N. A., Hao, E., Ai, X., Hastings, G. & Lian, T. Ultrafast and long-lived photoinduced charge separation in MEH-PPV/nanoporous semiconductor thin film composites. *Chemical Physics Letters* **347**, 304-310, doi:Doi: 10.1016/s0009-2614(01)01065-x (2001).
36 Ravirajan, P., Haque, S. A., Durrant, J. R., Bradley, D. D. C. & Nelson, J. The Effect of Polymer Optoelectronic Properties on the Performance of Multilayer Hybrid Polymer/TiO2 Solar Cells. *Advanced Functional Materials* **15**, 609-618, doi:10.1002/adfm.200400165 (2005).

37 Savenije, T. J., Warman, J. M. & Goossens, A. Visible light sensitisation of titanium dioxide using a phenylene vinylene polymer. *Chemical Physics Letters* **287**, 148-153, doi:Doi: 10.1016/s0009-2614(98)00163-8 (1998).
38 Weickert, J., Auras, F., Bein, T. & Schmidt-Mende, L. Characterization of Interfacial Modifiers for Hybrid Solar Cells. *The Journal of Physical Chemistry C* **115**, 15081-15088, doi:10.1021/jp203600z (2011).
39 Goh, C., Scully, S. R. & McGehee, M. D. Effects of molecular interface modification in hybrid organic-inorganic photovoltaic cells. *Journal of Applied Physics* **101**, 114503 (2007).
40 Powell, R. C. & Kepler, R. G. Evidence for Long-Range Exciton-Impurity Interaction in Tetracene-Doped Anthracene Crystals. *Physical Review Letters* **22**, 636-639 (1969).
41 Balagurov, B. Y. & Vaks, V. G. Random walks of a particle on lattices with traps. *Sov. Phys. JETP* **38**, 968 (1973).
42 Mikhnenko, O. V. *et al.* Effect of thermal annealing on exciton diffusion in a diketopyrrolopyrrole derivative. *Physical Chemistry Chemical Physics* **14**, 14196-14201, doi:10.1039/c2cp41359k (2012).
43 Raisys, S. *et al.* Exciton diffusion enhancement in triphenylamines via incorporation of phenylethenyl sidearms. *Journal of Materials Chemistry C* **2**, 4792-4798, doi:10.1039/c4tc00262h (2014).
44 Chandrasekhar, S. Stochastic Problems in Physics and Astronomy. *Reviews of Modern Physics* **15**, 1-89 (1943).
45 Collins, F. C. & Kimball, G. E. Diffusion-controlled reaction rates. *Journal of Colloid Science* **4**, 425-437, doi:http://dx.doi.org/10.1016/0095-8522(49)90023-9 (1949).
46 Crank, J. *The Mathematics of Diffusion*. 90-91 (Oxford University Press, 1975).
47 M. Yokota, O. Tanimoto, *Journal of the Physical Society of Japan*, **22**, 779.
48 U. Gösele, M. Hauser, U. K. A. Klein, R. Frey, *Chemical Physics Letters* **, 34**, 519.
49 U. K. A. Klein, R. Frey, M. Hauser, U. Gösele, *Chemical Physics Letters* **, 41**, 139.
50 U. Gösele, *Spectroscopy Letters* **, 11**, 445.

5

INVESTIGATING EXCITON DIFFUSION AND DIRECT ENERGY TRANSFER IN POLYMER DONOR MATERIALS

5.1. INTRODUCTION

In this chapter two compounds are investigated which gave highly efficient, time-dependent quenching. These materials, which are described in section 5.2, exhibited kinetics, shown in section 5.3, that significantly departed from what would be expected from a purely diffusion controlled system. This is extremely interesting because one of the materials is a highly efficient solar cell material. The possible reasons for these deviations are discussed in section 5.3. The volume quenching approach is implemented to determine exciton diffusion coefficients, and information on phase segregation and the mechanism of quenching at different acceptor concentrations is also determined and discussed. It is concluded that in the low concentration regime, the strongly time-dependent quenching kinetics are due to slow exciton diffusion in conjunction with strong direct resonance energy transfer to the acceptor. In section 5.4, two different techniques are used to calculate the donor-acceptor Förster radii, and their strengths and weaknesses are discussed.

In section 5.5 the surface quenching method for measuring exciton diffusion coefficients is applied with a novel quenching interface, tethered C_{60} and was found to agree very well with the volume quenching measurements carried out in section 5.3. In section 5.6 the conclusions are set out and the importance to future research in photovoltaic devices is discussed.

5.2. INTRODUCTION TO THE MATERIALS

The two conjugated polymers that will be discussed in this chapter are the conjugated polymer Poly[2-methoxy-5-(2-ethylhexyloxy)-1,4-phenylenevinylene] (MEH-PPV) and the new low-bandgap push-pull copolymer Poly[[9-(1-octylnonyl)-9H-carbazole-2,7-diyl]-2,5-thiophenediyl-2,1,3-benzothiadiazole-4,7-diyl-2,5-thiophenediyl] (PCDTBT). The chemical structures of both materials are shown in figure 5.1. MEH-PPV was chosen because it is a well studied organic semiconductor with more than 2,100 published papers and patents listed on Web of Science™ describing its behaviour. Though primarily an OLED material, it has been used in organic solar cells for the past 19 years having been an early, and for the time, comparatively efficient, organic solar cell material[1,2]. Consequently, it was used as model material in this project. The second polymer, PCDTBT, has been reported as having an internal quantum efficiency near 100% and a power conversion efficiency of 7.2% [3,4]. Such impressive solar cell performance characteristics provide a strong incentive to understand its fluorescence quenching and exciton harvesting properties.

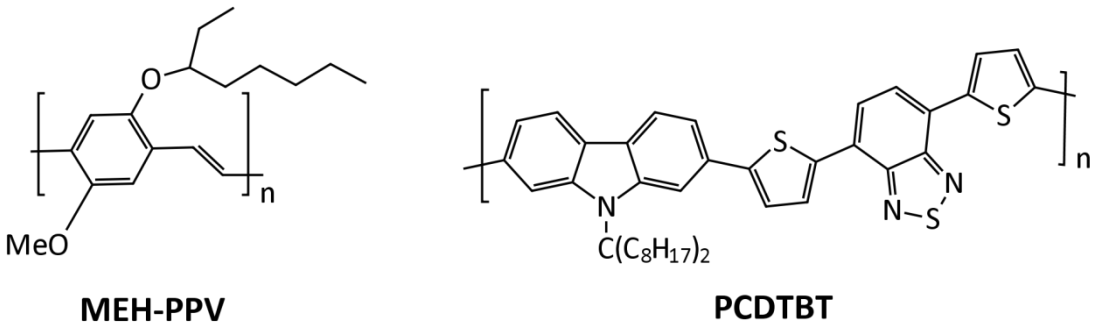

Figure 5.1. The chemical structures of the two conjugated polymers discussed in this chapter, MEH-PPV and PCDTBT.

5.3. FLUORESCENCE QUENCHING MEASUREMENTS AND TIME-DEPENDENCE

The fluorescence quenching properties of these materials were investigated by observing the time-resolved photoluminescence of dilute blends of these materials with their corresponding photovoltaic acceptor.

The acceptors used were C_{61}-PCBM for MEH-PPV and C_{71}-PCBM for PCDTBT and were chosen to match the most commonly used accepters in their respective photovoltaic device blends. TR-PL decays of these dilute blends are shown in panels a) and c) of figure 5.2. In order to measure the rate constant for PL quenching, the ratio of the quenched film to the pristine film was taken and the natural logarithm was taken of the resultant decay. As explained in chapter3, section 3.4.3, this gives the *ln(PL Ratio)* which has a gradient equal to the rate constant of the quenching process.

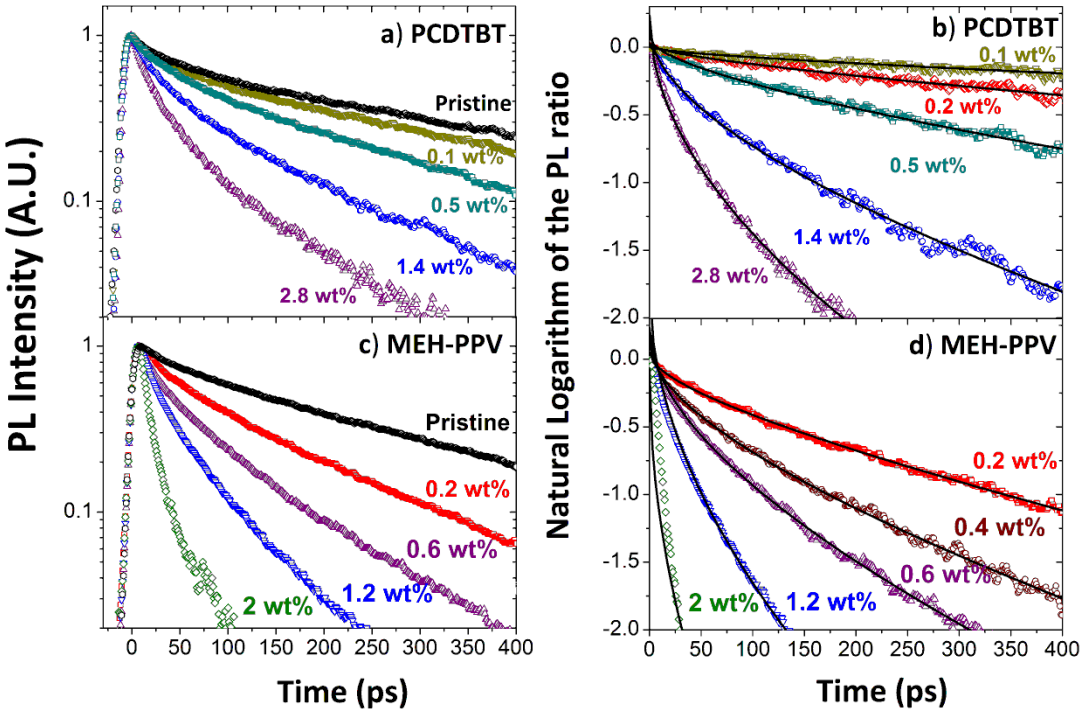

Figure 5.2. The time-resolved PL decays of PCDTBT and MEH-PPV films (panels a) and c)). The ln(PL ratios) of PCDTBT and MEH-PPV (panels b) and d))

It is immediately clear that, unlike the example shown chapter 3, section3.4.3, or those shown in chapter 8, the gradient of the *ln(PL decay)* and consequently the quenching rate constant, is strongly time-dependent, especially at higher blend concentrations. This means that excitons are quenched by the acceptor sites with a very fast initial rate that rapidly drops with time. There are numerous physical processes which could lead to such behaviour. One possibility is that instead of undergoing isoenergetic hopping, the exciton is instead undergoing downhill diffusion as described in section 4.2.4.[5,6]. Another possibility is that the exciton is not diffusing isotropically but instead has a preferential direction, for example along a π-stack in a crystal. This has been shown to lead to an increase in

the time-dependence of quenching due to diffusion[7-9].

If the diffusion is in some way downhill, then there will be a shift in the wavelength of emission to the red as the average exciton moves to lower and lower energy chromophores[10]. Plots of the PL decay of PCDTBT with spectral windows corresponding to the red, peak and the blue side of the emission are shown below. The emission spectrum is shown later in this chapter in figure 5.6.

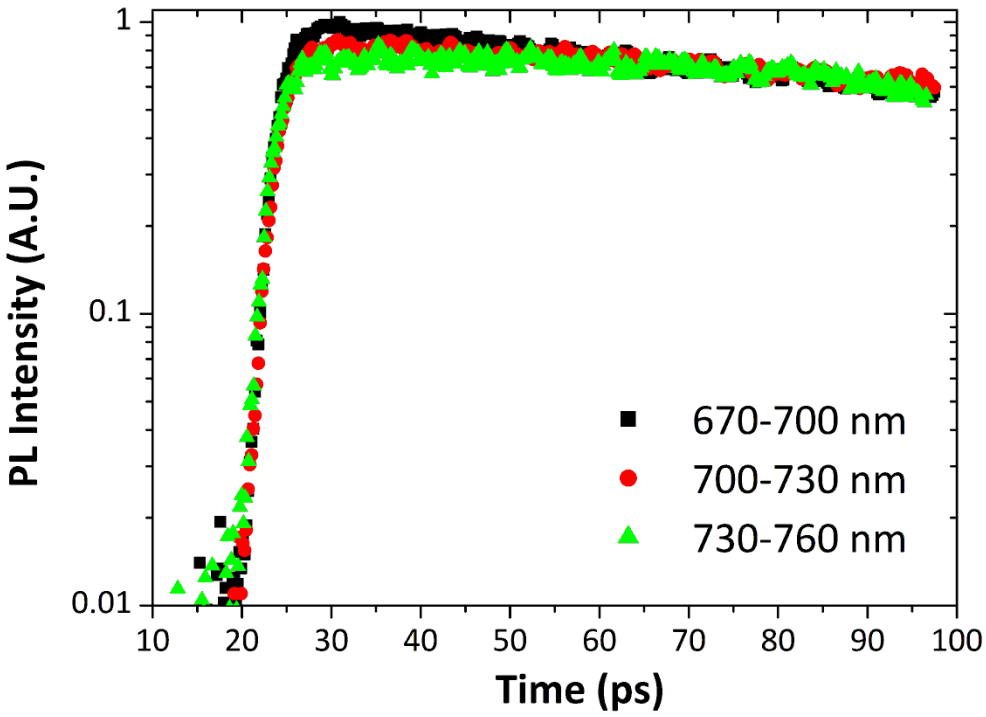

Figure 5.3. The blue, peak and red side of the time resolved emission of PCDTBT. This can be compared with the steady-state emission in figure 5.6.

It can be seen that though there is a difference in the kinetics, indicating a spectral shift at very short time, the rate of decay of the red side and blue side are equal after 60 picoseconds. As the time-dependence of quenching proceeds long after this time, it seems there is little evidence to back up dispersive diffusion.

Anisotropic diffusion can also be ruled out, as anisotropic diffusion can only occur if there is structure within the film and both MEH-PPV and PCDTBT have been shown to be largely amorphous[11,12].

A simple $t^{1/2}$ dependence (with or without an additional linear component) is characteristic of FRET-limited processes[13-15]. As both donor materials have a spectral overlap with their respective quencher materials, the simplest and most persuasive explanation is that direct resonance energy transfer plays a strong role in exciton harvesting in these blends.

5.3.1 Calculation of exciton diffusion coefficients

In order to extract information on the exciton diffusion coefficient in blends of donor and quencher it is necessary to be in a regime where exciton diffusion is making a substantial contribution to the quenching rate. In a very dilute regime, the majority of excitons will be far away from an acceptor when they are created and the only means by which they can be quenched is by exciton diffusion. Under these conditions equations 4.20 and 4.21 become valid (which of these will depend on how much FRET there is to the acceptor). A fundamental assumption of 4.20 and 4.21 is that each quenching chromophore can be treated as being entirely separate from any other quencher (semi-infinite boundary conditions in r). This has two implications, firstly that the modelling will only be valid if there is no clustering of the quenching sites, and secondly that the quenching sites must be spaced widely enough that the quenching from one site does not perturb the exciton population in the vicinity of another site. As discussed at the end of chapter 2, the ln(PL ratio) is equal to the logarithm of the quenching function Q. Thus from equation 4.20 and 4.21 the ln(PL ratio) can be described as

EQUATION 5.1.

$$ln\left(Q\left(t,N_q\right)\right) = ln(PL\ ratio) = -4\pi r_c D N_c\left(t + \frac{2r_c\sqrt{t}}{\sqrt{\pi D}}\right)$$

when FRET is small (Z_0<1 as defined by equation 4.23) and

EQUATION 5.2.

$$ln(PL\ ratio) = -4\pi D r_F N_c t - \frac{4}{3}\pi N_c\left[\frac{\pi {R_0}^6 t}{\tau}\right]^{1/2}$$

$$\text{where } r_F = 0.676\left[\frac{R_0^6}{D\tau}\right]^{1/4}$$

when FRET is significant (Z_0>1 as defined by equation 4.23).

In the very high concentration regime, all excitons are within a Förster radius of an acceptor at all times, and whichever way the excitons move they have a high probability of being quenched. This means that exciton diffusion is no longer a rate determining process in the harvesting of excitons. Because the rate of diffusive quenching is very small compared with the rate of FRET, the former can be neglected and the system can be modelled as if the excitons are static. The normalised population of excitons in the *static regime* (in the absence of other quenching) is given by[13]

EQUATION 5.3.

$$Q\left(t,N_q\right) = exp^{-\frac{N_c}{N_0}\left[\frac{\pi t}{\tau}\right]^{1/2}}$$

where N_0, the critical concentration is defined by

EQUATION 5.4.

$$N_0 = \frac{1}{\frac{4}{3}\pi R_0^3}$$

R_0 is the Förster radius, N_c is the concentration of quenching sites and τ is the lifetime of the donor.

In the static regime, the ln(PL ratio), which is equal to the exponent of equation 5.3, will be proportional to the square root of time. Thus a purely FRET limited process will have this very characteristic time-dependence;

EQUATION 5.5.

$$\ln(PL\ ratio) = -\frac{4}{3}\pi N_c \left[\frac{\pi {R_0}^6 t}{\tau}\right]^{1/2}$$

Having these different regimes where differing equations are valid to model the exciton population makes analysing the data challenging. We can however distinguish the regimes by collecting data over a wide range of concentration regimes and plotting fits to the data to see where the data departs from the each equation in turn. All the regimes, equations 5.1, 5.2 and 5.5 have the same basic functional form, which is shown below

EQUATION 5.6.

$$ln(PL\ Ratio) = -\alpha t - \beta t^{1/2}$$

What α and β represent will depend on the regime. In the very dilute regime, α and β will be dictated by the Gösele interpolation (equation 5.2) and will vary linearly with concentration of quencher, N_c. In the static regime, α will drop to zero, while β will be dictated by the static Förster quenching equation, 5.5, (meaning β remains unchanged from the Gösele regime). If phase segregation occurs, each quenching site will become less effective as any clustering of the quencher will bring it out of contact with the donor and hence per quenching site, the rate of quenching will be reduced. This is more likely to happen at higher quenching concentrations. Thus when equation 5.6 is fitted to the ln(PL decay)s, we can separate the different regimes according to how these fitted parameters depend on the concentration of quencher and thus calculated values from the diffusion coefficient from the low concentration regime.

Equation 5.6 was fitted to the ln(PL ratio)s of films with small concentration of quencher. Fits are the black lines in figure 5.2. The resultant fitted values of α and β are plotted in figures 5.4 and 5.5 below.

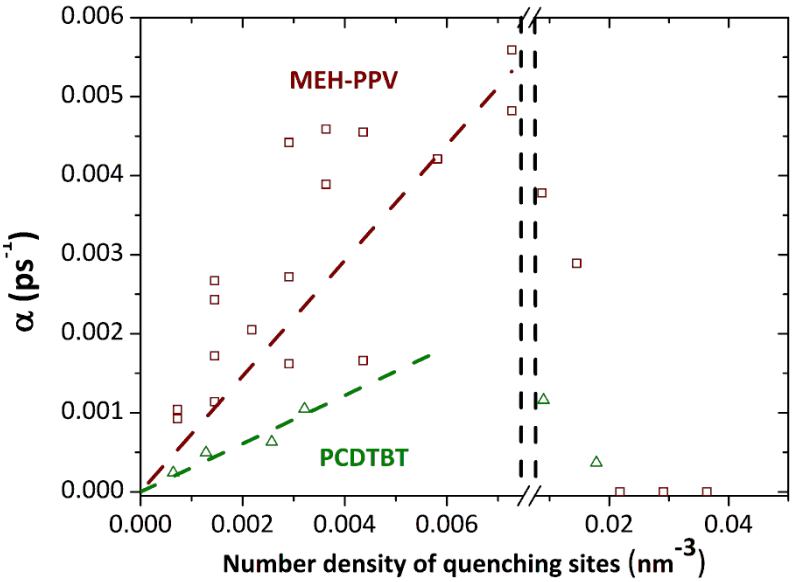

Figure 5.4. The linear component of the rate of quenching plotted from fits of equation 5.6 to the ln(PL ratios) in figure 5.2. The dashed lines are linear fits to the points below 0.007 nm^{-3}.

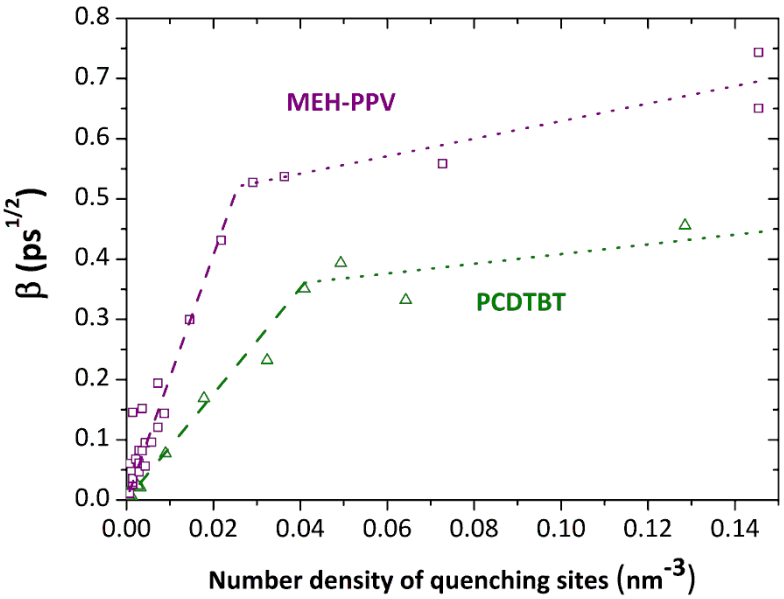

Figure 5.5. The time-dependent components of the rate of quenching, calculated from fits of equation 5.6 to the ln(PL ratios) in figure 5.2. The dashed line is not a fit, but a plot of value of static quenching expected (derived from equation 5.2) with the values of R_0 calculated in section 5.4.3.

The values of α and β both showed a linear increase with respect to the concentration of quenching sites for both materials at low quencher concentration. At higher concentrations, the linear component, α, dropped to zero while β continued to increase linearly with concentration. This transition happened at a concentration of approximately 0.007 nm^{-3} for both materials, and represents the transition from the Gösele regime, governed by equation 5.2 to the static quenching regime which is better described by equation 5.5. Only once α has fully reached zero is the system completely in the static quenching regime and this occurs at 0.023 sites per cubic nanometre (3 wt% of C_{61}-PCBM) for MEH-PPV and at 0.02 quenching sites per cubic nanometre (3 wt% of C_{71}-PCBM) for the PCDTBT blends. Above a certain threshold β also ceases to increase linearly with concentration as has been previously explained would be an expected indicator of phase segregation of the quencher. Phase segregation in PCDTBT is backed up by DSC measurements in the literature[11]. This occurs at 0.03 sites per nm^3 (4 wt% of C_{61}-PCBM) in MEH-PPV, and 0.05 sites per nm^3 for the PCDTBT blends (8 wt% C_{71}-PCBM).

The initial linear section of the plot of α, where the film is well described by the Gösele regime was fitted with a straight-line fit (dashed brown and green lines in figure 5.4). A validity requirement to using the Gösele interpolation is that Z_0, as defined in equation 4.23, is well above 1. With the values of D calculated from surface quenching later in this chapter, in section 5.5 and values of R_0 calculated in section 5.4, Z_0 satisfies this criterion for MEH-PPV and PCDTBT, for the time range under investigation (0-400 ps), even with trial values of the distance of closest approach, R_{AD} as unphysically large as 3 nm.

From equation 5.2 it is clear that

EQUATION 5.7.

$$\frac{d\alpha}{dN} = 0.676 \times 4\pi D^{\frac{3}{4}} \left[\frac{R_0^6}{\tau}\right]^{1/4}$$

Using values measured for τ and R_0 in section 5.4.3, D was calculated as $(2.0\pm1)\times10^{-4}$ cm^2s^{-1} and $(1.1\pm0.5)\times10^{-4}$ cm^2s^{-1} for MEH-PPV and PCDTBT respectively. These values agree well with the values for these materials measured in the following section, 5.5, by surface quenching.

Further to exciton diffusion coefficient measurement, the fluorescence decay kinetics can give us some interesting insights into exciton harvesting in these widely used photovoltaic materials. We have observed a clear transition between two quenching regimes, one in which exciton diffusion lends a helping hand toward harvesting excitons, and one where it is totally insignificant. This agrees very well with Herz *et* al.[45] who see the same transition between these two regimes with the same characteristic time-dependencies in a different conjugated material when they examined blends over differing time ranges and temperatures. In figure 5.4, this transition occurred at relatively low quencher concentrations of ~ 5%wt quencher. As a typical blend is composed of a ratio of 1:1 to 1:4 donor to acceptor, our results imply that exciton harvesting proceeds exclusively through FRET, in the static quenching regime. This means in these particular photovoltaic blends exciton diffusion is largely irrelevant to device functioning. This goes some way to explain the near 100% internal quantum efficiency of a PCDTBT:C_{71}-PCBM solar cell[3], as lower quantum efficiencies would be expected in blends that rely on random exciton diffusion. This contrasts with a well studied photovoltaic blend P3HT:C_{61}-PCBM what has been observed to segregate into pure crystalline polymer domains at device concentrations[16], and this happens before the concentrations necessary

to enter the static quenching regime[17]. The assertion that excitons are primarily harvested by FRET is corroborated by the short exciton diffusion lengths calculated in this work of 3.0 nm for both MEH-PPV and PCDTBT. Exciton diffusion simply is not fast enough to assist in exciton harvesting.

As already commented on, due to the linear relationship between β and the concentration of acceptors up to fairly high quencher concentrations, it can be inferred that there is no phase segregation even up to the point where each polymer chain is completely surrounded by acceptor molecules. This indicates that the phase segregation, when it does occur, is driven by the propensity of the fullerene acceptor to crystalize rather than the polymer. This observation is supported by DSC measurements which observe the presence of a fullerene crystal phase in the device blends[11], which contrasts with the high crystallinity of P3HT driving phase segregation in P3HT:PCBM blends[18].

5.4. CALCULATION OF THE FORSTER RADII

5.4.1 Introduction

Having assigned the time-dependence observed in the ln(PL ratio)s as being due to the influence of direct FRET, it is necessary to establish the magnitude of its influence. There are two methods commonly used to establish the Förster radius between a FRET donor and acceptor and each have their own strengths and weaknesses. The first is by calculating the spectral overlap in solution and using Förster's equation (equations 4.9–4.11) to calculate the Förster radius, as described in chapter 4. The second is to use high concentrations of quencher to push the system into a regime where the quenching sites are so concentrated the

rate at which the excitons arrive at the quenchers (via exciton diffusion) is no longer a rate limiting step in the harvesting of these excitons. This has been previously introduced in section 5.3 as the static quenching regime.

5.4.2 Spectral Overlap Calculation

In order to calculate the rate at which excitons in the donor material can be transferred to the FRET acceptor, it is necessary to measure the molar extinction coefficient of the acceptor and the emission of the donor. Plots of these are shown below.

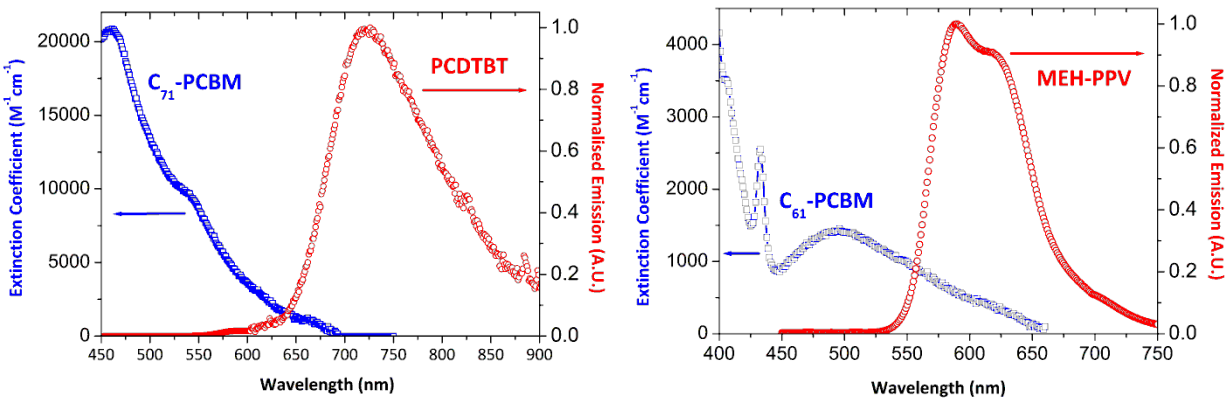

Figure 5.8. Fluorescence spectrum of PCDTBT (left) plotted with its corresponding acceptor, C71-PCBM's extinction coefficient. Fluorescence spectrum of MEH-PPV (right) with the molar extinction coefficient of its corresponding FRET acceptor, C_{61}-PCBM's molar extinction coefficient.

Using the above data we can calculate *J* the spectral overlap using equation 4.11. The spectral overlap integrand is shown in the plot below.

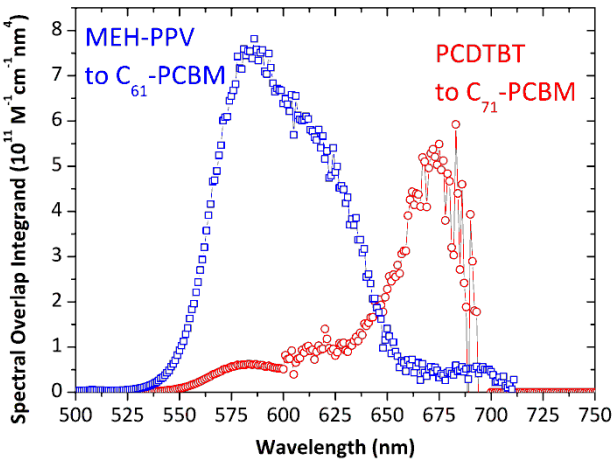

Figure 5.7. Spectral overlap integrand as defined by equation 4.11. The area under the curves represents the spectral overlap between the donors and their respective acceptors.

It is clear, both from figure 5.6 and figure 5.7, that there is much stronger spectral overlap between MEH-PPV and C_{61}-PCBM than PCDTBT and C_{71}-PCBM. Performing the integral confirms this, with MEH-PPV to C_{61}-PCBM giving a J of $5.3 \times 10^{13} M^{-1}cm^{-1}nm^4$ while PCDTBT to C_{71}-PCBM gives a value of $2.4 \times 10^{13} M^{-1}cm^{-1}nm^4$.

To apply this value to the rate of FRET occurring inside the blend, it is necessary to approximate the system to randomly orientated (but static) chromophores. Though the chromophores in the solid films are undoubtedly static, there is very little information on the relative orientation between the donor and acceptor at the blend interface. During volume quenching, each chromophore is essentially an individual island surrounded by donor material. Because the donor material surrounds the quencher, it is a not unreasonable assumption that the exciton can approach from any orientation and hence a given quencher will be randomly orientated compared to an incoming exciton.

In the scenario where the chromophores are randomly orientated and static the orientation factor k will be 0.6901[19]. If we assume the refractive index n to be 1.6, then equation 4.10 and 4.11 can be used to calculate R_0 for the processes under discussion. This resulted in R_0 = 1.8 nm for PCDTBT to C_{71}-PCBM,and R_0=2.0 nm for MEH-PPV to C_{61}-PCBM. If we use the spectral overlap between the emission of PCDTBT and the absorption of C_{61}-PCBM then R_0 = 1.1 nm for PCDTBT to C_{61}-PCBM.

5.4.3 Static Quenching regime

An alternative to looking at the spectral properties of the donor and acceptor, an estimate of the rate of FRET can be produced from the rate of quenching in a film with a high concentration of acceptor[13,17]. As is discussed in section 5.3.1, at high enough concentrations, exciton diffusion stops limiting exciton harvesting as the quenching is purely due to FRET. This gives a characteristic $t^{1/2}$ dependence of the ln(PL decay) and equation 5.5 can be used to calculate the Förster radius of the process. It is vital that equation 5.5 is used in a concentration regime where it is valid. This means the films must have a high enough concentration to be in the static regime, but low enough not to have experienced phase segregation. From the findings of section 5.3.1, this limits the concentrations to within 3-8 wt% C_{71}-PCBM in PCDTBT and 3-4% C_{61}-PCBM in MEH-PPV.

Below are the PL decays and ln(PL ratio)s of blends of PCDTBT and MEH-PPV with blend ratios larger than 1 wt%.

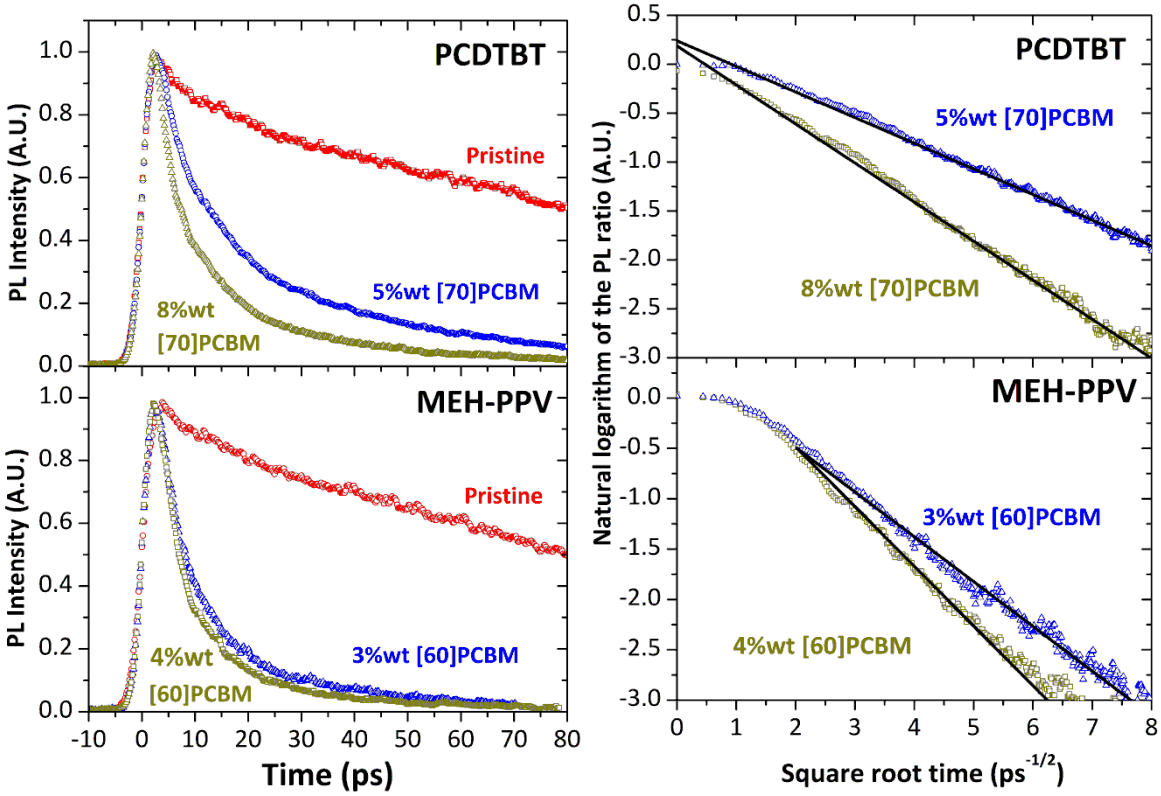

Figure 5.8. The left panel shows the PL decays of the donor material with higher concentrations of their coresponding quencher. The panel on the right shows the same data but plotted as a ln(PL ratio) on a $t^{1/2}$ axis.

As can be seen from figure 5.8, the ln(PL ratio) becomes largely linear for both polymers for these concentrations of quencher. This is good evidence that the film is in the *static quenching* regime. The fluorescent lifetime, τ, and the PLQY of the pristine film was measured by time-resolved fluorescence and using a Hamamatsu Integrated sphere respectively. The lifetime of the materials was calculated from the average of a two exponential fit to the pristine film as 220 ps for MEH-PPV and 320 ps for PCDTBT. The PLQY was measured as 18.5% for MEH-PPV and 22% for PCDTBT. This means that the only free parameter left in equation 5.5 is the Förster radius, R_0. The black lines in figure 5.8 are shared parameter fits

of equation 5.5 with the free parameter being the value of R_0 for each material. This gave R_0= 3.4 nm and R_0= 2.9 nm for MEH-PPV to C_{61}-PCBM and PCDTBT to C_{71}-PCBM.

5.4.4 Discussion of the Two Techniques

There is a discrepancy of about 1 nm between the Förster radii calculated from spectral overlap in solution, which are smaller, and those calculated from static quenching. Reasons for this difference will now be discussed.

The first technique, *Spectral Overlap* assumes that both the absorbing species and the emitting species are point dipoles. This assumption is adequate for long-range energy transfer, but fails for transfer over distances similar to the size of the species themselves[20,21]. At a centre-to-centre distance of 2 nm, for example, the spectral overlap method would assume that the interaction is still a through-space interaction whereas if the donor and acceptor each had a radius of 1 nm, 2nm centre-to-centre would put them physically in contact with each other. The radius of a fullerene chromophore is approximately 1nm[22]. The radius of emissive species, the exciton, is a subject of contention in the literature[23-26] but is often approximated as 10 repeat units of P3HT which would also make it approximately 1 nm large. In one of the lower concentration films, for example 1%wt C_{61}-PCBM in MEH-PPV, the average centre-to-centre distance of the chromophores is approximate 5 nm. The mean distance between a randomly placed exciton and fullerene will be approximately half that, on the order of 2.5 nm. Thus the assumption that donor and acceptor are point dipoles is not a very appropriate assumption in this context. That the nearest points of the donor and acceptor are far closer than the centre-to-centre distances will mean that more energy transfer

will be experienced than the Förster radius calculated from spectral overlap would suggest.

The second technique, the *Static Quenching* technique also involves several assumptions that will be discussed. Firstly, the assumption that the motion of the excitons can be neglected. If we neglected exciton diffusion when it ought to still contribute significantly to the exciton harvesting in these blends then it would lead to an overestimation of the Förster radii and thus is a contender for explaining the discrepancy. The rate of FRET is decreasing quite rapidly with time, leading to a linear decay of the ln(PL ratio) when plotted on a $t^{1/2}$ axis[17]. The rate of quenching due to a diffusive contribution will be constant with respect to time. A linear component in figure 5.8, that is not properly accounted for would be exhibited as a deviation from linear on the $t^{1/2}$ graph as the linear component begins to dominate at longer time. This is not observed in the figure, so the case for the static quenching regime is strengthened. The second assumption required for the appropriate use of equation 5.5 is the requirement that the positions of quenching sites are totally uncorrelated. The quenching sites must be randomly distributed, in an intimate mixture with the donor material; it is necessary to assume that there is no phase segregation in these blends. This is a rather wobbly assumption, as phase segregation (as described in chapter 1) has been observed in a wide variety of different material blends and becomes more and more prevalent at higher concentrations[17]. What is known, however, is that if phase segregation does occur, it leads to a reduction of the size of the interface between the two components and that a reduction in the area of the film where FRET can occur. This will mean that the overall rate at which excitons are harvested by FRET will be reduced and the

measured Förster radius will also be reduced. If this assumption was incorrect, it would actually make the discrepancy with the spectral overlap measurement larger. Thus we can discount it as a candidate to explain the discrepancy. Additional evidence is presented in section 5.3.1. that because there is a linear relationship between the time-dependent rate constant and the concentration of quencher in the blend, up until the phase segregation threshold, the onset of phase segregation was determined to be above 5 wt% for C_{61}-PCBM in MEH-PPV and 8 wt% for C_{71}-PCBM in PCDTBT; higher than the concentrations used in the calculation of the Förster radius.

In conclusion, though the two techniques disagree, they can reliably put upper and lower limits on the rate of FRET between donor and acceptor chromophores in these blends. The static quenching technique more reliably tests the rate of FRET under the exact conditions that we are most interested in, and hence the values calculated for R_0 using this technique were the ones used previously in conjunction with equation 5.7 to calculate the exciton diffusion coefficients of the materials in section 5.3.

5.5. SURFACE QUENCHING

5.5.1 Introduction

Surface quenching as described in chapter 4, is a method to measure the exciton diffusion coefficient of a material by monitoring the time-resolved fluorescence of thin films on a quenching interface.

5.5.2 Discussion of Suitable Quenching Surfaces

There are several considerations as to which quenching surface will give the most accurate and unambiguous measure of exciton diffusion. There are four attributes that an ideal quenching interface must have[27].

a) Firstly the interface must be extremely flat as well as being well defined. This means that there can be no mixing of the two components – there must be a clean interface. The quencher must not inter-diffuse with the material under investigation, otherwise the boundary conditions necessary for surface quenching will not be valid.

b) It simplifies the measurement if the quenching is exclusively due to short-range electron transfer rather than FRET. Eliminating FRET means that the simpler equation 4.12 can be used rather than 4.13.

c) It is important that any thin film interference effects are considered. If a high refractive index quencher is used, such as a transparent inorganic oxide, then the initial optical field intensity can be severely altered. This leads to a change in the initial conditions in equation 4.12 which are not adequately accounted for, and will lead to an exciton diffusion coefficient that may be highly inaccurate.

d) Finally, it is extremely important that once the excitons reach the interface, the excitons will be quenched much more rapidly than the excitons can move away from the interface. This is because the theoretical treatment described in chapter 4 assumes a perfectly

absorbing boundary at the quenching interface. Anything less than perfect quenching would lead to an erroneously small measured exciton diffusion coefficient.

The first attempts at surface quenching emerged in the 1960s, and were performed on molecular crystals, including tetracene[28] and perylene derivatives[29]. Molecular crystals have lifetimes on the scale of tens of nanoseconds and exciton diffusion lengths on the order of hundreds of nanometres. This means errors caused by a) and b) are insignificant compared to the diffusion lengths measured, and thick films can be used so c) is no longer a concern. As the quencher choice is determined entirely by d) and FRET acceptors are not excluded, a very efficient quencher can be chosen from a wide variety of possibilities.

When solution processed organic semiconductor photovoltaic devices emerged as a promising sustainable energy source, exciton diffusion was revisited in disordered organic photovoltaic materials. Theander *et al.*[30] use a planar heterojunction of a substituted polythiphene and C_{60} for a surface quenching experiment. The fullerene was chosen as a quencher because it has been shown to undergo efficient charge separation in organic solar cells as well as having been observed via photo-induced optical absorption and photo-induced electron spin resonance to rapidly accept an electron on the sub-picosecond timescale[31]. Thus C_{60} satisfies requirement d). C_{60} also has the advantage that, as an organic material its refractive index is similar to that of most conjugated polymers and thus thin film interference requirement c), is no longer a concern[27]. On the other hand C_{60} does have some spectral overlap with the donor and hence b) is a potential source of error that Theander *et al.* did not attempt to account for. Likewise a), the inter-

diffusion of C_{60} into polymers is a well-known problem and Theander *et al*. have been criticised for not accounting for this effect[27,28].

Attempts to overcome this problem of quencher inter-diffusion include work by Markov *et al*.[32] who include crosslinkable alkyne side-groups to a fullerene derivative in order to make an insoluble cross-linked slab from a soluble small molecule precursor. Making the implicit assumption that the modified C_{60} derivative is just as effective a quencher as unmodified C_{60}., this approach overcomes concerns a), c) and d). The rate of long-range quenching by FRET is however not taken into account and could be significant, as quenching to a slab only decays with x^{-3} rather than x^{-4} for a monolayer and x^{-6} for a single chromophore[33].

As an alternative to a fullerene acceptor, semiconducting metal oxide layers have the possibility of being entirely transparent, electron accepting layers. In particular titanium dioxide (TiO_2) has been used successfully as an electron acceptor in hybrid polymer/TiO_2 solar cells[34] and is known to induce rapid charge separation in such devices[35]. TiO_2 has the added advantage of being entirely transparent in the region where P3HT is emissive[36] and hence has no possibility to act as a FRET acceptor.

One attempt to use TiO_2 as a quencher for a surface quenching technique was by Savenjie *et al.*[37] who used steady-state fluorescence to monitor surface quenching in MEH-PPV. A flaw in this measurement is that TiO_2 has a very high refractive index meaning that thin-film interference effects can dominate the measurement. A subsequent study[27] indicates that the unaccounted for influence of

interference dominated this particular experiment meaning that the calculated diffusion length may not be reliable.

The first work to explicitly address all four of these critical considerations after they were described by Scully and McGehee[27], was Shaw *et al.* in their work on the surface quenching of P3HT on TiO_2[36]. Concerns a) and b) are mitigated as TiO_2 is known to give very flat surfaces, transparent in the spectral window that P3HT emits at. The authors address concern c) by modelling the relative electric field intensity through the film using the transfer matrix method. They found for TiO_2 thicknesses of 80 nm, the presence of TiO_2 did not significantly alter the relative field intensity compared to a bare silica interface. The authors comment on d) by citing literature that has shown rapid electron transfer to TiO_2 from conjugated polymers, but they concede the exciton diffusion coefficient they measure is properly a lower limit, as anything less than a perfect quenching interface would appear to reduce the exciton diffusion coefficient measured. It is not easy to make a TiO_2 interface that quenches reliably and later work has shown interface modifiers can help achieve effective electron transfer[38,39].

In this present work, concerns a) to d) are overcome with the use of a novel technique to covalently bond a monolayer of fullerene to a fused silica surface. That the C_{60} is covalently bound mitigates a), while b) is both accounted for in the modelling as well as being a smaller effect than a slab of acceptor because the distance dependence of thin sheet will be x^{-4} rather than x^{-3}. The third concern, c) is removed, both because C_{60} has a similar refractive index to conjugated polymers but also because the monolayer is very thin, being less than 2 nm and in the context of surface quenching, thin quenching layers have been modelled by Scully and

McGehee and shown not to perturb the electric field intensity with respect to the control film on bare fused silica[27]. Finally d) is mitigated because C_{60} has been shown many times to very rapidly accept electrons from a wide variety of organic semiconductors and the tethering does not hugely disrupt the C_{60} chromophore. The experimental procedure for preparing the tether C_{60} is described in the next section.

5.5.3 Preparation of Tethered Fullerene

In order to develop a reliable quenching surface it was necessary to develop a procedure for chemically attaching fullerenes to fused silica. This was based on Howarter and Youngblood's[40] procedure for silanising silica with APTES (aminopropyltriethoxysilane) followed by the procedure for fullerene addition to amino modified oxide surfaces described by Chen *et al*[41].

The fused silica substrates were subjected to the cleaning procedure described in chapter 3, then they were exposed to an oxygen plasma followed by treatment with piranha solution (3:1 concentrated sulphuric acid to 30%v/v hydrogen peroxide solution) which exposes a more reactive, highly polar surface of the silica[42]. After ten minutes submerged in the piranha solution, the substrates were removed, rinsed in deionised (DI) water, and then dried under vacuum. Please note that piranha solution will cause a violent explosion on contact with most organic materials, including organic solvents so must be treated with extreme caution. Nitrile gloves, gauntlets, an apron and safety glasses/face mask were used. In addition the piranha procedure was carried out in a wetdeck with the sash down with all solvent wash-bottles and beakers removed. The substrates were then placed in an oven dried powder jar in a nitrogen atmosphere glovebox. A 10%

solution of the silanising agent APTES was added. The reaction was allowed to proceed for 1 hour before the substrates were rinsed under flowing toluene, then methanol and then DI water. The substrates were left submerged in DI water overnight to ensure that any remaining APTES was hydrolysed.

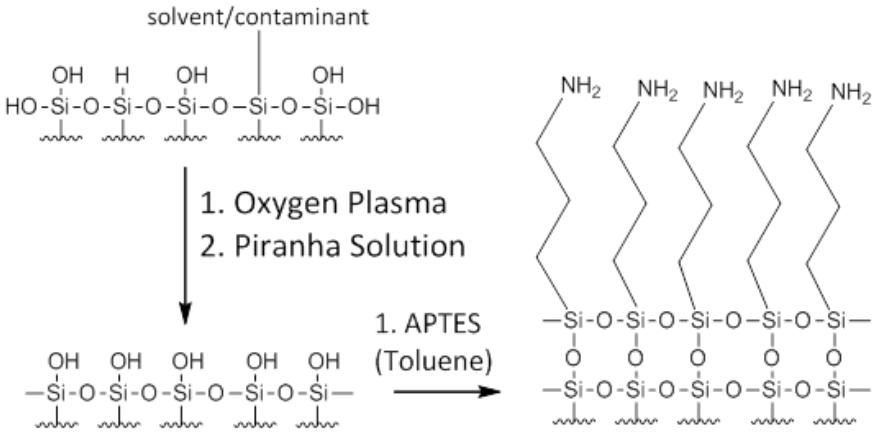

Figure 5.9. Reaction scheme for the amine functionalisation of a fused silica surface.

The amine functionalised substrates were then refluxed in a 1mM solution of C_{60} in toluene for 48 hours. The substrates were then removed and sonicated in warm toluene to remove any residual fullerene that was not covalently bonded to the substrate. It is believed from cyclic voltammetry measurements and steric arguments that each fullerene is covalently bonded to two amine units[43].

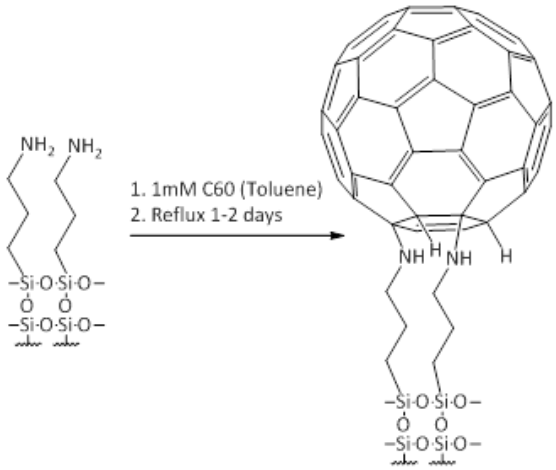

Figure 5.10. The reaction scheme for amine addition to a fullerene.

The finished substrates were analysed via contact angle measurements and absorption spectrometry to ascertain how complete the fullerene coverage was by comparing to similar fullerene monolayers reported with identical contact angles by Chen *et al*[41]. The surface roughness was calculated from AFM to confirm the smoothness of the interface.

Solutions of varying concentrations of MEH-PPV in chlorobenzene and PCDTBT in dichlorobenzene were spin-coated onto fused silica and tethered C_{60} substrates. Films of similar thicknesses on both the fused silica tethered C_{60} substrates were produced by spin-coating from the same solution and the same spin speed. The thicknesses were calculated from optical absorption using an absorption thickness plot calculated from the optical constants of the films on fused silica measured ellipsometry.

5.5.4 Results and Discussion

The time-resolved fluorescence spectra of the PCDTBT films are shown below.

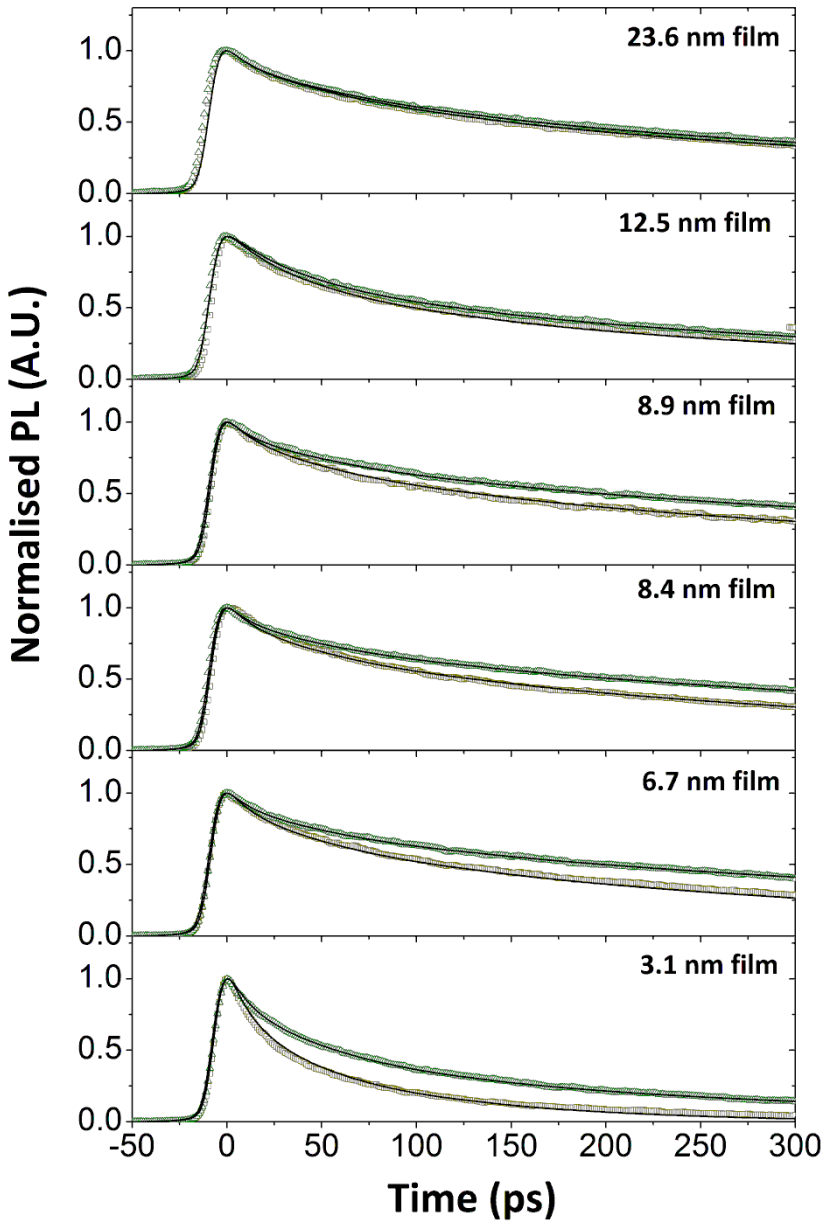

Figure 5.12. Time-resolved fluorescence spectra of PCDTBT films with a range of thicknesses on fused silica (green) and on tethered C60 (orange).

The equivalent plots for MEH-PPV films, are shown below.

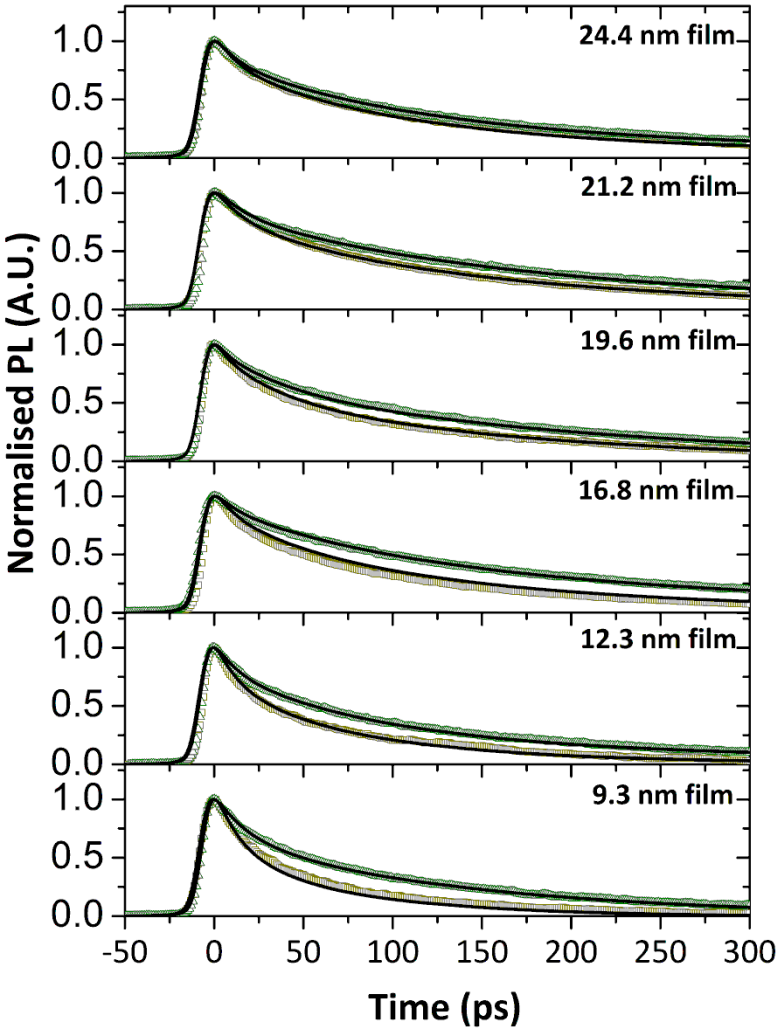

Figure 5.13. Time-resolved fluorescence spectra of MEH-PPV films with a range of thicknesses on fused silica (green) and on tethered C60 (orange).

Surface quenching was modelled using equation 4.13. The unquenched decay constant, $k_F(t)$, was calculated from a three exponential fit to the pristine film for each thickness and each material, convoluted with the response function (measured as described in chapter 3). These are the black lines fits to the green data in figures 5.11 and 5.12. The Förster radii were calculated from the static quenching regime for MEH-PPV, but as the quencher is C_{60} not C_{70}, for PCDTBT

spectral overlap calculations had to be used instead. The initial population for equation 4.13 was approximated as a decaying exponential from the top to the bottom face of the film, decaying with the optical field intensity of the excitation beam. The values for R_0 along with those of τ were substituted into equation 4.13, the equation was solved numerically and the results were convoluted with the instrument response function and fitted to the data using a single free parameter, the exciton diffusion coefficient. All the PL decays for each material were fitted with a single value of the exciton diffusion coefficient. This resulted in exciton diffusion coefficients of 2×10^{-4} cm^2s^{-1} and 1.4×10^{-4} cm^2s^{-1} for MEH-PPV and PCDTBT. Because there is only one free parameter and the model fits the data well across six different film thicknesses, the values calculated are likely to be fairly reliable.

5.6. CONCLUSIONS

In this chapter, two quenching techniques for measuring exciton diffusion have been used to measure exciton diffusion coefficients in two amorphous polymers. The exciton diffusion coefficient calculated from surface quenching agreed well with that calculated from volume quenching. This indicated that the exciton diffusion is likely to be isotropic. The most unexpected result from this section of work was that we saw a clear transition between a regime where exciton diffusion plays a role, to one where it plays no part in harvesting the excitons, at the higher acceptor concentrations. This is highly relevant to device fabrication because at concentrations of acceptor relevant to photovoltaic devices, the system is in this static quenching regime. Efficient harvesting via FRET may thus be a

possible explanation of the peculiarly high internal quantum efficiencies of PCDTBT:C_{71}-PCBM devices, and it opens up a new avenue of research into acceptors that have a strong spectral overlap with their corresponding donor material and thus do not rely on the fundamentally inefficient diffusion process to transport the exciton to the interface. A high profile example of where this approach has already been implemented is by Huang *et al.* In that work the authors introduce a squarine derivative as the acceptor in the donor material P3HT, which has a strong spectral overlap with the acceptor. They observe a significant enhancement of exciton harvesting due to FRET[44].

5.7. REFERENCES

1 Yu, G., Gao, J., Hummelen, J. C., Wudl, F. & Heeger, A. J. Polymer Photovoltaic Cells: Enhanced Efficiencies via a Network of Internal Donor-Acceptor Heterojunctions. *Science* **270**, 1789-1791, doi:10.1126/science.270.5243.1789 (1995).

2 Yu, G. & Heeger, A. J. CHARGE SEPARATION AND PHOTOVOLTAIC CONVERSION IN POLYMER COMPOSITES WITH INTERNAL DONOR-ACCEPTOR HETEROJUNCTIONS. *Journal of Applied Physics* **78**, 4510-4515, doi:10.1063/1.359792 (1995).

3 Park, S. H. *et al.* Bulk heterojunction solar cells with internal quantum efficiency approaching 100%. *Nat Photon* **3**, 297-302, doi:http://www.nature.com/nphoton/journal/v3/n5/suppinfo/nphoton.2009.69_S1.html (2009).

4 Sun, Y. *et al.* Efficient, Air-Stable Bulk Heterojunction Polymer Solar Cells Using MoOx as the Anode Interfacial Layer. *Advanced Materials* **23**, 2226-2230, doi:10.1002/adma.201100038 (2011).

5 Burlakov, V. M. *et al.* Discrete hopping model of exciton transport in disordered media. *Physical Review B* **72**, 075206 (2005).

6 Mikhnenko, O. V. *et al.* Temperature Dependence of Exciton Diffusion in Conjugated Polymers. *The Journal of Physical Chemistry B* **112**, 11601-11604, doi:10.1021/jp8042363 (2008).

7 Masri, Z. *et al.* Molecular Weight Dependence of Exciton Diffusion in Poly(3-hexylthiophene). *Advanced Energy Materials* **3**, 1445-1453, doi:10.1002/aenm.201300210 (2013).

8 Tamai, Y., Matsuura, Y., Ohkita, H., Benten, H. & Ito, S. One-Dimensional Singlet Exciton Diffusion in Poly(3-hexylthiophene) Crystalline Domains. *The Journal of Physical Chemistry Letters* **5**, 399-403, doi:10.1021/jz402299a (2014).

9 Markov, D. E. & Blom, P. W. M. Anisotropy of exciton migration in poly(p-phenylene vinylene). *Physical Review B* **74**, 085206 (2006).

10 Westenhoff, S. *et al.* Exciton migration in a polythiophene: Probing the spatial and energy domain by line-dipole Förster-type energy transfer. *The Journal of Chemical Physics* **122**, -, doi:doi:http://dx.doi.org/10.1063/1.1855292 (2005).

11 Wang, T. *et al.* Correlating Structure with Function in Thermally Annealed PCDTBT:PC70BM Photovoltaic Blends. *Advanced Functional Materials* **22**, 1399-1408, doi:10.1002/adfm.201102510 (2012).

12 Grage, M. M.-L. *et al.* Conformational disorder and energy migration in MEH-PPV with partially broken conjugation. *The Journal of Chemical Physics* **118**, 7644-7650, doi:doi:http://dx.doi.org/10.1063/1.1562190 (2003).

13 Powell, R. C. & Kepler, R. G. Evidence for Long-Range Exciton-Impurity Interaction in Tetracene-Doped Anthracene Crystals. *Physical Review Letters* **22**, 636-639 (1969).

14 Gösele, U., Hauser, M., Klein, U. K. A. & Frey, R. Diffusion and long-range energy transfer. *Chemical Physics Letters* **34**, 519-522, doi:10.1016/0009-2614(75)85553-9 (1975).
15 Klein, U. K. A., Frey, R., Hauser, M. & Gösele, U. Theoretical and experimental investigations of combined diffusion and long-range energy transfer. *Chemical Physics Letters* **41**, 139-142, doi:10.1016/0009-2614(76)85266-9 (1976).
16 van Bavel, S., Sourty, E., de With, G., Frolic, K. & Loos, J. Relation between Photoactive Layer Thickness, 3D Morphology, and Device Performance in P3HT/PCBM Bulk-Heterojunction Solar Cells. *Macromolecules* **42**, 7396-7403, doi:10.1021/ma900817t (2009).
17 Ruseckas, A., Shaw, P. E. & Samuel, I. D. W. Probing the nanoscale phase separation in binary photovoltaic blends of poly(3-hexylthiophene) and methanofullerene by energy transfer. *Dalton Transactions*, 10040-10043 (2009).
18 Ma, W., Yang, C., Gong, X., Lee, K. & Heeger, A. J. Thermally Stable, Efficient Polymer Solar Cells with Nanoscale Control of the Interpenetrating Network Morphology. *Advanced Functional Materials* **15**, 1617-1622, doi:10.1002/adfm.200500211 (2005).
19 Baumann, J. & Fayer, M. D. Excitation transfer in disordered two-dimensional and anisotropic three-dimensional systems: Effects of spatial geometry on time-resolved observables. *The Journal of Chemical Physics* **85**, 4087-4107 (1986).
20 Muñoz-Losa, A., Curutchet, C., Krueger, B. P., Hartsell, L. R. & Mennucci, B. Fretting about FRET: Failure of the Ideal Dipole Approximation. *Biophysical Journal* **96**, 4779-4788, doi:http://dx.doi.org/10.1016/j.bpj.2009.03.052 (2009).
21 Barford, W. Exciton transfer integrals between polymer chains. *The Journal of Chemical Physics* **126**, -, doi:doi:http://dx.doi.org/10.1063/1.2714516 (2007).
22 Ginzburg, B. M., Tuichiev, S., Tabarov, S. K., Shepelevskii, A. A. & Shibaev, L. A. X-ray diffraction analysis of C60 fullerene powder and fullerene soot. *Tech. Phys.* **50**, 1458-1461, doi:10.1134/1.2131953 (2005).
23 Rohlfing, M. & Louie, S. G. Optical Excitations in Conjugated Polymers. *Physical Review Letters* **82**, 1959-1962 (1999).
24 Mukamel, S., Tretiak, S., Wagersreiter, T. & Chernyak, V. Electronic Coherence and Collective Optical Excitations of Conjugated Molecules. *Science* **277**, 781-787, doi:10.1126/science.277.5327.781 (1997).
25 Köhler, A. *et al.* Charge separation in localized and delocalized electronic states in polymeric semiconductors. *Nature* **392**, 903-906 (1998).
26 Knupfer, M. *et al.* Size of Electron-Hole Pairs in Pi-Conjugated Systems. *Physical Review Letters* **83**, 1443-1446 (1999).
27 Scully, S. R. & McGehee, M. D. Effects of optical interference and energy transfer on exciton diffusion length measurements in organic semiconductors. *Journal of Applied Physics* **100**, 034907 (2006).
28 Geacintov, N., Pope, M. & Kallmann, H. Photogeneration of Charge Carriers in Tetracene. *The Journal of Chemical Physics* **45**, 2639-2649 (1966).

29 Popovic, Z. D., Hor, A.-m. & Loutfy, R. O. A study of carrier generation mechanism in benzimidazole perylene/tetraphenyldiamine thin film structures. *Chemical Physics* **127**, 451-457, doi:Doi: 10.1016/0301-0104(88)87143-x (1988).
30 Theander, M. *et al.* Photoluminescence quenching at a polythiophene/C_{60} heterojunction. *Physical Review B* **61**, 12957 (2000).
31 Sariciftci, N. S., Smilowitz, L., Heeger, A. J. & Wudl, F. Photoinduced Electron Transfer from a Conducting Polymer to Buckminsterfullerene. *Science* **258**, 1474-1476, doi:10.1126/science.258.5087.1474 (1992).
32 Markov, D. E., Amsterdam, E., Blom, P. W. M., Sieval, A. B. & Hummelen, J. C. Accurate Measurement of the Exciton Diffusion Length in a Conjugated Polymer Using a Heterostructure with a Side-Chain Cross-Linked Fullerene Layer. *The Journal of Physical Chemistry A* **109**, 5266-5274, doi:10.1021/jp0509663 (2005).
33 Kuhn, H. Classical Aspects of Energy Transfer in Molecular Systems. *The Journal of Chemical Physics* **53**, 101-108 (1970).
34 Ravirajan, P., Haque, S. A., Durrant, J. R., Bradley, D. D. C. & Nelson, J. The Effect of Polymer Optoelectronic Properties on the Performance of Multilayer Hybrid Polymer/TiO2 Solar Cells. *Advanced Functional Materials* **15**, 609-618, doi:10.1002/adfm.200400165 (2005).
35 Anderson, N. A., Hao, E., Ai, X., Hastings, G. & Lian, T. Ultrafast and long-lived photoinduced charge separation in MEH-PPV/nanoporous semiconductor thin film composites. *Chemical Physics Letters* **347**, 304-310, doi:Doi: 10.1016/s0009-2614(01)01065-x (2001).
36 Shaw, P. E., Ruseckas, A. & Samuel, I. D. W. Exciton Diffusion Measurements in Poly(3-hexylthiophene). *Advanced Materials* **20**, 3516-3520, doi:10.1002/adma.200800982 (2008).
37 Savenije, T. J., Warman, J. M. & Goossens, A. Visible light sensitisation of titanium dioxide using a phenylene vinylene polymer. *Chemical Physics Letters* **287**, 148-153, doi:Doi: 10.1016/s0009-2614(98)00163-8 (1998).
38 Weickert, J., Auras, F., Bein, T. & Schmidt-Mende, L. Characterization of Interfacial Modifiers for Hybrid Solar Cells. *The Journal of Physical Chemistry C* **115**, 15081-15088, doi:10.1021/jp203600z (2011).
39 Goh, C., Scully, S. R. & McGehee, M. D. Effects of molecular interface modification in hybrid organic-inorganic photovoltaic cells. *Journal of Applied Physics* **101**, 114503 (2007).
40 Howarter, J. A. & Youngblood, J. P. Optimization of Silica Silanization by 3-Aminopropyltriethoxysilane. *Langmuir* **22**, 11142-11147, doi:10.1021/la061240g (2006).
41 Chen, K., Caldwell, W. B. & Mirkin, C. A. Fullerene self-assembly onto (MeO)3Si(CH2)3NH2-modified oxide surfaces. *Journal of the American Chemical Society* **115**, 1193-1194, doi:10.1021/ja00056a080 (1993).
42 Han, Y., Mayer, D., Offenhäusser, A. & Ingebrandt, S. Surface activation of thin silicon oxides by wet cleaning and silanization. *Thin Solid Films* **510**, 175-180, doi:DOI: 10.1016/j.tsf.2005.11.048 (2006).
43 Ulman, A. Formation and Structure of Self-Assembled Monolayers. *Chemical Reviews* **96**, 1533-1554, doi:10.1021/cr9502357 (1996).

44 Huang, J.-S. *et al.* Polymer bulk heterojunction solar cells employing Forster resonance energy transfer. *Nat Photon* **7**, 479-485, doi:10.1038/nphoton.2013.82
http://www.nature.com/nphoton/journal/v7/n6/abs/nphoton.2013.82.html#supplementary-information (2013).
45 Herz, L. M.; Silva, C.; Grimsdale, A. C.; Müllen, K.; Phillips, R. T., Time-dependent energy transfer rates in a conjugated polymer guest-host system. *Physical Review B* **2004,** *70* (16), 165207.

6

INVESTIGATION INTO RATES OF ELECTRON TRANSFER IN PHOTOVOLTAIC BLENDS

6.1. INTRODUCTION

In this chapter a thorough investigation into what factors influence exciton transfer in the high performance photovoltaic material, PTB7, is performed. In section 6.2 the material, PTB7, is introduced and its significance stated. In section 6.3 the rate at which excitons in PTB7 diffuse is investigated using fluorescence depolarisation and volume quenching. In section 6.4 the most widely used theory to describe the rate of electron transfer processes is introduced and explained. A discussion of the experimental methods to measure the electron transfer process is then performed in section 6.4.3. Then in section 6.4.4 a short discussion of recently posited novel theories to discuss the ultra-fast electron transfer observed in high performance photovoltaic blends is carried out. In section 6.5 the influence of the electron affinity of the acceptor on the rate of electron transfer from PTB7 is investigated. Section 6.6 lays out the conclusions of the chapter.

6.2. DISCUSSION OF THE MATERIALS INVESTIGATED

6.2.1 PTB7

As discussed in chapter 2, organic solar cells are a very promising emerging technology for the generation of electricity from sunlight. To date the most efficient single-junction organic solar cell blend is given from the combination of the donor polymer poly[[4,8-bis[(2-ethylhexyl)oxy]benzo[1,2-b:4,5-b']dithiophene-2,6-diyl][3-fluoro-2-[(2-ethylhexyl)carbonyl]thieno[3,4-b]thiophenediyl]] (PTB7) and the acceptor, C_{71}-PCBM[1,2].

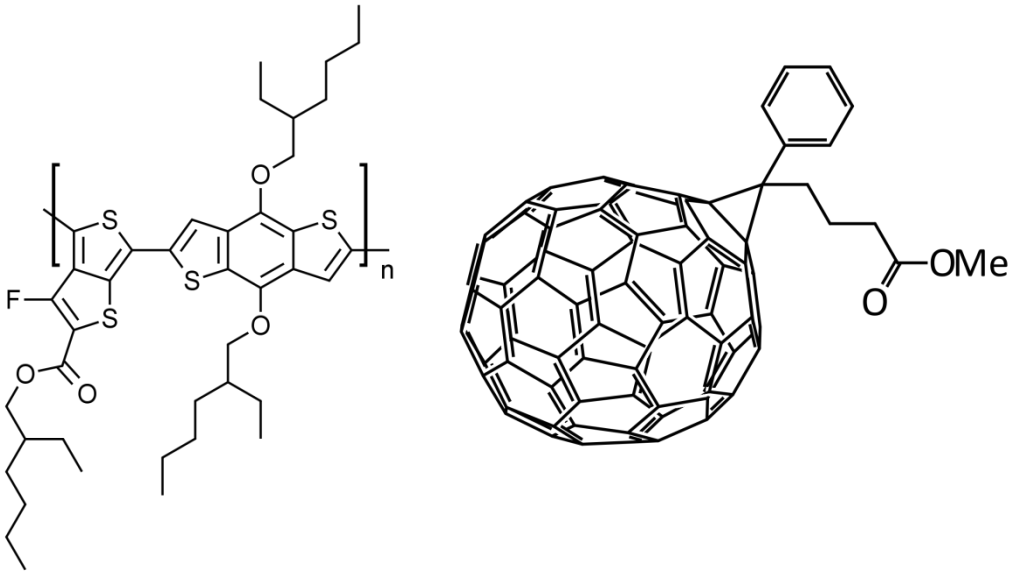

Figure 6.1. The chemical structures of PTB7 (left) and C_{71}-PCBM (right)

Because of its ability to produce solar cells that can deliver world-beating power conversion efficiencies of above 9%, much of the rest of the chapter, and indeed the thesis, delves into the photophysical properties of this material.

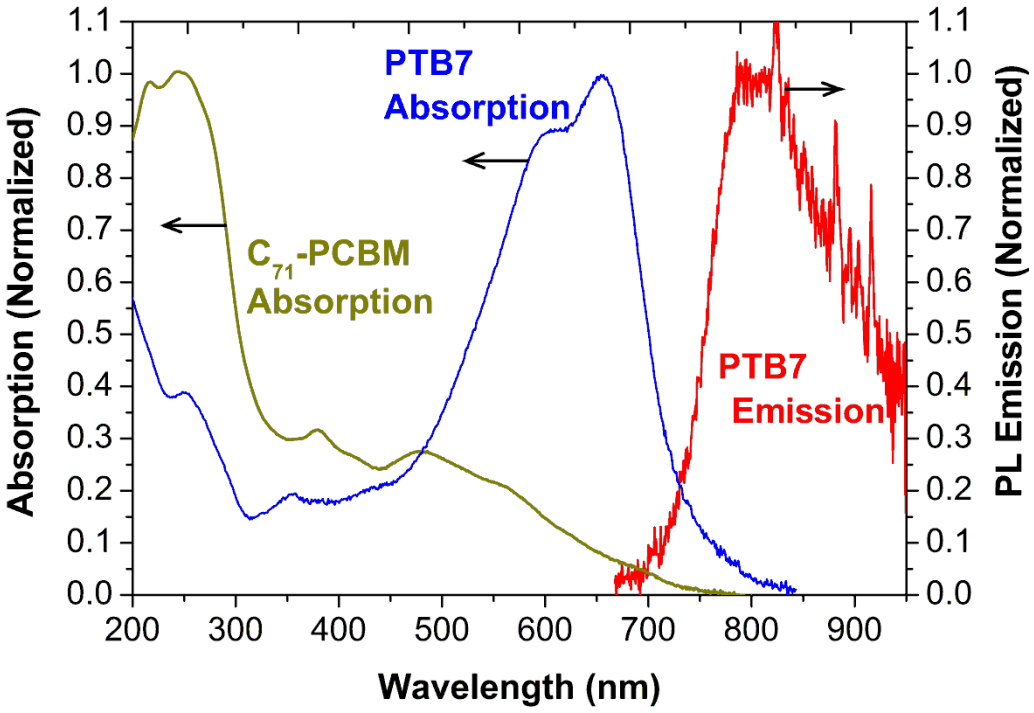

Figure 6.2. The steady-state absorption profiles of PTB7 (blue) and C_{71}-PCBM (brown) plotted with the emission spectrum of PTB7 (red).

6.3. MEASUREMENT OF THE RATE OF QUENCHING IN PTB7:C_{71}-PCBM BLENDS

6.3.1 Introduction

One possible explanation for the incredibly high photovoltaic performance of PTB7 devices could be due to extremely rapid exciton diffusion, some long-range exciton harvesting processes (as shown in the previous chapter) or perhaps a very rapid charge transfer step. In this chapter two different techniques to measure exciton migration in PTB7; volume quenching and time-resolved fluorescence anisotropy, are compared.

6.3.2 Fluorescence Anisotropy Measurements

Fluorescence anisotropy is a method commonly used to measure how the orientation of the exciton dipole changes with time. Firstly, the sample is excited with linearly polarised light and then the fluorescence in the parallel and perpendicular orientations is measured with respect to time. For molecules in solution this technique has historically been used to calculate the rate at which the chromophores are undergoing rotation due to Brownian motion[3]. Since its inception, the trend in time-resolved fluorescence has been towards shorter time-resolution. This means that fluorescence anisotropy can be used to probe faster transitions such as exciton hopping in organic semiconductors[4,5] and charge separation[6] as well as even more rapid processes like exciton self-localisation[7,8]. A schematic showing qualitatively how fluorescence depolarisation measurements can indicate exciton diffusion is shown in figure 6.3.

Fluorescence anisotropy is quantified using the following equation;

EQUATION 6.1.

$$r(t) = \frac{I_{para}(t) - I_{perp}(t)}{I_{para}(t) + 2I_{perp}(t)}$$

where I_{para} is the fluorescence intensity parallel to the pump polarisation and I_{perp} is the polarisation perpendicular to probe polarisation.

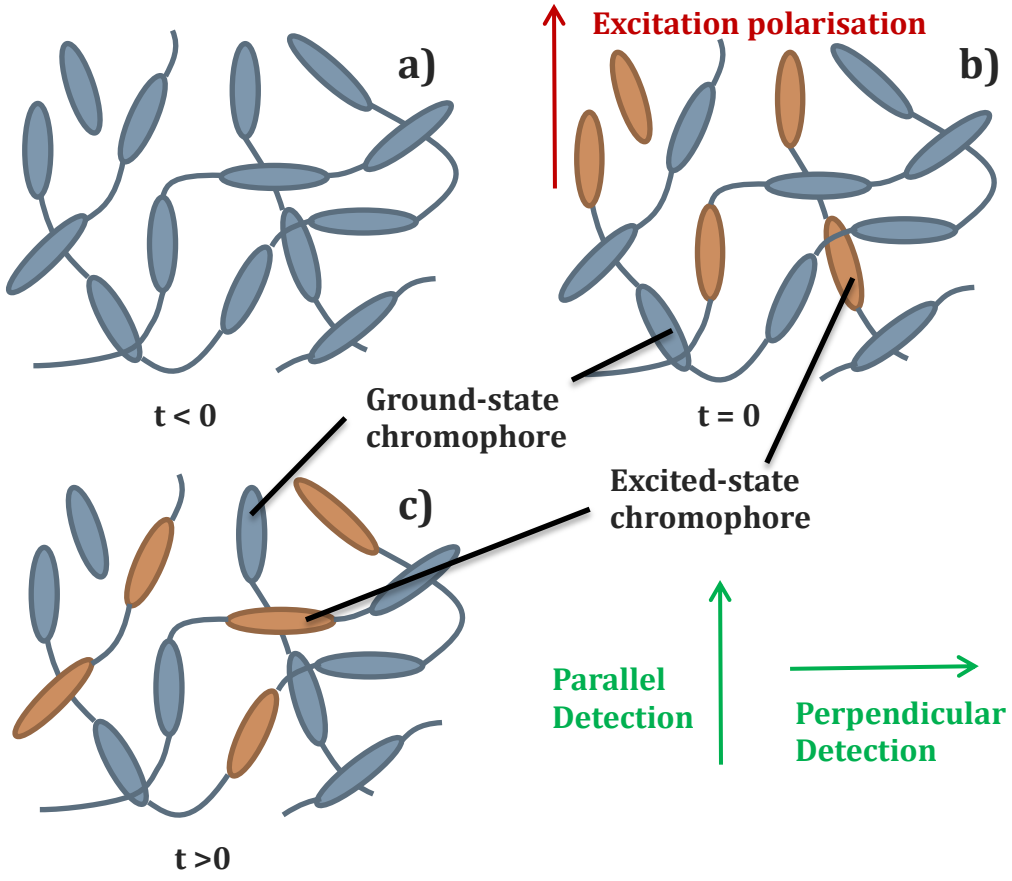

Figure 6.3. a) In a disordered conjugated polymer, the chromophores may be visualised as a series of randomly orientated chromophores which comprise of straight sections of the conjugated backbone linked by kinks in the chain. b) After excitation with linearly polarised light, chromophores aligned with the polarisation of the excitation beam will be preferentially excited. Emission from these chromophores will have the same polarisation as the pump beam. c) After certain time, the excitons can hop onto a nearby chromophore. If the chromophores are highly disordered, once every exciton has undergone a single hop the emission will retain none of the pump beam polarisation information.

To investigate the role of exciton diffusion we performed time-resolved fluorescence anisotropy. This technique is exactly as described in chapter 3, which the exception that a linearly polarised light was used for excitation and only linearly polarised light was detected, with the relative angle between detection and exciton varied using a Berek compensator. The results are shown in figure 6.4. PTB7 was observed to undergo fluorescence depolarisation extremely slowly. Over the course of 400 ps the anisotropy decays from the theoretical maximum for a disordered system of 0.4 to 0.22. This can be compared to another largely

amorphous polymer, MEH-PPV which has been shown to decay from 0.4 to 0.15 in the first 20 ps [9]. PTB7 has been demonstrated from grazing incidence x-ray diffraction (GIXD) to have notably short structural correlation lengths ($L_{c,010}$) of 1.2–1.7 nm[10]. As the very slow fluorescence depolarisation indicates that the excitons are not hopping to chromophores of different orientations, and the x-ray diffraction indicates that there are only short-range correlations between orientations of chromophores, we conclude that the exciton diffusion is either extremely slow or is confined to small ordered regions of the film.

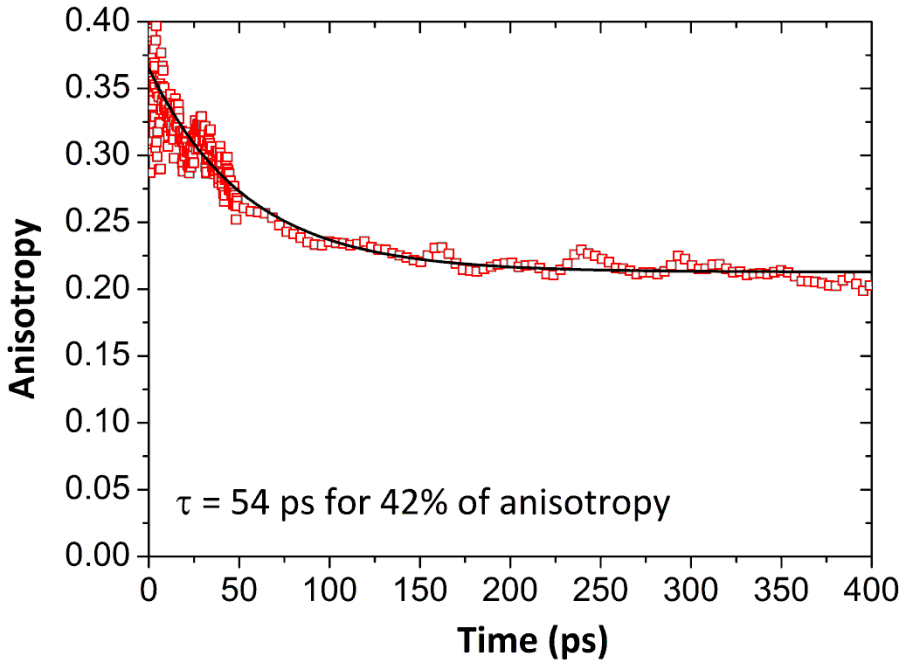

Figure 6.4. The fluorescence depolarisation of neat PTB7. Anisotropy was calculated from fluorescence measured with a polarisation parallel and perpendicular relative to a the polarised probe beam. Many thanks to Dr Gordon Hedley who aided in the acquisition of this dataset.

The lifetime for the partial depolarisation of PTB7 can be used to crudely estimate the exciton diffusion coefficient for the minority of excitons that do depolarise. If the chromophores are truly randomly orientated, as they would be in a totally disordered glass, then a single hop will totally depolarise an exciton. Thus

the lifetime to depolarise can be equated with hopping time, τ_{hop} in equation 4.8. If we make the assumption that the chromophore spacing is on the order of 1 nm, then from equation 4.8, D can be estimated as 3×10^{-5} cm^2s^{-1}. This would be one of the smallest exciton diffusion coefficients measured. As this lifetime is not associated with the total decay of excitons, merely the time taken to decay to a constant value, it would imply that many excitons are totally immobile.

A perhaps more plausible explanation is that the excitons do remain within partially ordered regions. A simple model for assigning an order parameter to chromophores with restricted rotation is the *wobble in a cone model* developed by Kinosita *et al.*[11] and refined by Lipari and Szabo[12] In this model the fluorescence is considered of chromophores in a membrane that are aligned with a particular orientation, called the director, but may wobble around this direction over the course of the fluorescent lifetime. The authors state that though this was derived to describe the anisotropy produced in a system in which the chromophores are themselves wobbling, it can equally be applied to a situation where the excited state is hopping between different chromophores which share the same director[11]. The assumption must be, however, that all chromophores sampled by a given exciton must share the same director, whereas a more physical model would be that the further the exciton travels the less likely the orientation of the chromophore occupied matches the orientation of the starting chromophore. Presuming the chromophores sampled during the lifetime of an exciton do share a single director, the following relationship allows the calculation of average angle, θ, that a chromophore deviates from the director[12,13].

EQUATION 6.2.

$$\frac{r(\infty)}{r(0)} = \left[\frac{1}{2}cos(\theta)\left(1 + cos(\theta)\right)\right]^2$$

From the above equation and the fit in figure 6.4, θ = 34°. This means that over the course of the lifetime it samples chromophores that have an average tilt of 34° from the director.

6.3.3 Volume Quenching

Films of blends of PTB7 with mass ratios 0 to 0.5 wt% C_{71}-PCBM were produced via spin-coating and then analysed using time-resolved fluorescent spectroscopy, exciting on the red side of the absorption spectrum at 750 nm (see figure 6.2). As in chapters 5, the PL decays of the films with quencher were divided by the PL decay of the films without quencher and the natural logarithm was taken of the result leading to what is known as the ln(PL ratio), which is equal to the integral of the rate constant for quenching with respect to time. Both the transient-fluorescence decays and the ln(PL ratios) are plotted in figure 6.5.

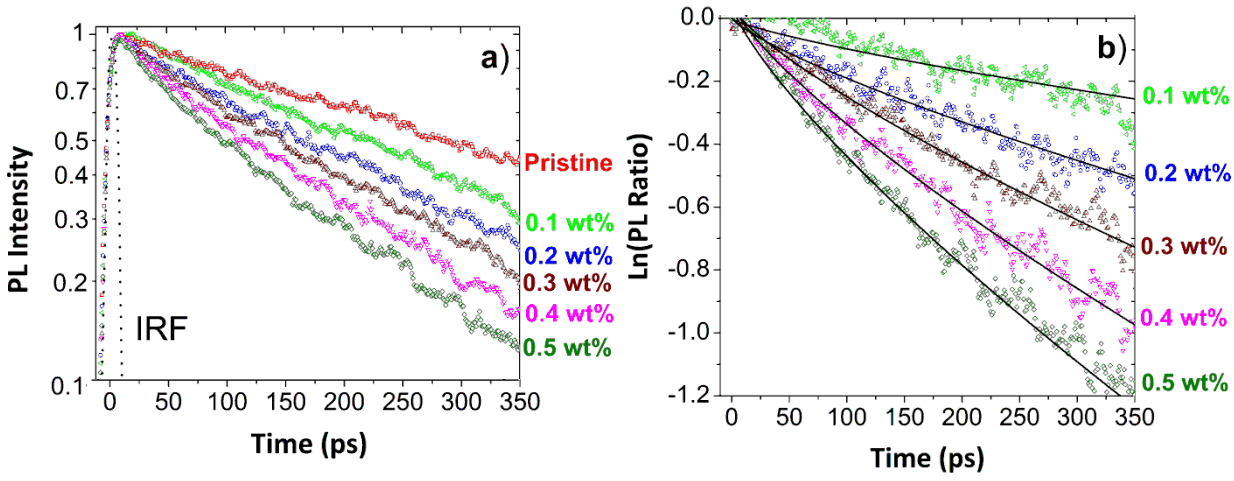

Figure 6.5. The time-resolved fluorescence and ln(PL ratio) of PTB7 with small, known, quantities of the electron acceptor C_{71}-PCBM.

This quenching data seems contradictory to the fluorescence anisotropy data because while in section 6.3.2, the very limited depolarisation observed, when

viewed in conjunction with the low levels of crystallinity reported for PTB7 in the literature, indicates that excitons either are largely static or confined to small ordered regions of the film. In the above case when a simple power law decay is fitted to the data (black lines) it is apparent that the rate constant shows only a modest reduction during the time period measured, dropping from 2.0 $nm^{-3}ps^{-1}$ at 5 ps to 0.8 $nm^{-3}ps^{-1}$ at 350 ps. This is in contrast to figure 6.4, which suggests that in a disordered polymer the exciton migration has ceased by ~200 ps.

As described in chapter 4, an apparent slowing of the diffusion coefficient can occur as a result of the exciton migrating to lower and lower energy sites. To investigate this effect, the volume quenching experiment was repeated using 400 nm excitation. As can be seen from figure 6.2, this is on the blue side of the absorption of PTB7. This was plotted against the equivalent plots using 750 nm excitation. Plots of these ln(PL ratio)s are shown below.

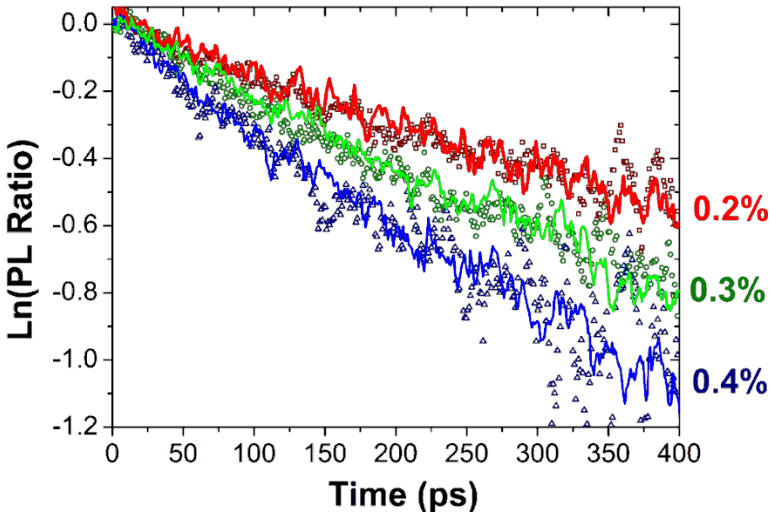

Figure 6.6. ln(PL decays) of films excited at 400 nm (hollow symbols) compared with those excited at 750 nm (solid lines). It is clear that these two curves are in very good agreement suggesting there is little or no effect whether the excitons are excited on the red or blue side of the absorption spectrum.

The strong agreement between the two excitation wavelengths is a good indication that excitation wavelength has little influence on the kinetics of exciton migration. This suggests that dispersive diffusion is not playing a big role in slowing down the rate of quenching, on the timescale observed.

As discussed in the previous chapter, time-dependent reaction rates can be explained by diffusion in restricted volumes such as those that happen in a micelle or protein[14,15] or when the diffusion is not properly free and instead is hindered by inert obstacles[16,17]. Sometimes a time dependent rate constant occurs because the diffusing species either have to diffuse in one direction or have a strong preference for a single direction[18-20]. There have been two recent studies that show a time-dependence of diffusion in P3HT, a semi-crystalline polymer, was due to preferentially 1-dimensional diffusion in P3HT, a semi-crystalline polymer[18,19]. If there is some degree of order within these films it may cause a time-dependence in the quenching, by restricting the diffusion or by encouraging exciton diffusion along only one crystal axis.

6.3.4 Discussion of Mechanism

It is challenging to confidently assign the exciton depolarisation and quenching kinetics. The moderate slow-down in the rate at which excitons encounter fullerenes cannot be explained using dispersive diffusion because they show no excitation wavelength dependence, or at least any discrepancy is much faster than the instrument response time of 10 ps. They also contradict the most naïve interpretation of the anisotropy data which suggests that exciton motion has halted by 200 ps. If the depolarisation measurement is interpreted through a model that allows for a degree of ordering both the fluorescence quenching and

depolarisation can be made to agree, but a large degree of order is contradicted by literature reports of GIXD measurements that suggest that the ordered regions are extremely small[10].

The simplest explanation that accounts for the phenomena seen is that there is some degree of order in the films, but with too much disorder to cause coherent scattering of the x-rays and that this order is sufficient influence on the movement of excitons to the extent that they no longer diffuse in an isotropic manner that can be described by the solutions to the diffusion equation described in chapter 4. In addition this long range order would provide a convincing explanation as to why a long lived fluorescence polarisation is observed. At the moment there is too little information to assign the time-dependence to these particular physical phenomena, but further research is being carried out. This further work includes computer modelling by collaborators as to how the degree of order in the blend would influence the depolarisation of fluorescence quenching in these films. Also further work includes a comparison of the volume quenching and fluorescence anisotropy measurements with a third technique to measure exciton diffusion, exciton-exciton annihilation, as well as a comparison between such measurements conducted at room temperature and 77 K.

Whatever the mechanism by which the exciton is delivered to the quenching sites, a full understanding of exciton harvesting must also include an investigation into the rate of electron transfer, once the exciton is at the interface. The remainder of this chapter focusses on this electron transfer step.

6.4. LITERATURE REVIEW OF ELECTRON TRANSFER PROCESSES

6.4.1 Introduction

Many different physical processes are governed by the rate at which an electron can be transferred from one species to another. Redox chemical reactions[21-23], such as natural[24-26] and artificial photosynthesis[27-29] as well as electron mobility in disordered solids[30,31] are examples of processes determined by the rate of electron transfer.

6.4.2 Marcus theory of Electron Transfer

Since its inception in 1956, Marcus theory has been the standard theoretical framework through which electron transfer processes are viewed. Marcus theory is an intuitive model that inputs relatively few physical parameters to generate strong predictions of the rate of electron transfer. Fundamental to Marcus theory is the Franck-Condon Principle[32,33], published in 1926, which states that because electronic movement is on a much more rapid timescale than the movement of nuclei, the transition probabilities for electronic processes can be calculated assuming fixed nuclei. Note this is a closely related concept to the Born-Oppenheimer approximation, published the following year[34], which uses similar reasoning to allow the separation of the nuclear and electronic wavefunctions of an atom or molecule. This assumption can be probed very approximately by considering two transitions. Firstly, the electronic transition that occurs after the absorption of visible light, for example 500 nm, which corresponds to a frequency of 600 ps^{-1} or a period of 2 fs. If we compare that to a vibronic transition, for example a C=C stretch, which resonates with light in the IR range (~1660 cm^{-1}

which is equal to 6000nm), this light has a frequency of 50 ps^{-1} and a period of 20 fs. Thus in a very crude sense, in this particular case, the electronic transition occurs on an order of magnitude faster than the vibronic transition. For processes that involves the absorption or emission of a photon, the Franck-Condon principle dictates that these processes can be written as vertical transition between potential energy surfaces, i.e. the electronic process which occur must not be combined with a change of reaction coordinate as such changes cannot occur as quickly.

Electron transfer processes do not involve an emission or an absorption of a photon and hence, due to the conservation of energy, are restricted to transitions between states that have the same energy. This introduces a new assumption, that the process is adiabatic, meaning that heat is not transferred to or from the surroundings during the course of the electron transfer step. It is necessary to assume isoenergetic hopping; electron transfer processes are required to be between isoenergetic states because of the law of conservation of energy.

Thus, electron transfer can only occur when the reactant and product have the same nuclear coordinates *and* are isoenergetic. If we plot the energy of an electronic state with respect to the position of its nuclear coordinates (which we can combine into a single representative parameter, called the reaction coordinate) we can generate the state's *potential energy surface* (PES). It is denoted as a surface (rather than a line) because the reaction coordinate is a simplified one-dimensional representation of what might be a complex multidimensional coordinate. A schematic of two potential energy surfaces is shown below.

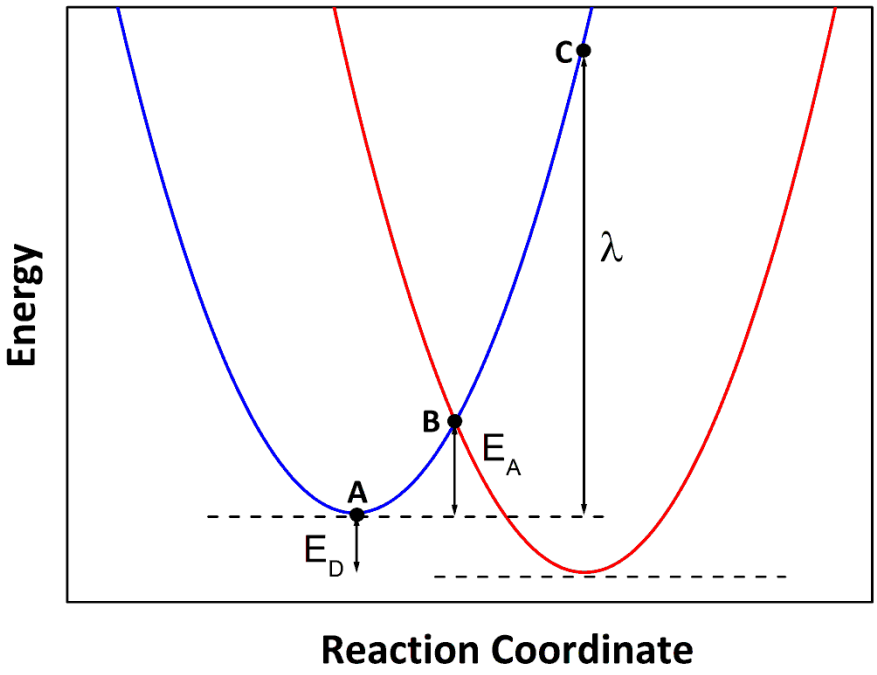

Figure 6.7. Two potential energy surfaces, one of the reactant (blue) and the product (red).

Due to the two restrictions on electron transfer; the Franck-Condon Principle and isoenergeticity, electron transfer can only occur between two potential energy surfaces at the crossing point, as this is the only point at which the surfaces have both the same energy and same position. Marcus theory is the formalism that relates this insight into a rate of reaction for a given process.

In its simplest form, Marcus theory relates the rate for the transition of reactant to product to the probability that the state at the intersection between the potential energy surfaces is occupied. This state represents the highest energy point in the course of the transition and is known as the transition state. If the reactant is at thermodynamic equilibrium, then the probability that a given vibrational state will be occupied will be determined by the Boltzmann Distribution.

This is described by the Arrhenius equation and will be dictated by the activation energy E_A, the temperature and the Boltzmann constant, as well as a pre-exponential factor which will be related to the relative entropy of the transition state.

EQUATION 6.3.

$$k_{ET} = Aexp\left(\frac{-E_A}{k_B T}\right)$$

Thus in order to calculate the rate constant for the process, the activation energy must be ascertained. For the case of the potential energy surfaces in figure 6.7, it is clear that the activation corresponds to the difference in energy between the lowest energy point, **A**, on the reactant surface to the crossing point between the surfaces, **B**. The point **B** is the highest energy point in the lowest energy path between the reactants and products and is hence known as the saddle point of the potential energy surface. If one was to imagine the physical meaning of moving along the reactant surface from **A** to **C**, through **B**, it would correspond to rearranging all nuclei from their equilibrium positions, all the way to the equilibrium positions of the product. For lower energy molecular vibrations, an individual bond is well approximated by a simple harmonic oscillator[35]. Thus if the path along the x-axis represents a molecular vibration that translates the reactant nuclei into the product nuclei, in most cases this vibration can be approximated as a harmonic oscillator. A harmonic oscillator will have a force which scales linearly with extension, and an energy that scales with the extension squared. Thus the potential energy surface for such a vibration will be parabolic, up until the point where the harmonic oscillator approximation breaks down at which point it is better approximated by the Morse potential[36]. The simplifying assumption that the

spring constant for the vibration that translates the product to the reactant is the same as the one that translates the reactant back into the product, leads to there being only 3 parameters that determine E_A. Firstly the breadth of the parabola (determined by the spring constant of the bond or the vibrational frequency of the transition). Secondly, the energetic driving force, E_D which is the offset between the bottom of the reactant parabola. Finally, the product parabola and the offset between the two parabolas along the x-axis which represents a measure of the displacement of the equilibrium positions of the reactant nuclei from the equilibrium positions of the product nuclei. Because the only factor that influences the rate is E_A, it is irrelevant to the calculation as to whether the intersection is between two, well-spaced, broad parabolas or two very close yet narrow parabolas (see figure 6.8 below).

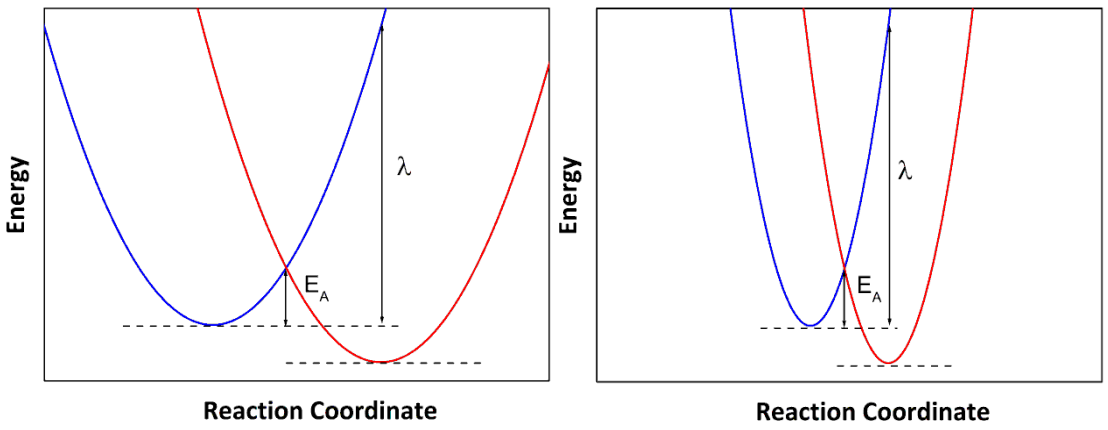

Figure 6.8. Because the rate of transfer is determined only by E_A, it does not matter whether the potential energy surfaces are broad but distanced (left) or narrow and nearby (right). Thus, these two parameters can be combined into a single critical value, the reorganisation energy, λ. This energy represents the energy required to translate the nuclei in the reactant to the equilibrium positions of the product without moving from one potential energy surface to the other.

As is illustrated in the above diagram, rather than deal with two free parameters, the displacement along the reaction coordinate and the steepness of

the parabolas, it is convenient to define the system by the reorganisation energy, λ, which is a measure of the energy required to rearrange the product nuclei from their equilibrium positions to the equilibrium positions of the nuclei in the reactant, *without* moving to the reactant potential energy surface. This energy could be expressed as

EQUATION 6.4.
$$\lambda = \frac{1}{2} k_s {x_{r-p}}^2$$

where k_s represents the spring constant for the reactant to product vibration, or vibrations, and $x_{r\text{-}p}$ represents the displacement of the reactant from the product along the reaction coordinate. The two parabolas can be described as

EQUATION 6.5.
$$E_{reactant} = \frac{1}{2} k_s x^2$$

EQUATION 6.6.
$$E_{product} = \frac{1}{2} k_s (x - x_{r-p})^2 - E_D$$

The crossing point will be when these are equal

EQUATION 6.7.
$$\frac{1}{2} k_s x^2 = \frac{1}{2} k_s (x - x_{r-p})^2 - E_D$$

EQUATION 6.8.
$$\frac{1}{2} k_s x^2 = \frac{1}{2} k_s (x^2 + {x_{r-p}}^2 - 2x x_{r-p}) - E_D$$

Substituting in equation 6.4 and simplifying;

EQUATION 6.9.
$$\frac{-(E_D - \lambda)}{k_s x_{r-p}} = x$$

E_A will be equal to the potential energy of the reactant at this displacement

EQUATION 6.10.
$$E_A = \frac{(E_D - \lambda)^2}{4\lambda}$$

By substituting equation 6.10 into equation 6.3, the rate constant of the reaction can be described as

EQUATION 6.11.

$$k_{ET} = Aexp\left(\frac{-(E_D - \lambda)^2}{4\lambda k_B T}\right)$$

Equation 6.11 has some quite surprising implications. It indicates the while the driving force is less than λ, increasing the driving force, increases the rate – as would be consistent with intuitions about the rates of reaction – with larger energetic incentives leading to a faster rate of reaction. When E_D becomes greater than λ, the reverse occurs, with higher driving forces leading to slow rates of reaction. This can lead to a somewhat surprising situation where a chemical process is so energetically favoured it happens on an immeasurably slow timescale. These two regimes are illustrated below;

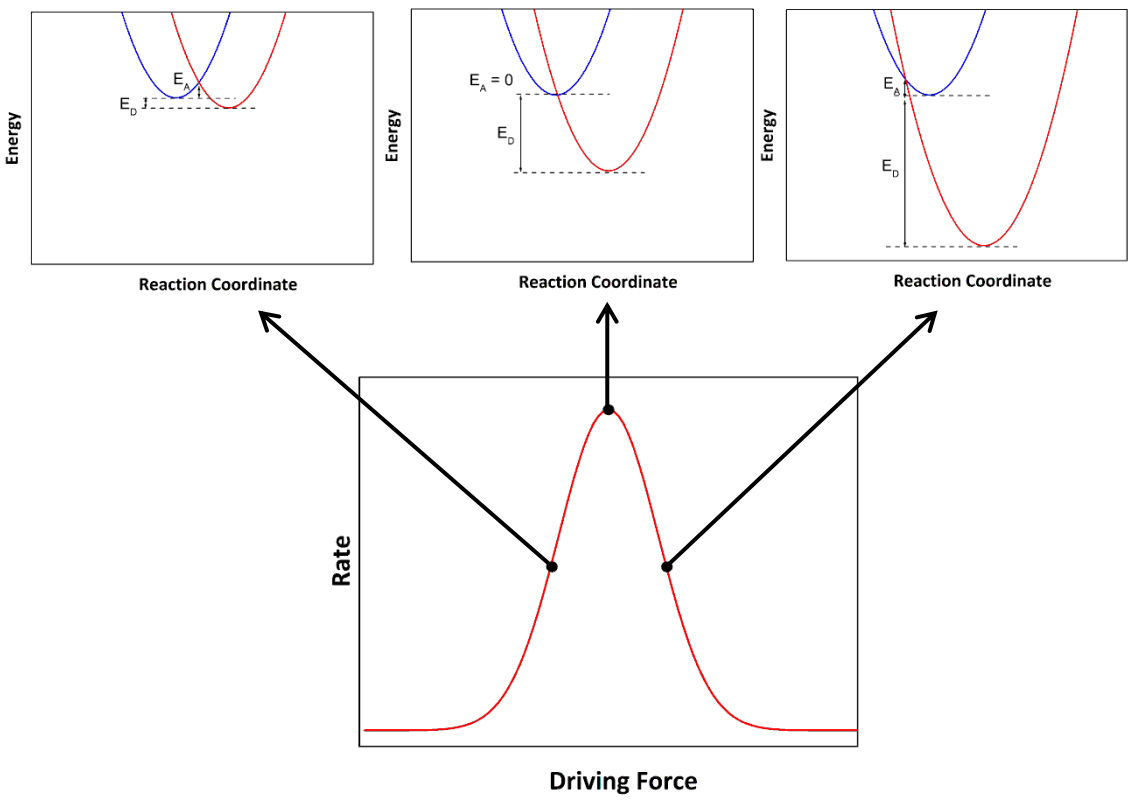

Figure 6.9. Three different regimes with driving forces increasing from left to right. Firstly the regime where the driving force is less than the reorganisation energy. In this regime raising the driving force lowers the activation energy and hence increases the rate. In the second regime the driving force is approximately equal to the reorganisation energy and hence the activation energy is zero and the rate is very fast. In the final regime the driving force is larger than the reorganisation energy and raising the driving force lowers the rate. This is called the *Marcus Inverted Region.*

6.4.2.1 *The Strong Coupling Regime and Quantum Effects*

6.4.2.1.1 The strong coupling regime

It is a fundamental axiom of molecular orbital theory that if the wavefunctions of two overlapping molecular orbitals are close in energy, and one is occupied and one is unoccupied, they will undergo mixing, to produce two new molecular orbitals (with the caveat that the two original orbitals must have the appropriate symmetry to interact). Of the two new orbitals, one will be higher

energy and one will have a lowered energy. Because the lower energy orbital will be occupied and the higher one will be unoccupied the overall energy of the system will be lowered. If the initial and final states in the electron transfer process are close enough in space and energy as well as having the appropriate symmetry to interact, the orbitals will mix leading to the potential energy surfaces to apparently avoid crossing each other[37]. The electronic coupling term, V, quantifies this degree of wavefunction overlap.

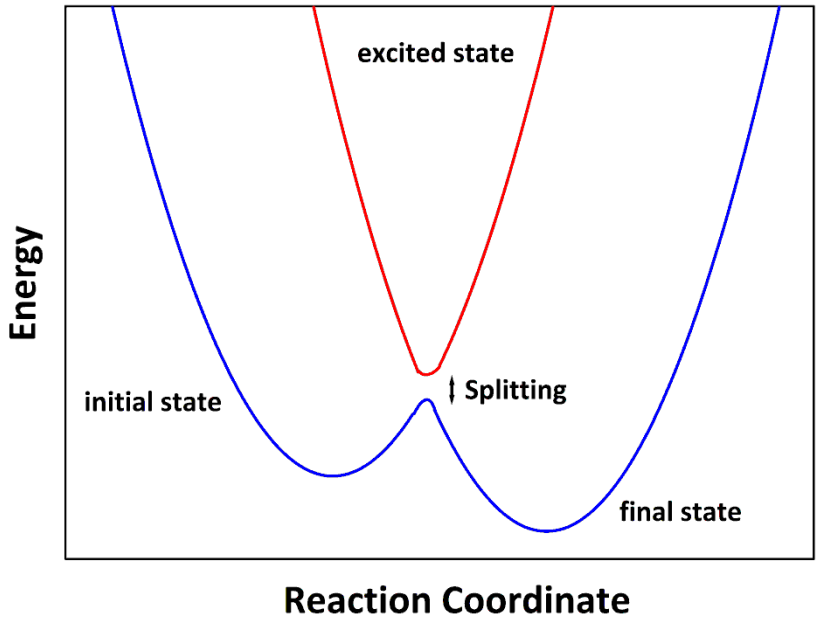

Figure 6.10. A diagram showing the potential energy surfaces of an initial and final state, in isolation, both parabolic but after experiencing mixing at the crossing point have a shared potential energy surface.

The above diagram shows the potential energy surfaces of an initial and final state that have undergone mixing. This has some important implications. Firstly it means that if the splitting is large enough, any vibration which surmounts the saddle point (the highest point in the lowest energy pathway to the products), will be converted into a product state. Contrast this with figure 6.7 in which the reactant can traverse the saddle point **B** many times without electron transfer

occurring. Thus while in this weak coupling regime, equation 6.11 has an unknown pre-factor *A* describing the probability of electron transfer occurring once the transition state **B** is populated, in the strong coupling regime this probability depends only on the strength of the electronic coupling and can be quantified[38,39].

The second important observation we can make about figure 6.10 is that a product vibration that has a high enough energy to overcome the saddle point energy, will actually be shared between the reactant and products state. To reiterate this point, one could imagine a vibration on the initial-final PES that oscillates between the initial and final states. This would be manifested as the electron being transferred forward and backwards between the reactant and product state as part of a shared molecular vibration. This quantum oscillation between reactant and product states is characteristic behaviour of vibrationally coherent electron transfer[40-42].

For Marcus theory still to be valid, the degree of splitting must not hugely alter the position of the activation energy; the overall perturbation of the PES must be small. If the mixed section is of lower energy than the purely reactant or product potential energy surfaces then the ultimate product would be a mixed state between the donor and the acceptor. This corresponds to bond forming, so ultimately this criterion is a reiteration that Marcus theory describes only the electron transfer process, *not* bond forming or bond breaking processes[43].

As mentioned, the strong-coupling regime illustrated by figure 6.10 allows us to determine the pre-exponential factor for the rate constant as it will depend on the overlap integral for electronic coupling, V. In the non-adiabatic regime, Levich, Dogonadze and Kuznetsov used a similar approach to Marcus theory, but in

conjunction with Landau-Zener theory, to derive the following expression for the rate of electron transfer[43,44].

EQUATION 6.12.

$$k_{ET} = \frac{2\pi V^2}{h\sqrt{4\pi\lambda k_B T}} exp\left[-\frac{(\lambda - E_D)^2}{4\lambda k_B T}\right]$$

where V has already been introduced as the degree of electronic coupling defined by the wavefunction overlap between the initial and final states and h is Planck's constant. The pre-exponential factor, which represents the rate when $E_D = \lambda$, when the coupling is strong, is usually replaced by a frequency[45] k_0 of 10^{12}–10^{14} s^{-1}.

The key message when comparing equation 6.11 to equation 6.12, is that both exhibit a rate that has a Gaussian distribution with respect to driving force and have an optimum rate when $E_D = \lambda$. Thus in this work I do not dwell on the differences between the two regimes as the overall functional form with respect to the variables is identical in both cases.

6.4.3 Brief Review of Methods to Measure Rates of Electron Transfer

Measuring electron transfer between species in solution is very challenging because once electron transfer becomes fast enough then the rate the reaction sites move through solution becomes the critical parameter and the process becomes diffusion limited. For nearly 30 years after Marcus' original prediction of the inverted region almost all investigations found no evidence for this region, instead finding that the reaction rates plateaued with increasing driving force[46-49]. These studies introduced both reactants into solution and initiated flash photolysis on ruthenium complexes using heteroaromatic systems as quenchers [47,48] or from the

acceptor material triplet duroquinone with predominantly Fe^{2+} complexes as the donor[49]. The systems were modelled to take into account the formation and separation of the encounter complex and the electron transfer step. Miller *et al.*[50] were first to observe the Marcus inverted region using a system where the donor and acceptor are held apart by a rigid alkyl spacer and assign the previous failures in the literature to failures to account for the diffusive limit of the reaction. Subsequently, the introduction of a rigid spacer separating the donor and acceptor, and probing the rate of photoinduced electron transfer using luminescence quenching has become the standard in chemical kinetics. The spacer is either saturated alkyl fused ring systems[51-54] or unsaturated bridges [55-59]. Inclusion of a spacer is not a perfect solution to the problem of measuring electron transfer rates as the very presence of bonds between the initial and the final state can enhance the rate[52,60]. The effect is most pronounced in donor-acceptor systems with unsaturated bridges[60].

There have been a few attempts to probe electron transfer rates in rigid media where the donor and acceptor are separate molecules, and randomly distributed. An early attempt by Beitz *et al.*[61] showed some evidence of a slowing rate of electron transfer with increasing driving force, but the trend was somewhat noisy. This work was only revisited by Coffey *et al.*[62] when they measured the relative yield of free charges in dilute donor-acceptor blends using time-resolved microwave conductivity measurements.

6.4.4 Recent Theories of Charge Separation in Organic Solar Cells

In recent years some different theories have been developed to explain the very rapid electron transfer processes.

Savoie *et al.*[63] argue that the observed extremely rapid electron transfer can be explained by considering on the timescale that excitons are harvested in device blends, the exciton has not had time to vibronically relax and that these 'hot' excitons are harvested. In addition the authors perform density functional theory calculation on fullerene clusters of differing sizes and conclude that there are a multitude of acceptor aggregate states, rather than a single fullerene LUMO to which the electron can be transferred. Thus they conclude that because there is a broad density of acceptor states electron transfer can proceed via a resonant (activationless) process for any offset between the donor and acceptor. This theory can explain the very rapid quenching involved in photovoltaic blends and predicts the absence of a Marcus inverted region as any energetic offset can undergo resonant electron transfer.

Bakuline *et al*.[64] use experimental results from a pump-push experiment to argue that charge separation occurs after electron transfer from the donor to a higher energy delocalised band-state. They propose that the required offset between the donor and the acceptor in an efficient device is required so that the electron is injected into the delocalised band states which are critical for long-range charge separation. The authors recommend that small driving forces would be required for materials that support highly delocalised polaronic states due to their structural rigidity, which would also correspond to a smaller reorganisation energy, if interpreted through Marcus theory.

A third explanation, proposed by Kaake and co-workers, is that charge separation can be explained with reference to the uncertainty principle[65]. The authors suggest that the uncertainty principle dictates that an excited state created

by visible light must have a length-scale on the order of 20 nm. They argue that because there is some evidence that coherent states exist over a lifetime of ~100 fs which is on a similar timescale to the fastest rates of quenching observed, uncertainty in the position of the electron and hole that make up the exciton may contribute to efficient exciton harvesting. Thus they conclude that exciton harvesting proceeds from highly delocalised weakly bound exciton state via a coherent process.

6.5. INVESTIGATION INTO THE RATES OF ELECTRON TRANSFER IN PTB7 BLENDS

6.5.1 Introduction

As was discussed in Chapter 1, one of the key processes in the function of organic solar cells is the process that separates the exciton into an electron a hole, a process known as charge separation. This process can proceed extremely rapidly, with charges (as probed with transient absorption spectroscopy) often appearing within 1 ps[6,66-70]. Although a huge range of different donor materials, such as PCDTBT[71,72], P3HT[73] and PTB7[1] have been investigated and give solar cells with high power conversion efficiencies, the highest efficiency blends always use soluble fullerene derivatives for electron acceptors. What is it about a molecule that makes it able to rapidly accept electrons from an incoming exciton? This section, 6.5, seeks to answer this question using PTB7 as a model donor material. In particular, the influence on the energetic driving force will be investigated. This is a key parameter because the trend in organic solar cells has been toward near infrared (1.3–1.5 eV) absorbing materials in order to harvest sunlight most efficiently[74]. As

these materials tend to have a larger photocurrent but smaller photo-voltage than visible absorbing devices, any excess driving force between the donor and the acceptor can significantly lower the power conversion efficiency of the devices[75].

Several different blends of PTB7 with small quantities of acceptors with different electron affinities will be analysed using time-resolved fluorescence and then the contributions from exciton diffusion and electron transfer will be separated.

6.5.2 Quenchers used

Quenchers must not absorb light in the region that PTB7 emits. Any spectral overlap between PTB7 and a quencher will mean that FRET will be enhancing the rate of quenching of an exciton in the region of a quenching site and hence any information on the rate of electron transfer will be lost. The quenchers used in this section are shown in the panel below.

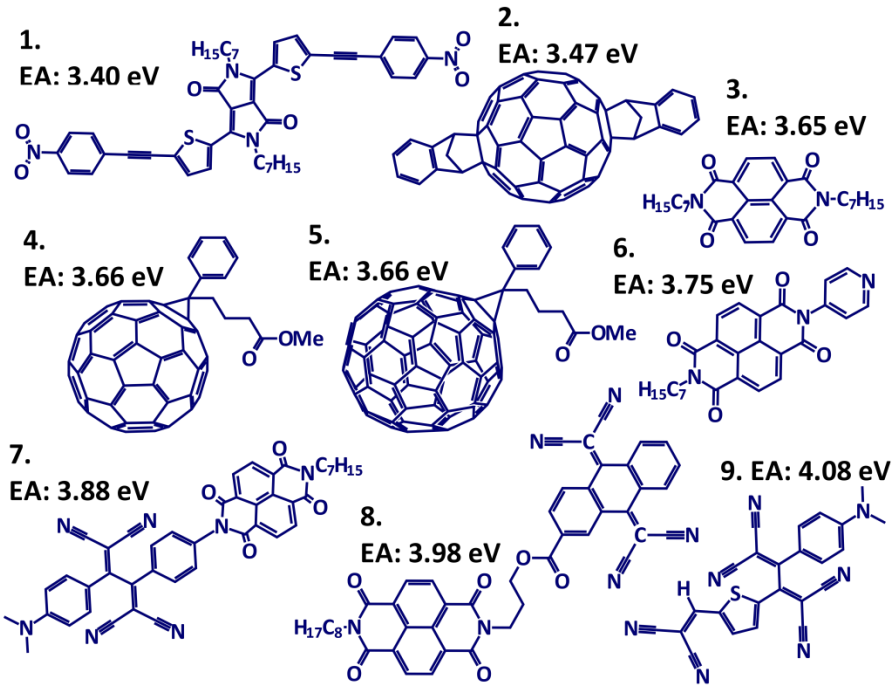

Figure 6.11. Panel of small molecule quenchers with a range of electron affinities.

These particular quenchers were chosen because they showed very little absorption in the spectral region where PTB7 emits. The molecules were numbered in order of increasing electron affinity. This can be further quantified by calculating the molar absorption coefficient of each quencher in solution and then using equation 4.11 to calculate the spectral overlap *J* between the donor and the acceptor. Molar absorption coefficients are shown in the charts below.

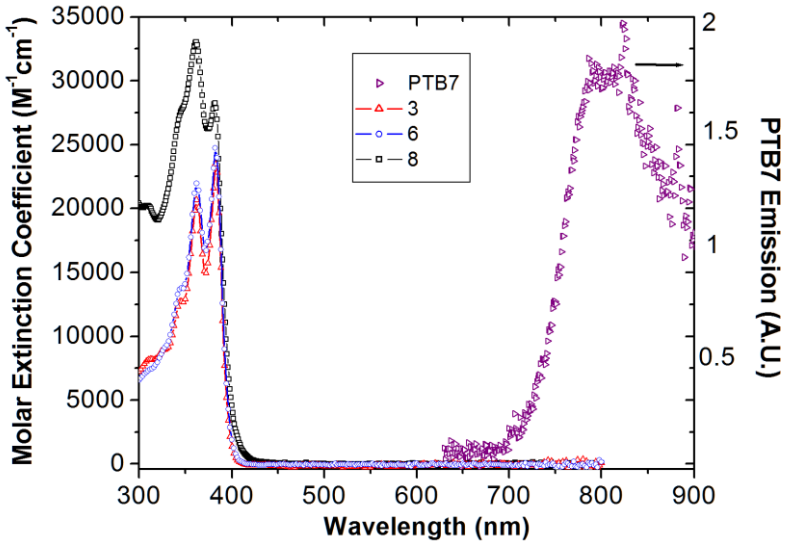

Figure 6.12. Molecules 3, 6 and 8 have absolutely no spectral overlap with the emission of PTB7.

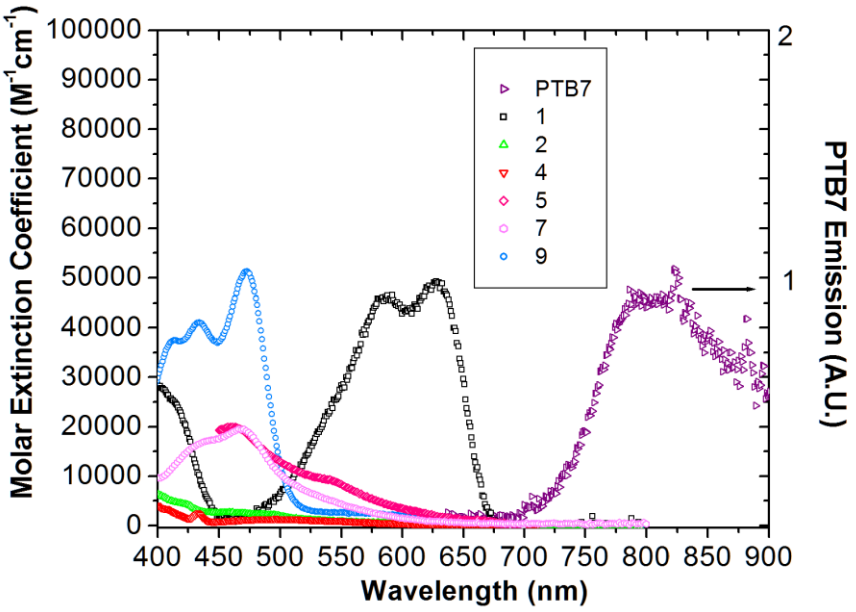

Figure 6.13. The remaining molecules had extremely small spectral overlap with the emission of PTB7.

6.5.3 Results and Discussion

6.5.3.1 *Qualitative Discussion of the Observed Trends*

Films were prepared with 0.005 nm^{-3} concentration of quenchers 1-9, with the structures as illustrated in figure 6.11. The time-resolved fluorescent decays were then measured (figure 6.14, below) and the lifetimes (as approximated by the time the normalised decay drops to 1/e) were plotted against the electron affinity offset between the donor and acceptor (figure 6.15). The lifetime first decreases as the offset gets more negative before increasing again after a certain threshold. This indicates that there is an optimum offset to promote electron transfer and in the case of PTB7, it is when the electron affinity (E_{ea}) of the acceptor is approximately 0.6 eV deeper than the E_{ea} of PTB7.

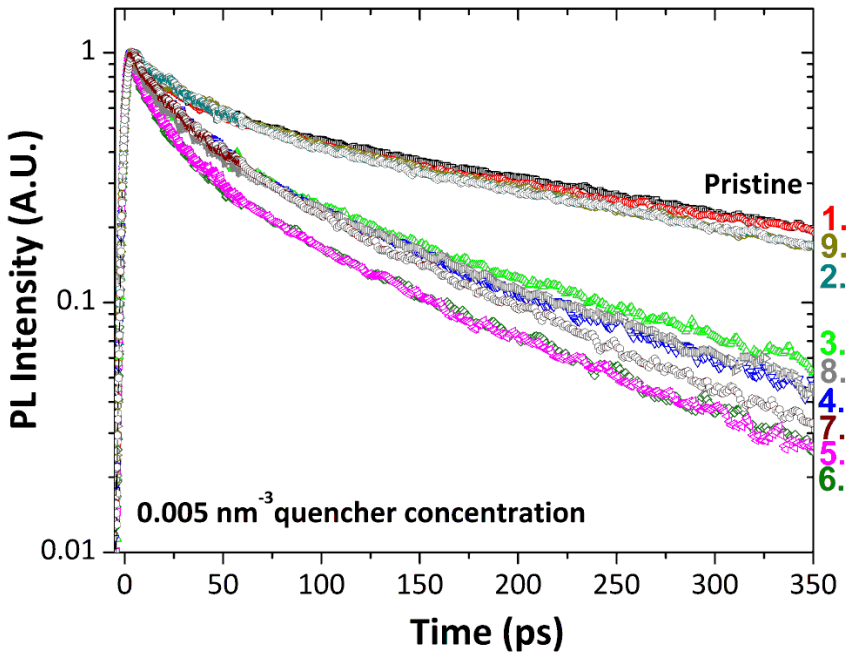

Figure 6.14. The time-resolved photoluminescent decays of PTB7 with a concentration of 0.005 nm^{-3} of small molecules 1–9 as illustrated in figure 6.11.

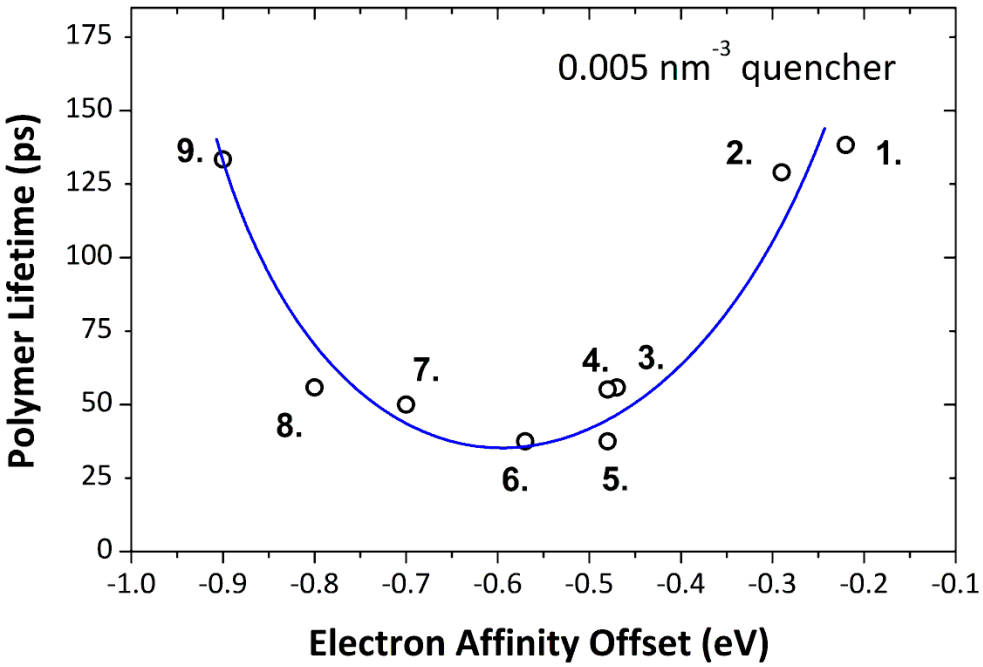

Figure 6.15. The lifetime of PTB7 when it is blended to a number density of 0.005 nm^{-3} of quenchers 1-9. The blue line is a guide to the eye.

The above strong trend in lifetime with respect to electron affinity is a convincing indication that exciton diffusion cannot be wholly limiting exciton harvesting – if that were the case, different types of quencher would give approximately similar quenching kinetics.

That the rate of quenching of excitons is not entirely limited by the rate at which the excitons are transported to the interface through exciton diffusion makes the analysis of the data more complicated. In previous investigations of photoluminescence quenching[76-79], as in chapter 4, a key assumption has been that the encounter rate as dictated by the Smoluchowski rate equation (equation 4.20) can be considered to be equivalent to the rate of quenching. This assumes every exciton encounter with a quenching site will lead to the exciton being quenched. Another commonly made assumption in OPVs is that the requirement for an offset between the donor and the acceptor is merely to overcome the exciton binding

energy. Though it is generally understood that there is some subtlety to the process it is often quoted that as long as the offset is above this threshold, charge separation will occur[80-82]. Both of these assumptions are in disagreement with the trend shown in figure 6.15. As described in 6.5.2 the quenchers used were carefully chosen so that they would not act as FRET acceptors as well as electron acceptors so any influence on FRET (which has been recently shown to play an important role in exciton harvesting[83,84]) can be discounted. In addition it would be unlikely that FRET is playing a large role considering the strong trend observed with respect to electron affinity offset and the lack of any relationship when electron affinity is plotted against the donor-accept Förster radius (shown below).

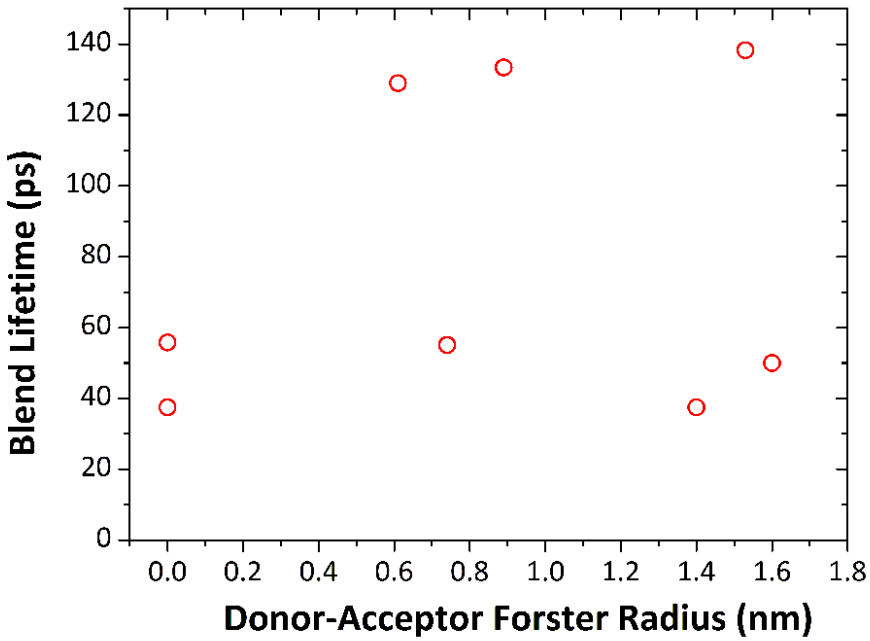

Figure 6.16. The fluorescence lifetime of blends with 0.005 nm^{-3} quencher plotted against the donor-acceptor Förster radius. No trend is discernible.

Compare the above plot, which shows the lack of correlation between the quenching in blends, and the donor-acceptor Förster radius to figure 6.15, in which

a trend is clearly visible with respect to quencher electron affinity. If FRET significantly contributed to quenching there would be a negative correlation between the Förster radius and the blend lifetime because a large Förster radius would lead to strong quenching and hence a short lifetime. This is not observed in figure 6.16.

Having ruled out FRET we are left with two consecutive processes that lead to exciton quenching. Firstly the exciton must move through the film via some sort of diffusive process and then, once at a quenching site it must undergo electron transfer. This situation is common in chemical kinetics where the diffusive process relates to molecules moving through solution and can be expressed as[14,85,86]

EQUATION 6.13.

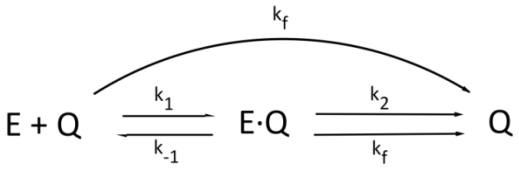

where E is an exciton; Q is a quencher, E·Q is an exciton and a quencher that are close enough to undergo electron transfer, k_1 is the rate constant for the diffusive process that delivers excitons to the quencher, k_{-1} is the rate constant for the reverse diffusive process, k_2 is the rate constant for electron transfer (once the exciton is close to the quenching site) and k_f is the rate constant for the decrease of population of PTB7 excitons in the absence of quencher.

We separate the processes by which the excitons decay into two types, the first in which the exciton will encounter the acceptor and is then quenched (which will depend both on the concentration of excitons, [E], and the concentration of quencher sites, [Q]) and the second which happens spontaneously in which the

rate of decay depends only on the concentration of excitons. If we define the rate constant for the first, quenching process as k_q and the rate constant for the second spontaneous process as k_f then the following rate equation can be written[14]

EQUATION 6.14. $$\frac{d[E]_{total}}{dt} = -k_q(t)[Q][E]_{total} - k_f[E]_{total}$$

Where $[E]_{total}$ represents the total concentration of excitons regardless of how close to a quenching site they are. We are able to measure k_q, directly from the data as it will be equal to the derivative of the ln(PL ratio), as described in chapter 3. A plot of the ln(PL ratio)s of the time-resolved fluorescence data shown in figure 6.17 is shown in the figure below.

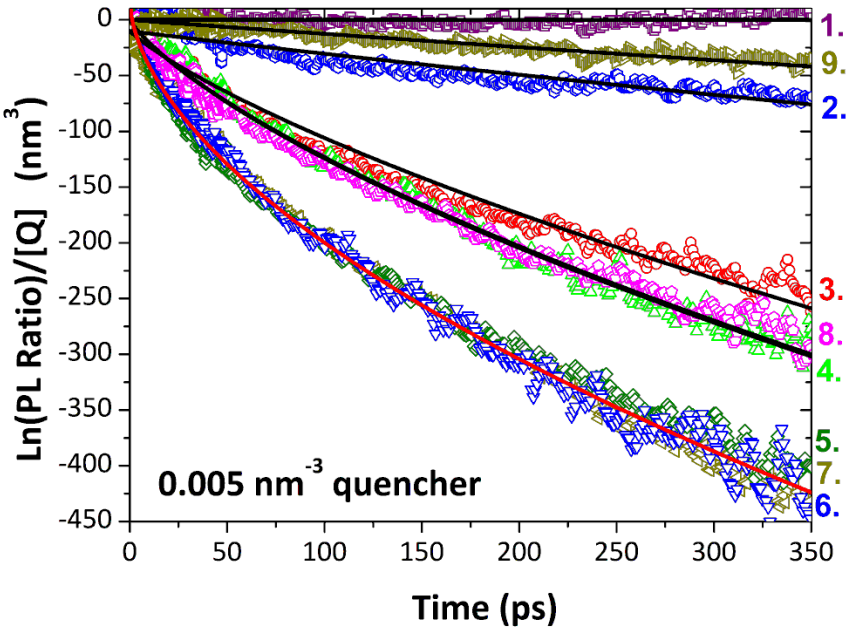

Figure 6.17. ln(PL ratio)s/[Q] of 0.005 nm^{-3} quenching sites of small molecules 1–9 in PTB7. The derivative with respect to time of these curves corresponds to the rate constant k_q.

As the derivative of the above curves corresponds to the rate constants for quenching for the different small molecule acceptors it is clear firstly that different materials give very different quenching rates, which is consistent with the variation in blend lifetimes in figure 6.14 and 6.15. Additionally it can be seen from the curvature of the lines that the rate constants for the quenching process are quite strongly time-dependent: the rate constant is slowing with increasing time.

6.5.3.2 *Calculating the equilibrium constant for the diffusive process*

Before the processes of exciton diffusion and electron transfer can be commented on, the overall rate of quenching k_q must be expressed in terms of the rate constants for the individual process, k_1, k_{-1} and k_2. As k_1 and k_{-1} will both be dictated by the diffusion coefficient D, they ought to be able to be condensed into a single free parameter.

Assuming that the movement of excitons to and from the quenching site is truly a diffusive process, i.e. there is no energetic incentive to either move toward or away, the equilibrium constant for the process can be calculated $K=k_1/k_{-1}$. Let us first imagine a scenario where there is no quenching, ($k_2=0$). This ought not to influence the diffusion coefficient of the excitons which will be a property of PTB7,

and will be entirely unaffected by the presence of quencher.

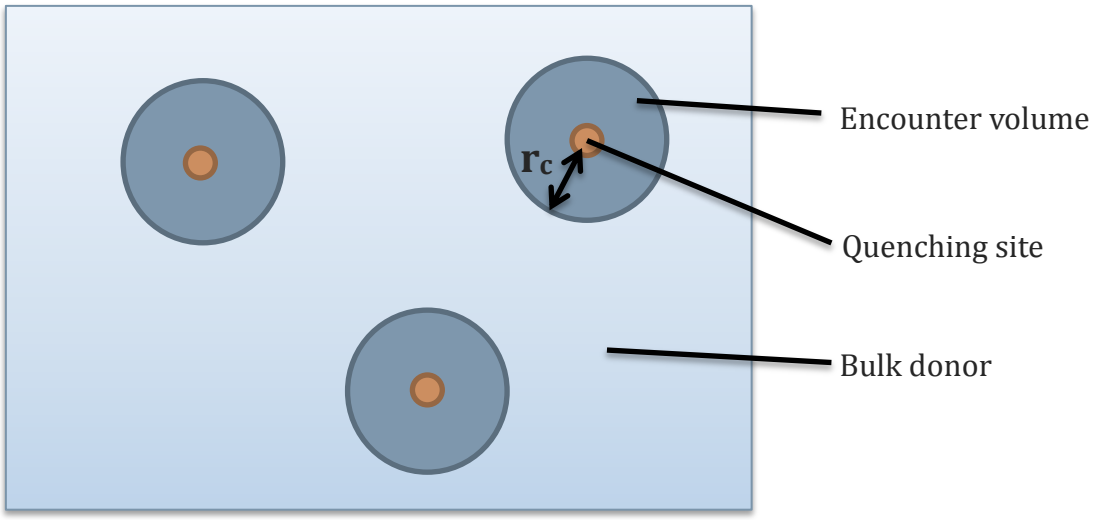

Figure 6.18. The diagram above illustrates a donor material with a small number of randomly distributed quenching sites, each of which are surrounded by a sphere, inside which excitons are considered close enough to undergo electron transfer.

In the scenario described the reaction scheme is best described as the following

EQUATION 6.15.

$$E + Q \underset{k_{-1}}{\overset{k_1}{\rightleftarrows}} E \cdot Q$$

As this is analogous to basic chemical equilibrium, the equilibrium constant can be written in terms of the equilibrium coefficient.

EQUATION 6.16.

$$\frac{k_1}{k_{-1}} = K = \frac{[E \cdot Q]_{eq}}{[E]_{eq}[Q]_{eq}}$$

Because an exciton has no energetic preference for being within r_c or further away from r_c, on a microscopic level the volume within this radius and bulk will have the same density of excitons. On the macroscopic level, this means that the relative concentrations of excitons inside and outside the encounter volume will be related to relative volume of the film within and without the encounter

radius r_c. If the total number of quenchers N_q is equal to [Q]V where V is the total volume of the film then

EQUATION 6.17.

$$K = \frac{V_q}{V}\frac{1}{[Q]_{eq}} = \frac{\frac{4}{3}\pi {r_c}^3 N_q}{V[Q]_{eq}} = \frac{4}{3}\pi {r_c}^3$$

The magnitude of r_c cannot be measured but can be estimated. Electron transfer processes are typically very short range, with lengthscales on the order of a few angstroms because the process requires wavefunction overlap between the donor and acceptor[87]. As r_c is a centre-to-centre distance the finite size of the donor and acceptor must also be taken into account. A C_{60} chromophore is approximately 0.5 nm in size[88]. If the distance for electron transfer and exciton radius is approximated as another 0.5 nm then r_c can be estimated as the sum of these radii, 1 nm which gives $K \approx 4.2$ nm^3. A critical radius of 1 nm, while an estimate, can be considered reasonably reliable for several reasons. The size of the fullerene is well known and rate of electron transfer is highly distance dependent, decaying with the wavefunction overlap betweenn the donor and the accepter within a few angstroms of separation (see section 6.5.3). The largest source of uncertainty is in the size of the exciton. Shaw *et al.*[110] found that the encounter distance between to excitons was ~2 nm, putting an upper limit on the excitons size as 1 nm.

6.5.3.3 *Expressing k_q in terms of k_1 and k_2*

As stated previously in this chapter, in order to comment on the rate constants of the intermediate processes of exciton diffusion and electron transfer, we must find a way of expressing the overall rate constant for the quenching

process in terms of k_1 and k_2. This is because k_q is the only experimentally accessible parameter. k_q is the rate constant for quenching of all excitons, excluding the natural decay, k_f. From equation 6.13, neglecting k_f, the following rates can be written

EQUATION 6.18.
$$\frac{d([E]+[E\cdot Q])}{dt} = -k_2[E\cdot Q]$$

EQUATION 6.19.
$$\frac{d[E\cdot Q]}{dt} = k_1[Q][E] - k_{-1}[E\cdot Q] - k_2[E\cdot Q]$$

If the quasi-steady-state approximation is applied to [E·Q]

EQUATION 6.20.
$$0 = k_1[Q][E] - k_{-1}[E\cdot Q] - k_2[E\cdot Q]$$

EQUATION 6.21.
$$[E\cdot Q] = \frac{k_1[Q][E]}{k_{-1}+k_2}$$

EQUATION 6.22.
$$\frac{d[E]}{dt} = -\frac{k_1k_2[Q][E]}{k_{-1}+k_2}$$

EQUATION 6.23.
$$\frac{d[E]}{dt} = -\frac{k_2k_1[Q][E]}{\frac{k_1}{K}+k_2}$$

EQUATION 6.24.
$$k_q(t) = -\frac{k_2k_1}{\frac{k_1}{K}+k_2}$$

To derive this equation it was necessary to apply the quasi-steady state approximation (QSSA). In the scheme as described in equation 6.13, the QSSA is valid if $[E]+[Q] \ll (k_2+k_{-1})/k_1$[89]. From the sub-picosecond lifetimes of device concentration PTB7:PCBM blends, we can infer that k_2 must be on the order of

1000 ns^{-1} or higher[79]. At its highest point, when t=0, the concentration of excitons is calculated as ~10^{-5} nm^{-3} , calculated from the photon flux and absorption of the film at the excitation wavelength. The concentration of quenching sites is constant at 5 × 10^{-3} nm^{-3}. We have previously shown that k_1/k_{-1} can be approximated as 4.2 nm^3, where the critical radius is 1 nm. Thus the QSSA is valid for all positive values of k_1. In other words, it is valid to approximate the system as being in quasi-steady-state if there is any exciton diffusion whatsoever.

6.5.3.4 *Time-dependence of the Rate of Quenching*

As discussed in section 6.5.3.1, the ln(PL ratio) shows a pronounced curvature meaning that the derivative, the rate constant of quenching, k_q, is time-dependent. Of the consecutive processes leading to quenching – the rate of diffusive transport and the rate of electron transfer – only the rate of diffusive transport can vary with time. The rate constant for electron transfer must be time independent; if driving force and distance for a given process is constant, and everything else remains the same, then the rate constant for electron transfer must also remain constant. Thus the time-dependent aspect of the quenching process can be confidently assigned to the rate at which the excitons are reaching the quenching site.

There are numerous examples of time-dependent diffusion across a range of different areas of science.

For biological processes, time-dependent diffusion controlled processes are typically explained with reference to a process that restricts the reactant from diffusing in a restricted volume (for example, chemical processes going on in a

micelle or protein[14,15,86]), or to diffusion occurring in just one or two dimensions, such as reactants diffusing along a membrane[90]. In addition if the solutions are saturated with inert obstacles, diffusion limited processes can develop a time-dependence in their rate constants[54,55]. For the time-dependent diffusion of excitons and charges in organic semiconductors, time dependence in the rate is typically assigned to a downhill diffusive processes such as dispersive diffusion[91-94], or 1 or 2 dimension or highly anisotropic diffusion[18-20]. A time-dependent rate constant may mean the process is not diffusive, for example a long-range process such as FRET harvesting the majority of the excitons[84,95]. Exciton harvesting by FRET is discussed at length in chapter 5, and has already been ruled out as a possible harvesting mechanism for these materials combinations in section 6.5.2.

A huge amount of early work on exciton diffusion in disordered semiconductors was performed by Prof. Heinz Bässler and co-workers using a range of modelling and experimental techniques. They found that time-dependence of diffusion can be described by a decaying power-law[92,93,96]. In the other mechanisms for time-dependent diffusion in biological systems power law decays are also typically used[14,86,64]. Thus to describe the unknown time-dependent diffusive process we will also use a power law decay;

EQUATION 6.25. $$k_1 = k_1' t^{-h}$$

In the equation above k_1' is a time-independent rate constant and the exponent, h, is restricted to values between 0 and 1. The scaling of the forward and the reverse rates has been shown to have the same time dependence for a diffusive process[86,97]. This means that k_{-1} can be considered to have the same time dependence as k_1.

Substituting equation 6.25 into equation 6.24 gives

EQUATION 6.26.

$$k_q(t) = \frac{k_1{}' k_2 t^{-h}}{\frac{k_1{}'}{K} t^{-h} + k_2}$$

Equation 6.26 has three unknown parameters, k_1, h and k_2 (if we calculate K using the method 6.5.3.2). k_1 and h will be common to all the different quencher concentrations as these will depend on the exciton diffusivity in PTB7. The rate constant of electron transfer, k_2, will depend the type of quencher used. From inspection of equation 6.26 it is clear that for very low values of k_2, $k_q(t)$ becomes approximately equal to Kk_2. This represents a regime where exciton diffusion no longer limits the rate. On the other hand when k_2 is very large, $k_q(t) \approx k_1 t^{-h}$, ie if k_2 is very large, the overall rate is entirely limited by the rate at which the excitons can arrive at the quenching sites due to exciton diffusion.

For the lowest non-zero rate shown in figure 6.17, that of quencher 9 (beige), the ln(PL ratio)/[Q] is highly linear and can be fitted using $k_q=Kk_2$ corresponding to the electron transfer limited regime. As the gradients of the ln(PL ratio)/[Q] lines in figure 6.17 increase, the time dependence becomes more and more prominent. The fastest quenching curves, corresponding to quenchers 5, 6 and 7, have close to identical ln(PL ratios). The simplest explanation for this very similar behaviour is that for the high rates of quenching, k_q has passed into the regime where quenching is diffusion limited. As the exciton diffusion is a property of PTB7, not the quencher, it would be no coincidence that the most quenched films would have very similar ln(PL decays). If the quenching in films with quenchers 5, 6 and 7 can be considered to be diffusion limited, then they can be fitted with k_q-

(t)=$k_1 t^{-h}$. The fit of this equation is the red line in figure 6.17 with best fits of k_1' = 9.1 $ps^{-0.66}$ and h = 0.44.

The values of $k_1$and h generated from this fit can then substituted back into equation 6.26, which can be fitted to the other films in figure 6.17, where each decay is fitted with a single free parameter, k_2. These fits are the black lines in figure 6.17. More detail on the fitting procedure and examples of miss-fits are given in section 6.5.4.2.

6.5.4 Discussion of the rates of electron transfer

In the previous section we outlined a model which allowed the rate constant for the diffusive process to be distinguished from the rate constant of the electron transfer process. The values of k_2 were calculated from fits to the ln(PL Ratios)/[Q] in figure 6.17 as described in the previous section. These values for the different films are plotted against the driving force below.

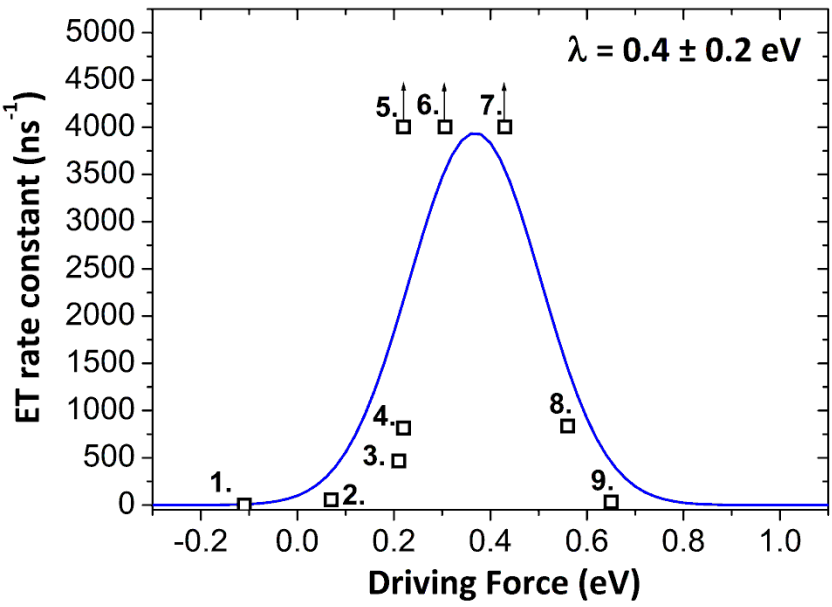

Figure 6.19. The rate constant for electron transfer plotted against the driving force for acceptors 1–9. Points 5-7 have arrows denoting that they are lower limits.

6.5.4.1 Discussion of the Energetic Driving Force Calculation

The energetic driving force for electron transfer was estimated from the difference in the electron affinities of the donor and acceptor states minus the difference in binding energies between the polymer exciton and the charge pair created after electron transfer ($\Delta G^0 = EA_A - EA_B - \Delta E_b$).The electron affinities of PTB7 and the acceptors 1–9 measured by our collaborators, Graeme Cooke and co-workers using square wave voltammetry-derived reduction potentials. Using this method it was found the EA_{PTB7} was 3.18 eV and the EA of the acceptors are listed in figure 6.11. The change in binding energy, ΔE_b was estimated as 0.3±0.2 eV. This parameter was estimated from typically reported values of exciton binding energies of 0.4-0.7 eV found in conjugated polymer films [98-101] minus typical CT binding energies of 0.15 eV[102]. Note that ΔE_b is hard to estimate and the large error bounds represent the dominant error in the measurement. In any case, the systematic error introduced will alter the absolute values of the driving force but will not affect the overall conclusions of this section.

It is well known that the electron affinities calculated from a solution measurement can be quite different from those calculated in the film, because the surrounding π-conjugation in the film can polarise to stabilise an introduced charge, thus lowering the energy[103]. In this case, both the donor and the acceptor EAs were measured in solution and the relevant parameter is the offset between the two. During a photoluminescence quenching measurement both the donor and acceptor ought to be in the same environment; totally surrounded by PTB7 molecules. Thus the stabilisation due to surrounding π conjugation, ought be the same for both chromophores. This being the case, when the difference of the

electron affinities is taken to calculate the driving force, these errors will cancel, and thus polarisation effects can be neglected.

6.5.4.2 Discussion of Rates for the Diffusion Limited Quenchers

In section 6.5.3.4, in is argued that the overall rate constant, k_q, for the three most effective quenching sites is limited by diffusion. In this regime, k_q will be dictated entirely by the rate constant by which excitons arrive at the quencher, $k_1 t^{-h}$. The simulated value of k_q is plotted below, using the values derived from fits measured to the highest three quenchers.

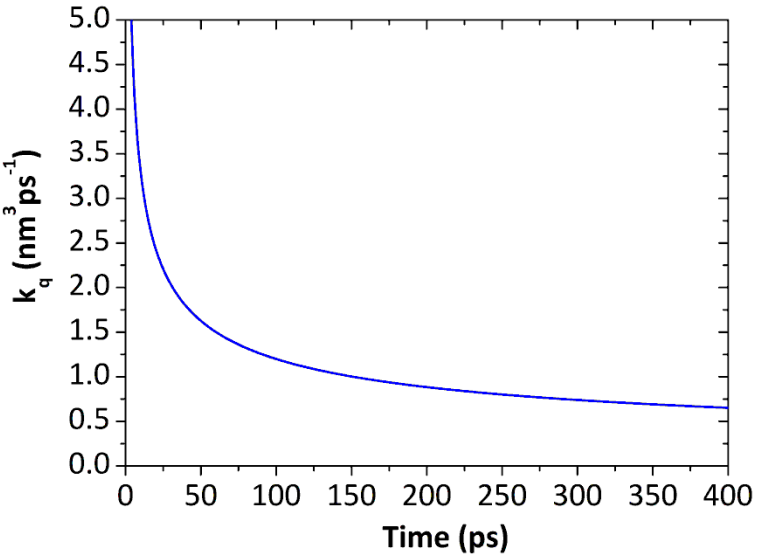

Figure 6.20. The modelled rate of quenching using $k_q=k_1't^{-h}$ with values of k_1' and h calculated from the fit to the most efficient quenchers in figure 6.17.

Above, the simulated k_q is equal to 4.5 nm^3ps^{-1} at 5 ps and drops to 0.65 nm^3ps^{-1} at 400 ps. It is important to note that k_q is a bimolecular rate constant (see equation 6.13). As [Q] is constant during the process, at 0.005 nm^{-3}, these values can be converted into a monomolecular rate constant that corresponds to lifetimes of 44 ps through to 308 ps; far from being instrument limited.

In order for these highest decays to be exciton diffusion limited, it is necessary for the following inequality to be true (from equation 6.26)

EQUATION 6.27. $$\frac{k_1'}{K} t^{-h} \ll k_2$$

This is the intuitive deduction that for excitons to be diffusion limited, the rate constant for excitons near the quencher to be quenched must be much greater than the rate constant for excitons near the quencher to move back into the bulk material. In other words, once the excitons get within the critical radius, the quencher must act as a perfectly absorbing surface.

Because the rate of electron transfer is not a limiting factor in the rate of PL quenching in these films, values for k_2 cannot be generated. On the other hand, because of the inequality in the previous paragraph (equation 6.27), if the decays are truly exciton diffusion limited, then approximate lower limits of k_2 can be calculated. In order to calculate the lower limit of k_2 for the highest concentration quenchers, we can take the left hand side of the inequality labelled as equation 6.27, when it is near its peak but outside the instrument response function, at 10 ps. This corresponds to $k_1't^{-h}/K \approx 0.79$ ps^{-1}, if we consider much greater than to be at least 5 times greater than, then this give a lower limit of approximately 4 ps^{-1}. We can check this by plotting equation 6.26 with varying values of k_2 to how much having finite values of k_2 perturbs the fit. These modelled decays and the average ln(PL decay)/[Q] for the fastest three quenchers (red data points) is shown in figure 6.21, on the following page.

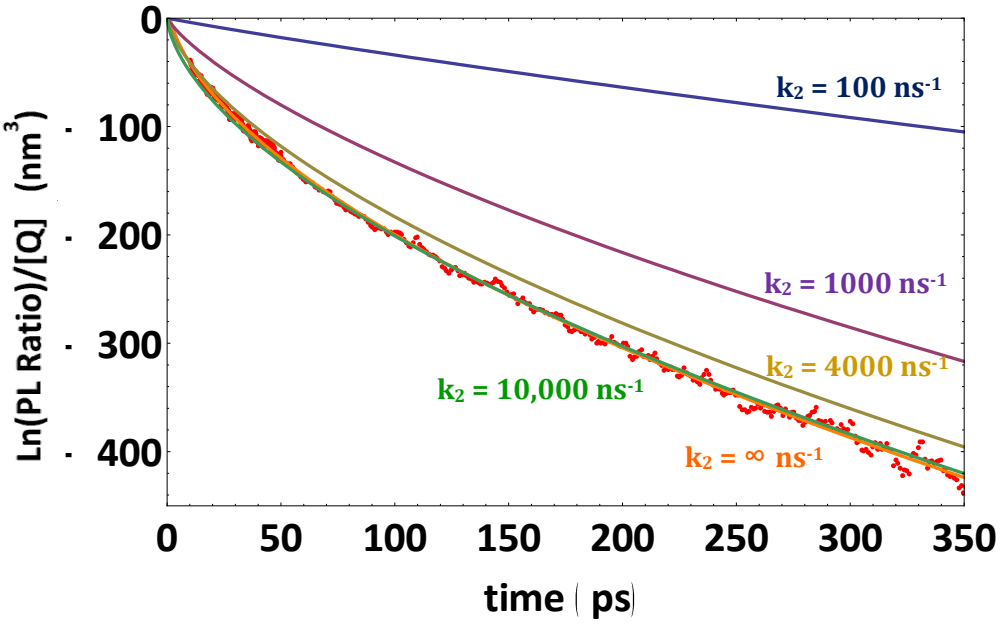

Figure 6.21. Equation 6.24 is plotted with varying values of k_2 to estimate lower limits for k_2 if the system is truly diffusion limited.

It is clear from the graph above that extremely high values of the rate constant are required for the model to fit the data for the most efficient quenching blends. This means that for the system to be in the regime where the rate of fluorescence quenching is entirely dictated by the rate at which excitons are arriving at the quenching site, high values of k_2 are required . From the diagram it is clear that the lower limit of $k_2 > 4000$ ns^{-1} assumed for the purposes of this chapter, is a very cautious lower limit, and it may well be much higher. In figure 6.19, quenchers 5, 6 and 7 marked on the diagram with this lower limit of 4000 ns^{-1} but have arrows indicating these values are lower limits.

It is important to note that this rate constant does not apply to the total population of excitons, just to the excitons in the vicinity to the quenching site. Thus it is not appropriate to take the inverse rate and equate that to the blend lifetime as could be done for a simple single-stage monomolecular process. Thus to say that ¼ ps is at a shorter timescale than the response of the instrument, which

has a breadth of ~3 ps does not undermine the rate constants calculated. Imagine that there was blend with a concentration of 0.005 nm^{-3} of quenching sites and the rate of electron transfer within 1 nm of a quenching site was 4 ps^{-1}. Even if exciton diffusion was infinite, the lifetime of the film would not be 250 fs, because this rate constant (k_2) only applies to excitons within 1 nm of each quenching site. In this particular case the lifetime would be approximately equal to $1/Kk_2[Q]$ = 13 ps (see equation 6.26). Actual films were diffusion limited so had longer lifetimes than this.

A useful observation made along similar lines is that if the entire film was within a critical radius of a quenching site, the lifetime must be at most ¼ ps (250 fs). This happens when the concentration of quenching sites is equal to $1/(4/3\pi r_c^3)$. This occurs at very approximately 40% mass ratio of C_{71}-PCBM. This observation agrees well with the reported PL lifetime of the 60 wt% blend, in which the majority of the signal decayed with a lifetime of 100 fs[79,104].

6.5.4.3 Interpretation of the Trend in Electron Transfer Rate Constant

It can be seen in figure 6.19 that the rate of electron transfer, k_2, increases with increasing energetic driving force, until it reaches a maximum at approximately 0.4 eV before decreasing again. The energetic driving force of 0.4 eV corresponds to an activation energy offset of 0.6 eV which represents the lowest point of figure 6.15. This behaviour is characteristic of Marcus theory (see section 6.4.2) and similar trends have been attributed to Marcus theory in the relative yields of free carriers in donor-acceptor blends[62].

The lower limit for the rate constant of the fastest three acceptors is 4000 ns^{-1}. This is rather high for a photoinduced electron transfer process[27] which are

typically between 1–1,000 ns^{-1}. It is however within the range of electron transfer rate constants reported in the literature for organic solar cell materials which tend to be very rapid, having been optimised to separate charges and generate photocurrent. The rate is still consistant with Marcus theory because a typical molecular vibration with an IR absorption at 1000 cm^{-1} would have a frequency of ~30,000 ns^{-1} and thus our maximum rate does not exceed the rate of molecule vibration. A system undergoing electron transfer in the strong coupling regime is typically reported[45] to have a pre-exponential factor that is 1000-10,000 ns^{-1}.

In solar cell materials the rate of electron transfer has been reported as 100 ns^{-1} for transfer between a thiophene oligomer and a covalently bonded fullerene[105] and 80 ns^{-1} for electron transfer in a similar experiment between a phenylene vinylene oligomer and a covalently bound fullerene[106]. That the rate of electron transfer between the exciton and C_{71}-PCBM is extremely rapid is of no surprise, as the fluorescence in device blends of 60wt% fullerene failed to detect any fluorescence from PTB7 using femtosecond optical gating techniques, indicating that the lifetime of excitons in the blends is much less than the instrument response of these measurements, 100 fs[79]. In these device concentration blends we can predict the lifetime using the following, derived from the limit of equation 6.26, assuming that the fullerene sites are evenly distributed and exciton diffusion does not limit the rate.

EQUATION 6.28. $$\tau_{Blend} \approx \frac{1}{[Q]Kk_2}$$

At 60 wt% the fullerene will have an approximate concentration of 0.4 nm^{-3} while k will be approximately equal to 4.2 nm^3 and k_2 will have a lower bound of

4000 ns^{-1}. This gives a maximum blend lifetime of 150 fs which agrees well with our own measurement of the same material[79].

Equation 6.11 was fitted to the rate constants of electron transfer (blue line in figure 6.19). The only free parameter in this fit was the reorganisation energy, λ, which was found to be 0.4 ± 0.2 eV. These large error bars represent the uncertainty in the driving force as described in section 6.5.4.1. That the breadth and position of the Gaussian is determined by a single free parameter and such a simple model fits well is extremely encouraging. The value of 0.4 eV is fairly small, and is comparable to the reorganisation energy measured for another solar cell material, Si-PCPDTBT to a variety of fullerene derivatives[107] which had reorganisation energies of 0.22-0.27 eV. Additionally Coffey *et al.* found values of 0.4 eV to 0.8 eV for blue absorbing PPV derivatives when they investigated the yield of free charges in blends with a variety of fluorinated fullerene derivatives[62]. At 0.4 eV, the reorganisation energy for PTB7 measured in this chapter was at the lower end of the reported reorganisation energies which is one possible explanation as to why PTB7 is such a highly efficient photovoltaic donor material.

As discussed in 6.2.4 it has been suggested by Savoie *et al.* and others[63] that exciton harvesting may occur through hot, vibronically excited excitons undergoing electron tranfer to a wide variety of acceptor cluster states. If the exciton is hot, then the predictions of the Arrhenius equation (equation 6.3) will be invalid. This failure is because the Arrhenius equation is only valid to describe systems at thermal equilibrium, because it is based on Boltzmann statistics. As the Arrhenius equation is not valid, any rates derived from the activation energy, such as those calculated from Marcus theory, will not be valid. As thermal equilibrium will be

reached extremely rapidly this resonant electron transfer must occur extremely quickly, on a sub-ps timescale[70]. In the model system discussed in this chapter, the low concentration of acceptor means that the majority of excitons are harvested in tens to hundreds of picoseconds so are thermally equilibrated when harvested. In addition the presence of the Marcus inverted region indicates that the electron transfer is not to a distribution of acceptor levels or band state. It is thus an interesting observation that in this situation, where hot, coherent harvesting is forbidden, we still see extremely rapid rate constants of 4000 ns^{-1} for the most effective quenchers. This suggests that the ultrafast behaviour can be explained without introducing the added complication of hot excitons or a distribution of delocalised or crystallite acceptor states.

The reorganisation energy is a very important parameter for several critical processes that contribute to the functioning of organic solar cells. Creating a material with the minimum possible reorganisation energy will mean that a smaller energetic offset between the donor and acceptor electron affinities is required for rapid charge separation. This will result in smaller thermalisation losses and higher power conversion efficiencies. The second process in which the reorganisation energy plays an important role is in charge transport[108]. This is because charge transport consists of a series of incoherent hopping steps and the activation energy for such hops will be related to the reorganisation energy. Thus charge transport could be considered to be a series of near isoenergetic hops (with a small driving force provided by the built-in or applied electric field).

On the other hand, having a small reorganisation energy does have the disadvantage that a relatively narrow range of driving forces will then lead to rapid

electron transfer. This is because a smaller reorganisation energy would narrow the Gaussian in figure 6.19, meaning that fewer of the acceptors would be suitable as the corresponding acceptor in a bulk heterojunction. For PTB7 it is fortuitous that C_{71}-PCBM falls within this narrow ~0.2 eV electron affinity window meaning it is a suitable acceptor. For many polymers this may not be the case, and promising leads for new solar cell material may be missed due to an electron affinity mismatch. Of course the acceptor that does have the correct electron affinity must also have the same high charge transport properties as a fullerene and form the correct morphology in the photovoltaic blend in order to make an efficient device.

6.6. CONCLUSIONS

In this chapter the diffusion of excitons in a high performance photovoltaic material, PTB7, was investigated using two techniques, fluorescence depolarisation and volume quenching. The two measurement techniques gave quite different exciton diffusion coefficients and it was concluded that the most likely explanation for the time-dependence in the rate of quenching and the prolonged fluorescence anisotropy was that there was some degree of molecular ordering within the film. This explanation is not comprehensive and a program of further work was outlined which would clear up any uncertainty about the movement of the excitons in this material.

The theory of photoinduced electron transfer in organic solar cells was then discussed with particular emphasis on Marcus theory, and novel electron transfer theories in the literature were discussed. By investigating the photoluminescence kinetics of blends of PTB7 with a variety of electron acceptors with differing

electron affinities, it was found that the rate of exciton harvesting strongly depends on how much of an energetic driving force is provided by the electron affinity offset between the two components of the blend. It was found that the optimum electron affinity offset was at 0.6 eV for PTB7 which corresponds to the acceptor with the highest efficiency reported in a single junction photovoltaic blend, C_{71}PCBM. As the trend in the rates of electron transport followed an approximately Gaussian distribution, they were interpreted through Marcus theory and a reorganisation energy of 0.4 ± 0.2 eV was calculated. This small reorganisation energy and the fact it is well matched to C_{71}-PCBM is a possible explanation for the extremely short, <100 fs, lifetime of PTB7 excitons in photovoltaic blends and thus may contribute to the high solar cell performances. This is because a small reorganisation energy allows a smaller driving force to separate charges and hence allows for lower voltage losses; the highest efficiency P3HT devices (PCE 6.43%) experience voltage losses (E_g-V_{OC}) of 1.4 eV[109] in comparison to PTB7 devices which experience equivalent losses of just 1.1 eV[2].

6.7. REFERENCES

1 Liang, Y. *et al.* For the Bright Future—Bulk Heterojunction Polymer Solar Cells with Power Conversion Efficiency of 7.4%. *Advanced Materials* **22**, E135-E138, doi:10.1002/adma.200903528 (2010).

2 He, Z. *et al.* Enhanced power-conversion efficiency in polymer solar cells using an inverted device structure. *Nat Photon* **6**, 591-595, doi:http://www.nature.com/nphoton/journal/v6/n9/abs/nphoton.2012.190.html#supplementary-information (2012).

3 Weber, G. in *Advances in Protein Chemistry* Vol. Volume 8 (eds Kenneth Bailey M.L. Anson & T. Edsall John) 415-459 (Academic Press, 1953).

4 Bjorklund, T. G., Lim, S.-H. & Bardeen, C. J. Use of Picosecond Fluorescence Dynamics as an Indicator of Exciton Motion in Conjugated Polymers: Dependence on Chemical Structure and Temperature. *The Journal of Physical Chemistry B* **105**, 11970-11977, doi:10.1021/jp0124746 (2001).

5 Gulbinas, V. *et al.* Exciton diffusion and relaxation in methyl-substituted polyparaphenylene polymer films. *The Journal of Chemical Physics* **127**, -, doi:doi:http://dx.doi.org/10.1063/1.2790901 (2007).

6 Matheson, A. B., Pearson, S. J., Ruseckas, A. & Samuel, I. D. W. Charge Pair Dissociation and Recombination Dynamics in a P3HT–PC60BM Bulk Heterojunction. *The Journal of Physical Chemistry Letters* **4**, 4166-4171, doi:10.1021/jz4020426 (2013).

7 Ruseckas, A. *et al.* Ultrafast depolarization of the fluorescence in a conjugated polymer. *Physical Review B* **72**, 115214 (2005).

8 Ruseckas, A. & Samuel, I. D. W. Exciton self-trapping in MEH-PPV films studied by ultrafast emission depolarization. *physica status solidi (c)* **3**, 263-266, doi:10.1002/pssc.200562715 (2006).

9 Grage, M. M.-L. *et al.* Conformational disorder and energy migration in MEH-PPV with partially broken conjugation. *The Journal of Chemical Physics* **118**, 7644-7650, doi:doi:http://dx.doi.org/10.1063/1.1562190 (2003).

10 Hammond, M. R. *et al.* Molecular Order in High-Efficiency Polymer/Fullerene Bulk Heterojunction Solar Cells. *ACS Nano* **5**, 8248-8257, doi:10.1021/nn202951e (2011).

11 Kinosita Jr, K., Kawato, S. & Ikegami, A. A theory of fluorescence polarization decay in membranes. *Biophysical Journal* **20**, 289-305, doi:http://dx.doi.org/10.1016/S0006-3495(77)85550-1 (1977).

12 Lipari, G. & Szabo, A. Effect of librational motion on fluorescence depolarization and nuclear magnetic resonance relaxation in macromolecules and membranes. *Biophysical Journal* **30**, 489-506, doi:http://dx.doi.org/10.1016/S0006-3495(80)85109-5 (1980).

13 Valeur, B. in *Molecular Fluorescence* 125-154 (Wiley-VCH Verlag GmbH, 2001).

14 Dewey, T. G. Fractal analysis of proton exchange kinetics in lysozyme. *Proceedings of the National Academy of Sciences* **91**, 12101-12104 (1994).

15 Kosmidis, K., Karalis, V., Argyrakis, P. & Macheras, P. Michaelis-Menten Kinetics under Spatially Constrained Conditions: Application to Mibefradil Pharmacokinetics. *Biophysical Journal* **87**, 1498-1506, doi:http://dx.doi.org/10.1529/biophysj.104.042143 (2004).

16 Dorsaz, N., De Michele, C., Piazza, F., De Los Rios, P. & Foffi, G. Diffusion-Limited Reactions in Crowded Environments. *Physical Review Letters* **105**, 120601 (2010).
17 Mourao, M., Kreitman, D. & Schnell, S. Unravelling the impact of obstacles in diffusion and kinetics of an enzyme catalysed reaction. *Physical Chemistry Chemical Physics* **16**, 4492-4503, doi:10.1039/c3cp52417e (2014).
18 Tamai, Y., Matsuura, Y., Ohkita, H., Benten, H. & Ito, S. One-Dimensional Singlet Exciton Diffusion in Poly(3-hexylthiophene) Crystalline Domains. *The Journal of Physical Chemistry Letters* **5**, 399-403, doi:10.1021/jz402299a (2014).
19 Masri, Z. *et al.* Molecular Weight Dependence of Exciton Diffusion in Poly(3-hexylthiophene). *Advanced Energy Materials* **3**, 1445-1453, doi:10.1002/aenm.201300210 (2013).
20 Markov, D. E. & Blom, P. W. M. Anisotropy of exciton migration in poly(p-phenylene vinylene). *Physical Review B* **74**, 085206 (2006).
21 Marcus, R. A. On the Theory of Oxidation-Reduction Reactions Involving Electron Transfer. I. *The Journal of Chemical Physics* **24**, 966-978, doi:doi:http://dx.doi.org/10.1063/1.1742723 (1956).
22 Marcus, R. A. Electron transfer reactions in chemistry. Theory and experiment. *Reviews of Modern Physics* **65**, 599-610 (1993).
23 Heller, B., Holten, D. & Kirmaier, C. Control of electron transfer between the L- and M-sides of photosynthetic reaction centers. *Science* **269**, 940-945, doi:10.1126/science.7638616 (1995).
24 Martin, J.-L., Breton, J., Hoff, A. J., Migus, A. & Antonetti, A. Femtosecond spectroscopy of electron transfer in the reaction center of the photosynthetic bacterium Rhodopseudomonas sphaeroides R-26: Direct electron transfer from the dimeric bacteriochlorophyll primary donor to the bacteriopheophytin acceptor with a time constant of 2.8 ± 0.2 psec. *Proceedings of the National Academy of Sciences* **83**, 957-961 (1986).
25 Moser, C. C., Keske, J. M., Warncke, K., Farid, R. S. & Dutton, P. L. Nature of biological electron transfer. *Nature* **355**, 796-802 (1992).
26 Stowell, M. H. B. *et al.* Light-Induced Structural Changes in Photosynthetic Reaction Center: Implications for Mechanism of Electron-Proton Transfer. *Science* **276**, 812-816, doi:10.1126/science.276.5313.812 (1997).
27 Wasielewski, M. R. Photoinduced electron transfer in supramolecular systems for artificial photosynthesis. *Chemical Reviews* **92**, 435-461, doi:10.1021/cr00011a005 (1992).
28 Imahori, H. & Sakata, Y. Fullerenes as Novel Acceptors in Photosynthetic Electron Transfer. *European Journal of Organic Chemistry* **1999**, 2445-2457, doi:10.1002/(sici)1099-0690(199910)1999:10<2445::aid-ejoc2445>3.0.co;2-g (1999).
29 GUST, D. & MOORE, T. A. Mimicking Photosynthesis. *Science* **244**, 35-41, doi:10.1126/science.244.4900.35 (1989).
30 Ferraris, J., Cowan, D. O., Walatka, V. & Perlstein, J. H. Electron transfer in a new highly conducting donor-acceptor complex. *Journal of the American Chemical Society* **95**, 948-949, doi:10.1021/ja00784a066 (1973).
31 Brédas, J. L., Calbert, J. P., da Silva Filho, D. A. & Cornil, J. Organic semiconductors: A theoretical characterization of the basic parameters

governing charge transport. *Proceedings of the National Academy of Sciences* **99**, 5804-5809, doi:10.1073/pnas.092143399 (2002).
32 Franck, J. & Dymond, E. G. Elementary processes of photochemical reactions. *Transactions of the Faraday Society* **21**, 536-542, doi:10.1039/tf9262100536 (1926).
33 Condon, E. U. Nuclear Motions Associated with Electron Transitions in Diatomic Molecules. *Physical Review* **32**, 858-872 (1928).
34 Born, M. & Oppenheimer, R. Zur Quantentheorie der Molekeln. *Annalen der Physik* **389**, 457-484, doi:10.1002/andp.19273892002 (1927).
35 Reichenbächer, M. P., Jürgen. (Springer, 2012).
36 Morse, P. M. Diatomic Molecules According to the Wave Mechanics. II. Vibrational Levels. *Physical Review* **34**, 57-64 (1929).
37 Uzer, T., Noid, D. W. & Marcus, R. A. Uniform semiclassical theory of avoided crossings. *The Journal of Chemical Physics* **79**, 4412-4425, doi:doi:http://dx.doi.org/10.1063/1.446326 (1983).
38 Barbara, P. F., Meyer, T. J. & Ratner, M. A. Contemporary Issues in Electron Transfer Research. *The Journal of Physical Chemistry* **100**, 13148-13168, doi:10.1021/jp9605663 (1996).
39 Zhao, Y. & Liang, W. Charge transfer in organic molecules for solar cells: theoretical perspective. *Chemical Society Reviews* **41**, 1075-1087, doi:10.1039/c1cs15207f (2012).
40 Skourtis, S. S., Beratan, D. N. & Waldeck, D. H. Coherence in electron transfer pathways. *Procedia Chemistry* **3**, 99-104, doi:http://dx.doi.org/10.1016/j.proche.2011.08.016 (2011).
41 Dorner, R., Goold, J., Heaney, L., Farrow, T. & Vedral, V. Effects of quantum coherence in metalloprotein electron transfer. *Physical Review E* **86**, 031922 (2012).
42 Wynne, K., Reid, G. D. & Hochstrasser, R. M. Vibrational coherence in electron transfer: The tetracyanoethylene–pyrene complex. *The Journal of Chemical Physics* **105**, 2287-2297, doi:doi:http://dx.doi.org/10.1063/1.472097 (1996).
43 Likhtenshtein, G. in *Solar Energy Conversion* 1-44 (Wiley-VCH Verlag GmbH & Co. KGaA, 2012).
44 German, E. D. & Kuznetsov, A. M. Quantum Mechanical Theory of Dissociative Electron Transfer in Polar Solvents. *The Journal of Physical Chemistry* **98**, 6120-6127, doi:10.1021/j100075a014 (1994).
45 Koslowski, T., Burggraf, F., Krapf, S., Steinbrecher, T. & Wittekindt, C. Recent progress in biological charge transfer: Theory and simulation. *Biochimica et Biophysica Acta (BBA) - Bioenergetics* **1817**, 1955-1957, doi:http://dx.doi.org/10.1016/j.bbabio.2012.02.025 (2012).
46 Rehm, D. & Weller, A. Kinetics of Fluorescence Quenching by Electron and H-Atom Transfer. *Israel Journal of Chemistry* **8**, 259-271, doi:10.1002/ijch.197000029 (1970).
47 Bock, C. R., Meyer, T. J. & Whitten, D. G. Photochemistry of transition metal complexes. Mechanism and efficiency of energy conversion by electron-transfer quenching. *Journal of the American Chemical Society* **97**, 2909-2911, doi:10.1021/ja00843a055 (1975).

48 Nagle, J. K., Dressick, W. J. & Meyer, T. J. Electron-transfer reactions in the "abnormal" free-energy region. *Journal of the American Chemical Society* **101**, 3993-3995, doi:10.1021/ja00508a062 (1979).
49 Scheerer, R. & Graetzel, M. Laser photolysis studies of duroquinone triplet state electron transfer reactions. *Journal of the American Chemical Society* **99**, 865-871, doi:10.1021/ja00445a032 (1977).
50 Miller, J. R., Calcaterra, L. T. & Closs, G. L. Intramolecular long-distance electron transfer in radical anions. The effects of free energy and solvent on the reaction rates. *Journal of the American Chemical Society* **106**, 3047-3049, doi:10.1021/ja00322a058 (1984).
51 Closs, G. L., Calcaterra, L. T., Green, N. J., Penfield, K. W. & Miller, J. R. Distance, stereoelectronic effects, and the Marcus inverted region in intramolecular electron transfer in organic radical anions. *The Journal of Physical Chemistry* **90**, 3673-3683, doi:10.1021/j100407a039 (1986).
52 Newton, M. D. Quantum chemical probes of electron-transfer kinetics: the nature of donor-acceptor interactions. *Chemical Reviews* **91**, 767-792, doi:10.1021/cr00005a007 (1991).
53 Perkins, T. A., Hauser, B. T., Eyler, J. R. & Schanze, K. S. Photoinduced organic donor to metal electron transfer across a rigid spacer. *The Journal of Physical Chemistry* **94**, 8745-8748, doi:10.1021/j100388a001 (1990).
54 Chen, K.-Y., Chow, T. J., Chou, P.-T., Cheng, Y.-M. & Tsai, S.-H. Photoinduced electron transfer reactions across rigid linear spacer groups of high symmetry. *Tetrahedron Letters* **43**, 8115-8119, doi:http://dx.doi.org/10.1016/S0040-4039(02)01917-2 (2002).
55 Ikemoto, J. *et al.* Porphyrin−Oligothiophene−Fullerene Triads as an Efficient Intramolecular Electron-Transfer System. *Organic Letters* **4**, 309-311, doi:10.1021/ol016511n (2002).
56 Sachs, S. B. *et al.* Rates of Interfacial Electron Transfer through π-Conjugated Spacers. *Journal of the American Chemical Society* **119**, 10563-10564, doi:10.1021/ja972244y (1997).
57 Guldi, D. M., Illescas, B. M., Atienza, C. M., Wielopolski, M. & Martin, N. Fullerene for organic electronics. *Chemical Society Reviews* **38**, 1587-1597, doi:10.1039/b900402p (2009).
58 Göransson, E. *et al.* Long-Range Electron Transfer in Zinc-Phthalocyanine-Oligo(Phenylene-ethynylene)-Based Donor-Bridge-Acceptor Dyads. *Inorganic Chemistry* **51**, 11500-11512, doi:10.1021/ic3013552 (2012).
59 Joran, A. D. *et al.* Effect of exothermicity on electron transfer rates in photosynthetic molecular models. *Nature* **327**, 508-511 (1987).
60 Lambert, C., Noll, G. & Schelter, J. Bridge-mediated hopping or superexchange electron-transfer processes in bis(triarylamine) systems. *Nat Mater* **1**, 69-73, doi:http://www.nature.com/nmat/journal/v1/n1/suppinfo/nmat706_S1.html (2002).
61 Beitz, J. V. & Miller, J. R. Exothermic rate restrictions on electron transfer in a rigid medium. *The Journal of Chemical Physics* **71**, 4579-4595, doi:doi:http://dx.doi.org/10.1063/1.438211 (1979).

62 Coffey, D. C. *et al.* An Optimal Driving Force for Converting Excitons into Free Carriers in Excitonic Solar Cells. *The Journal of Physical Chemistry C* **116**, 8916-8923, doi:10.1021/jp302275z (2012).
63 Savoie, B. M. *et al.* Unequal Partnership: Asymmetric Roles of Polymeric Donor and Fullerene Acceptor in Generating Free Charge. *Journal of the American Chemical Society*, doi:10.1021/ja411859m (2014).
64 Bakulin, A. A. *et al.* The Role of Driving Energy and Delocalized States for Charge Separation in Organic Semiconductors. *Science* **335**, 1340-1344, doi:10.1126/science.1217745 (2012).
65 Kaake, L. G., Moses, D. & Heeger, A. J. Coherence and Uncertainty in Nanostructured Organic Photovoltaics. *The Journal of Physical Chemistry Letters* **4**, 2264-2268, doi:10.1021/jz4010569 (2013).
66 Cook, S., Katoh, R. & Furube, A. Ultrafast Studies of Charge Generation in PCBM:P3HT Blend Films following Excitation of the Fullerene PCBM. *The Journal of Physical Chemistry C* **113**, 2547-2552, doi:10.1021/jp8050774 (2009).
67 Howard, I. A., Mauer, R., Meister, M. & Laquai, F. Effect of Morphology on Ultrafast Free Carrier Generation in Polythiophene:Fullerene Organic Solar Cells. *Journal of the American Chemical Society* **132**, 14866-14876, doi:10.1021/ja105260d (2010).
68 Brabec, C. J. *et al.* Tracing photoinduced electron transfer process in conjugated polymer/fullerene bulk heterojunctions in real time. *Chemical Physics Letters* **340**, 232-236, doi:http://dx.doi.org/10.1016/S0009-2614(01)00431-6 (2001).
69 Scheblykin, I. G., Yartsev, A., Pullerits, T., Gulbinas, V. & Sundström, V. Excited State and Charge Photogeneration Dynamics in Conjugated Polymers. *The Journal of Physical Chemistry B* **111**, 6303-6321, doi:10.1021/jp068864f (2007).
70 Grancini, G. *et al.* Hot exciton dissociation in polymer solar cells. *Nat Mater* **12**, 29-33, doi:http://www.nature.com/nmat/journal/v12/n1/abs/nmat3502.html#supplementary-information (2013).
71 Park, S. H. *et al.* Bulk heterojunction solar cells with internal quantum efficiency approaching 100%. *Nat Photon* **3**, 297-302, doi:http://www.nature.com/nphoton/journal/v3/n5/suppinfo/nphoton.2009.69_S1.html (2009).
72 Sun, Y. *et al.* Efficient, Air-Stable Bulk Heterojunction Polymer Solar Cells Using MoOx as the Anode Interfacial Layer. *Advanced Materials* **23**, 2226-2230, doi:10.1002/adma.201100038 (2011).
73 Zhao, G., He, Y. & Li, Y. 6.5% Efficiency of Polymer Solar Cells Based on poly(3-hexylthiophene) and Indene-C60 Bisadduct by Device Optimization. *Advanced Materials* **22**, 4355-4358, doi:10.1002/adma.201001339 (2010).
74 Koppe, M. *et al.* Near IR Sensitization of Organic Bulk Heterojunction Solar Cells: Towards Optimization of the Spectral Response of Organic Solar Cells. *Advanced Functional Materials* **20**, 338-346, doi:10.1002/adfm.200901473 (2010).

75 Janssen, R. A. J. & Nelson, J. Factors Limiting Device Efficiency in Organic Photovoltaics. *Advanced Materials* **25**, 1847-1858, doi:10.1002/adma.201202873 (2013).
76 Mikhnenko, O. V. *et al.* Exciton diffusion length in narrow bandgap polymers. *Energy & Environmental Science* **5**, 6960-6965 (2012).
77 Mikhnenko, O. V. *et al.* Trap-Limited Exciton Diffusion in Organic Semiconductors. *Advanced Materials*, n/a-n/a, doi:10.1002/adma.201304162 (2013).
78 Ruseckas, A., Shaw, P. E. & Samuel, I. D. W. Probing the nanoscale phase separation in binary photovoltaic blends of poly(3-hexylthiophene) and methanofullerene by energy transfer. *Dalton Transactions*, 10040-10043 (2009).
79 Hedley, G. J. *et al.* Determining the optimum morphology in high-performance polymer-fullerene organic photovoltaic cells. *Nat Commun* **4**, doi:10.1038/ncomms3867 (2013).
80 Muntwiler, M., Yang, Q., Tisdale, W. A. & Zhu, X. Y. Coulomb Barrier for Charge Separation at an Organic Semiconductor Interface. *Physical Review Letters* **101**, 196403 (2008).
81 Baranovskii, S. D., Wiemer, M., Nenashev, A. V., Jansson, F. & Gebhard, F. Calculating the Efficiency of Exciton Dissociation at the Interface between a Conjugated Polymer and an Electron Acceptor. *The Journal of Physical Chemistry Letters* **3**, 1214-1221, doi:10.1021/jz300123k (2012).
82 Clarke, T. M. & Durrant, J. R. Charge Photogeneration in Organic Solar Cells. *Chemical Reviews* **110**, 6736-6767, doi:10.1021/cr900271s (2010).
83 Coffey, D. C., Ferguson, A. J., Kopidakis, N. & Rumbles, G. Photovoltaic Charge Generation in Organic Semiconductors Based on Long-Range Energy Transfer. *ACS Nano* **4**, 5437-5445, doi:10.1021/nn101106b (2010).
84 Ward, A. J., Ruseckas, A. & Samuel, I. D. W. A Shift from Diffusion Assisted to Energy Transfer Controlled Fluorescence Quenching in Polymer–Fullerene Photovoltaic Blends. *The Journal of Physical Chemistry C* **116**, 23931-23937, doi:10.1021/jp307538y (2012).
85 Jordan, P. C. *Chemical Kinetics and Transport*. (Plenum Press, 1979).
86 Dewey, T. *Fractals in Molecular Biophysics*. (1997).
87 Hush, N. S. Distance Dependence of Electron Transfer Rates. *Coordination Chemistry Reviews* **64**, 135-157, doi:http://dx.doi.org/10.1016/0010-8545(85)80047-3 (1985).
88 Kratschmer, W., Lamb, L. D., Fostiropoulos, K. & Huffman, D. R. Solid C60: a new form of carbon. *Nature* **347**, 354-358 (1990).
89 Tzafriri, A. R. & Edelman, E. R. On the validity of the quasi-steady state approximation of bimolecular reactions in solution. *Journal of Theoretical Biology* **233**, 343-350, doi:http://dx.doi.org/10.1016/j.jtbi.2004.10.013 (2005).
90 Berry, H. Monte carlo simulations of enzyme reactions in two dimensions: fractal kinetics and spatial segregation. *Biophysical Journal* **83**, 1891–1901 (2002).
91 Burlakov, V. M. *et al.* Discrete hopping model of exciton transport in disordered media. *Physical Review B* **72**, 075206 (2005).

92 Schnönherr, G., Eiermann, R., Bässler, H. & Silver, M. Dispersive exciton transport in a hopping system with gaussian energy distribution. *Chemical Physics* **52**, 287-298, doi:http://dx.doi.org/10.1016/0301-0104(80)85232-3 (1980).
93 Schönherr, G., Bässler, H. & Silver, M. Dispersive hopping transport via sites having a Gaussian distribution of energies. *Philosophical Magazine Part B* **44**, 47-61, doi:10.1080/01418638108222366 (1981).
94 Mikhnenko, O. V. *et al.* Temperature Dependence of Exciton Diffusion in Conjugated Polymers. *The Journal of Physical Chemistry B* **112**, 11601-11604, doi:10.1021/jp8042363 (2008).
95 Kandada, A. R. S. *et al.* Ultrafast Energy Transfer in Ultrathin Organic Donor/Acceptor Blend. *Sci. Rep.* **3**, doi:10.1038/srep02073 http://www.nature.com/srep/2013/130625/srep02073/abs/srep02073.html#supplementary-information (2013).
96 Scheidler, M., Cleve, B., Bässler, H. & Thomas, P. Monte Carlo simulation of bimolecular exciton annihilation in an energetically random hopping system. *Chemical Physics Letters* **225**, 431-436, doi:http://dx.doi.org/10.1016/0009-2614(94)87107-8 (1994).
97 Kang, K. & Redner, S. Scaling Approach for the Kinetics of Recombination Processes. *Physical Review Letters* **52**, 955-958 (1984).
98 Alvarado, S. F., Seidler, P. F., Lidzey, D. G. & Bradley, D. D. C. Direct Determination of the Exciton Binding Energy of Conjugated Polymers Using a Scanning Tunneling Microscope. *Physical Review Letters* **81**, 1082-1085 (1998).
99 Conwell, E. M. & Mizes, H. A. Photogeneration of polaron pairs in conducting polymers. *Physical Review B* **51**, 6953-6958 (1995).
100 Deibel, C. *et al.* Energetics of excited states in the conjugated polymer poly(3-hexylthiophene). *Physical Review B* **81**, 085202 (2010).
101 Biank, H. C. *et al.* Optical spectroscopy of photovoltaic systems based on low-bandgap polymers. *Thin Solid Films*, doi:http://dx.doi.org/10.1016/j.tsf.2013.11.025.
102 Yost, S. R., Wang, L.-P. & Van Voorhis, T. Molecular Insight Into the Energy Levels at the Organic Donor/Acceptor Interface: A Quantum Mechanics/Molecular Mechanics Study. *The Journal of Physical Chemistry C* **115**, 14431-14436, doi:10.1021/jp203387m (2011).
103 Bredas, J.-L. Mind the gap! *Materials Horizons* **1**, 17-19, doi:10.1039/c3mh00098b (2014).
104 Szarko, J. M. *et al.* Photovoltaic Function and Exciton/Charge Transfer Dynamics in a Highly Efficient Semiconducting Copolymer. *Advanced Functional Materials* **24**, 10-26, doi:10.1002/adfm.201301820 (2014).
105 van Hal, P. A. *et al.* Full temporal resolution of the two-step photoinduced energy–electron transfer in a fullerene–oligothiophene–fullerene triad using sub-10 fs pump–probe spectroscopy. *Chemical Physics Letters* **345**, 33-38, doi:http://dx.doi.org/10.1016/S0009-2614(01)00874-0 (2001).
106 van Hal, P. A., Meskers, S. C. J. & Janssen, R. A. J. Photoinduced energy and electron transfer in oligo(p-phenylene vinylene)-fullerene dyads. *Appl Phys A* **79**, 41-46, doi:10.1007/s00339-003-2500-2 (2004).

107 Albrecht, S. *et al.* On the Efficiency of Charge Transfer State Splitting in Polymer:Fullerene Solar Cells. *Advanced Materials*, n/a-n/a, doi:10.1002/adma.201305283 (2014).
108 Coropceanu, V. *et al.* Charge Transport in Organic Semiconductors. *Chemical Reviews* **107**, 926-952, doi:10.1021/cr050140x (2007).
109 Cheng, F. *et al.* Enhancing the performance of P3HT:ICBA based polymer solar cells using LiF as electron collecting buffer layer and UV–ozone treated MoO3 as hole collecting buffer layer. *Solar Energy Materials and Solar Cells* **110**, 63-68, doi:http://dx.doi.org/10.1016/j.solmat.2012.12.006 (2013).
110 Shaw, P. E., Ruseckas, A. & Samuel, I. D. W. Exciton Diffusion Measurements in Poly(3-hexylthiophene). *Advanced Materials* **20**, 3516-3520, doi:10.1002/adma.200800982 (2006)

7

USING EXCITON DIFFUSION TO PREDICT MORPHOLOGY IN PHOTOVOLTAIC BLENDS

7.1. INTRODUCTION

In this chapter, I measure the diffusion coefficient, D, for C_{71}-PCBM and then I introduce and test a new technique to measure the characteristic domain size of C_{71}-PCBM in a photovoltaic blend with PTB7, by using the diffusion coefficient to predict the morphology from the time-resolved fluorescence quenching of the blend. In section 7.2, I use the volume quenching method to measure the exciton diffusion coefficient of the commonly used electron acceptor C_{71}-PCBM. In section 7.3, current methods to measure domain size in organic photovoltaic blends are discussed and the domain sizes of PTB7:C_{71}-PCBM blends spin-coated from chlorobenzene and dichlorobenzene are measured using atomic force microscopy (AFM). The fluorescence dynamics of these blends are then measured using time-resolved fluorescence and compared to the decay of pristine C_{71}-PCBM. A model is applied to the film to predict domain sizes using the exciton diffusion coefficient calculated earlier, in section 7.2.

The results are compared, and the blend spin-coated from chlorobenzene is examined using scanning electron microscopy, additional AFM and differential scanning calorimetry. All the results are then discussed and conclusions are drawn in section 7.4.

7.2. MEASUREMENT OF THE C_{71}-PCBM EXCITON DIFFUSION COEFFICIENT

7.2.1 Introduction to C_{71}-PCBM

Though there is a huge variety of donor materials, both polymers and small molecules, so far all the top performing solar cell combinations use a functionalised fullerene as the electron acceptor[1,2]. The main development in the field of acceptors is the shift from C_{61}-PCBM to C_{71}-PCBM, as the latter makes up the accepting component of the most efficient single junction organic solar cell blend[3,4]. Of the 19 published single-junction materials combinations with power conversion efficiencies above 7%, 14 used C_{71}PCBM as the electron acceptor and all used fullerene derivatives of some sort[5].

Considering its ubiquity, it is surprising how few exciton diffusion studies there have been on the fullerene acceptor. While a really broad range of exciton diffusion coefficients have been measured in donor materials[6-24], to date only one article (excluding the data presented in this chapter) has been published on exciton diffusion in the fullerene acceptor. That work was in C_{61}-PCBM by Cook *et al.* and used the exciton annihilation technique to calculate the exciton diffusion length[25]. There are several practical reasons why C_{61}-PCBM has not been widely investigated. Firstly, it is rather difficult to spin-coat smooth, pristine, films of the

small molecule as it tends to form millimetre sized crystals. Secondly it is barely emissive, with a PLQY of the film below the minimum threshold to be measured using the equipment available (<0.1% PLQY). Thirdly, the fullerenes have been demonstrated to have a probability of spontaneously separating into charge pairs[26] making interpretation of transient absorption challenging. Finally, there is a strategic reason why an exciton diffusion coefficient in C_{61}-PCBM has not been strongly sought by the solar cell community; C_{61}-PCBM has a fairly small molar extinction coefficient and only absorbs very blue light[22]. Thus its contribution to the power conversion efficiency when excited with the solar spectrum is small[27]. If the acceptor is not absorbing many photons, few excitons are being created on it and the exciton diffusion coefficient of that material matters to a far lesser extent.

Newly published solar cell blends with high efficiencies more frequently use C_{71}-PCBM than C_{61}-PCBM, largely because the broader more intense absorption boosts the efficiency by increasing the number of incident photons absorbed. That the photons absorbed in the C_{71}-PCBM strongly contribute to the device efficiency (as measured from the Incident Photon to Charge Carrier Efficiency (IPCE)), provides a strong incentive to measure the exciton diffusion coefficient. This is because if C_{71}-PCBM photons contribute to the function of the device, exciton diffusion is critical, as whether or not the acceptor excitons can migrate to an interface will impact on the device performance. Additionally, C_{71}-PCBM is at least partially emissive, and can be detected using a streak camera, though the PLQY is still below 1%[28]. The fullerenes being small rigid molecules will have a lesser degree of inhomogeneous broadening of the density of states because the conjugation length of each chromophore is identical. This means that the exciton

diffusion is much more likely to exhibit Fickian diffusive behaviour, and thus the analysis will be much more straightforward. Finally, high solution concentrations of C_{71}-PCBM (~30 mg/ml in chlorobenzene) can be spin-coated into smooth films on quartz disks. The ubiquity of C_{71}-PCBM as an acceptor and the utility of the exciton diffusion coefficient, coupled with its relative ease of measurement makes measuring the exciton diffusion coefficient in this material a valuable, but achievable, goal in organic semiconductor research.

7.2.2 Measurement of the Diffusion Coefficient

7.2.2.1. Introduction

As in previous chapters the volume quenching technique was used to measure the exciton diffusion coefficient in C_{71}-PCBM. The major difference between this and previous volume quenching measurements in this thesis, is that because the material being investigated is an electron acceptor, the quencher must be an electron donor. In order to make the analysis of the quenching measurement tractable, the quencher must be a small molecule, as a polymer could either curl up or stretch out significantly changing the surface area available for quenching.

7.2.2.2. Choice of Quencher

The quencher must be chosen so that the exciton in C_{71}-PCBM is rapidly quenched, either by FRET or electron transfer, when it encounters the quenching site. The quencher must distribute evenly through the film when blended with C_{71}-PCBM and each molecule must act as a single quenching site; the quencher must be a small molecule not a polymer.

A small molecule, diketopyrrolopyrrole (DPP) derivative; 3,6-Bis(5-((4-(dimethylamino)phenyl)ethynyl)thiophen-2-yl)-2,5-bis(2-ethylhexyl)pyrrolo[3,4-c]pyrrole-1,4(2H,5H)-dione (DPP-NMe_2), was chosen as a suitable quencher for fulfilling the above criteria. The structure of DPP-NMe_2 is shown below. The material was synthesised and characterised by Dr Luis A. Serrano and Prof. Graeme Cooke, collaborators at the University of Glasgow. Full details of the synthesis and characterisation are available in the work published by Hedley *et al.*[28].

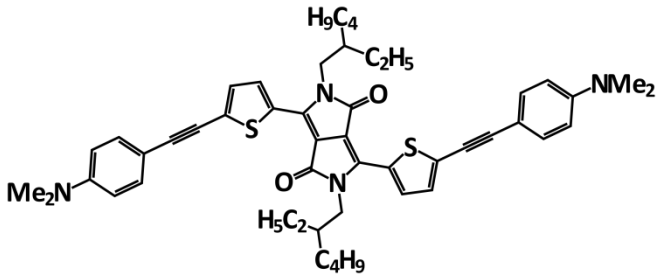

Figure 7.1. The molecular structure of the small molecule donor, DPP-NMe2.

Because the PLQY of C_{71}-PCBM is so low the chance of direct FRET from the fullerene to the small molecule is low[28] and thus the quenching can be described using the simplest model, simple contact quenching (equation 4.19).

7.2.2.3 Results and Discussion

Equation 4.19 was used to determine the rate constant for the quenching process. Additionally the rate of natural decay ($k_f(t)$) of the excitons was approximated from a two exponential decay of the pristine C_{71}-PCBM film.

EQUATION 7.1.
$$\frac{dN}{dT} = -4\pi r_c D N_c \left(1 + \frac{r_c}{\sqrt{\pi D t}}\right) N - k_F(t) N$$

The above equation was solved to give a stretched-exponential solution, which was then convoluted with the response function of the streak camera (with

the additional condition that N=0 when t<0) to generate a simulated time-resolved PL decay.

EQUATION 7.2. if t≥0

$$N(t) = exp\left(-4\pi r_c D N_c \left(t + \frac{2r_c\sqrt{t}}{\sqrt{\pi D}}\right) - \int_0^t k_F(t)\,dt\right)$$

if t<0

$$N(t) = 0$$

EQUATION 7.3. $$PL(t) = N(t) * RF$$

where PL(t) is the simulated PL decay and RF is the response function of the streak camera measured using the method described in chapter 3.

A global fit of equation 7.3 was performed on 8 films with concentrations of DPP-NMe_2 ranging from 0 to 5 wt%. The pristine film was used to calculate k_f while the only free parameters fitted in the other seven films were the diffusion coefficient and the critical radius, D and r_c respectively. The time-resolved fluorescence data and the corresponding fits of equation 7.3 are shown in figure 7.2 below.

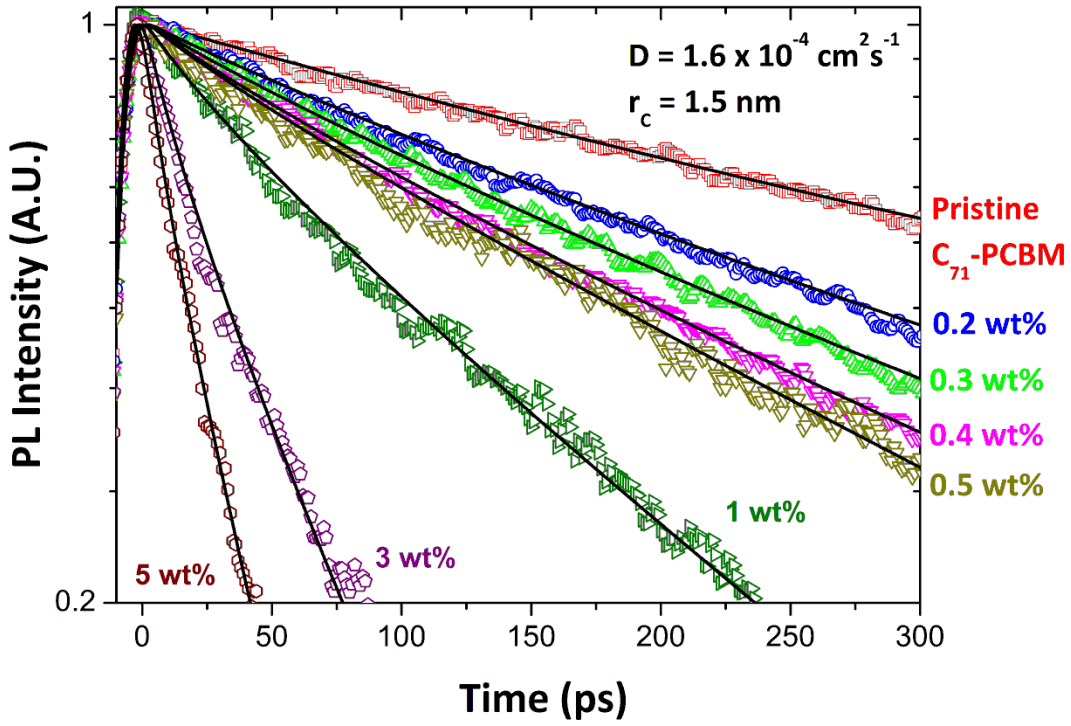

Figure 7.2. The time-resolved fluorescence decays of C_{71}-PCBM with varying amount of the small molecule quencher DPP-NMe_2. The black lines are global fits of equation 7.3 to the data, using the diffusion coefficient and the critical radius and fitting parameters.

From the above diagram it can be seen that a very broad range of quencher concentrations can be fit globally, with only two free parameters. This is strong evidence that there is minimal phase segregation in these films. The linearity of the lines (as plotted on a log scale) is a very good indication that the rate of quenching is largely exponential and the assertion that the quenching is predominantly both diffusive and time-independent, requirements for using the Smoluchowski rate constant, is justified.

The critical radius was fitted to be 1.5 nm and the diffusion coefficient was fitted to be 1.6×10^{-4} cm^2s^{-1}. As FRET in the scenario will be minimal, the critical radius essentially represents the centre to centre distance the exciton has to be from the acceptor before electron transfer can occur. The density of C_{71}-PCBM can

be approximated as the density reported[29] for C_{61}-PCBM of 1.3 g/cm^3. Thus if the molecules were perfectly distributed in the solid, then the centre to centre distance of C_{71}-PCBM (M_w of 1031 g) would be approximately 1.1 nm. Thus a fit of 1.5 nm approximately agrees with this observation taking into account the finite size of the DPP-Me_2 molecule as well.

The diffusion coefficient is fairly small at 1.6×10^{-4} cm^{2}s^{-1} but is comparable with the only other reported value for a fullerene accepter photovoltaic material, which was C_{61}-PCBM with a diffusion coefficient of 2×10^{-4} cm^{2}s^{-1} reported by Cook *et al.*[25]. Using equation 4.5 in conjunction with the lifetime of the pristine C_{71}-PCBM film measured in figure 7.2, the diffusion length is given by 4.4 nm.

7.3. PREDICTION OF DOMAIN SIZES IN PTB7:C_{71}- PCBM PHOTOVOLTAIC BLENDS

7.3.1 Introduction to Morphology Determination and Literature Review

As discussed in section 2.4.3 of chapter 2, the domain size in a bulk heterojunction has a critical impact on the exciton harvesting and charge recombination of a functional solar cell. Considering how critical the domain size is, it is somewhat surprising how few experimental techniques there are that reliably give information about it. There are two broad categories of experimental techniques that have been used to probe the degree of phase segregation in organic solar cells; those that probe reciprocal space and those that are real-space measurements.

Reciprocal-space measurements use diffraction, scattering or reflection of X-rays or neutrons in order to build up information about characteristic length-

scales from the bulk heterojunction[30]. Reciprocal-space techniques that have been used to probe domain size in organic solar cells include wide- angle scattering, small-angle scattering and reflectivity measurements.

The most commonly used wide angle scattering technique is grazing incidence wide-angle x-ray scattering (GIWAX). This technique can be used to indirectly estimate the crystallite size by considering that the broader the peak observed in reciprocal space, the shorter the correlation length in real-space. As the simplest interpretation is that the correlation length is the minimum crystal size, this can be used as an estimate of morphology. This reasoning is typically quantified using the Scherrer equation which allows quantitative predictions of structural correlation lengths[31]. Chen *et al*. use this procedure to demonstrate that the crystal sizes in PTB7 remain similarly sized in films processed with, or without the solvent additive 1,8-diiodooctane[32] (DIO). A similar investigation on the influence of solvent additives on the polymer PCPDTBT was conducted by Rogers *et al.*[33]. Likewise Hammond *et al.* use the technique to show that PTB7 has rather small crystal sizes compared to another photovoltaic polymer, P3HT[34]. By using more of the spatial information of the diffraction pattern and by recording how the pattern changes with time, Rogers *et al.* in a separate paper, were able to explore the time dynamics of bulk heterojunction formation by monitoring the time-resolved structural correlation length of PCPDTBT[35]. There are two major drawbacks of this technique. Firstly, like all diffraction techniques, because both components of the blend incorporate the same, light elements (predominantly carbon, hydrogen and oxygen), this leads to very small x-ray scattering cross-sections, and little contrast between the two components. Secondly the technique

can only be used to calculate structural correlation lengths. This value represents the characteristic distance over which there is enough order for coherent scattering of the x-ray beam. This is usually interpreted as the characteristic size of a defect-free crystallite, but may indicate larger crystals with structural defects. Additionally, the size of the crystal does not necessarily indicate the domain size, as domain may consist of crystalline and non-crystalline material.

Small angle diffraction techniques use a slightly different detector angle which makes the technique more suitable for the detection of larger features in the morphology[30]. An example of a small angle technique is grazing incidence small-angle x-ray diffraction (GISAX). Wu *et al.* used GISAX in combination with GIWAX to calculate fullerene domain sizes by applying a model that assumes the fullerene domains are poly-disperse spheres[36]. They found that the as-cast films had a domain size of 7 nm which rose to 17.5 nm after prolonged annealing. This agreed well with a GISAX investigation by Kozub[37] and co-workers who modelled the scattering observed in P3HT:C_{61}-PCBM blends using a Teubner–Strey model[38]. Small angle neutron diffraction was used in conjunction with some complex modelling to calculate domain sizes in P3HT:C_{61}-PCBM by Ruderer *et al.*[39]. Again, like wide-angle x-ray scattering, small-angle scattering techniques are hampered by small scattering cross-sections, though neutron scattering offers a small advantage over x-ray scattering in this respect[30]. The major disadvantage is that it is a very indirect technique and requires several assumptions to be made, such as that the domains are spherical, before information can be extracted from the scattering data, and the results generated can be very model dependent.

Reflection techniques, such as x-ray reflectivity and neutron reflectivity can be used to probe the vertical phase segregation of films. Of these, neutron reflectivity is the favoured technique because typically there is only enough contrast between the two blend components when using x-ray reflection if one of the blend components is deuterated[30]. Parnell *et al.* use neutron reflectivity measurements to calculate vertical phase segregation in P3HT:C_{61}-PCBM blends[40], finding that C_{61}-PCBM congregates at the film:substrate interface. This observation was corroborated by Kiel and co-workers using phase-sensitive neutron reflectometry [29,41].

Real-space techniques can give a much more direct measurement of a small section of the film (as opposed to reciprocal space techniques which average over a large area). Typically only a two-dimensional picture of the blend morphology is captured.

Scanning probe (SP) microscopy is a way of building up an image by scanning an atomically sharp tip across a surface. The tip in some way senses the a property of the surface, but what it senses depends on the type of SP technique. The most commonly used SP technique is atomic force microscopy, where the probe is just an atomically sharp tip attached to a cantilever which can measure the height of the material that the tip is interacting with. By scanning the tip across the film the nanoscale topology can be imaged. It has been used extensively to try and build a map of phase segregation in organic photovoltaic blends[42-53]. One disadvantage is that the similar physical properties of the donor and acceptor materials often lead to little contrast when surveying the surface. In photovoltaic blends, this can be uniquely overcome by measuring the photoconductive

properties of the blends, with photo-generated electrons being present in the electron acceptor phase and holes in the electron donor. Thus photoconductive AFM has recently emerged as a way of generating excellent contrast nanoscale morphology of photovoltaic blends[50,54-60].

Another real space technique that is commonly used is transmission electron microscopy (TEM). This technique simply involves passing a focussed beam of electrons through a thin film and looking for changes in transmission. It has been used to monitor phase segregation in OPV films[3,61-64]. One disadvantage of TEM is again the contrast between the different phases. The attenuation of the electron beam is related to the atomic mass of the nuclei in the medium through which the beam is travelling. This means that TEM can offer very good contrast in blends where the acceptor is an inorganic nanocrystal[65], but discerning structures can be challenging if both components of the blend are predominantly carbon. To remedy this, energy filtered TEM can provide high contrast if a particular element, such as sulphur, is only present in one of the blend components[62,66].

Scanning probe techniques and TEM variants have the disadvantage, unlike the inverse-space techniques, that only a two dimensional image of the blend is being produced. In the case of scanning probe techniques, the only part of the morphology that is being probed is the very surface layer, which may not be representative of the blend as a whole. On the other hand TEM techniques only see a 2D representation of the morphology, but it represents a view through the entirety of the thin film. By only being able to measure the phase segregation in the x and y directions, these techniques give a limited view of the bulk heterojunction. This shortcoming is sometimes improved by using these two dimensional

techniques on the cross-section of the film, to see the vertical phase segregation[67,68]. A technique to generate a complete 3-dimensional picture of the nanoscale morphology is electron tomography. In this technique many TEM images are captured as the sample is tilted to different orientations relative to the probe beam and computer modelling is used to reconstitute this images into the 3D model. This technique has been used in organic photovoltaic blends[69,70] but the most reliable results arise when one component is inorganic to provide better contrast[71].

One final technique, unrelated to real or inverse space techniques is the time-resolved fluorescence technique published by Ruseckas *et al*[72]. The authors used the time-resolved fluorescence of the blend in conjunction with a published diffusion coefficient in the blend to predict the size of the PCBM domains by assuming that quenching only occurred when the excitons diffuse into the interface. This technique is similar to the volume quenching technique presented in section 7.2.2 of this chapter, with the difference that in that case the quenching domains rather than being assumed to be individual molecules, were modelled to be spherical domains. This technique is similar to the one being presented in the next section and both of these two scenarios are described in chapter 4, sections 4.5.3-4.5.4.

7.3.2 Measuring the Nanoscale Morphology in PTB7-Fullerene Blends

The morphology of the high performance photovoltaic blend PTB7:C_{71}-PCBM has been well studied. TEM conducted by Liang *et al*. suggests that the blend, when spin-coated from chlorobenzene[3] forms domains of 400-600 nm, while blends spin-coated from dichlorobenzene had much smaller grains of diameter 20-

100 nm[3]. X-ray scattering investigations indicated that in blends spin-coated from chlorobenzene pure C_{71}-PCBM domains of diameter 177 nm[73] are formed, while an x-ray scattering investigation of a PTB7:C_{61}-PCBM suggested a hierarchical morphology with multiple length-scales of domain sizes[32]. If the CB blend did consist of very large pure domains of C_{71}-PCBM then this would severely hamper exciton harvesting in these blends as many excitons within these domains would be spatially separate from the hetero-interface, and hence charge separation would be low.

In the next sections AFM is used to measure the domain sizes in films of PTB7:C_{71}-PCBM spin-coated from chlorobenzene and dichlorobenzene. This measured morphology is then compared with a completely novel technique to measure domain size from the time-resolved fluorescence of the blend.

7.3.3 AFM Measurements of Blends

Films were prepared via spin-coating from photovoltaic blend concentrations (1:1.5 PTB7:C_{71}-PCBM), either from the solvent chlorobenzene or dichlorobenzene. In order to check to see whether the large features in the chlorobenzene and the small features in dichlorobenzene reported in the literature could be reproduced, the films were sent to collaborators at the University of Glasgow to be analysed by Dr Alexander Alekseev, an expert in scanning probe microscopy, using atomic force microscopy (AFM). The results are shown below.

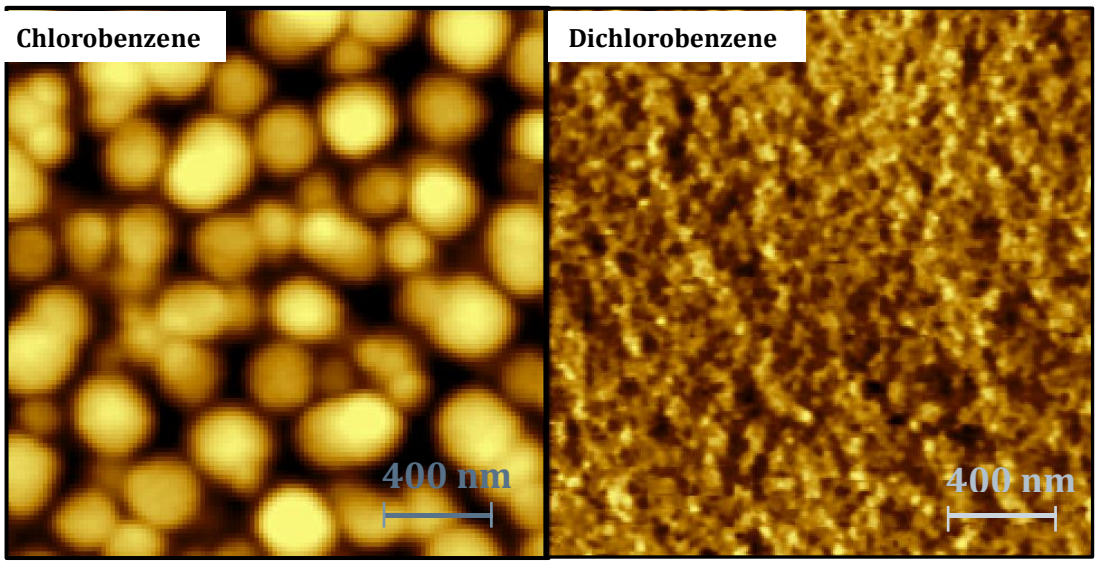

Figure 7.3. Phase-contrast mode AFM plots of identical blend ratio (1:1.5 PTB7 to C_{71}-PCBM), identical spin conditions and post-processing. The only difference between the two samples is the solvent from which the blends were spincoated; chlorobenzene (left) and dichlorobenzene (right). Many thanks to Dr Alexander Alekseev and Aizhan Sabitova for acquisition of the AFM data.

The above AFM images largely agree with the reported morphologies for the two solvents in the literature with chlorobenzene giving 300 – 400 nm diameter spherical domains and dichlorobenzene giving a texture on a much smaller lengthscale. A larger scale image is shown of these blends below.

.

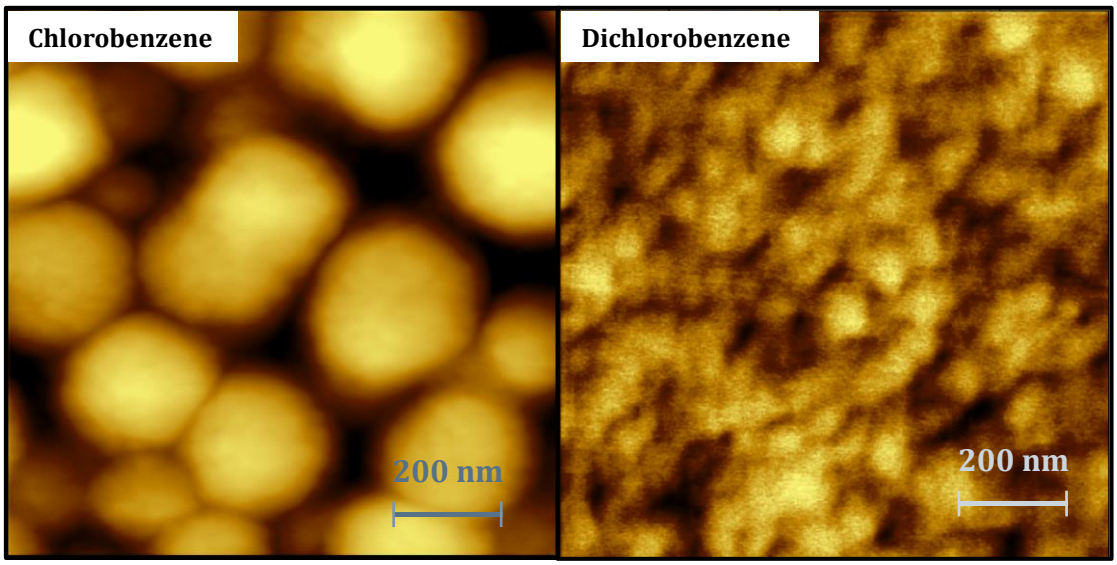

Figure 7.4. Phase contrast AFM images of blends spin-coated from chlorobenzene and dichlorobenzene. Many thanks to Dr Alexander Alekseev and Aizhan Sabitova for acquisition of the AFM data.

From the zoomed in images, the domain size in the chlorobenzene blends can be determined to be on the order of 200 – 400 nm while the dichlorobenzene blends have a much finer texture to of approximately 30 – 80 nm diameter.

7.3.4 Using Exciton Diffusion to Predict Domain Sizes

Having calculated the exciton diffusion coefficient in C_{71}-PCBM in section 7.2, and seeing from AFM measurements that the morphology in PTB7:C_{71}-PCBM blends can be well approximated as C_{71}-PCBM spheres surrounded by a PTB7 rich phase in the blend, it was decided to apply a diffusive model as a novel approach to calculate domain size. In this model excitons are considered to move freely within a spherical domain of C_{71}-PCBM with a lifetime identical to the lifetime of excitons in the pristine C_{71}-PCBM film. If the excitons encountered the edge of the sphere, coming into contact with the PTB7-rich phase, then they are considered to be instantly quenched. If we make the assumption that all spheres are similarly sized, and that the fluorescence of intimately mixed fullerene in the PTB7 rich phase

decays more rapidly than the response of the streak-camera, then the only free parameter in the quenching process is the characteristic domain size of the spheres. Thus by convoluting equation 4.30, after including a term accounting for the rate of fluorescence decay of unquenched excitons, k_f, with the instrument response function and fitting to the PL decay, it is possible to predict the characteristic domain size from the time-resolved fluorescence of the blend.

If $t \geq 0$

EQUATION 7.4.
$$P = exp\left(-\int_0^t k_F(t)dt\right)\frac{6}{\pi^2}\sum_{n=1}^{\infty}\frac{1}{n^2}exp\left(\frac{-Dn^2\pi^2 t}{a^2}\right)$$

else

EQUATION 7.5.
$$P = 0$$

EQUATION 7.6.
$$PL = P * RF$$

where P is the population of excitons, normalised to 1 at t=0, k_f is the rate of fluoresence decay in the pristine fullerene, a is the radius of the fullerene domain and D is the exciton diffusion coefficient of C_{71}-PCBM calculated in the previous section.

Blends of 1:1.5 PTB7 to C_{71}-PCBM spin-coated from either chlorobenzene or dichlorobenze were selected as model systems with which to test this novel method for domain size determination. These systems were chosen because they have been observed using TEM and scattering techniques to have very different nanostructures and also have been found to give approximately spherical domains, which is a requirement of the model. In blends spin-coated from

chlorobenzene large 100-200 nm domains have been observed[3,73-75] suggesting that there ought to be very little quenching of the C_{71}-PCBM as the diffusion length of the fullerene was found in section 7.2.2 to be only 4.4 nm, meaning that the vast majority of the excitons in C_{71}-PCBM would be further than this distance from the interface and thus be totally unaffected by the presence of PTB7 in the blend. On the other hand, when spin-coated from dichlorobenzene the blends formed appear from TEM to be much better mixed. Thus there ought to be significant contrast between blends prepared from the two solvents. The time-resolved fluoresence spectra of pristine C_{71}-PCBM and 1.5:1 blends with PTB7 after being spin-coated from chlorobenzene or dichlorobenzene are shown below. The fits to equation 7.6 are shown below.

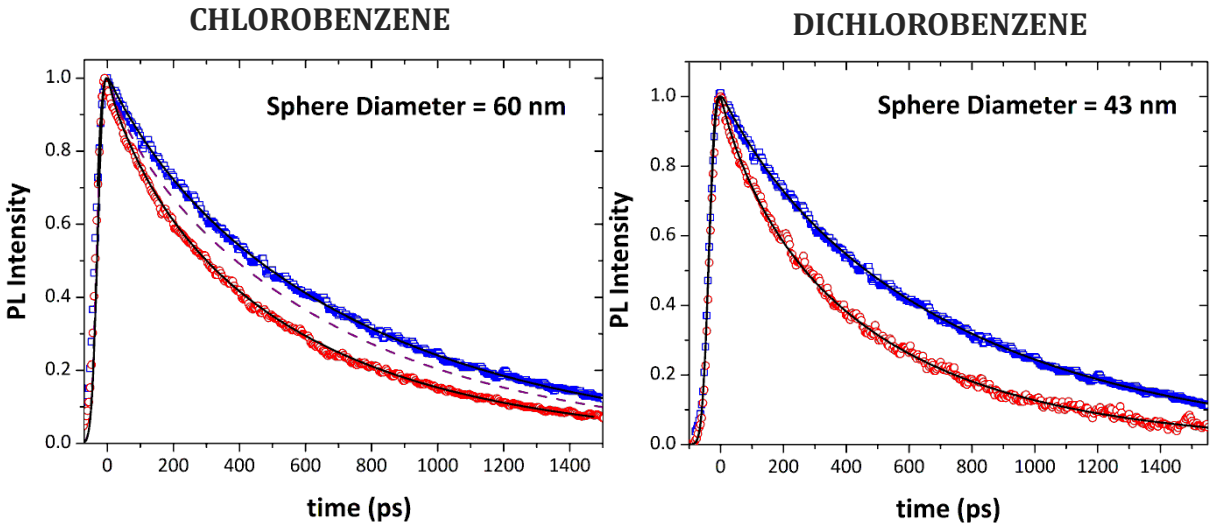

Figure 7.5. Time-resolved fluorescence of pristine C_{71}-PCBM (blue squares) and 1:1.5 PTB7:C_{71}-PCBM blends (red circles), spin-coated from chlorobenzene (left) or dichlorobenzene (right). On the left the purple dotted line indicated the expected decay in a blend with a sphere size of 200 nm (as would be expected from AFM). Many thanks to Dr Gordon Hedley for the data acquisition.

What is notable in the figures above is that there is little difference between the time-resolved fluorescence dynamics of the two blends. Though the dichlorobenzene blend predicts spheres with diameters of 43 nm, which agree well

with those seen in the AFM presented in section 7.3.2, the chlorobenzene film predicts a sphere diameter of 60 nm which is vastly smaller than the 200-400 nm films observed using AFM. It seems that the assumption that the large structures evident from the topological measures quoted in the literature and the analysis of the x-ray diffraction conducted by Collins *et al.*[73] cannot be correct. If the two components are finely mixed as has been demonstrated using the solvent additive DIO, the blend lifetime would be below 100 fs[28]. If the domains in chlorobenzene have a diameter of 200 nm and are pure C_{71}-PCBM then the lifetime of the blend would barely change relative to pristine C_{71}-PCBM, as is illustrated by the purple dashed line in the left panel of 7.5. Thus we can only conclude that blends are in an intermediate regime where the effective domain size is smaller.

7.3.5 Additional Morphological Investigation of Films Spin-coated from Chlorobenzene

Additional scanning electron microscopy (SEM) measurements were performed on the blend spin-coated from chlorobenzene (shown below).

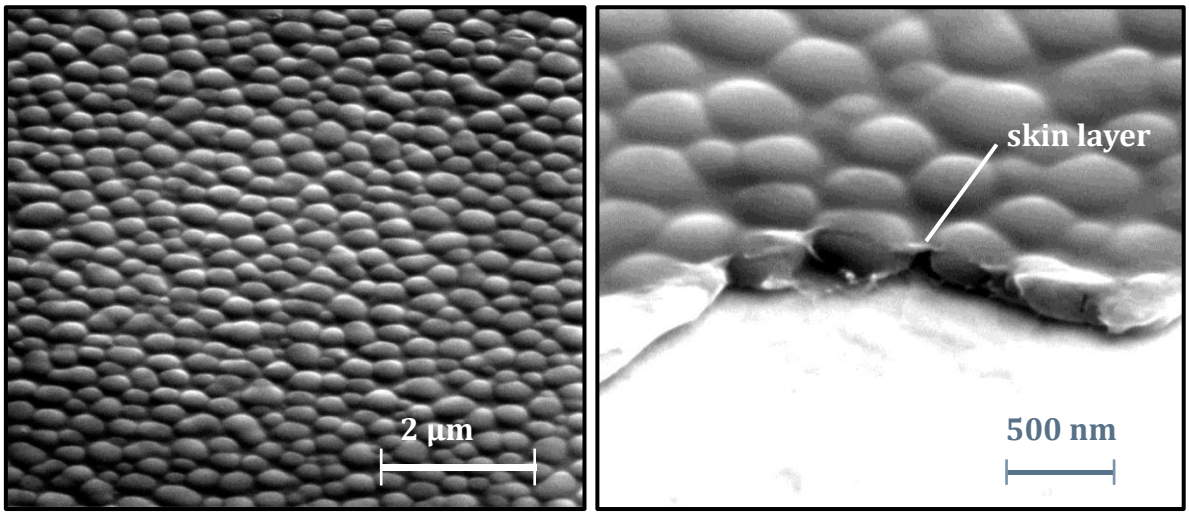

Figure 7.6. SEM images of PTB7:C_{71}-PCBM films spin-coated from chlorobenzene. The very large features seen in the AFM images are visible. After a score was made in the film a thin skin layer can be seen attached to the top of the spheres. Many thanks to Dr Alexander Alekseev for carrying out the SEM imaging.

In the above SEM images the prominent, 200-400 nm features are present. In addition after a score was made in the film using a sharp edge, a visible skin layer can be seen. The skin layer is reminiscent of the thin layer of tomato sauce adhering to the surface of baked beans that protrude from the bean-sauce mixture. It is likely this skin layer is of the polymer-rich domain, which precipitates from the solution last.

Because AFM is only a measure of topology it was hypothesised that this thin skin layer may be cloaking any substructure in the large C_{71}-PCBM domains. To remove it and probe a horizontal cross-section of the film, the PTB7:C_{71}-PCBM films were subjected to an oxygen plasma to remove 30-40 nm of the top layer of the blend. The films were then re-examined using AFM. The AFM images are shown below.

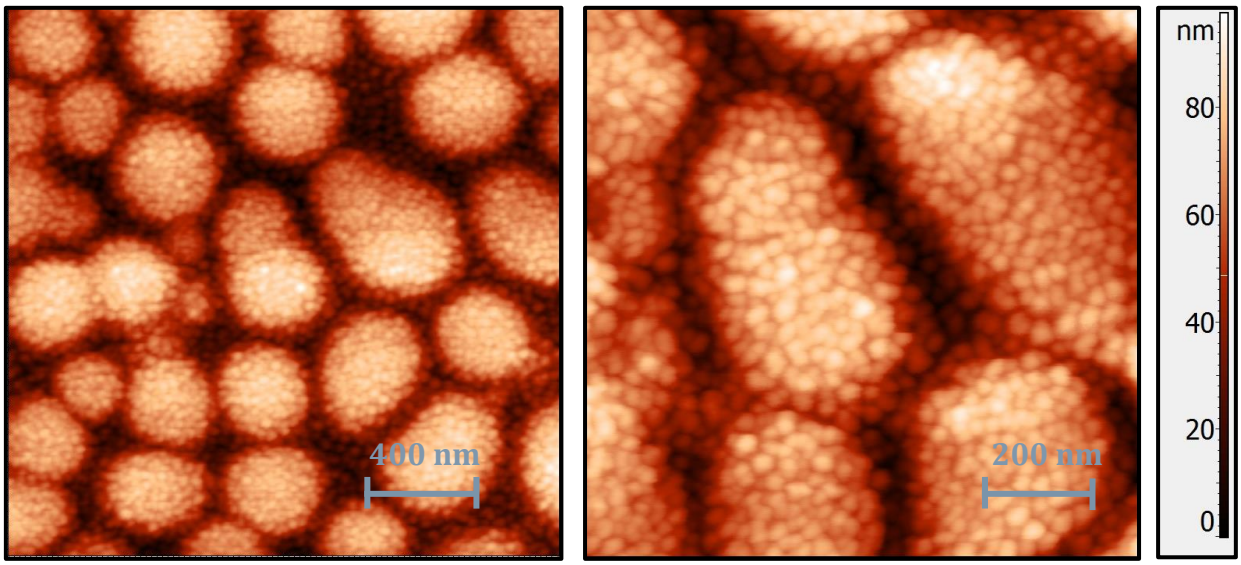

Figure 7.7. AFM images of the cross-section of a PTB7:C_{71}-PCBM blend spun from chlorobenzene. Cross-section was achieved through the removal of 30-40 nm of the top layer using plasma ashing.

From the above images, a clear substructure within the large ~300 nm domains is visible. This substructure consists of roughly spherical domains with an approximate diameter of 60 nm. This substructure agrees very well with the predictions made by modelling the time-resolved fluorescence spectroscopy in section 7.3.4.

7.3.6 Testing the purity of the domains using DSC

An important requirement to use exciton diffusion to measure the domain size in photovoltaic blends is the requirement that within the C_{71}-PCBM blends, the domains themselves are pure. This is because a necessary assumption of the model described in section 7.3.4 is that an exciton within a C_{71}-PCBM domain has the same lifetime as an exciton within a pure C_{71}-PCBM film until it comes into contact with the edge of a domain. A powerful test for domain purity is differential scanning calorimetry (DSC). This instrument measures the discontinuities in specific heat due to phase transitions, such as glass transitions or crystal melts of a

material, by measuring the thermal load required to change the temperature. It can be used to measure domain purity because a relatively small amount of impurity will shift the temperature at which these phase transitions occur or completely suppress them; an impure phase will melt at a lower temperature than the pure material, for example[76]. DSC measurements of pure PTB7, pure C_{71}-PCBM and the blend, all spin-coated from chlorobenzene are shown below.

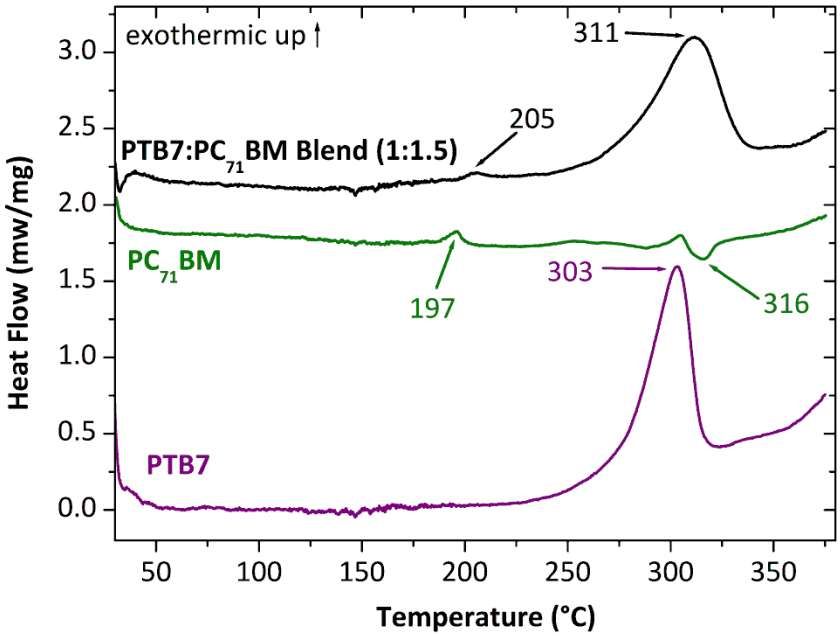

Figure 7.8. DSC measurements of the PTB7:C_{71}-PCBM blend, C_{71}-PCBM and PTB7 films. Many thanks to Sylvia Williamson for performing the measurement.

The crystal melt temperature reported for C_{61}-PCBM in the literature was 290 °C[77] and 319 °C for C_{71}-PCBM[78]. These values agree well with the measured crystal melt temperature of 316 °C, measured in the pure C_{71}-PCBM film. Unfortunately, this peak is obscured in the blend by a much more intense glass transition in the PTB7 at 303 °C in the pristine film (the combined peak shifted to 311 °C in the blend). In order to comment on the domain purity it is necessary to compare the much weaker crystal melt crystallisation peak, which occurs a 197 °C

in the pristine C_{71}-PCBM. In the blend this transition is just as strong and only slightly displaced to 205 °C. Thus we can conclude that there is likely to be significant pure C_{71}-PCBM within the blend, corroborating our assumption that excitons within the smaller substructure can be assumed to decay with the same rate as excitons in the pristine material.

7.4. CONCLUSIONS

This chapter explores the exciton diffusion coefficient of an electron acceptor ubiquitous in high performance photovoltaic blends; C_{71}-PCBM. This material was found to have a relatively short exciton diffusion length of 4.4 nm. This finding offers some explanation as to why the best performing photovoltaic blends tend to have very small fullerene domains. The measured exciton diffusion coefficient for C_{71}-PCBM, 1.6×10^{-4} cm^2s^{-1} was then used as part of a novel technique to measure the domain size of the fullerene in high performance blend PTB7:C_{71}-PCBM spin-coated from chlorobenzene and dichlorobenzene. While the characteristic domain size predicted from this technique closely matched domain sizes calculated from AFM measurements, for the blend spin-coated from dichlorobenzene, there was a stark discrepancy between the equivalent measurements in blends spin-coated from chlorobenzene. The AFM indicated that very large 200-400 nm domains were present in the chlorobenzene cast film, but the time-resolved fluorescence indicated a much smaller domain size, on the order of 60 nm, indicating a substructure to these larger domains. SEM images revealed a thin skin layer on the surface of the films. When this skin layer was removed using an oxygen plasma to remove the top 30-40 nm of film, and the newly exposed

surface was subjected to AFM, the smaller grains indicated from the time-resolved fluorescence were clearly visible. Thus in this chapter a new technique to use exciton diffusion to predict domain size from the time-resolved fluorescence of the blend was introduced and validated using high resolution AFM measurements.

7.5. REFERENCES

1 Liu, T. & Troisi, A. What Makes Fullerene Acceptors Special as Electron Acceptors in Organic Solar Cells and How to Replace Them. *Advanced Materials* **25**, 1038-1041, doi:10.1002/adma.201203486 (2013).

2 Brabec, C. J. *et al.* Polymer–Fullerene Bulk-Heterojunction Solar Cells. *Advanced Materials* **22**, 3839-3856, doi:10.1002/adma.200903697 (2010).

3 Liang, Y. *et al.* For the Bright Future—Bulk Heterojunction Polymer Solar Cells with Power Conversion Efficiency of 7.4%. *Advanced Materials* **22**, E135-E138, doi:10.1002/adma.200903528 (2010).

4 He, Z. *et al.* Enhanced power-conversion efficiency in polymer solar cells using an inverted device structure. *Nat Photon* **6**, 591-595, doi:http://www.nature.com/nphoton/journal/v6/n9/abs/nphoton.2012.190.html#supplementary-information (2012).

5 Liao, H.-C. *et al.* Additives for morphology control in high-efficiency organic solar cells. *Materials Today* **16**, 326-336, doi:http://dx.doi.org/10.1016/j.mattod.2013.08.013 (2013).

6 Kroeze, J. E., Savenije, T. J., Vermeulen, M. J. W. & Warman, J. M. Contactless Determination of the Photoconductivity Action Spectrum, Exciton Diffusion Length, and Charge Separation Efficiency in Polythiophene-Sensitized TiO2 Bilayers. *The Journal of Physical Chemistry B* **107**, 7696-7705, doi:10.1021/jp0217738 (2003).

7 Gaab, K. M. & Bardeen, C. J. Anomalous Exciton Diffusion in the Conjugated Polymer MEH–PPV Measured Using a Three-Pulse Pump–Dump–Probe Anisotropy Experiment. *The Journal of Physical Chemistry A* **108**, 10801-10806, doi:10.1021/jp0464472 (2004).

8 Burlakov, V. M. *et al.* Discrete hopping model of exciton transport in disordered media. *Physical Review B* **72**, 075206 (2005).

9 Markov, D. E., Amsterdam, E., Blom, P. W. M., Sieval, A. B. & Hummelen, J. C. Accurate Measurement of the Exciton Diffusion Length in a Conjugated Polymer Using a Heterostructure with a Side-Chain Cross-Linked Fullerene Layer. *The Journal of Physical Chemistry A* **109**, 5266-5274, doi:10.1021/jp0509663 (2005).

10 Lewis, A. J. *et al.* Singlet exciton diffusion in MEH-PPV films studied by exciton–exciton annihilation. *Organic Electronics* **7**, 452-456, doi:10.1016/j.orgel.2006.05.009 (2006).

11 Markov, D. E. & Blom, P. W. M. Anisotropy of exciton migration in poly(p-phenylene vinylene). *Physical Review B* **74**, 085206 (2006).

12 Scully, S. R. & McGehee, M. D. Effects of optical interference and energy transfer on exciton diffusion length measurements in organic semiconductors. *Journal of Applied Physics* **100**, 034907 (2006).

13 Mikhnenko, O. V. *et al.* Temperature Dependence of Exciton Diffusion in Conjugated Polymers. *The Journal of Physical Chemistry B* **112**, 11601-11604, doi:10.1021/jp8042363 (2008).

14 Ribierre, J. C. *et al.* Triplet Exciton Diffusion and Phosphorescence Quenching in Iridium(III)-Centered Dendrimers. *Physical Review Letters* **100**, 017402 (2008).
15 Shaw, P. E., Ruseckas, A. & Samuel, I. D. W. Exciton Diffusion Measurements in Poly(3-hexylthiophene). *Advanced Materials* **20**, 3516-3520, doi:10.1002/adma.200800982 (2008).
16 Athanasopoulos, S., Emelianova, E. V., Walker, A. B. & Beljonne, D. Exciton diffusion in energetically disordered organic materials. *Physical Review B* **80**, 195209 (2009).
17 Mikhnenko, O. V. *et al.* Exciton Quenching Close to Polymer–Vacuum Interface of Spin-Coated Films of Poly(p-phenylenevinylene) Derivative. *The Journal of Physical Chemistry B* **113**, 9104-9109, doi:10.1021/jp9012637 (2009).
18 Mikhnenko, O. V. *et al.* Exciton diffusion length in narrow bandgap polymers. *Energy & Environmental Science* **5**, 6960-6965 (2012).
19 Masri, Z. *et al.* Molecular Weight Dependence of Exciton Diffusion in Poly(3-hexylthiophene). *Advanced Energy Materials* **3**, 1445-1453, doi:10.1002/aenm.201300210 (2013).
20 Mikhnenko, O. V. *et al.* Trap-Limited Exciton Diffusion in Organic Semiconductors. *Advanced Materials*, n/a-n/a, doi:10.1002/adma.201304162 (2013).
21 Tamai, Y., Matsuura, Y., Ohkita, H., Benten, H. & Ito, S. One-Dimensional Singlet Exciton Diffusion in Poly(3-hexylthiophene) Crystalline Domains. *The Journal of Physical Chemistry Letters* **5**, 399-403, doi:10.1021/jz402299a (2014).
22 Ward, A. J., Ruseckas, A. & Samuel, I. D. W. A Shift from Diffusion Assisted to Energy Transfer Controlled Fluorescence Quenching in Polymer–Fullerene Photovoltaic Blends. *The Journal of Physical Chemistry C* **116**, 23931-23937, doi:10.1021/jp307538y (2012).
23 Raisys, S. *et al.* Exciton diffusion enhancement in triphenylamines via incorporation of phenylethenyl sidearms. *Journal of Materials Chemistry C* **2**, 4792-4798, doi:10.1039/c4tc00262h (2014).
24 Rothe, C. & Monkman, A. P. Triplet exciton migration in a conjugated polyfluorene. *Physical Review B* **68**, 075208 (2003).
25 Cook, S., Furube, A., Katoh, R. & Han, L. Estimate of singlet diffusion lengths in PCBM films by time-resolved emission studies. *Chemical Physics Letters* **478**, 33-36, doi:10.1016/j.cplett.2009.06.091 (2009).
26 Kazaoui, S. *et al.* Comprehensive analysis of intermolecular charge-transfer excited states in C60 and C70 films. *Physical Review B* **58**, 7689-7700 (1998).
27 Sharma, S. S., Sharma, G. D. & Mikroyannidis, J. A. Improved power conversion efficiency of bulk heterojunction poly(3-hexylthiophene):PCBM photovoltaic devices using small molecule additive. *Solar Energy Materials and Solar Cells* **95**, 1219-1223, doi:http://dx.doi.org/10.1016/j.solmat.2010.12.013 (2011).
28 Hedley, G. J. *et al.* Determining the optimum morphology in high-performance polymer-fullerene organic photovoltaic cells. *Nat Commun* **4**, doi:10.1038/ncomms3867 (2013).

29 Kiel, J. W., Kirby, B. J., Majkrzak, C. F., Maranville, B. B. & Mackay, M. E. Nanoparticle concentration profile in polymer-based solar cells. *Soft Matter* **6**, 641-646 (2010).
30 Chen, W., Nikiforov, M. P. & Darling, S. B. Morphology characterization in organic and hybrid solar cells. *Energy & Environmental Science* **5**, 8045-8074, doi:10.1039/c2ee22056c (2012).
31 Smilgies, D.-M. Scherrer grain-size analysis adapted to grazing-incidence scattering with area detectors. *Journal of Applied Crystallography* **42**, 1030-1034, doi:doi:10.1107/S0021889809040126 (2009).
32 Chen, W. *et al.* Hierarchical Nanomorphologies Promote Exciton Dissociation in Polymer/Fullerene Bulk Heterojunction Solar Cells. *Nano Letters* **11**, 3707-3713, doi:10.1021/nl201715q (2011).
33 Rogers, J. T., Schmidt, K., Toney, M. F., Kramer, E. J. & Bazan, G. C. Structural Order in Bulk Heterojunction Films Prepared with Solvent Additives. *Advanced Materials* **23**, 2284-2288, doi:10.1002/adma.201003690 (2011).
34 Hammond, M. R. *et al.* Molecular Order in High-Efficiency Polymer/Fullerene Bulk Heterojunction Solar Cells. *ACS Nano* **5**, 8248-8257, doi:10.1021/nn202951e (2011).
35 Rogers, J. T., Schmidt, K., Toney, M. F., Bazan, G. C. & Kramer, E. J. Time-Resolved Structural Evolution of Additive-Processed Bulk Heterojunction Solar Cells. *Journal of the American Chemical Society* **134**, 2884-2887, doi:10.1021/ja2104747 (2012).
36 Wu, W.-R. *et al.* Competition between Fullerene Aggregation and Poly(3-hexylthiophene) Crystallization upon Annealing of Bulk Heterojunction Solar Cells. *ACS Nano* **5**, 6233-6243, doi:10.1021/nn2010816 (2011).
37 Kozub, D. R. *et al.* Polymer Crystallization of Partially Miscible Polythiophene/Fullerene Mixtures Controls Morphology. *Macromolecules* **44**, 5722-5726, doi:10.1021/ma200855r (2011).
38 Teubner, M. & Strey, R. Origin of the scattering peak in microemulsions. *The Journal of Chemical Physics* **87**, 3195-3200, doi:doi:http://dx.doi.org/10.1063/1.453006 (1987).
39 Ruderer, M. A., Meier, R., Porcar, L., Cubitt, R. & Müller-Buschbaum, P. Phase Separation and Molecular Intermixing in Polymer–Fullerene Bulk Heterojunction Thin Films. *The Journal of Physical Chemistry Letters* **3**, 683-688, doi:10.1021/jz300039h (2012).
40 Parnell, A. J. *et al.* Depletion of PCBM at the Cathode Interface in P3HT/PCBM Thin Films as Quantified via Neutron Reflectivity Measurements. *Advanced Materials* **22**, 2444-2447, doi:10.1002/adma.200903971 (2010).
41 Kiel, J. W., Mackay, M. E., Kirby, B. J., Maranville, B. B. & Majkrzak, C. F. Phase-sensitive neutron reflectometry measurements applied in the study of photovoltaic films. *The Journal of Chemical Physics* **133**, -, doi:doi:http://dx.doi.org/10.1063/1.3471583 (2010).
42 Chen, J. *et al.* Ternary behavior and systematic nanoscale manipulation of domain structures in P3HT/PCBM/P3HT-b-PEO films. *Journal of Materials Chemistry* **22**, 13013-13022, doi:10.1039/c2jm31124k (2012).

43 Giridharagopal, R., Shao, G., Groves, C. & Ginger, D. S. New SPM techniques for analyzing OPV materials. *Materials Today* **13**, 50-56, doi:http://dx.doi.org/10.1016/S1369-7021(10)70165-6 (2010).
44 Hamadani, B. H., Gergel-Hackett, N., Haney, P. M. & Zhitenev, N. B. Imaging of nanoscale charge transport in bulk heterojunction solar cells. *Journal of Applied Physics* **109**, -, doi:doi:http://dx.doi.org/10.1063/1.3595669 (2011).
45 Giridharagopal, R. *et al.* Submicrosecond Time Resolution Atomic Force Microscopy for Probing Nanoscale Dynamics. *Nano Letters* **12**, 893-898, doi:10.1021/nl203956q (2012).
46 Shaheen, S. E. *et al.* 2.5% efficient organic plastic solar cells. *Applied Physics Letters* **78**, 841-843, doi:doi:http://dx.doi.org/10.1063/1.1345834 (2001).
47 Xu, Z. *et al.* Vertical Phase Separation in Poly(3-hexylthiophene): Fullerene Derivative Blends and its Advantage for Inverted Structure Solar Cells. *Advanced Functional Materials* **19**, 1227-1234, doi:10.1002/adfm.200801286 (2009).
48 Yao, Y., Hou, J., Xu, Z., Li, G. & Yang, Y. Effects of Solvent Mixtures on the Nanoscale Phase Separation in Polymer Solar Cells. *Advanced Functional Materials* **18**, 1783-1789, doi:10.1002/adfm.200701459 (2008).
49 Walker, B. *et al.* Nanoscale Phase Separation and High Photovoltaic Efficiency in Solution-Processed, Small-Molecule Bulk Heterojunction Solar Cells. *Advanced Functional Materials* **19**, 3063-3069, doi:10.1002/adfm.200900832 (2009).
50 Hoven, C. V. *et al.* Improved Performance of Polymer Bulk Heterojunction Solar Cells Through the Reduction of Phase Separation via Solvent Additives. *Advanced Materials* **22**, E63-E66, doi:10.1002/adma.200903677 (2010).
51 Peet, J. *et al.* Efficiency enhancement in low-bandgap polymer solar cells by processing with alkane dithiols. *Nat Mater* **6**, 497-500, doi:http://www.nature.com/nmat/journal/v6/n7/suppinfo/nmat1928_S1.html (2007).
52 Moulé, A. J. & Meerholz, K. Controlling Morphology in Polymer–Fullerene Mixtures. *Advanced Materials* **20**, 240-245, doi:10.1002/adma.200701519 (2008).
53 Kim, J.-S., Ho, P. K. H., Murphy, C. E. & Friend, R. H. Phase Separation in Polyfluorene-Based Conjugated Polymer Blends: Lateral and Vertical Analysis of Blend Spin-Cast Thin Films. *Macromolecules* **37**, 2861-2871, doi:10.1021/ma035750i (2004).
54 Coffey, D. C., Reid, O. G., Rodovsky, D. B., Bartholomew, G. P. & Ginger, D. S. Mapping Local Photocurrents in Polymer/Fullerene Solar Cells with Photoconductive Atomic Force Microscopy. *Nano Letters* **7**, 738-744, doi:10.1021/nl062989e (2007).
55 Bull, T. A., Pingree, L. S. C., Jenekhe, S. A., Ginger, D. S. & Luscombe, C. K. The Role of Mesoscopic PCBM Crystallites in Solvent Vapor Annealed Copolymer Solar Cells. *ACS Nano* **3**, 627-636, doi:10.1021/nn800878c (2009).
56 Dang, X.-D. *et al.* Nanostructure and Optoelectronic Characterization of Small Molecule Bulk Heterojunction Solar Cells by Photoconductive Atomic Force Microscopy. *Advanced Functional Materials* **20**, 3314-3321, doi:10.1002/adfm.201000799 (2010).

57 Guide, M., Dang, X.-D. & Nguyen, T.-Q. Nanoscale Characterization of Tetrabenzoporphyrin and Fullerene-Based Solar Cells by Photoconductive Atomic Force Microscopy. *Advanced Materials* **23**, 2313-2319, doi:10.1002/adma.201003644 (2011).
58 Tsoi, W. C. *et al.* Surface and subsurface morphology of operating nanowire:fullerene solar cells revealed by photoconductive-AFM. *Energy & Environmental Science* **4**, 3646-3651, doi:10.1039/c1ee01944a (2011).
59 Dang, X.-D., Mikhailovsky, A. & Nguyen, T.-Q. Measurement of nanoscale external quantum efficiency of conjugated polymer:fullerene solar cells by photoconductive atomic force microscopy. *Applied Physics Letters* **97**, -, doi:doi:http://dx.doi.org/10.1063/1.3483613 (2010).
60 Hamadani, B. H., Jung, S., Haney, P. M., Richter, L. J. & Zhitenev, N. B. Origin of Nanoscale Variations in Photoresponse of an Organic Solar Cell. *Nano Letters* **10**, 1611-1617, doi:10.1021/nl9040516 (2010).
61 Martens, T. *et al.* Disclosure of the nanostructure of MDMO-PPV:PCBM bulk hetero-junction organic solar cells by a combination of SPM and TEM. *Synthetic Metals* **138**, 243-247, doi:http://dx.doi.org/10.1016/S0379-6779(02)01311-5 (2003).
62 Drummy, L. F. *et al.* Molecular-Scale and Nanoscale Morphology of P3HT:PCBM Bulk Heterojunctions: Energy-Filtered TEM and Low-Dose HREM†. *Chemistry of Materials* **23**, 907-912, doi:10.1021/cm102463t (2010).
63 Yang, X., van Duren, J. K. J., Janssen, R. A. J., Michels, M. A. J. & Loos, J. Morphology and Thermal Stability of the Active Layer in Poly(p-phenylenevinylene)/Methanofullerene Plastic Photovoltaic Devices. *Macromolecules* **37**, 2151-2158, doi:10.1021/ma035620+ (2004).
64 Maturová, K., van Bavel, S. S., Wienk, M. M., Janssen, R. A. J. & Kemerink, M. Morphological Device Model for Organic Bulk Heterojunction Solar Cells. *Nano Letters* **9**, 3032-3037, doi:10.1021/nl901511a (2009).
65 Dowland, S. *et al.* Direct Growth of Metal Sulfide Nanoparticle Networks in Solid-State Polymer Films for Hybrid Inorganic–Organic Solar Cells. *Advanced Materials* **23**, 2739-2744, doi:10.1002/adma.201100625 (2011).
66 DeLongchamp, D. M., Kline, R. J. & Herzing, A. Nanoscale structure measurements for polymer-fullerene photovoltaics. *Energy & Environmental Science* **5**, 5980-5993, doi:10.1039/c2ee02725a (2012).
67 Sakai, J., Taima, T. & Saito, K. Efficient oligothiophene:fullerene bulk heterojunction organic photovoltaic cells. *Organic Electronics* **9**, 582-590, doi:http://dx.doi.org/10.1016/j.orgel.2008.03.008 (2008).
68 Peet, J., Senatore, M. L., Heeger, A. J. & Bazan, G. C. The Role of Processing in the Fabrication and Optimization of Plastic Solar Cells. *Advanced Materials* **21**, 1521-1527, doi:10.1002/adma.200802559 (2009).
69 Bavel, S. S. v., Sourty, E., With, G. d. & Loos, J. Three-Dimensional Nanoscale Organization of Bulk Heterojunction Polymer Solar Cells. *Nano Letters* **9**, 507-513, doi:10.1021/nl8014022 (2008).
70 Loos, J. *et al.* Electron Tomography on Micrometer-Thick Specimens with Nanometer Resolution. *Nano Letters* **9**, 1704-1708, doi:10.1021/nl900395g (2009).

71 Oosterhout, S. D. *et al.* The effect of three-dimensional morphology on the efficiency of hybrid polymer solar cells. *Nat Mater* **8**, 818-824, doi:http://www.nature.com/nmat/journal/v8/n10/suppinfo/nmat2533_S1.html (2009).
72 Ruseckas, A., Shaw, P. E. & Samuel, I. D. W. Probing the nanoscale phase separation in binary photovoltaic blends of poly(3-hexylthiophene) and methanofullerene by energy transfer. *Dalton Transactions*, 10040-10043 (2009).
73 Collins, B. A. *et al.* Absolute Measurement of Domain Composition and Nanoscale Size Distribution Explains Performance in PTB7:PC71BM Solar Cells. *Advanced Energy Materials* **3**, 65-74, doi:10.1002/aenm.201200377 (2013).
74 Liu, F. *et al.* Understanding the Morphology of PTB7:PCBM Blends in Organic Photovoltaics. *Advanced Energy Materials* **4**, n/a-n/a, doi:10.1002/aenm.201301377 (2014).
75 Ochiai, S., Imamura, S., Kannappan, S., Palanisamy, K. & Shin, P.-K. Characteristics and the effect of additives on the nanomorphology of PTB7/PC71BM composite films. *Current Applied Physics* **13, Supplement 2**, S58-S63, doi:http://dx.doi.org/10.1016/j.cap.2013.01.010 (2013).
76 Brown, M. E. Determination of purity by differential scanning calorimetry (DSC). *Journal of Chemical Education* **56**, 310, doi:10.1021/ed056p310 (1979).
77 Müller, C. *et al.* Binary Organic Photovoltaic Blends: A Simple Rationale for Optimum Compositions. *Advanced Materials* **20**, 3510-3515, doi:10.1002/adma.200800963 (2008).
78 Miller, N. C. *et al.* The phase behavior of a polymer-fullerene bulk heterojunction system that contains bimolecular crystals. *Journal of Polymer Science Part B: Polymer Physics* **49**, 499-503, doi:10.1002/polb.22214 (2011).

8

INVESTIGATION OF EXCITON HARVESTING IN P3HT

8.1. INTRODUCTION

In this chapter, the fluorescence quenching rate constants for blends of P3HT with three acceptors, M10, C_{61}-PCBM and C_{71}-PCBM are investigated. The understanding of the rates of quenching in small dispersed blends of acceptor is then used as a tool to measure the morphology in device-concentration bulk heterojunctions.

In section 8.2 the fluorescence quenching of P3HT is investigated in small dilute blends of the polymer with the small acceptor molecules M10, C_{61}-PCBM and C_{71}-PCBM. Intriguingly it is found that the rate of quenching in blends of P3HT with M10 is on the order of 5–6 times larger than the equivalent blends with fullerene. As this cannot be explained using a purely exciton diffusion limited model, the Smoluchowski-Collins-Kimball model is implemented which allows for a finite rate of electron transfer upon an encounter between an exciton and a quenching site. The measurement of these electron transfer rates leads to the conclusion that in P3HT:PCBM blends the exciton harvesting is far from being limited by exciton diffusion.

In light of the conclusions of section 8.2, section 8.3 uses the knowledge that the rate of quenching depends predominantly on the amount of available interface between the donor and acceptor, to calculate the amount of exposed surface-area in high concentration blends. The measured surface area is used in conjunction with two models to calculate a characteristic feature size for domains in the P3HT:C_{61}-PCBM bulk heterojunction. Section 8.4 explains the main conclusions generated from the work in this chapter.

8.2. COMPARISON OF EXCITON QUENCHING OF P3HT WITH DIFFERENT QUENCHERS

8.2.1 Introduction

In this section the photo-physical properties of a widely studied[1-18] photovoltaic donor material, poly (3-hexylthiophene-2,5 diyl) (P3HT), are investigated. This is done by introducing small, known quantities of a quencher material into the donor and then measuring the time resolved fluorescence of the resulting blend. Different acceptors were used with the intention of ascertaining whether the fluorescence quenching was limited by the rate of exciton diffusion, or by the rate of electron transfer at the interface, as was the case for the majority of quenchers for PTB7 in chapter 6.

8.2.2 Introduction to Materials Used

8.2.2.1 *P3HT*

Poly (3-hexylthiophene-2,5 diyl) was, for several years, the highest efficiency photovoltaic donor material[1], and achieved such ubiquity in OPV research that it is still a commonly used model system for photophysics research[17-

[19] despite having been far surpassed in terms of photovoltaic efficiency by more recent polymers[20,21]. The P3HT used in this work was *Sepiolid P200* P3HT purchased from Rieke Metals. It had a molecular weight 40,00–50,000 $gmol^{-1}$, and a regioregularity of 98%.

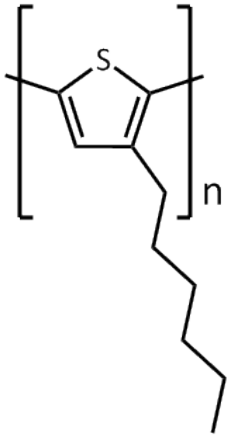

Figure 8.1. Chemical structure of P3HT

The exciton diffusion coefficient in P3HT has been well studied with Shaw *et al.*[15] using a combination of absorption and surface quenching techniques to assign a value of $D = 1.8 \times 10^{-3}$ cm^2s^{-1}, which corresponds to a one dimensional diffusion length of approximately 8.5 nm. The quenchers used for volume quenching were C_{61}-PCBM and C_{71}-PCBM which have been described in chapters 5 and 6 as well as a new electron acceptor, M10 which is introduced in the following section.

8.2.2.2 *M10*

9,10-Dioxo-9,10-dihydro-anthracene-2-carboxylic acid 3-(7-octyl-1,3,6,8-tetraoxo-3,6,7,8-tetrahydro-1H-benzo[lmn][3,8]phenanthrolin-2-yl)-propyl ester, henceforth referred to as *M10* is a small molecule electron acceptor (structure shown below). The material was chosen for its electron affinity of 3.7 eV (calculated from cyclic voltammetry conducted by Dr Brian Fitzpatrick) which

provided a strong driving force for charge separation with P3HT (electron affinity 3.2 eV[22,23]). In addition, the molecule was specifically chosen so that its optical absorption in no way overlapped with the P3HT emission (figure 8.3), meaning that any quenching produced must be short-range (i.e. no long-range FRET as described in chapter 5).

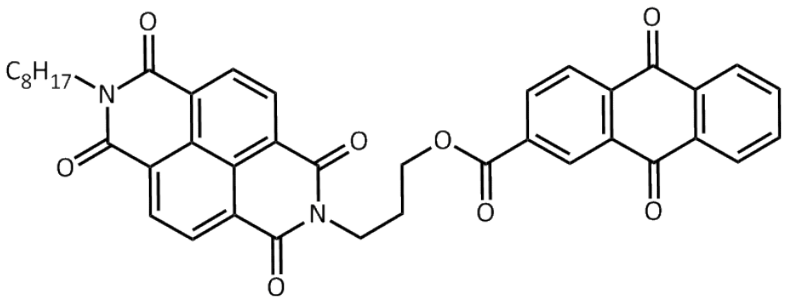

Figure 8.2. The molecular structure of M10, a small molecule electron acceptor. Note the break in conjugation caused by the alkyl-ester link in the centre of the molecule.

The material was synthesised and characterised by Dr Luis Serrano, Dr Brian Fitzpatrick and Prof. Graeme Cooke at the University of Glasgow.

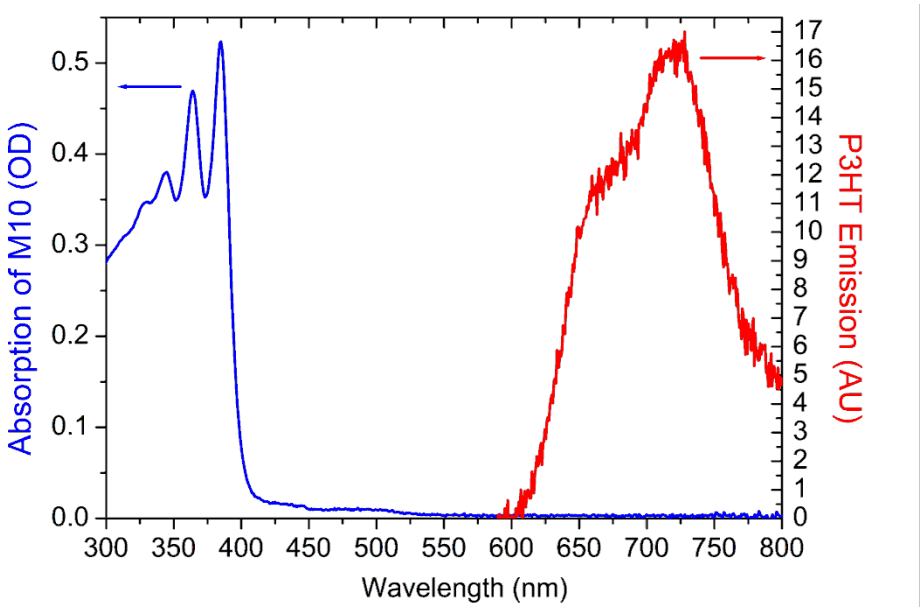

Figure 8.3. The absorption of M10 (blue) and the emission of P3HT (red). There is almost zero spectral overlap between these species and the tail in the absorption of M10 in the range 450–600 nm is very likely to be better assigned to reflection rather than absorption.

8.2.3 Volume Quenching

Blend ratios of 0.2 wt% and 1 wt% quencher in P3HT were spin-coated onto fused silica disks and the time-resolved fluorescence was measured using the streak camera. The time-resolved fluorescence and the corresponding ln(PL ratio)s of the data are shown in the figure below.

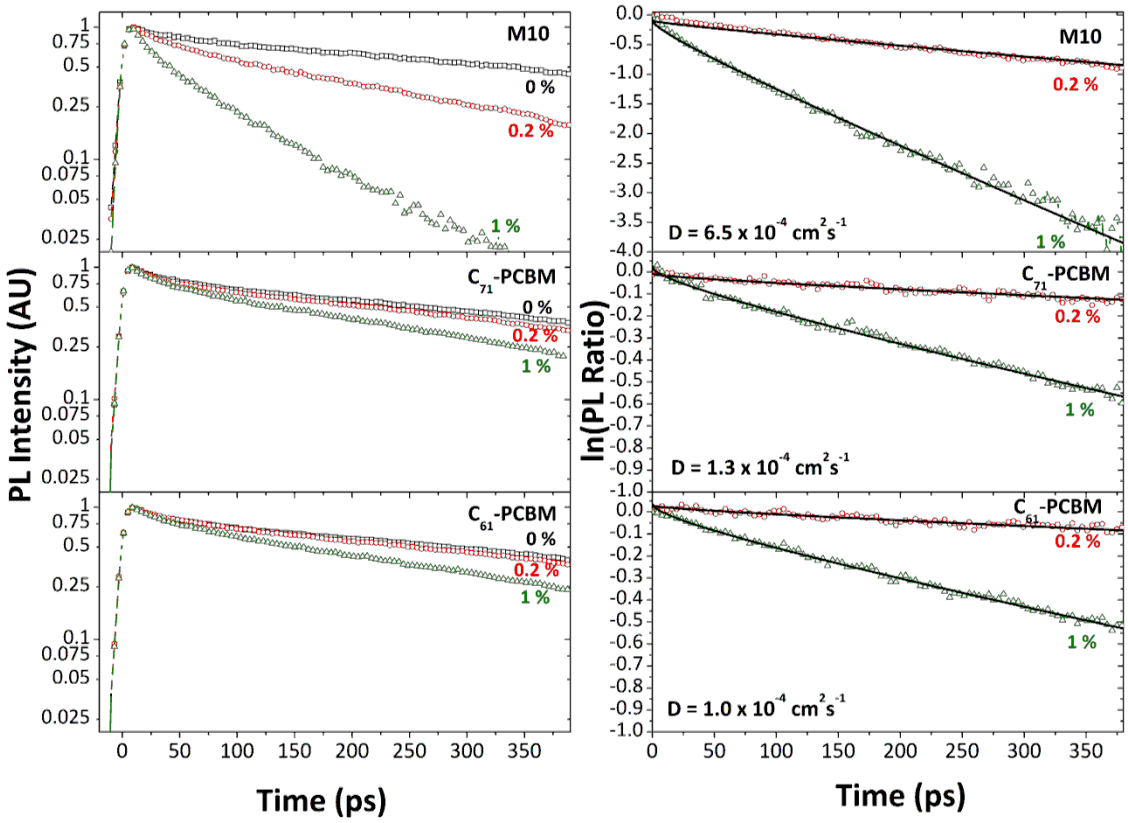

Figure 8.4. Time-resolved fluorescence decays of P3HT with either 0.2 or 1 wt% quencher (left panel). The ln(PL ratio), which represents the natural logarithm of the ratio of quenched film to that of the unquenched film, and the derivative of which is equal to the quenching rate constant. Black lines are fits of equation 8.1 to the data.

If the assumption is made that the limiting factor in fluorescence quenching is the rate at which excitons are arriving at the interface, and that the quenching molecules are well distributed through the solution (assumptions that will be revisited later in this chapter), then the rate of quenching can be described using Smoluchowski boundary conditions (section 4.4.3).

From equation 4.19;

EQUATION 8.1. $$\ln(PL\ ratio) = \int_0^t k_q(t)dt = 4\pi r_c D N_c \left(t + \frac{2r_c\sqrt{t}}{\sqrt{\pi D}}\right) + c$$

where r_c is the distance from a quencher site at which an exciton is quenched, D is the diffusion coefficient, N_c is the concentration of quenching sites and c is an arbitrary constant that is equal to zero for perfectly normalised data.

The critical radius r_c will be equal to the radius of the quencher plus the radius of the exciton. We approximate the radius as the radius of the C_{60} fullerene which is equal to ~0.4 nm[24]. The size of exciton must be less than half the exciton-exciton encounter radius which is 1.8 ± 0.4 nm[15] as this encounter radius will include a long-range FRET component. Thus a reasonable approximation of r_c is 1 nm.

Using this estimate of 1 nm for r_c, equation 8.1 was fitted to the ln(PL ratio)s in figure 8.4, to calculate values of the diffusion coefficient of P3HT. The equation fitted very well to the data but gave the rather surprising result that the apparent exciton diffusion coefficient in P3HT depended on the type of quencher used in the experiment. The fits gave an exciton diffusion coefficient for P3HT of 6.5×10^{-4} cm^2s^{-1} with M10, 1.3×10^{-4} cm^2s^{-1} with C_{71}-PCBM and 1.0×10^{-4} cm^2s^{-1} with C_{61}-PCBM. As the exciton diffusion coefficient is a property of the donor material, not a property of the blend, the choice of quencher ought to have little or no influence on the amount of quenching observed. Additionally all three of these diffusion coefficients are significantly lower than the reported value of diffusion coefficient in the literature, $1.8 \times 10^{-3}cm^2s^{-1}$.

There are three assumptions required for the application of the Smoluchowski model that, if incorrect, will lead to an error in the diffusion coefficient calculated;

a) The critical radius for each molecule must be approximately similar for each quencher.

b) The quenching molecule must remain dispersed in P3HT at the concentrations used.

c) The excitons must be well approximated by instantaneous quenching upon encountering the quencher – it is not permissible for an exciton to pass closer than r_c and then escape.

The validity of these assumptions will now be addressed.

The quencher can influence the critical radius, r_c as a larger molecule will give a larger radius. M10 is approximately twice the radius of a fullerene along one axis, but is significantly shorter along the other two axes. As the rate of quenching depends approximately linearly on the radius this influence is nowhere near sufficient to explain the 5-6 times larger diffusion coefficient calculated using M10. As shown in figure 8.3, the total lack of spectral overlap between the donor and the acceptor means that the long-range Förster Resonance Energy Transfer process, which may increase the effective value of r_c, cannot occur.

Another possible explanation is that the fullerene quenchers are not well distributed through the film, and are instead located in pure fullerene clusters which will reduce the amount of fluorescence quenching that they cause as they will be in contact with a smaller area of P3HT. The miscibility of blends of

P3HT:PCBM is very well studied in the literature and though there is disagreement about the critical concentration at which the two components start to phase segregate, there is consensus that this value is well above 1 wt%. Collins *et al.* measure this value from scanning transmission X-ray microscopy to be 4-10 wt% for highly regioregular P3HT, depending on the batch and annealing temperature[9]. On the other hand Yin *et al.*[25] use small-angle neutron scattering to determine that the miscibility limit for P3HT:PCBM blends is as high as ~20% PCBM in P3HT. In addition, even in the absence of these studies in the literature, the fact that both the 0.2 wt% film and the 1 wt% film can be fit with a single fitting parameter indicates that the morphology for both must be identical. If phase segregation is occurring then it would be expected that a reduction in the quenching efficiency per acceptor molecule would occur, as the larger domains lead to a reduced heterojunction interface and this influence would be larger at higher concentrations[26]. Thus, for these films we can be quite confident that the requirement for molecular dispersion of the quencher is satisfied.

The final requirement, that the rate of electron transfer after an encounter is much faster than the rate at which excitons can escape via diffusion, cannot be so easily justified. In the light of the findings of chapter 6, which showed that in PTB7, another high performance polymer, in many cases the rate of electron transfer did indeed partially limit the rate of fluorescence quenching, it seems entirely possible that the rate of electron transfer is limiting fluorescence quenching in P3HT as well. If the rate of electron transfer from excitons, after encountering the quenching sites, was a limiting factor this would also explain why the exciton diffusion coefficients derived from fits of equation 8.1 to the data in figure 8.4 are 3–18 times

lower than the literature value of exciton diffusion in P3HT calculated from surface quenching and annihilation[15]. It also explains why techniques that calculated exciton diffusion in P3HT using Monte-Carlo modelling of quenching by fullerenes show similar erroneously small values for diffusion coefficients in P3HT[16].

If all the criteria are fulfilled apart from the last requirement for extremely rapid quenching at the interface, then the Smoluchowski-Collins-Kimball (SCK) model should be used.

8.2.4 Smoluchowski-Collins-Kimball Model

The SCK model is an extension of the Smoluchowski model that allows a finite rate constant, k_a, that dictates the rate of quenching once the exciton encounters the quenching site. This model was derived by Frank Collins and George Kimball[27] and is derived and discussed in chapter 4, section 4.4.4. Using the value of the SCK rate constant for quenching from equation 4.26;

EQUATION 8.2.

$$\ln(PL\ ratio) = \int_0^t k_q(t)dt$$

EQUATION 8.3.

$$\ln(PL\ ratio) = \frac{k_a N_c}{k_a + k_d}\left(\frac{8k_a {r_c}^{3/2}\sqrt{k_d t}}{k_a + k_d} + k_d t + \frac{16Dexp\left(\frac{(k_a + k_d)^2 Dt}{(k_d)^2 {r_c}^2}\right) k_a \pi^2 {r_c}^4 ERFC\left(\frac{(k_a + k_d)\sqrt{Dt}}{k_d r_c}\right)}{(k_a + k_d)^2}\right) + c$$

Where k_a is the second order rate constant for quenching of excitons that arrive at the critical radius and $k_d=4\pi Dr_c$ and is the time independent diffusive rate constant.

Equation 8.3 reduces to equation 8.1 when $k_a>>k_d$, as would be expected as it enters the diffusion limited regime. Equation 8.3 was fitted to the same data as in figure 8.4 which is replotted below. The diffusion coefficient used was the literature value[15] of 1.8×10^{-3} cm^2s^{-1} and the critical radius r_c was kept to be 1 nm, following the same justification as described in section 8.2.3.

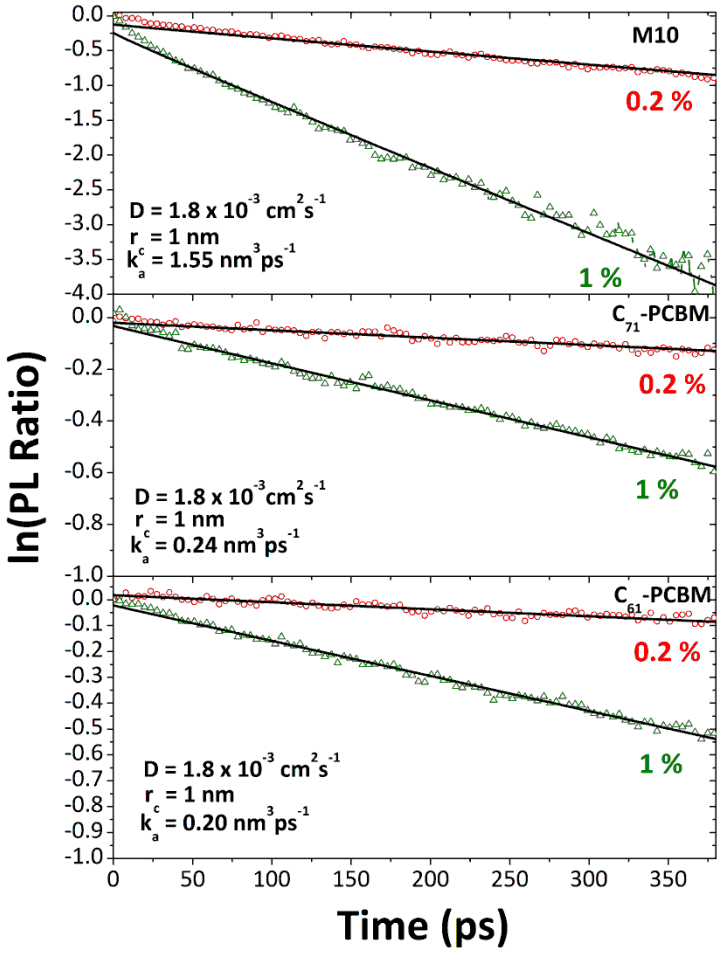

Figure 8.5. The ln(PL ratio) of P3HT with small quantities of the 3 quenchers, M10, C_{71}-PCBM and C_{61}-PCBM . The black lines are fits of the Smoluchowski-Collins-Kimball model (equation 8.3) to the data.

The SCK model fitted very well to the data in all but very short times. k_a is found to be 1.55 nm^3ps^{-1} for quenching by M10, 0.24 nm^3ps^{-1} for quenching by C_{71}-PCBM and 0.20 nm^3ps^{-1} for quenching by C_{61}-PCBM. The values given for the rate constant for electron transfer for excitons at r_c is reasonable, in good agreement with the reported value of exciton harvesting in the very similar photovoltaic material oligothiophene which undergoes energy transfer to a covalently bound fullerene acceptor[28], followed by photoinduced electron transfer with a rate constant (k_q) of 0.1 ps^{-1}. To compare this value directly with k_a it is necessary to make some assumptions to convert it into a second-order rate constant. If it is assumed the electron transfer between these covalently bound molecules (with two fullerenes bound to each oligomer) is analogous to the rate constant in which all excitons are within the quenching radius of two acceptors ($N_c=2/(4/3\pi r_c^3)$) then the value of k_q= 0.1 ps^{-1} corresponds to k_a=0.2 nm^3ps^{-1}.

Because the overall quenching is almost completely controlled by k_a, the value of D used has little influence on the calculated value of k_a. Using the example of C_{71}-PCBM blends, if D is halved compared to the literature value, then the value of k_a fitted is only 11% increased while a 50% increase in the value of D only results in a ~2% decrease in the fitted value of k_a.

There are several interesting implications to these results. Firstly, the finding suggests that in P3HT:fullerene blends, the very long exciton diffusion length means that for these materials combinations, exciton diffusion is not limiting the rate at which excitons can be harvested, even in the dilute regime where diffusion is most important. This is possibly one reason why P3HT is such a successful solar cell material, as its diffusion length has been highly optimised. The

second point is that because diffusion is far from being limiting, we can infer other properties of a quenching process. Analogously to how in a rate in non-diffusion limited chemical reaction depends only on the concentration of reactants and the rate of heterogeneous catalysis (in cases that are limited by the turnover rate of the catalyst) will depend only on the catalytic surface area, the rate of fluorescence quenching is determined entirely by the area of interface available for excitons to undergo electron transfer. If the rate constant for excitons arriving at the quencher k_d is 11 times larger than the rate constant for electron transfer, k_a, as is the case for C_{61}-PCBM, then crudely we might expect on the order of 11 encounters between an exciton and a quencher before the exciton is quenched. This means that in a blend, the quenching rate is only weakly dependent on the exciton diffusion coefficient but is instead controlled almost entirely by simply the amount of interface available between the donor and acceptor at which the quenching process can occur.

8.3. MORPHOLOGY INVESTIGATION

8.4.1 Introduction

Having demonstrated that the rate is limited by the rate of electron transfer at the interface with the acceptor, it can be expected that there will be a linear dependence between the rate of fluorescence quenching and the interfacial area between the donor and acceptor. This allows for a unique opportunity to use the fluorescence of the blend to probe morphology.

8.3.2 Rates of reaction at surfaces

If the rate is dictated by the available surface area then reaction kinetics can be described using the theoretical framework from surface chemistry regarding inhomogeneous catalysis. This is because the situation where a reactant is converted to a product after adsorbing onto a catalytic surface is fully analogous to the situation where an exciton undergoes charge transfer after encountering the fullerene interface. The major difference between typical heterogeneous catalyst kinetics[29] and the rates of exciton quenching in blends is that the concentration of excitons is extremely low compared with the concentration of quenching sites. A typical exciton concentration at t = 0 is 10^{-5} nm^{-3}, while a typical fullerene concentration density would be higher than 10^{-3} nm^{-3} (which would correspond to a mass ratio of less than 0.1 wt%). This means that while in chemical catalysis reaction rates often slow down because all available catalyst sites are occupied (for example in the high concentration regime of a Michaelis-Menten process[29]), in a OPV blend the concentration of excitons is so low compared with the concentration of quenching sites, the probability of two excitons encountering each other at a quenching site or elsewhere is negligible.

In a photovoltaic blend the rate of fluorescence quenching will simply depend on the rate constant for electron transfer, multiplied by the concentration of excitons close enough to the interface to undergo electron transfer. This can be expressed as

EQUATION 8.4. $$\frac{dN}{dt} = -k_a[S]_0\theta[N] - k_f[N]$$

where $[S]_0$ is the total concentration of surface sites, θ is the ratio of occupied sites and k_f is the rate at which the population of excitons falls in the absence of quencher. As there is no attractive interaction between the quenching interface and the diffusing species, (unlike a reactant adsorbing onto a catalyst surface), and the number of sites available is vastly larger than the concentration of excitons, the ratio of occupied sites will depend on an equilibrium constant, K, multiplied by the concentration of excitons;

EQUATION 8.5. $$\frac{dN}{dt} = -k_a[S]_0K[N] - k_f[N]$$

therefore the rate constant for fluorescence quenching can be written as

EQUATION 8.6. $$k_q = k_a[S]_0K$$

The concentration of quenching sites will be proportional to the amount of interfacial area per volume. If we define the ratio of the total exposed fullerene interface as R_I and A_F as the surface area of an individual quencher, then

EQUATION 8.7. $$k_q = k_a c_0 R_I A_F [Q]K$$

where c_0 is the density of quenching sites per unit area of the interface.

In situations where the fullerene is completely dispersed in the film, R_I will be equal to 1 as every quencher has its entire exterior in contact with P3HT. In situations where phase segregation occurs R_I will be reduced. R_I can be thought of as a measure of connectivity as it represents the fraction of the fullerene surface area that is touching other fullerenes. R_I's link to morphology is illustrated in the figure below.

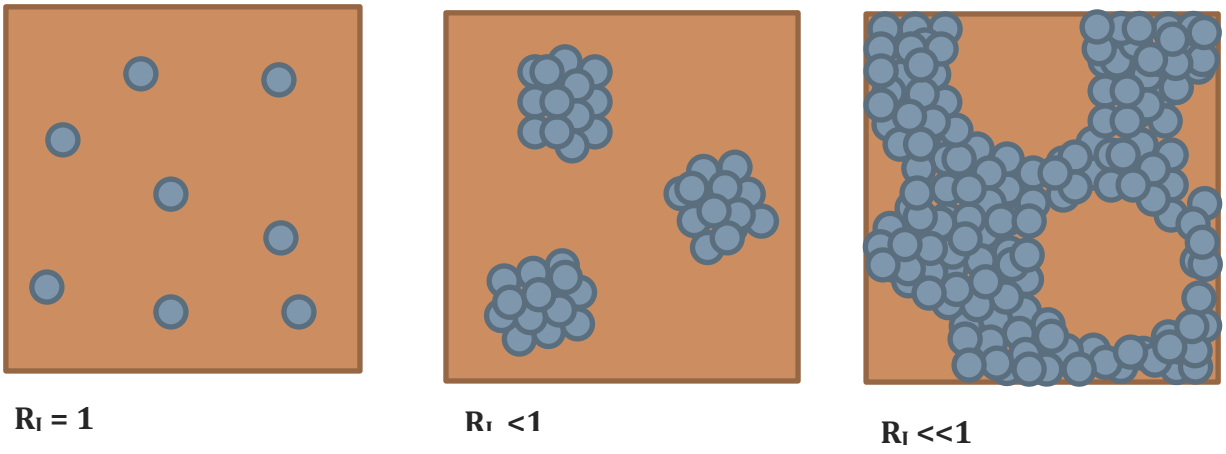

Figure 8.6. As the concentration of fullerene (blue circles) increases, the rate of quenching per fullerene molecule decreases as the fullerene clumps together and hence comes out of contact with the surrounding polymer.

8.3.3 Measuring the rate of quenching in annealed and unannealed P3HT:PCBM Blends

Commonly P3HT:C_{61}-PCBM blends are subjected to thermal annealing in order to improve photovoltaic efficiency, and it is believed that one effect this processing step has is to change the morphology[30-33]. Films of P3HT with varying concentrations of C_{61}-PCBM were spin-coated onto fused silica disks. For each concentration of C_{61}-PCBM, two films were produced, one of which was thermally annealed under nitrogen at 130°C for 20 minutes. The time-resolved fluorescence of the films was then probed using the streak camera. The ln(PL decays) were produced by dividing by the pristine films and taking the natural logarithm of the resulting ratio. These curves are shown in the figure on the following page.

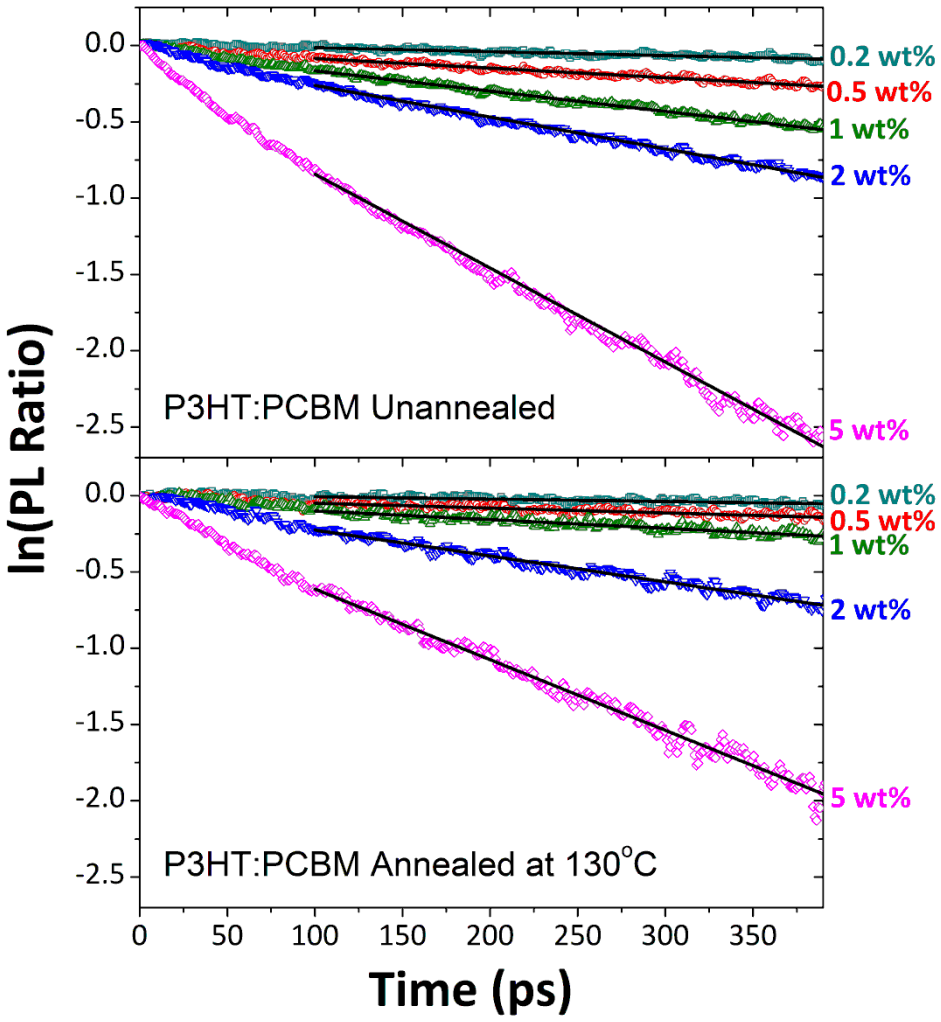

Figure 8.7. The ln(PL ratio) of various concentrations of C_{61}-PCBM in P3HT, either unannealed (above) or annealed at 130°C (below). Black lines are linear fits to the curves, from 100 ps to 380 ps. The gradient of these lines represents k_q.

If the values of k_q, as calculated from the gradients of the black lines in figure 8.7, and other similar plots with different concentrations, are plotted against the mass ratio of the quencher in the blend the following chart can be generated.

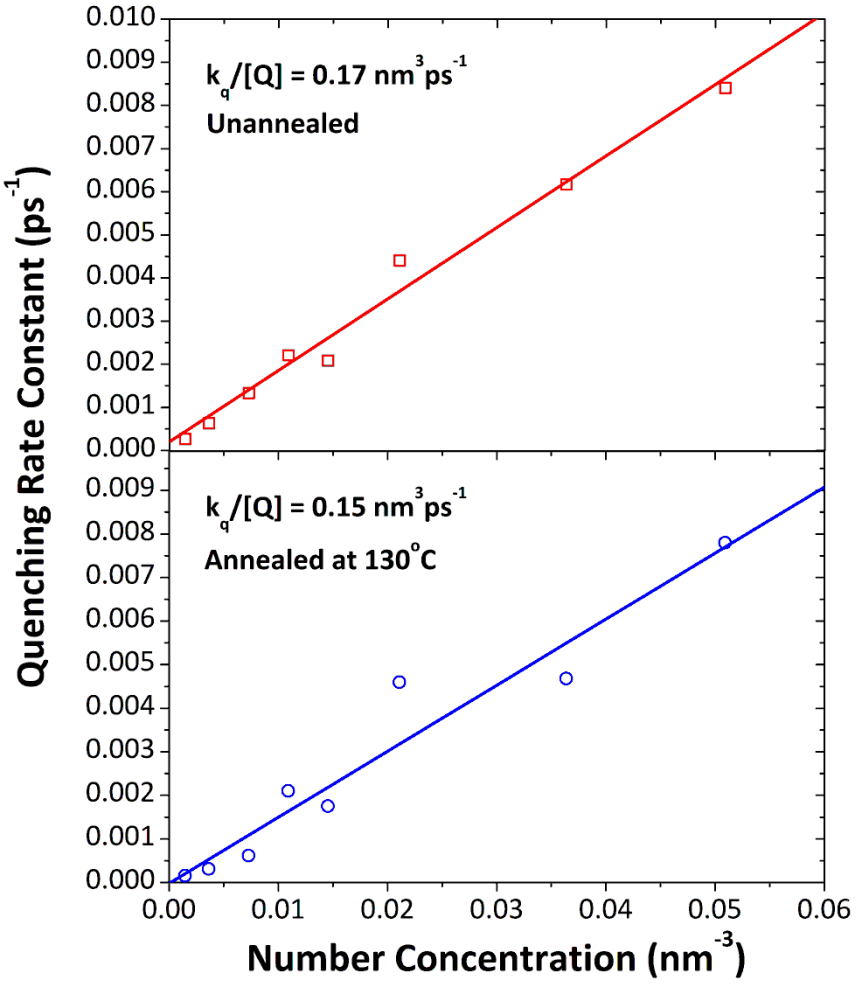

Figure 8.8. The quenching rate constant k_q of different blend concentrations, ranging from 0.2 wt% to 7 wt% are plotted against the number concentration of the quenching sites. The solid lines are linear fits to the data.

The quenching rate constant has a linear dependence on the concentration of quencher, up until 7 wt%. This is an important finding. From equation 8.7 it can be seen that the rate of quenching depends on several coefficients, and the observation that k_q/[Q] is a constant is a strong indication that all of these coefficients are also constant with respect to [Q]. While k_a, c_0 and A_F (the rate of electron transfer at the interface, the concentration of acceptor sites per unit area and the surface area of a fullerene), would be expected to be constant, R_I would be expected to change as the morphology of the blend changes. Thus this linear fit is

evidence that little or no phase segregation occurs in films up until at least 7 wt% C_{61}-PCBM.

The second important implication is that annealing has little or no effect on the film properties. $k_q/[Q]$ was found to be 0.17 nm^3ps^{-1} in annealed films and 0.15 nm^3ps^{-1} in annealed films. This is a very subtle difference and there is inadequate data to determine whether the difference between the annealed and unannealed films is significant. Logically, the coefficients that might change upon annealing are k_a, R_I and K. This is because annealing has been reported[34] to change the electronic properties of the film and hence the rate of electron transfer at the interface. As previously discussed in this chapter, R_I could possibly change after annealing, because the film is believed to change morphology after this processing step. This does not appear to have happened because this change in morphology would be dependent on the concentration of quencher, and the linear fit demonstrates that this is not the case. K could possibly change because this constant depends (weakly) on the rate of exciton diffusion which may increase or decrease after annealing[35,36]. The similarity in the value of $k_q/[Q]$ before and after annealing indicates that it is likely that these values remain approximately similar after this processing step. It is also possible that multiple coefficients change but these changes cancel each other out, for example the exciton diffusion coefficient increases upon annealing but the increasing phase segregation cancels this out and the overall value of $k_q/[Q]$ remains approximately unchanged. This would be a fairly unlikely coincidence that the two effects were of opposite sign and approximately the same magnitude. Additionally, while the morphology effect also ought to depend on the concentration of quencher, the influence on exciton

diffusion will be a property of the donor material and will be independent of the concentration of C_{61}-PCBM in the blend.

The method used to derive k_q from the derivative of the ln(PL ratio) could be extended to encompass blends with higher concentrations in order to observe a drop in R_I and hence infer the blend morphology. Because at higher concentrations the amounts of light produced are hugely decreased, it becomes technically challenging to measure a PL decay in the linear region (100-400 ps) with low enough noise to fit a linear model. While further work is being carried on using this approach, an alternative method to measure the rate of quenching that does not require time resolution, is to use the photoluminescence quantum yield (PLQY) to determine the ratio of excitons quenched in a blend. This method is described in the next section.

8.3.4 Using the blend PLQY to probe phase segregation in P3HT:C_{61}-PCBM blends

Annealed and unannealed blends of P3HT and C_{61}-PCBM as described in the previous section, were analysed using the Hammamatsu Integrating Sphere PLQY instrument. As would be expected the PLQY of the blends decreases as the concentration of PCBM is increased. This is because on average fewer excitons decay radiatively in these higher concentration blends because a higher proportion have been non-radiatively decomposed into their constituent charges upon contact with quenching molecules. A plot of the blend PLQY with respect to blend composition is shown in the figure below.

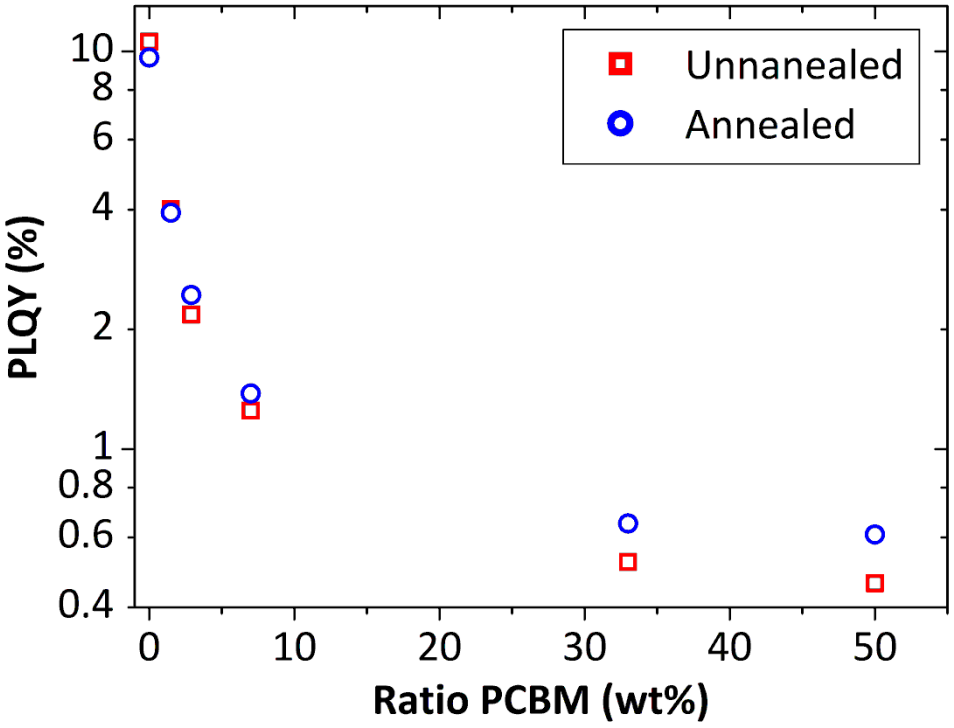

Figure 8.9. A plot of PLQY of P3HT:PCBM blends with respect to the blend ratio. There is a small difference between blends annealed at 130°C (blue circles) compared with those unannealed (red squares).

It can be seen that there is a small difference between the annealed and unannealed blends at high concentration. The unannealed blends at 33 wt% and 50 wt% have a lower PLQY than their equivalent annealed blends. This could be indicative of increased phase segregation in the annealed film. This can be quantified in the following way.

EQUATION 8.8. $$PLQY_{pristine} = \frac{k_r}{k_{nr} + k_r}$$

The PLQY represents the ratio between the rate of radiative decay to the rate of non-radiative decay.

EQUATION 8.9. $$PLQY_{blend} = \frac{k_r}{k_{nr} + k_r + k_q}$$

therefore

EQUATION 8.10.

$$\frac{k_q}{k_{nr} + k_r} = \frac{PLQY_{pristine}}{PLQY_{blend}} - 1$$

Using equation 8.10 and the data in figure 8.9, the following plot of k_q/k_{nr} versus the concentration of C_{61}-PCBM was produced.

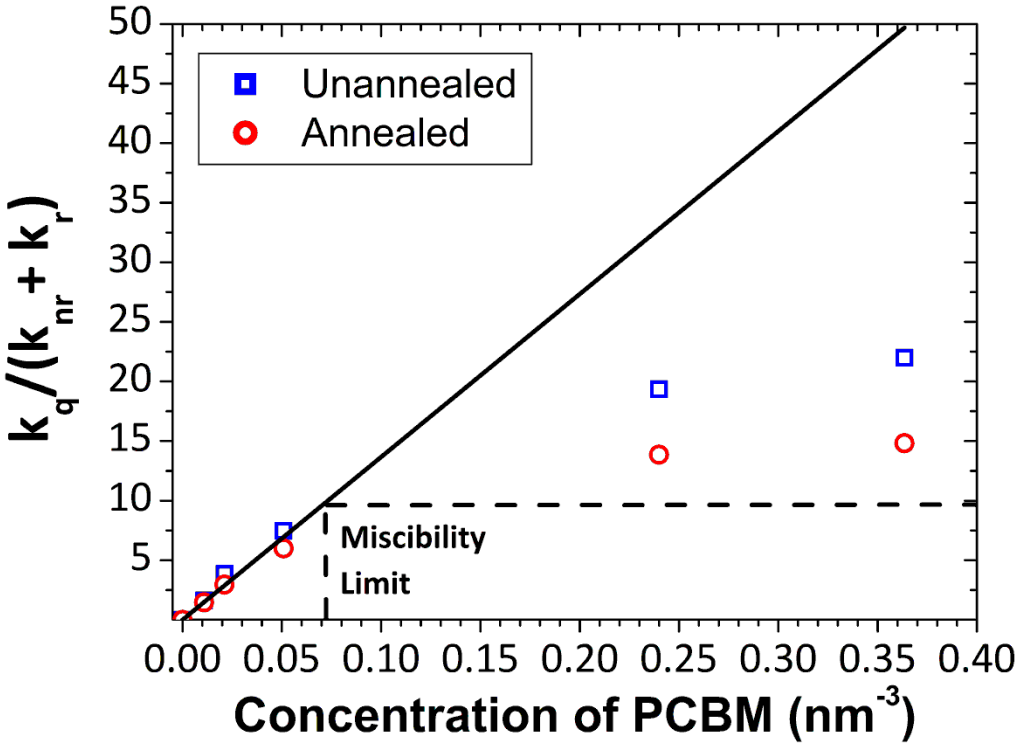

Figure 8.10. The rate constant for quenching (k_q) divided by the rate constant for non-radiative recombination (k_{nr}). The solid black line is a linear fit to the lowest 4 concentrations, 0, 1.5 2.9 and 7 wt% for both the annealed and unannealed quenchers. Dashed line (vertical) represents the concentration of PCBM up to which the two components are fully miscible. Dashed line (horizontal) represents the value of k_q/k_{nr} given by a saturated film of PCBM in P3HT at the miscibility limit.

At the lower blend concentrations, it has been demonstrated in the previous section (figure 8.8), that the value of k_q varies linearly with the concentration of quencher at least up until 7 wt%. As k_{nr} and k_r will be constant for all the films, $k_q/(k_{nr} + k_r)$ will also vary linearly with concentration of quencher (below concentrations of 10 wt%).

8.3.5 Using the Rate of Quenching to Predict Morphology: A Naïve Approach

Though k_q depends on many parameters multiplied by [Q], (as described in equation 8.7) the previous section (8.3.3) demonstrated that these are all constants with respect to annealing and [Q]. The exception is R_I which must change at high concentration if phase segregation occurs. In figure 8.10 it is clear that at lower concentration k_q/k_{nr} increases approximately linearly with the concentration of quencher, until it reaches a point between 0.05 nm^{-3} and 0.24 nm^{-3} (7 wt% and 33 wt%) at which it decreases significantly from this linear trend. The simplest explanation for this behaviour is that while the other parameters, for example the rate of quenching at the interface and rate of exciton diffusion remain constant, R_I the connectivity ratio, decreases as a result of increased connectivity due to the formation of C_{61}-PCBM domains. If the other parameters remain constant, and in the low concentration, linear regime R_I is equal to 1 (as expected, see figure 8.6), then R_I for the two highest concentrations can be calculated as follows;

EQUATION 8.11.
$$linear\ fit = m_{disp}[Q] = \frac{k_a c_0 A_F K[Q]}{k_{nr} + k_r}$$

EQUATION 8.12.
$$\frac{\frac{k_q}{k_{nr} + k_r}}{m_{disp}[Q]} = R_I$$

where m_{disp} is equal to the gradient of the linear fit and represents the value of $k_q/(k_{nr} + k_{nr})$ for a given concentration of dispersed quencher.

It follows that by taking the ratio of the actual reported value of k_q/k_{nr} to the value of the linear fit at the same concentration of quencher, R_I can be calculated.

REDUCED SURFACE AREA RATIO (R_I)	UNANNEALED	ANNEALED
33 wt%	0.59	0.42
50 wt%	0.44	0.30

Thus as the concentration of quencher is increased, the ratio of exposed fullerene surface to total fullerene surface decreases, suggesting an increased connectivity between fullerenes at higher concentrations. It is also clear that this effect is more pronounced after annealing as R_I is significantly smaller in annealed films compared to their unannealed counterparts. This dovetails well with literature observations of phase segregation occurring in highly regioregular P3HT films above 10 wt%[9].

A naïve way to interpret the above values of R_I would be to assume that all domains are pure and the heterojunction can be described as equally sized spherical domains of C_{61}-PCBM.

EQUATION 8.13.

$$R_I = \frac{n_d 4\pi {r_d}^2}{n_q 4\pi {r_q}^2}$$

where n_d represents the concentration of quencher domains, r_d represents the size of these domains, n_q represents the concentration of quenching sites if the quencher was dispersed and r_q the radius of an individual quencher. Because the total volume of the domains formed must be the same as the total volume of the individual quenchers then

EQUATION 8.14

$$n_d \frac{4}{3}\pi {r_d}^3 = n_q \frac{4}{3}\pi {r_q}^3$$

EQUATION 8.15. $$\frac{n_d}{n_q} = \frac{{r_q}^3}{{r_d}^3}$$

consequently R_I can be simplified to

EQUATION 8.16. $$R_I = \frac{r_q}{r_d}$$

This means that by estimating r_d as 1 nm, using the same justification as earlier in the chapter, the following values for a uniform domain size can be calculated using the values of R_I previously tabulated in this section.

UNIFORM DOMAIN SIZE (NM)	UNANNEALED	ANNEALED
33 wt%	1.7	2.4
50 wt%	2.3	3.3

The above values are fairly short compared to many reported domain sizes in 50 %wt P3HT:C_{61}-PCBM blends which have been reported as ~10 nm[4,37,38].

There are many reasons to be sceptical about this domain size calculation, the most significant being that this model assumes homogeneous, pure domains while there is strong evidence in section 8.3.3 and in the literature that C_{61}-PCBM is miscible with P3HT, at least to some extent, meaning that pure P3HT domains ought not to feature in a bulk heterojunction. Additionally the assumption that the fullerene domains are spherical and surrounded by P3HT may not be true,

particularly at 50 wt% when there is as much P3HT as there is C_{61}-PCBM, and hence could be just as easily envisioned as P3HT surrounded by PCBM. In the next section a more sophisticated approach is used to assign characteristic domain sizes from the fluorescence quenching behaviour of the blends.

8.3.6 A More Sophisticated Model to Predict Morphology

The formation of bulk heterojunction morphologies is often explained as being the result of the three component mixture of solvent, donor and acceptor, which forms an emulsion and then dries as the concentration of the solvent decreases during the drying process[39]. Thus a bulk heterojunction may be thought of as a solid emulsion. In order for phase segregation to occur there must be energy associated with the interfacial area between the domains. In interfacial physics this is typically known as the surface energy, γ_s. If the surface energy was zero, two combined liquids would be fully miscible, while if it was extremely high the two components would rapidly separate. Because, in an emulsion, any phase separation indicates a non-zero surface energy, typically the two phases will form shapes with the lowest possible interfacial area between them. In the vast majority of emulsions this means that one material will form what is known as the continuous phase, and one will form what is known as the dispersed phase.

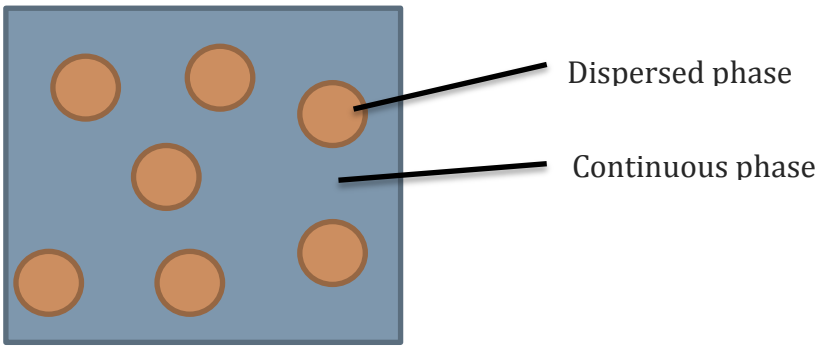

Figure 8.11. A simple illustration of the dispersed phase and the continuous phase in an emulsion. For a given domain size a sphere is the lowest possible interfacial area.

The picture as described above is a simplification of reality. Firstly, the two main emulsion decomposition routes, coagulation and Ostwald-ripening, will rapidly lead to a situation where the domains have a distribution of sizes, the former leading to an increase in average domain size with time and the latter leading to smaller domains shrinking and larger domains growing with respect to time. Secondly, the phase segregation of an emulsion is not a perfect analogue for the phase segregation of a bulk heterojunction. Though there have been some reports of spherical structures forming in bulk heterojunctions of MDMO-PPV[39,40] and PTB7[41,42] which are consistent with a solid emulsion producing minimal interfacial area morphology, there have also been reports of morphology driven by crystal formation giving high anisotropic angular structures[43], something that would never occur in a liquid-liquid emulsion. If we, for now, overlook these shortcomings and approximate the bulk heterojunction as a solid emulsion, then we can describe the trends as follows. At low concentrations of acceptor in donor, below a miscibility threshold, the acceptor is dispersed as single molecules in the donor. As the concentration of acceptor is increased above this threshold, a second acceptor-rich phase emerges, phase segregating into a morphology that minimises

the surface area contact between the two phases; either as the dispersed or the continuous phase.

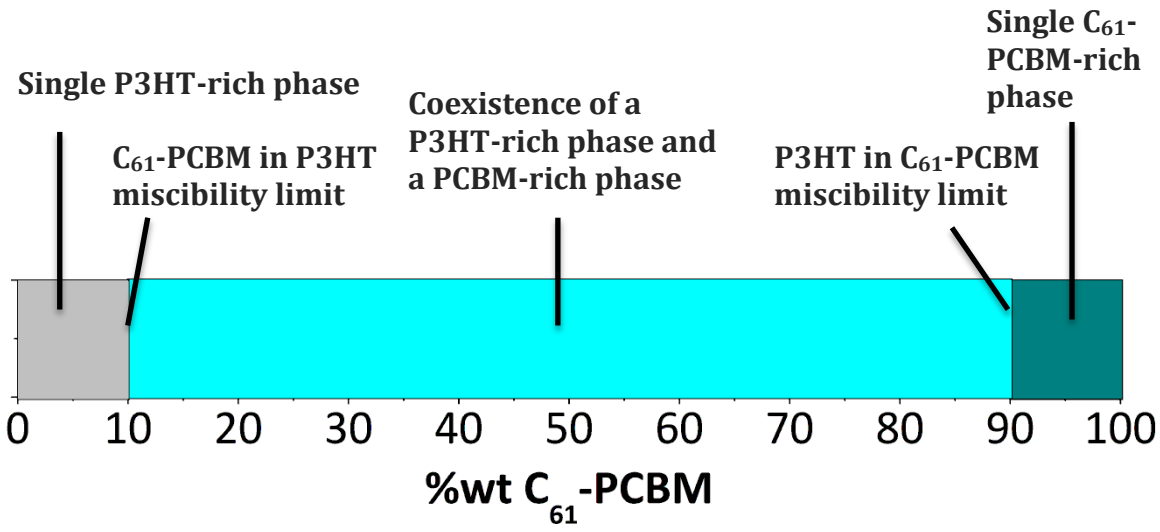

Figure 8.12. The two component phase diagram of P3HT assuming that the behaviour of the mixture is analogous to the mixing of two partially miscible liquids.

Before any further analysis is possible, it is necessary to determine the miscibility limit of C_{61}- PCBM in P3HT, the maximum concentration of C_{61}-PCBM at which the molecules remain fully dispersed in P3HT before forming a new, C_{61}-PCBM rich phase. This could be determined from figure 8.10, as it would be the point at which the trend departs from linearity. Unfortunately due to the lack of data points, this point can only be narrowed down to be between 7 and 33 wt%. In the literature C_{61}-PCBM has been reported to be miscible with high regioregularity P3HT up until 4, 5 and 10 wt%[9,44] depending strongly on the batch of P3HT used. As we have ascertained that the point of phase segregation occurs above 7 wt% we use the highest of these three values, 10 wt% (corresponding to 0.073 nm^{-3}) for the purposes of this analysis.

Thus below 10 wt% the C_{61}-PCBM is considered to be perfectly mixed with the P3HT, above this value the P3HT continues to be in contact with 10 wt%

dispersed fullerene but is also in contact with a new PCBM rich phase. Above the fullerene miscibility limit, the value of $k_q/(k_{nr} + k_r)$ caused by dispersed fullerene will be constant and equal to the value of $k_q/(k_{nr} + k_r)$ at the miscibility limit. This value can be measured from figure 8.10 (dashed line). Therefore k_q/k_{nr} can be described as

EQUATION 8.17. $$\frac{k_q}{k_{nr} + k_r} = \frac{k_{misc}}{k_{nr} + k_r} + \frac{k_{seg}}{k_{nr} + k_r}$$

where k_{misc} is the rate constant for quenching caused by the miscible fullerene, with $k_{misc}/(k_{nr} + k_{nr})$ =9.94 from figure 8.10, and k_{seg} being the rate constant for quenching caused by the phase-segregated component. To calculate the domain size of the phase segregated component it is necessary to calculate the reduced surface area ratio specifically for the fullerene in the phase segregated domains. Combining equations 8.12 and 8.17 gives

EQUATION 8.18. $$R_{Seg} = \frac{\frac{k_q}{k_{nr} + k_r} - \frac{k_{misc}}{k_{nr} + k_r}}{m_{disp}([Q] - [Q]_{misc})} = \frac{\frac{k_q}{k_{nr} + k_r} - \frac{k_{misc}}{k_{nr} + k_r}}{m_{disp}[Q] - \frac{k_{misc}}{k_{nr} + k_r}}$$

where R_{seg} is the reduced surface area ratio, specifically for fullerenes in the C_{61}-PCBM-rich phase and $[Q]_{misc}$ is the concentration at the miscibility limit . Applying equation 8.18 to the data in figure 8.10 gives

REDUCED SURFACE AREA RATIO (R_{SEG})	UNANNEALED	ANNEALED
33 wt%	0.41	0.17
50 wt%	0.30	0.12

If we make the assumption that the C_{61}-PCBM-rich phase is the dispersed, spherical phase, then using equation 8.16 and assuming a quenching radius of a single fullerene of 1 nm, the following domain sizes for the fullerene rich phase can be produced.

R_D (NM)	UNANNEALED	ANNEALED
33 wt%	2.4 nm	5.8 nm
50 wt%	3.3 nm	8.1 nm

These values are larger and in better agreement with the domain sizes of the ~10 nm domain sizes reported in annealed 50 wt% fullerene blends[4,37,38].

For the 50 wt% blends, making the approximation that the miscibility limit of fullerene in polymer is roughly similar to the miscibility limit of polymer in fullerene and that the mass densities are similar, i.e. that the volume of the polymer-rich phase is approximately similar to the fullerene-rich phase, it is actually irrelevant whether the polymer-rich or the fullerene-rich domains are the continuous or dispersed phase; the characteristic domain size of the dispersed phase is the same.

8.4. CONCLUSIONS

This chapter has thoroughly investigated factors that influence the fluorescence quenching of P3HT blends. The first part of the chapter demonstrated that in comparison to a small molecule quencher, M10, C_{61}-PCBM and C_{71}-PCBM quench excitons on a much slower timescale. This is strongly indicative that the exciton undergoes several encounters with the quenching site before electron transfer, meaning that the diffusion limited model of exciton harvesting is inappropriate for these blends. The fluorescence quenching in blends with low concentrations of these three acceptors was fitted with the Smoluchowski-Collins-Kimball model, a model that allows for a finite rate of electron transfer on contact with a quenching site after an encounter due to exciton diffusion. Using literature values of the exciton diffusion coefficient, this allowed the rate of electron transfer from P3HT to M10, C_{61}-PCBM and C_{71}-PCBM of 1.55 nm^3ps^{-1}, 0.20 nm^3ps^{-1} and 0.24 nm^3ps^{-1}, respectively.

Being far from the diffusive limit presented a unique opportunity to measure properties of the higher concentration polymer:fullerene heterojunction morphology. The second half of the chapter described how as diffusion was not limiting, the rate of reaction could be described using the theoretical framework of heterogeneous catalysis, essentially the rate of quenching depends on some constants multiplied by the surface area of heterojunction between donor and acceptor. By using the low concentration films as a measure of how much quenching occurs when all the fullerene molecules are fully dispersed and the entire fullerene surface is in contact with polymer, it is possible to calculate the drop in exposed surface area as the concentration increased. This was assigned to

the fullerene phase segregating, in doing so coming into contact with other fullerene molecules reducing the interface between the donor and acceptor. We found that the average fullerene in a 50 wt% blend was only in contact with P3HT with 44% of its surface area, dropping to 30% after annealing. This measure of fullerene connectivity translated into a characteristic domain size using two models, one very simplistic approximating the blend using pure domains of homogeneous size, and the other more plausible model assuming mixed domains of homogeneous size. This later model found that the domain size increased as the concentration of acceptor increased (up until 50 wt%) and then further increased upon annealing. There is a lot of room for further work in the modelling of characteristic domain size. Future endeavours could involve measuring a wider range of different acceptors to experimentally verify the miscibility limit of C_{61}-PCBM in P3HT. In addition the technique ought to be compared with more direct measures of domain size, such as conductive AFM, allowing a more sophisticated model that can cope with a distribution of domain sizes to be implemented.

8.5. REFERENCES

1 Al-Ibrahim, M., Ambacher, O., Sensfuss, S. & Gobsch, G. Effects of solvent and annealing on the improved performance of solar cells based on poly(3-hexylthiophene): Fullerene. *Applied Physics Letters* **86**, -, doi:doi:http://dx.doi.org/10.1063/1.1929875 (2005).

2 Hoppe, H. & Sariciftci, N. S. Organic solar cells: An overview. *Journal of Materials Research* **19**, 1924-1945, doi:doi:10.1557/JMR.2004.0252 (2004).

3 Cook, S., Katoh, R. & Furube, A. Ultrafast Studies of Charge Generation in PCBM:P3HT Blend Films following Excitation of the Fullerene PCBM. *The Journal of Physical Chemistry C* **113**, 2547-2552, doi:10.1021/jp8050774 (2009).

4 Ruseckas, A., Shaw, P. E. & Samuel, I. D. W. Probing the nanoscale phase separation in binary photovoltaic blends of poly(3-hexylthiophene) and methanofullerene by energy transfer. *Dalton Transactions*, 10040-10043 (2009).

5 van Bavel, S., Sourty, E., de With, G., Frolic, K. & Loos, J. Relation between Photoactive Layer Thickness, 3D Morphology, and Device Performance in P3HT/PCBM Bulk-Heterojunction Solar Cells. *Macromolecules* **42**, 7396-7403, doi:10.1021/ma900817t (2009).

6 Drummy, L. F. *et al.* Molecular-Scale and Nanoscale Morphology of P3HT:PCBM Bulk Heterojunctions: Energy-Filtered TEM and Low-Dose HREM†. *Chemistry of Materials* **23**, 907-912, doi:10.1021/cm102463t (2010).

7 Parnell, A. J. *et al.* Depletion of PCBM at the Cathode Interface in P3HT/PCBM Thin Films as Quantified via Neutron Reflectivity Measurements. *Advanced Materials* **22**, 2444-2447, doi:10.1002/adma.200903971 (2010).

8 Zhao, G., He, Y. & Li, Y. 6.5% Efficiency of Polymer Solar Cells Based on poly(3-hexylthiophene) and Indene-C60 Bisadduct by Device Optimization. *Advanced Materials* **22**, 4355-4358, doi:10.1002/adma.201001339 (2010).

9 Collins, B. A., Tumbleston, J. R. & Ade, H. Miscibility, Crystallinity, and Phase Development in P3HT/PCBM Solar Cells: Toward an Enlightened Understanding of Device Morphology and Stability. *The Journal of Physical Chemistry Letters* **2**, 3135-3145, doi:10.1021/jz2014902 (2011).

10 Sharma, S. S., Sharma, G. D. & Mikroyannidis, J. A. Improved power conversion efficiency of bulk heterojunction poly(3-hexylthiophene):PCBM photovoltaic devices using small molecule additive. *Solar Energy Materials and Solar Cells* **95**, 1219-1223, doi:http://dx.doi.org/10.1016/j.solmat.2010.12.013 (2011).

11 Wang, H. *et al.* Exciton diffusion and charge transfer dynamics in nano phase-separated P3HT/PCBM blend films. *Nanoscale* **3**, 2280-2285 (2011).

12 Chen, J. *et al.* Ternary behavior and systematic nanoscale manipulation of domain structures in P3HT/PCBM/P3HT-b-PEO films. *Journal of Materials Chemistry* **22**, 13013-13022, doi:10.1039/c2jm31124k (2012).

13 Cheng, F. *et al.* Enhancing the performance of P3HT:ICBA based polymer solar cells using LiF as electron collecting buffer layer and UV–ozone treated MoO3 as hole collecting buffer layer. *Solar Energy Materials and Solar Cells* **110**, 63-68, doi:http://dx.doi.org/10.1016/j.solmat.2012.12.006 (2013).
14 Matheson, A. B., Pearson, S. J., Ruseckas, A. & Samuel, I. D. W. Charge Pair Dissociation and Recombination Dynamics in a P3HT–PC60BM Bulk Heterojunction. *The Journal of Physical Chemistry Letters* **4**, 4166-4171, doi:10.1021/jz4020426 (2013).
15 Shaw, P. E., Ruseckas, A. & Samuel, I. D. W. Exciton Diffusion Measurements in Poly(3-hexylthiophene). *Advanced Materials* **20**, 3516-3520, doi:10.1002/adma.200800982 (2008).
16 Mikhnenko, O. V. *et al.* Exciton diffusion length in narrow bandgap polymers. *Energy & Environmental Science* **5**, 6960-6965 (2012).
17 Armbruster, O., Lungenschmied, C. & Bauer, S. Dielectric response of doped organic semiconductor devices: P3HT:PCBM solar cells. *Physical Review B* **84**, 085208 (2011).
18 Kang, H. *et al.* Effect of Fullerene Tris-adducts on the Photovoltaic Performance of P3HT:Fullerene Ternary Blends. *ACS Applied Materials & Interfaces* **5**, 4401-4408, doi:10.1021/am400695e (2013).
19 Aarnio, H. *et al.* Spontaneous Charge Transfer and Dipole Formation at the Interface Between P3HT and PCBM. *Advanced Energy Materials* **1**, 792-797, doi:10.1002/aenm.201100074 (2011).
20 Liang, Y. *et al.* For the Bright Future—Bulk Heterojunction Polymer Solar Cells with Power Conversion Efficiency of 7.4%. *Advanced Materials* **22**, E135-E138, doi:10.1002/adma.200903528 (2010).
21 He, Z. *et al.* Enhanced power-conversion efficiency in polymer solar cells using an inverted device structure. *Nat Photon* **6**, 591-595, doi:http://www.nature.com/nphoton/journal/v6/n9/abs/nphoton.2012.190.html#supplementary-information (2012).
22 Umeyama, T. *et al.* Synthesis and photovoltaic properties of thiophene-imide-fused thiophene alternating copolymers with different alkyl side chains. *Journal of Materials Chemistry* **21**, 12454-12461, doi:10.1039/c1jm11531f (2011).
23 Kim, J. Y. *et al.* Efficient Tandem Polymer Solar Cells Fabricated by All-Solution Processing. *Science* **317**, 222-225, doi:10.1126/science.1141711 (2007).
24 Goel, A., Howard, J. B. & Vander Sande, J. B. Size analysis of single fullerene molecules by electron microscopy. *Carbon* **42**, 1907-1915, doi:http://dx.doi.org/10.1016/j.carbon.2004.03.022 (2004).
25 Yin, W. & Dadmun, M. A New Model for the Morphology of P3HT/PCBM Organic Photovoltaics from Small-Angle Neutron Scattering: Rivers and Streams. *ACS Nano* **5**, 4756-4768, doi:10.1021/nn200744q (2011).
26 Ward, A. J., Ruseckas, A. & Samuel, I. D. W. A Shift from Diffusion Assisted to Energy Transfer Controlled Fluorescence Quenching in Polymer–Fullerene Photovoltaic Blends. *The Journal of Physical Chemistry C* **116**, 23931-23937, doi:10.1021/jp307538y (2012).

27 Collins, F. C. & Kimball, G. E. Diffusion-controlled reaction rates. *Journal of Colloid Science* **4**, 425-437, doi:http://dx.doi.org/10.1016/0095-8522(49)90023-9 (1949).
28 van Hal, P. A. *et al.* Full temporal resolution of the two-step photoinduced energy–electron transfer in a fullerene–oligothiophene–fullerene triad using sub-10 fs pump–probe spectroscopy. *Chemical Physics Letters* **345**, 33-38, doi:http://dx.doi.org/10.1016/S0009-2614(01)00874-0 (2001).
29 Davis, M. E. & Davis, R. J. *Fundamentals of Chemical Reaction Engineering*. (McGraw-Hill, 2003).
30 Lu, Y. *et al.* Temperature-dependent morphology evolution of P3HT:PCBM blend solar cells during annealing processes. *Synthetic Metals* **162**, 2039-2046, doi:http://dx.doi.org/10.1016/j.synthmet.2012.10.012 (2012).
31 Verploegen, E. *et al.* Effects of Thermal Annealing Upon the Morphology of Polymer–Fullerene Blends. *Advanced Functional Materials* **20**, 3519-3529, doi:10.1002/adfm.201000975 (2010).
32 Li, G., Shrotriya, V., Yao, Y. & Yang, Y. Investigation of annealing effects and film thickness dependence of polymer solar cells based on poly(3-hexylthiophene). *Journal of Applied Physics* **98**, -, doi:doi:http://dx.doi.org/10.1063/1.2008386 (2005).
33 Motaung, D. *et al.* Comparative study: the effect of annealing conditions on the properties of P3HT:PCBM blends. *J Mater Sci* **48**, 1763-1778, doi:10.1007/s10853-012-6937-6 (2013).
34 Clarke, T. M., Ballantyne, A. M., Nelson, J., Bradley, D. D. C. & Durrant, J. R. Free Energy Control of Charge Photogeneration in Polythiophene/Fullerene Solar Cells: The Influence of Thermal Annealing on P3HT/PCBM Blends. *Advanced Functional Materials* **18**, 4029-4035, doi:10.1002/adfm.200800727 (2008).
35 Mikhnenko, O. V. *et al.* Effect of thermal annealing on exciton diffusion in a diketopyrrolopyrrole derivative. *Physical Chemistry Chemical Physics* **14**, 14196-14201, doi:10.1039/c2cp41359k (2012).
36 Markov, D. E., Tanase, C., Blom, P. W. M. & Wildeman, J. Simultaneous enhancement of charge transport and exciton diffusion in poly(<math xmlns="http://www.w3.org/1998/Math/MathML" display="inline"><mi>p</mi></math>-phenylene vinylene) derivatives. *Physical Review B* **72**, 045217 (2005).
37 Zhokhavets, U., Erb, T., Hoppe, H., Gobsch, G. & Serdar Sariciftci, N. Effect of annealing of poly(3-hexylthiophene)/fullerene bulk heterojunction composites on structural and optical properties. *Thin Solid Films* **496**, 679-682, doi:http://dx.doi.org/10.1016/j.tsf.2005.09.093 (2006).
38 Chen, D., Nakahara, A., Wei, D., Nordlund, D. & Russell, T. P. P3HT/PCBM Bulk Heterojunction Organic Photovoltaics: Correlating Efficiency and Morphology. *Nano Letters* **11**, 561-567, doi:10.1021/nl103482n (2010).
39 Hoppe, H. & Sariciftci, N. S. Morphology of polymer/fullerene bulk heterojunction solar cells. *Journal of Materials Chemistry* **16**, 45-61, doi:10.1039/b510618b (2006).

40 Hoppe, H. *et al.* Nanoscale Morphology of Conjugated Polymer/Fullerene-Based Bulk- Heterojunction Solar Cells. *Advanced Functional Materials* **14**, 1005-1011, doi:10.1002/adfm.200305026 (2004).
41 Collins, B. A. *et al.* Absolute Measurement of Domain Composition and Nanoscale Size Distribution Explains Performance in PTB7:PC71BM Solar Cells. *Advanced Energy Materials* **3**, 65-74, doi:10.1002/aenm.201200377 (2013).
42 Hedley, G. J. *et al.* Determining the optimum morphology in high-performance polymer-fullerene organic photovoltaic cells. *Nat Commun* **4**, doi:10.1038/ncomms3867 (2013).
43 Kozub, D. R. *et al.* Polymer Crystallization of Partially Miscible Polythiophene/Fullerene Mixtures Controls Morphology. *Macromolecules* **44**, 5722-5726, doi:10.1021/ma200855r (2011).
44 Collins, B. A. *et al.* Molecular Miscibility of Polymer–Fullerene Blends. *The Journal of Physical Chemistry Letters* **1**, 3160-3166, doi:10.1021/jz101276h (2010).

9

GENERAL CONCLUSIONS

Exciton diffusion has long been viewed as a critical process in the functioning of organic photovoltaic cells. It is the mechanism by which excitons are delivered for harvesting at the heterojunction interface and is hence a vital part of photocurrent generation. This thesis re-examined these assertions through the direct measurement of exciton harvesting in blends.

The main thrust of the work contained in this PhD was the refinement of a method of measuring exciton diffusion, known as volume quenching. This involves introducing a small amount of molecules, known as quenchers, into an organic semiconductor that will quench the fluorescence of excitons that encounter them. This system is entirely analogous to a chemical reaction in solution, in which the reactants diffuse until an encounter with another reactant occurs. Because the fluorescence of the film is proportional to the population of the reactant (the excitons), the rate of fluorescence quenching is equivalent to rate of reaction. Thus, much of the theoretical framework with which the rate constant of diffusion-controlled, (or partly diffusion-controlled) chemical reactions can be calculated, is directly applicable to fluorescence quenching in solid films of organic photovoltaic materials.

It has typically been supposed that the electron transfer step occurs on a timescale much more rapid than the rate at which excitons arrive at the interface. Thus, typically excitons are modelled as being quenched instantly on contact with a quenching site, or quenching interface[1-4]. This corresponds to the rate constant of an entirely diffusion-limited chemical reaction which has a rate constant defined by the Smoluchowski rate equation[5]. One of the major findings of this thesis is that a very small proportion of materials investigated fit this simple picture of exciton harvesting. More sophisticated models that include a long-range quenching process, a finite rate of quenching at the interface or a time-dependent diffusion coefficient, have been found to provide the most reasonable explanation of the fluorescence quenching observed.

One of the other major findings of this work is that once the exciton diffusion is properly characterised, and accounted for, the fluorescence quenching can reveal a great deal of information about the other processes that contribute to the exciton harvesting. How much does Förster Resonance Energy Transfer (FRET) contribute to exciton harvesting? What is the rate of electron transfer once the exciton reaches the interface? What is the nanoscale morphology of the film? Exciton diffusion may not, in every case, control the number of excitons harvested, but it is a key piece in the jigsaw when it comes to the overall understanding of the functioning of solar cells. Without being able to characterise the exciton diffusion, the time-resolved fluorescence of the blend can tell you very little about these related critical processes.

In chapter 5 the fluorescence quenching of blends of a high performance photovoltaic material; PCDTBT with C_{71}-PCBM is investigated and compared with

MEH-PPV:C_{61}-PCBM blends. The extremely time-dependent quenching in conjunction with the variation in quenching with respect to the concentration of acceptor, indicated that at low concentrations, in the regime where the acceptors are widely spaced in the film, exciton diffusion helped exciton harvesting in both materials. At higher concentrations long-range energy transfer was the mechanism behind the fluorescence quenching and so exciton diffusion was largely irrelevant. The strong role of FRET in exciton harvesting has been hypothesised and reported in the literature[6-8] and is part of a gradual shift in our understanding of how excitons reach the interface. If FRET does commonly contribute to delivering the exciton to the interface, its role can be enhanced by choosing acceptor materials with a strong absorption overlap with the emission of the donor. This insight has recently been successfully implemented in the literature by the incorporation of a squareine derivative as an electron acceptor that has had its absorption matched to the emission of P3HT, a common photovoltaic donor material[9].

In chapter 6 the time-resolved fluorescence quenching of the highest performance single-junction OPV material, PTB7, was investigated. After the time-dependent exciton diffusion coefficient was measured, the rate of electron transfer to various fullerene and non-fullerene electron acceptors was explored. It was found that the rate of electron transfer varied considerably with respect to the acceptor material and that this dependence was a function of the electron affinity of the acceptor. The rate of electron transfer was found to first increase with increasing electron affinity, before reaching a maximum and then decreasing with further increases in electron affinity. Because the electron affinity of the electron acceptor will determine the energetic driving force for the electron transfer

process, this behaviour is well described by Marcus theory of electron transfer. A critical parameter in a Marcus process is the reorganisation energy, which was found to be approximately 0.4 eV for these materials combinations. Understanding how the reorganisation energy influences the exciton harvesting in the device is very important for designing new materials combinations. This is because it controls the minimum offset between the electron affinities of the donor and acceptor required for efficient electron transfer. As any excess energy difference is at best wasted, and at worst detrimental to charge separation, a good understanding of the reorganisation energy is critical to future OPV materials design.

In chapter 7, instead of investigating a donor material (as was done in previous chapters), the time-resolved fluorescence quenching of a very commonly used electron acceptor, C_{71}-PCBM was investigated. The fluorescence quenching of this material was well described by a time-independent diffusion coefficient, 1.6×10^{-4} cm^2s^{-1}. Knowing the exciton diffusion coefficient of this material offered a unique opportunity to pioneer a new technique to measure the domain size of pure crystals of C_{71}-PCBM from the time-resolved fluorescence of the high performance photovoltaic blend, C_{71}-PCBM:PTB7. This could be achieved because if it is known that quenching will only occur on contact with the donor material, and this can only happen at the edge of the crystal, if the exciton diffusion coefficient is known the characteristic domain size can be measured from the time-resolved fluorescence. The domain size predicted from this new technique of 60 nm was very different from the size of features observed on the surface of the AFM which was found to be 200 nm. The new technique prompted the studying of a horizontal

cross-section of the film by AFM which revealed the previously observed 200 nm features had an internal substructure of 60 nm crystallites. The presence of these smaller domains of pure material was further corroborated with differential scanning calorimetry measurements. The development of a new technique for accurately measuring domain size is a useful additional tool for the OPV community. Admittedly, the method has fairly narrow bounds of applicability; the excitons must be quenched rapidly at the interface, the domains must be pure and approximately spherical and there can be no confounding fluorescence at the same wavelength by the surrounding quencher. Nevertheless, structural information about length-scales smaller than 100 nm is hard to come by in this context where both the donor and acceptor are composed of the same elements, so the technique may well see future use. Furthermore, the linking of the fairly abstract parameter, exciton diffusion coefficient, with much more tangible structural features is an interesting development in itself.

Time-resolved fluorescence quenching measurements in chapter 8 of the commonly used OPV donor material, P3HT, showed that exciton harvesting in these blends was severely limited by the rate of electron transfer at the interface. This was found by comparing the rate of fluorescence quenching in blends of P3HT with a novel non-fullerene electron acceptor, M10, with the rate of fluorescence quenching with the commonly used fullerene electron acceptors C_{61}-PCBM and C_{71}-PCBM. It was found that the rate of quenching in the M10 blend was approximately 6 times faster than that with the fullerene acceptors. If the exciton harvesting was limited by the rate that excitons could reach the quencher then there would be very little dependence on the type of quencher used. Thus a model that allows a rate of

reaction based on diffusion to the acceptor followed by a slower electron transfer step, (the Smoluchowski-Collins-Kimball (SCK) model), was used to fit the time-resolved fluorescence quenching data. Fits using this model indicated that the rate constant for electron transfer from an exciton in P3HT to an adjacent acceptor is 0.20 nm^3ps^{-1} if the acceptor is C_{61}-PCBM, but as high as 1.55 nm^3ps^{-1} if the acceptor is M10. This finding is extremely pertinent to C_{61}-PCBM:P3HT blends because it contradicts the historical view that once the exciton reaches the interface, it will be rapidly quenched. In actuality, a bulk heterojunction must be engineered so that the donor and acceptor mix much more finely than the exciton diffusion length, because the exciton must undergo several encounters with the quenching interface before electron transfer will occur. This agrees well with literature that shows that the P3HT-rich domains have upwards of 10% PCBM[10] in them, meaning a reality of much finer mixing than 10 nm pure domains.

If the exciton harvesting in bulk heterojunctions is almost entirely determined by the rate of transfer at the interface, this greatly simplifies the analysis of fluorescence quenching in these structures at device concentrations because the rate of quenching will be determined exclusively by the amount of donor-acceptor interface. Similarly to the chapter 7 this was used to make predictions about the morphology from the fluorescence quenching. Making some reasonable assumptions about the miscibility of P3HT and C_{61}-PCBM, the steady state fluorescence quenching indicated that the 50 wt% blend had a characteristic domain size (both the donor and acceptor) of 3.3 nm radius in the unannealed film which rises to 8.4 nm after thermal annealing. This final morphological technique requires further external confirmation before the technique can be widely applied

and has the same limitations that apply to the morphological technique in the chapter 7. Nevertheless it offers a glimpse of what might be achieved when linking fluorescence quenching measurements to morphology in device-concentration bulk-heterojunctions.

The work contained in this thesis represents a study of the exciton diffusion coefficients in a wide variety of solar cell materials. It was found that elucidating the role of exciton diffusion in each material opened the door to assigning the contribution of the associated processes in exciton harvesting; FRET, electron transfer and morphology. It is hoped that the holistic understanding of exciton harvesting uncovered by the techniques described in the thesis aids in the rational design of future solar cell materials and the improvement of organic photovoltaic device efficiencies.

9.2. REFERENCES

1 Ruseckas, A., Shaw, P. E. & Samuel, I. D. W. Probing the nanoscale phase separation in binary photovoltaic blends of poly(3-hexylthiophene) and methanofullerene by energy transfer. *Dalton Transactions*, 10040-10043 (2009).

2 Shaw, P. E., Ruseckas, A. & Samuel, I. D. W. Exciton Diffusion Measurements in Poly(3-hexylthiophene). *Advanced Materials* **20**, 3516-3520, doi:10.1002/adma.200800982 (2008).

3 Mikhnenko, O. V. *et al.* Exciton diffusion length in narrow bandgap polymers. *Energy & Environmental Science* **5**, 6960-6965 (2012).

4 Mikhnenko, O. V. *et al.* Temperature Dependence of Exciton Diffusion in Conjugated Polymers. *The Journal of Physical Chemistry B* **112**, 11601-11604, doi:10.1021/jp8042363 (2008).

5 Chandrasekhar, S. Stochastic Problems in Physics and Astronomy. *Reviews of Modern Physics* **15**, 1-89 (1943).

6 Coffey, D. C., Ferguson, A. J., Kopidakis, N. & Rumbles, G. Photovoltaic Charge Generation in Organic Semiconductors Based on Long-Range Energy Transfer. *ACS Nano* **4**, 5437-5445, doi:10.1021/nn101106b (2010).

7 Kandada, A. R. S. *et al.* Ultrafast Energy Transfer in Ultrathin Organic Donor/Acceptor Blend. *Sci. Rep.* **3**, doi:10.1038/srep02073 http://www.nature.com/srep/2013/130625/srep02073/abs/srep02073.html#supplementary-information (2013).

8 Ward, A. J., Ruseckas, A. & Samuel, I. D. W. A Shift from Diffusion Assisted to Energy Transfer Controlled Fluorescence Quenching in Polymer–Fullerene Photovoltaic Blends. *The Journal of Physical Chemistry C* **116**, 23931-23937, doi:10.1021/jp307538y (2012).

9 Huang, J.-S. *et al.* Polymer bulk heterojunction solar cells employing Forster resonance energy transfer. *Nat Photon* **7**, 479-485, doi:10.1038/nphoton.2013.82 http://www.nature.com/nphoton/journal/v7/n6/abs/nphoton.2013.82.html#supplementary-information (2013).

10 Collins, B. A., Tumbleston, J. R. & Ade, H. Miscibility, Crystallinity, and Phase Development in P3HT/PCBM Solar Cells: Toward an Enlightened Understanding of Device Morphology and Stability. *The Journal of Physical Chemistry Letters* **2**, 3135-3145, doi:10.1021/jz2014902 (2011).